Spinel oxides as petrogenetic indicator minerals: Providing a basis for ascent chronometry and geohygrometry using experimental petrology and high-precision *in situ* analysis

A dissertation submitted in partial fulfilment of the requirements for the degree of

Doctor of Philosophy

in

Earth Science

at Massey University, Manawatū campus, New Zealand

Daniel A. Coulthard Jr.

2021

Abstract

The spinel-structured oxides are near-ubiquitously observed accessory phases in ultramafic-felsic igneous rocks. Their status as so-called “petrogenetic indicator” minerals reflects the sensitivity of their composition to changes in the thermodynamic state of magmatic systems. Analyses of their compositions has thus elucidated a wealth of insight into the states and evolution of magmatic systems in general. This thesis builds upon this foundation by illustrating that ionic diffusion within chromian spinel is also highly sensitive to oxygen fugacity. Using the results of internally heated pressure vessel experiments, I show that increasing oxygen fugacity is correlated with higher Fe^{3+} mobility within the spinel structure at the expense of Al over Cr, while Fe^{2+}-Mg systematics follow established empirical relationships. Cr mobility remains slow under highly oxidizing conditions but is still expected to diffuse and approach an equilibrium composition over longer timescales. These observations can be utilized to infer ascent rates for chromite-bearing mafic igneous rocks. Using sparse mineral data from the Troodos Ophiolite, model results indicate that not only are chromites out of equilibrium with residual melts but that they were disequilibrated less than 200 years prior to eruption. Another potential use for spinel minerals is as sensitive geohygrometers. However, routine spectroscopic methods cannot be used for these minerals due to the effect that abundant Fe has on the detection limit of OH during analysis. Instead, ion microprobe methods were utilized and demonstrate that H detection is achievable for titanomagnetite. While chromian spinels do not appear to hold any H, titanomagnetites produced during IHPV experiments and those sourced from natural samples contain an intrinsic H signal intensity that indicates H is soluble to trace concentrations. These results suggest that titanomagnetite should be systematically studied through experimental methods in order to identify how H is incorporated. Thus, the “petrogenetic indicator” status of both chromian and Fe-rich spinel minerals may be expanded into the fields of diffusion chronometry and geohygrometry, respectively.

Dedication

To my folks, Dan Sr. and Paula. To my brother, Brian. To my grandparents, Dixie, John, and Verla. To my aunts, uncles, and cousins- to my family, to whom I owe a great debt, I dedicate this thesis.

Acknowledgments

None of this could have happened without my supervisors Georg, Gert, Hamada-san, Yurimoto-sensei, and Mark. I am grateful for the confidence you have all shown in this endeavour.

Special thanks go to Kenny Horkley at The University of Iowa for accommodating my samples into his busy analytical schedule, Sébastien Jégo for being an amazing host in France, Michel Pichavant for spending time discussing with me some of the intricacies of IHPV work and experimental petrology in general, Kenichiro Tani and Akihiko Tomiya for being outstanding hosts during my time in Tsukuba, Akiko Matsumoto and Takeshi Kuritani for facilitating critical analyses at Hokkaido University, Chris Conway for doing most of the leg work getting my feet wet in Japan, Anja Moebis for the support in the Massey labs, and my office mates, Romana, Chao, Abi, Nessa, Idri, and Raimundo for all of the wonderful times and company during the writing of this thesis.

I would also like to thank the many friends I have made here in New Zealand as well as abroad in France, Japan, and everyone back home in the US. Without the good times we have shared none of this would have felt remotely worth it.

Finally, I would also like to acknowledge Aylin Şen. She has been here with me and for me while I finish this text and has made my life in New Zealand so much fuller.

Thank you all…

Table of Contents

List of Figures

List of Tables

Chapter 1: Introduction

1.1 Spinel-structured oxides as petrogenetic indicators

Spinel-structured oxides (hereafter spinel or spinels) exist in nature as a compositionally complex solid solution of transition metals distributed throughout a cubic close-packed O^{2-} lattice (Figure 1.1). The status of spinel as a "petrogenetic indicator" mineral (Irvine, 1965, 1967) was founded on the premise of the sensitivity of the composition of spinel (with respect to the transition metals) to changes in the thermodynamic state of the petrogenetic system it appears in. State variables temperature (T), composition (X_i) and oxygen fugacity (f_{O_2}) exert primary control over the composition of spinel in equilibrium with a silicate melt. The pressure (P) of the system is thought to exert a minor (if any) influence (Roeder and Reynolds, 1991).

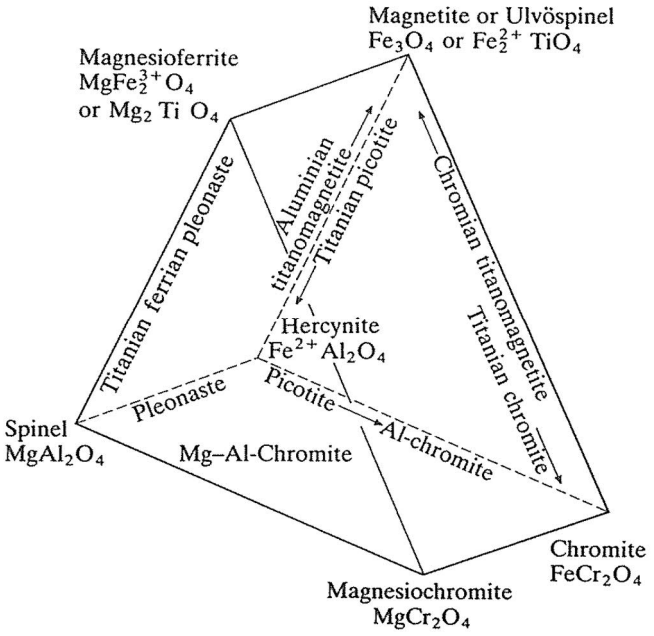

Figure 1.1: Spinel prism showing the various named solid-solutions and endmembers that represent naturally complex spinel minerals. Taken from Deer et al. (1992).

If spinel forms early in the crystallization of primary mantle-derived magmas, then it will either remain stable throughout subsequent differentiation and may even be entrained in melt destined to erupt onto the surface, or it will become an unstable mineral phase and may be resorbed or scavenged by new mineral phases (Roeder, 1994). In the latter scenario spinel may exhibit reaction textures and/or appear as

mineral inclusions in early co-stable mineral phases (e.g. olivine or orthopyroxene) that will still give credence to its prior stability.

The former scenario is a major premise for this thesis. Consider a hypothetical early-formed chromite and the melt immediately surrounding it as a system. For simplicity, let the initial condition of the melt be analogous to those entering deep crust in a continental setting (25 km): *c*. 670 MPa, 1200 °C, f_{O_2} a little more oxidizing than the quartz-fayalite-magnetite (QFM) redox buffer, and a composition (X_i) close to that of primitive arc basalt. These P-T-f_{O_2}-X_i conditions will produce a spinel with a composition that is high in Cr relative to the other transition metals, will likely contain major proportions of Mg and Al, and minor proportions of Fe and possibly Ti.

As the hypothetical magma rises through the crust it will cool and crystallize other distinct mineral phases. These changes have now completely reset the state variables initialized in the previous paragraph. If the chromite that formed early in the melt remains in the melt that was derived from this sequence of displacement and thermochemical differentiation, then the composition of that chromite will have to change in order to maintain an equilibrium condition so long as it remains a stable mineral phase.

1.2 Ionic diffusion in spinel as a function of oxygen fugacity

A great deal of experimental effort has been exerted to investigate the stability and composition of spinel minerals as a function of the state variables above. However, while an understanding of the equilibrium behaviour of spinel is valuable, ionic diffusion within the material is not well constrained with respect to change in some state variables (Vogt et al., 2015).

Turning back to the example of the hypothetical primitive chromite and its melt: as the primitive arc basalt differentiates, common silicate minerals like olivine and/or orthopyroxene will crystallize and deplete the melt in Mg and Fe^{2+}. Elements that are incompatible in these phases (Al, Ti, Fe^{3+}, etc.) will become enriched in the residual melt phase. If these silicate minerals are left behind (fractionated), then the melt-chromite system will approach a new equilibrium condition set by the new P-T-f_{O_2}-X_i condition. As long as the chromite is not destabilized, it will diffusively equilibrate with

the new melt composition towards the new equilibrium condition along vectors in compositional space determined by the diffusivities of the major-minor elements within the spinel structure.

While traditional kinetic studies rely on changing one or two of the state variables (often temperature and pressure) in order to derive inferences regarding diffusivity, Vogt et al. (2015) showed that the diffusivity of Fe is dramatically affected by f_{O_2}. This is important because f_{O_2} exerts primary control over spinel stability and composition, and because it has been shown to co-vary with changes in crystallinity and volatile element pressure/vapour saturation (Cottrell et al., 2020). Such changes may be interlinked (Tollan and Hermann, 2019). Thus, while the diffusivities of many elements in spinels are known (Van Orman and Crispin, 2010), they are known only within a small range of thermodynamic space. To rephrase a conclusion of Vogt et al. (2015), our knowledge of the effect of varying f_{O_2} on the diffusion behaviour in spinel-structured oxides is woefully inadequate.

Thus, one of the objectives of this thesis is to systematically investigate spinels in primitive mafic (boninite) and relatively evolved (low-Mg alkali basalt) compositions using experimental techniques that enable the precise control and monitoring of f_{O_2}. Seed spinels will be chosen and initialized in these experiments to provide a substrate for the diffusion of transition metals into and out of the seed grains. These experiments will be conducted over brief durations corresponding to several hours ($t < 6$ hrs), and then the effects of elemental diffusion will be evidenced by comparing the initial compositions of the seeds to the compositions of the spinels at the end of each experiment.

1.3 The synthesis of hydrous spinel for ion microprobe experiments

Spinels are known as nominally anhydrous minerals (NAMs). While H is not listed in the chemical composition of any NAM, the presence of trace concentrations of H have been reported for several silicate minerals (e.g. Bell and Rossman, 1992). Since mid-ocean ridge basalts, primitive arc tholeiites, and boninites lack primary hydrous mineral phases, the quantification of H in their NAMs is the one of the only ways to infer information regarding the distribution and behaviour of H in the systems that generated the aforementioned magmas. The geohygrometric analysis of silicate minerals suffers

from the fact that H diffuses rapidly in silicate frameworks cooled under low thermal gradients (e.g. Lloyd et al., 2016) and the susceptibility of many mafic minerals to alteration. Chromite, as an early forming mineral, is less susceptible to chemical weathering (Wieland et al., 1988), and the diffusivity of H in spinel-structured minerals is lower at high temperature than other silicate phases (namely clinopyroxene, cf. Bromiley et al., 2017; Lloyd et al., 2016). Thus, spinels may be a better recorder of magmatic H concentrations and a valuable tool for geohygrometric analysis of primitive igneous systems.

The analysis of H in silicate NAMs has been facilitated by Fourier-transform infrared (FTIR) spectroscopy. In Fe-bearing spinel, FTIR cannot be used to determine the concentration of H because the Fe in the crystal structure dramatically raises the detection limit of H to minor concentrations (Figure 1.2, Halmer, 2006; Lenaz et al., 2008). Because of this, a different method of detection must be used to investigate terrestrial spinels for their potential H incorporation, as Fe is almost ubiquitously observed in terrestrial igneous spinels (Barnes and Roeder, 2001).

To this end, the experiments mentioned in the previous sub-section will be initialized under hydrous conditions to synthetically equilibrate seed spinel minerals with hydrous melt compositions. It is anticipated that the diffusivity of H in spinel will allow it to completely equilibrate over the brief durations of the experiments (cf. Bromiley et al., 2017; Van Orman and Crispin, 2010). These samples will then be used in ion microprobe experiments to determine if secondary ion mass spectrometry (SIMS) is a more capable technique than FTIR in quantifying H concentration in Fe-bearing spinel. The quantification of H in synthetic spinel will utilize state-of-the-art ion probe imaging techniques and recently obtained relative sensitivity factors (RSFs, Appendix 1) for spinel minerals, which are required for standardless quantitative SIMS analysis.

1.4 The analysis of natural spinels for their H concentrations

The establishment of a reliable method for the detection and quantification of H in spinel is a major undertaking. Once this objective has been met, it will be possible to use the same method on naturally formed Fe-bearing spinels found in rocks. Natural spinels have been separated from rocks sourced from a variety of tectonic environments

including arcs, ocean islands, and ophiolite complexes representing a wide compositional range from ultramafic-felsic bulk compositions.

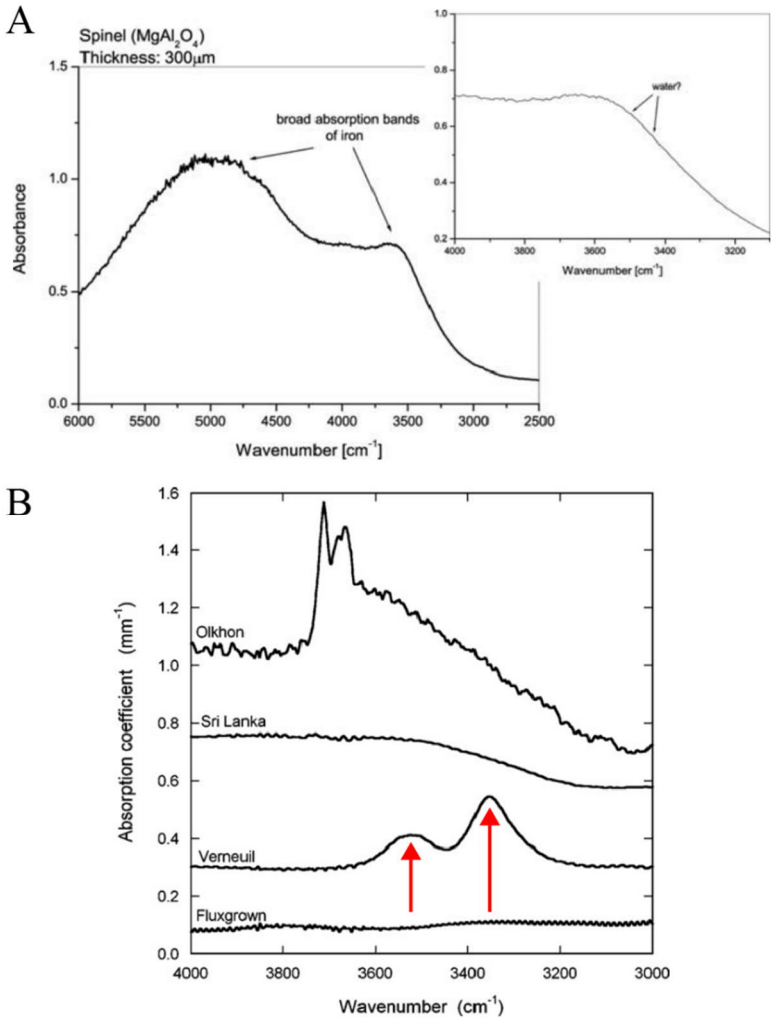

Figure 1.2: FTIR spectra for spinel group minerals. A) taken from Halmer (2006) showing the absorption peaks for Fe in $MgAl_2O_4$ Spinel as well as where the OH peaks should be in spectral space (inset); B) adapted after Lenaz et al. (2008) showing the spectra for natural spinels from the Olkhon composite terrane (Lake Baikal, Russia) and Sri Lanka along with synthetic gem-quality spinels grown via either the flux or Verneuil method. OH peaks are absent in the fluxgrown spinel but are visible in the spectra recovered from the Verneuil-grown spinel (red arrows). The peaks shown reflect 90 μg/g H_2O.

The rationale for studying these samples is multifaceted. Spinels are almost ubiquitously observed accessory mineral phases. They are present during melt generation as the main aluminous phase of the upper mantle (Haggerty, 1995), they again form early in mafic melts (as chromite) in tholeiites and boninites, Ti-rich magnetite forms late in differentiated tholeiites, and in calc-alkaline series volcanics

they are constant liquidus phases. Finally, knowledge of volatile element behaviour is invaluable for predictive modelling of volcanic hazards, so if spinel becomes a suitable material for geohygrometric analysis, then the results of this study will have a high impact in the geologic hazard community.

Thus, the last objective is to perform ion microprobe experiments using routine analysis techniques on natural Fe-bearing spinels from the Izu-Bonin arc, arc rocks from Taranaki Volcano and the Taupo Volcanic Zone (New Zealand), Hawaii, and the Troodos Ophiolite (Cyprus). These data will be the first of their kind, and the results of these experiments will comprise the foundation of a new field of study in geohygrometry.

1.5 Objectives

This thesis attempts to broaden the applicability of chromian and Fe-rich spinels as petrogenetic indicator minerals. The sensitivity of the former to change in magmatic redox state is an underutilized and understudied phenomenon in geoscience, and the solubility of H in both mineral phases is completely unknown at this time. Thus, using novel experimental and analytical techniques, the objectives of this thesis are the following:

1. To conduct IHPV experiments at oxidizing conditions analogous to mid- to lower crustal environments in arc settings to enable the kinetic equilibration of seed spinel minerals with either boninitic or basaltic melts and to improve our understanding on the effect of oxidation state on equilibration rates. The presence of H in these melts will facilitate the hydration of the spinels.
2. To conduct high-resolution ion microprobe experiments on the products of the IHPV experiments to determine if H can be detected in Fe-bearing spinel minerals.
3. To conduct routine ion microprobe experiments on natural spinel minerals prepared in the same way as the equilibrated synthetic spinels so that the H concentrations of natural Fe-bearing spinels may be quantified for the first time.

Chapter 2: Literature Review

2.1 Introduction

The topics covered in this review include geologic backgrounds for the Troodos Ophiolite (Cyprus), the Manganui D member of the Manganui Formation of Taranaki Volcano (New Zealand), the shore sediments of Whangamata Bay of Lake Taupo (New Zealand), Papakolea Beach (Hawaii), and Ani-jima of the Chichi-jima Island Group (Ogasawara Islands, Japan). Also included are sections detailing current knowledge of H in nominally anhydrous minerals, including spinels, and finally a synthesis of the contributions of experimental petrology to our understanding of spinels.

2.2 Geological backgrounds for natural samples investigated

2.2.1 The Troodos Ophiolite, Cyprus

2.2.1.1 Origin of debate surrounding the tectonic emplacement of Cyprus,

The Troodos Ophiolite (Figure 2.1) is a piece of oceanic lithosphere that is currently exposed on the island of Cyprus in the eastern Mediterranean Sea. It is *c.* 65 km south of Turkey, *c.* 100 km west of Syria, a geoheritage site, and an important locality in terms of geologic history. For many decades, the Troodos Ophiolite has been studied as a natural laboratory with many models of seafloor structure, alteration, and ore mineralization having originated there.

Debate surrounding the tectonic origin of the Troodos Ophiolite can be traced back to the earliest publications describing the structures and field relationships preserved on the island. Initial reports came from Bishopp (1952), who provided a brief synopsis of what was known at the time from geological survey reports and reported that extensive reconnaissance mapping of the igneous suite was underway. The first real synthesis of data came from Gass (1968), who integrated early geophysical work (Gass and Masson-Smith, 1963) and results from land surveying (Gass, 1958) to define the units of the igneous stratigraphy present within the geologic context of the rest of the island. Discussion in this text is mainly concerned with forming a hypothesis regarding the origin of the igneous suite. According to Gass (1968), the north-south strike of the sheeted dike complex correlates well to off-shore magnetic anomalies (Vogt and Higgs,

1968), which led him to postulate that at least the ultramafic core and the overlying intrusive complex could have formed at a mid-ocean ridge (which was also suggested by Gass and Masson-Smith, 1963).

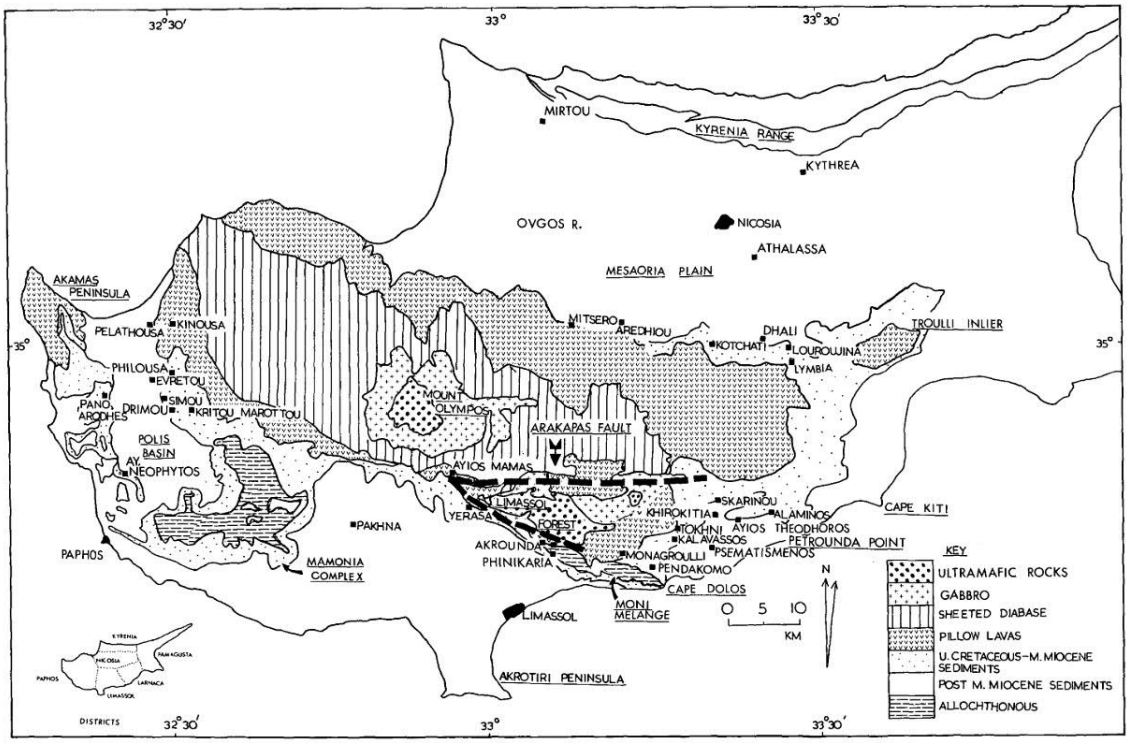

Figure 2.1: Map of Cyprus with the major units of the Troodos Ophiolite given. Taken from Robertson (1977).

The model of a mid-ocean ridge origin was thus established in the late sixties. In the early seventies, Moores and Vine (1971) published a systematic overview of multiple hypotheses that had branched out from the work of Gass (1968), while making it clear that their preferred tectonic model was still that the Troodos Massif represented a slice of oceanic crust and mantle that had been upthrust with the closure of the Tethys Ocean. Two years later, Miyashiro (1973) published a novel geochemical study of the Troodos extrusive sequence and proposed that many samples from the “lower pillow lavas” form calc-alkaline trends in FeO/MgO vs SiO_2 space. It is important to note that many samples also did not form calc-alkaline trends (roughly 2/3 of the samples). Nevertheless, using this dataset Miyashiro (1973) suggested that the Troodos Ophiolite formed near an island arc rather than at a mid-ocean ridge environment as concluded by Moores and Vine (1971). These early studies established a foundation for debate that has continued to the present day (e.g. Pearce and Robinson, 2010; Regelous et al., 2014; Woelki et al., 2020).

There is a major structure preserved in the southern portion of the Troodos ophiolite separating the core of the massif, including the sheeted dike complex, from the Limassol Forest complex. This structure is the Arakapas Fault belt (upper dashed line in Figure 2.1), and Simonian and Gass (1978) interpreted the feature as an oceanic transform fault similar to those observed in modern mid-ocean ridge systems.

Robertson (1977) detailed the recent tectonic evolution of the ophiolite. Based on several preliminary reports from the Geological Survey of Cyprus, Robertson (1977) begins by outlining the late-Cretaceous basin development that occurred prior to extensive uplift during Miocene times. Beginning in the early-Miocene, Robertson (1977) points out that reef development and erosional features in the northwest portion of Troodos (Akamas Peninsula) indicate that focused regional uplift was occurring. High-angle normal faults separate this block from the nearby Polis Basin, where pelagic sedimentation was occurring at the same time interval, which indicated that Cyprus was, at that time, perhaps set in a marine slope environment. The middle-Miocene saw punctuated and rapid uplift of most of the core of the modern island, and subaerial exposure and erosion occurred throughout the Troodos Massif at this time. Direct evidence of this is found at Petrounda Point (Larnaca District, Figure 2.1), where slumped sedimentary beds and tightly folded soft-sediment deformation features abound. However, the Limassol Forest region (Figure 2.1) was not significantly eroded until the late middle-Miocene, indicating that the southern portion of the Troodos was not rendered subaerial until a little later. The northern part of the island saw the development of the Kyrenia Range by this time, and at the end of the Miocene, a large sedimentary basin had formed between it and the main part of the igneous complex (*op. cit*.). Broad regional uplift of most of Cyprus would not occur until Pliocene-Pleistocene times.

2.2.1.2 The 1975 debate over the tectonic setting of the Troodos Ophiolite

In 1975, a series of comments and replies to Miyashiro (1973) appeared in Earth and Planetary Science Letters. Here are reviewed the fundamental arguments of those comments and replies.

Direct response to the work of Miyashiro (1973) was compiled by Hynes (1975). Hynes (1975) disputed the use of altered whole rock chemistry to infer tectonic origin and

pointed out that the regional geologic context supported a mid-ocean ridge, rather than an island arc, origin for the Troodos Ophiolite. In reply, Miyashiro (1975a) criticized the assumptions Hynes (1975) made in regard to the application of regional geology to the tectonic setting of the Troodos; insisting that the regional structures cannot definitively be used to assign tectonic setting to either a mid-ocean ridge or an island arc. Instead, Miyashiro (1975a) doubled down on the assertion that the distribution of SiO_2 vs FeO/MgO data for the Troodos were more similar to island arc examples (providing data from Kermadec, Northeast Japan, Abyssal tholeiites, and others) than they were to rocks derived from mid-ocean ridges. He also disputed the claim that the rocks of the Troodos were altered enough to overprint their calc-alkaline signatures and SiO_2 concentrations, citing that the amount of silica metasomatism would need to exceed 70%. Additional comment by Moores (1975) offered some support for the arguments of Miyashiro (1975a) while agreeing with Hynes (1975) regarding the alteration of the whole rock samples. Moores (1975) insists that the original bulk compositions of lavas are strongly altered by burial metamorphism, and he further points to petrographic descriptions of the Troodos rocks to show that they are all altered, at least, to a zeolite-greenschist facies metamorphic grade. In the end, Moores (1975) claims that the geochemical arguments are invalid in light of strong structural and stratigraphic/sedimentological arguments that strongly support the hypothesis that the Troodos Ophiolite formed at a mid-ocean ridge; although he also acknowledged that ophiolites, in principle, may form anywhere in an ocean basin including at island arcs. Miyashiro (1975b) replied to Moores (1975) in a thorough rebuttal. Here, Miyashiro (1975b) insisted that the hypothesis of a mid-ocean ridge origin for the Troodos cannot be proven using the evidence cited by Moores (1975). Additional argument centred around the style of metamorphism observed in the rocks of the Troodos, and in the end, Miyashiro (1975b) pointed out that the style of metamorphism observed in the Troodos does not occur in a mid-ocean ridge setting. Finally, Gass et al. (1975) offered a final critical comment on the discourse between Hynes (1975) and Miyashiro (1975a). Here, Gass et al. (1975) systematically applied field observations and chemical weathering arguments to show that the calc-alkaline trends in the dataset of Miyashiro (1973) were just as likely generated by alteration and that the volcanological argument given did not adequately represent the observable geology exposed in the Troodos Ophiolite.

2.2.1.3 Modern interpretation of the Troodos Ophiolite

Pearce and Robinson (2010) revisited the debate started by Miyashiro (1973) using the "Mehegan-Robinson" glass samples and formed comparisons between their compositions and compositions of fresh glasses recovered from several proposed tectonic analogues for the Troodos Massif. They also updated and expanded upon the model of Miyashiro (1973) with revised classifications of boninite rocks and new subdivisions of the tholeiites of the pillow lava sequence. Importantly, new developments were proposed based on revised interpretation of major element geochemistry, and together, these data were used to suggest that the Troodos Massif is composed of oceanic crust that was built from tholeiite then boninite near a trench setting. Geodynamic interpretation is offered in the form of slab roll-back, which the authors believe is justified based on inferred high mantle potential temperatures for the tholeiites of the igneous suite (T_P = *c*. 1400 °C). Since the trace element compositions of the glasses supported an island arc origin for the Troodos, so Pearce and Robinson (2010) proposed that the Troodos formed during subduction initiation.

Regelous et al. (2014) offered a different interpretation of glass compositions. Combining high-resolution igneous stratigraphy, mass spectrometry, and detailed field observations, the authors proposed that a lack of evidence for sub-aerial exposure among the pillow lavas, the internal structure of the igneous stratigraphy (including the shallow intrusive section of the complex), and tectonic models made for Troodos analogues to suggest that the Troodos Massif was formed at a triple junction. They propose that the tholeiites they analysed belong to a back-arc basin domain and that later boninites likely formed as the ridge propagated towards a shallow and hot subduction-modified mantle source, which melted to form boninitic liquids. They disputed the causal relationship proposed by Pearce and Robinson (2010), claiming that subduction initiation need not be invoked to explain the geochemical trends preserved in the glasses of the Troodos Ophiolite.

The study of Woelki et al. (2020) is a direct extension of the work of Regelous et al. (2014), which focused on the well-known Akaki Canyon locality in the northern part of the Ophiolite. Woelki et al. (2020) studied several additional localities and focused on adding a wealth of glass data sourced from the southern region of the Ophiolite. Also added was an extensive study of glass water concentrations (via FTIR), which were

used in conjunction with traditional laser ablation and electron probe analyses to show that the lavas that made-up the extrusive sequence were likely emplaced five kilometres below the seafloor and that the Ophiolite likely formed in the tectonic setting defined by Regelous et al. (2014). A secondary but important observation was that boninitic glass was found only in the southern portion of the Ophiolite complex, which contends with earlier research performed on the Troodos (Cameron, 1985). Boninites found in the northern part of the Ophiolite were likely classified based on whole-rock geochemistry, which is common in other boninite localities (e.g. Coulthard Jr et al., 2021).

2.2.2 The Manganui D member of the Manganui Formation, Taranaki Volcano, New Zealand

The Manganui formation was named by S.J. Whitehead in his unpublished 1976 thesis describing the eastern flanks of Taranaki Volcano, New Zealand. He postulated that the tephras he mapped were derived from Fanthams Peak, the satellite vent on the southern flank of Taranaki, rather than the main vent. These hypotheses would not be accepted until this century (Torres-Orozco et al., 2016; Turner et al., 2008a). However, by the mid nineteen nineties the extent and thickness of the formation had been more or less established (Alloway et al., 1995).

A detailed description of the tephra sampled for this study is found in Torres-Orozco et al. (2016). Precisely, we targeted titanomagnetite-bearing scoria from the Manganui D2 member of the Manganui formation as sampled by the authors. The Manganui D member is the thickest member in the Manganui formation. At least three pyroclastic deposits comprise this member (D1, D2, and D3). Layers D1 and D2 are exposed in several localities and are reverse to normally graded well-sorted clast-supported beds. They are dominated by juvenile lithics, moderately crystalline pumice lapilli, and scoria lapilli. Layer D3 is a complex deposit with 4 bedsets. The degree of alteration for the lithics and lapilli in this layer is high relative to the other two. For this reason, scoria samples from near the top of D2, according to the thesis of Dr. Torres-Orozco (2017), were selected for analysis.

Contemporary correlations and age constraints for Taranaki extrusives have been provided by Turner et al. (2011) who suggested that the Manganui tephras were deposited over a period of at least 600 years. The dataset in this study is based on lake

core sediments and limited sampling from the flanks of the volcano itself. Later, Damaschke et al. (2017a) compiled a high-fidelity database of Taranaki eruptive units using cores taken from a greater number of lakes surrounding the volcano. The correlations provided by the authors are based on multiple methods including lithostratigraphy and titanomagnetite-based chemostratigraphy, the latter method being pioneered by Cronin et al. (1996) and built upon by Turner et al. (2008a). A later publication (Damaschke et al., 2017b) combined these results with observations made by Torres-Orozco et al. (2016) to provide a comprehensive correlation between proximal and distal Taranaki tephras. Based on these recent data, the Manganui D member was erupted from Fanthams peak *c*. 3,000 years ago and was deposited as a fall tephra.

2.2.3 Shoreline sediments at Kinloch, Whangamata Bay, Lake Taupo, New Zealand

The most recent large-scale excavation of the Taupo Caldera occurred at *c*. 1.8 ka to generate the Taupo Ignimbrite (Wilson and Walker, 1985). This ignimbrite radically altered the local environment, stripping *c*. 20,000 km^2 of vegetation from the surface (Smith, 1991). The resulting topographic changes to the landscape, i.e. the mantling of local topographic highs by *c*. 15 m of ignimbrite and the filling of topographic lows by much higher volumes of volcaniclastic material (Wilson, 1985) completely destroyed the local hydrology creating a landscape dominated by ephemeral small-scale lakes and ponds (Manville, 2001). The short-lived nature of these features owes to the fact that the unconsolidated volcaniclastic sediments of the Taupo Ignimbrite formed weak dams, which broke frequently to drain the basins and re-establish the hydrologic network in the region. A prime example of this is found in Lake Reporoa, which drained to re-establish the Waikato River system and the primary natural tributary filling Lake Taupo (Manville, 2001).

Lake Taupo itself (Figure 2.2) was likely emptied during the eruption at *c*. 1.8 ka, and refilling this lake to its high-stand (*c*. 34 meters above current lake level) took at least 15 years if infill rates were sustained at or near a natural maximum (Riggs et al., 2001). A more conservative estimate is *c*. 20 years using modern average infill rates (*op. cit.*). During this time, transgressive lacustrine deposits were generated and are preserved at and below the terrace surrounding the modern lake.

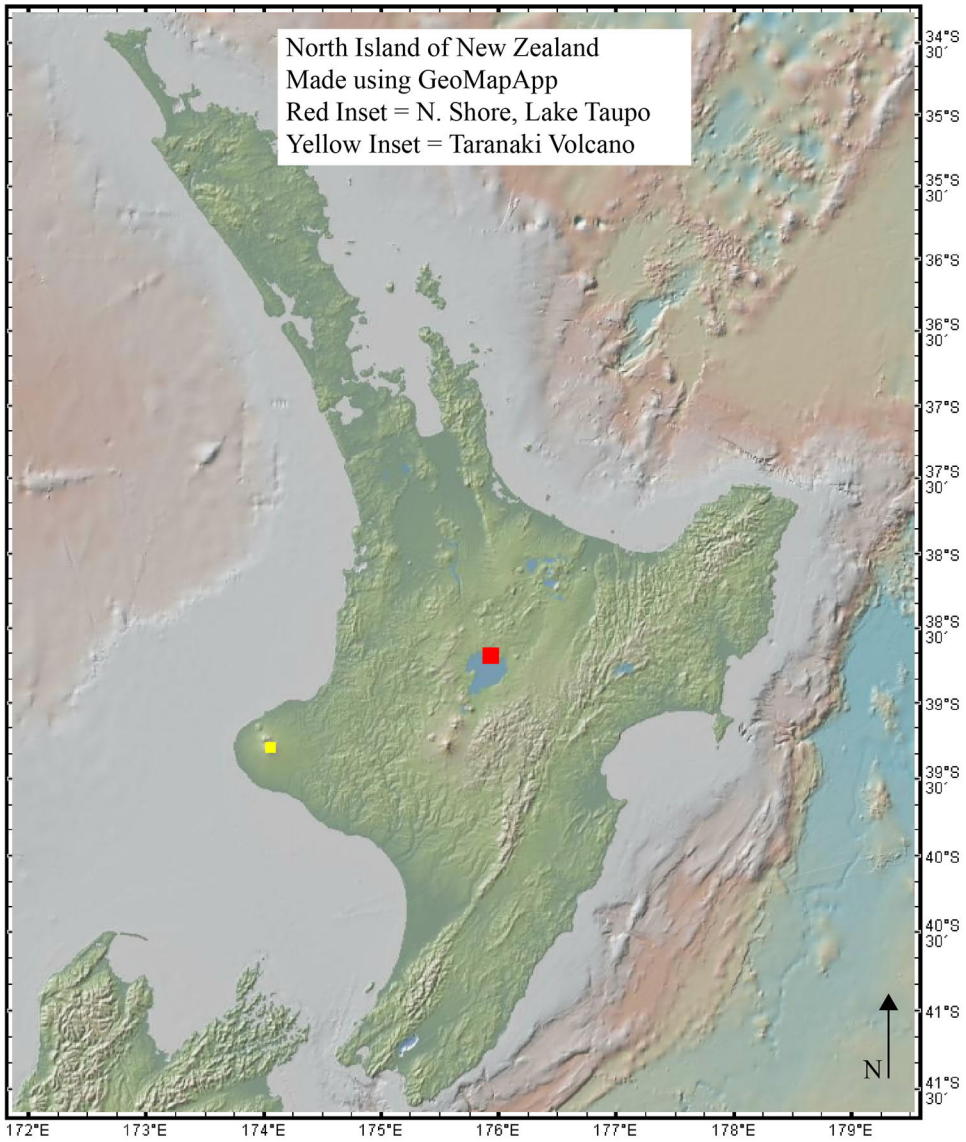

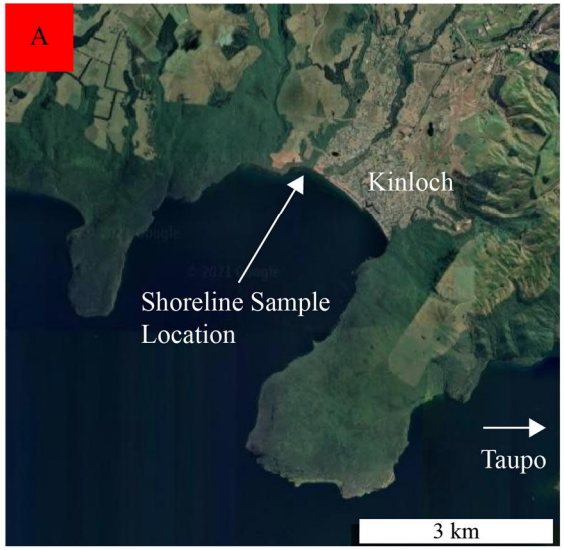

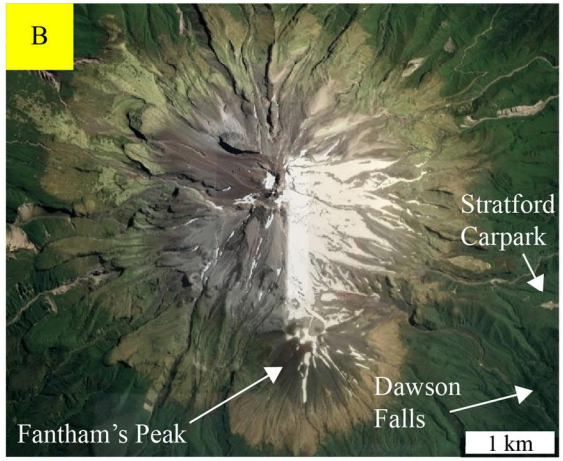

Figure 2.2: Map of the North Island of New Zealand and the study areas (insets A and B) of this thesis. GeoMapApp (Ryan et al., 2009) was used for the large map and Google Earth for the insets.

For this research, shoreline deposits were sampled immediately to the east of the mouth of the Okaia stream near Kinloch along the Kawakawa Bay Track (Whangamata Bay). The sediment was observed to be very dark (Figure 2.3), which contrasts with the white cliffs surrounding the bay and the quartzofeldspathic sand of Kinloch beach. Upon further investigation via stereo microscope, the sand was observed to contain a high proportion of magnetite.

Figure 2.3: Shoreline sand sampled for Taupo titanomagnetite along Whangamata Bay (Kinloch).

Between the shore and the terrace demarking the high-stand lake level are unique lacustrine sediments (for Lake Taupo) characterized by their lack of coarse-grained high-energy deposits. In fact, based on the abundance of fine-grained sands and suspension deposits, with local debris-flow deposits confidently ascribed to the

ephemeral Okaia stream, Riggs et al. (2001) postulated that Kinloch may be situated on top of an old lagoon or ephemeral lake (not unlike Lake Reporoa) that formed before draining into Lake Taupo as the lake level rose. Other local rock formations include Taupo Group rhyolite lavas (classified as crystal-rich, forming the ridges to the east and west of Whangamata Bay), flows, and fall deposits, Ongaroto Group rhyolite, abundant Taupo pumice, and the upstream (from the mouth of the Okaia) hinterland dominated by older Oruanui Ignimbrite (Leonard et al., 2010). Note that the QMAP compiled by Leonard et al. (2010) classified the sedimentary deposits described by Riggs et al. (2001) above as Taupo Ignimbrite. Minor abundances of Acacia Bay Formation basalt are also locally present.

The provenance of the spinel in the sand sampled here is uncertain. Compositionally, magnetites/titanomagnetites derived from Taupo Caldera are remarkably similar between the Whakamaru, Oruanui, and Taupo ignimbrites as well as Taupo pumice (cf. Brathwaite et al., 2017; Ewart, 1965, 1967; Shane, 1998; Wilson et al., 2005), so EPMA is likely unable to distinguish between spinel derived from any one of these units.

2.2.4 Papakolea Beach, Hawai'i

Papakolea Beach is situated directly in the centre of Pu'u Mahana, which is a tuff ring located very near to South Point on the island of Hawaii (Figure 2.3). Very little information on this location is currently published. However, some controversy surrounding the origin of this ring exists in the literature.

Originally interpreted as a littoral cone (Stearns and Macdonald, 1946), Walker (1992) compiled a novel lithofacies description of the exposed stratigraphy and contrasted it with the stratigraphy of a known littoral cone (the historical Sandhills locality associated with the 1840 eruption of Kilauea, see Figure 2.3) in order to argue that the deposits of the Pu'u Mahana cone are more consistent with its generation as a Surtseyan tuff ring. In addition to the volcanological evidence, Walker (1992) pointed out that, in order for Pu'u Mahana to be a littoral cone, it had to be emplaced at or near sea level. Radiocarbon age dating performed on the overlying formation demonstrate that Pu-u Mahana is at least 28,000 years old (Rubin et al., 1987). Walker thus argued that, since the island of Hawaii is subsiding at a rate of *c*. 2.4 mm/year (Moore, 1987), the eruption of Pu'u Mahana must have occurred at least 69 meters higher than the current level.

Thus, it is more likely that the sediment of Papakolea Beach is derived from a primary vent rather than a littoral cone.

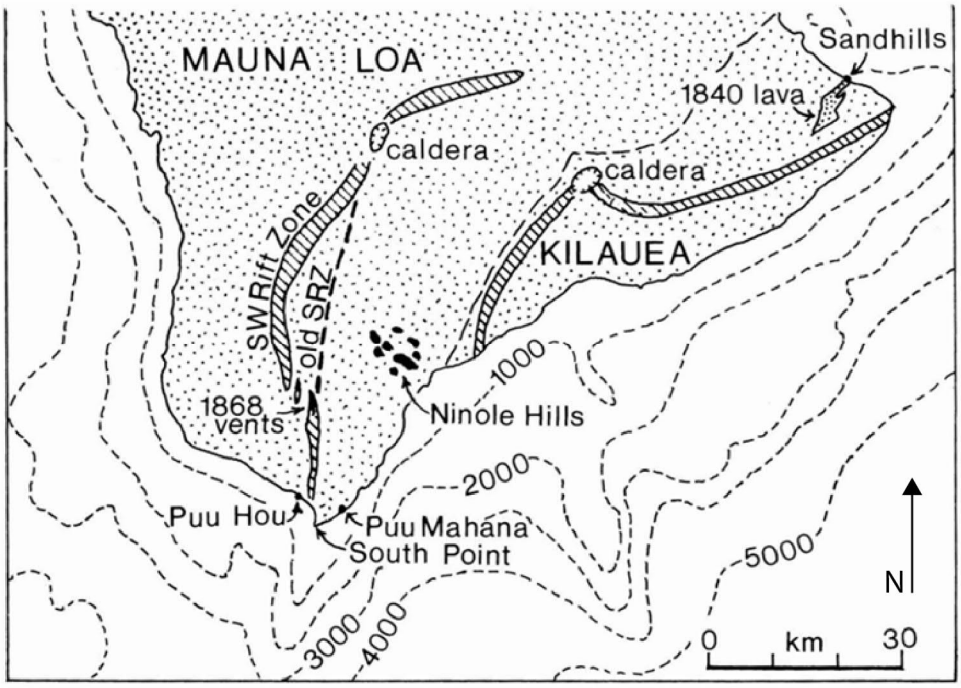

Figure 2.4: Sketched index map of the southern portion of the island of Hawaii taken from Walker (1992). Papakolea Beach is the same location as "Puu Mahana".

2.2.5 Ani-jima, Chichi-jima island group, Ogasawara Islands, Japan

Situated on the Philippine Sea Plate, the Izu-Bonin-Mariana (IBM) arc is a type example of an intraoceanic arc system (Stern and Bloomer, 1992). This arc has resulted from the melting of mantle asthenosphere above the subducting Pacific Plate and stretches from 34° N near the island of Honshu, Japan to 7° N at the island of Palau (Figure 2.4). Along the periphery of the modern Philippine Sea plate are several large Mesozoic aged crustal fragments, remnant arc terranes, and basins. These include the Palau Basin, which is inferred to be Mesozoic in age based on bathymetry (Taylor and Goodliffe, 2004), the Huatung Basin near Taiwan to the west (Deschamps et al., 2000; Hickey-Vargas et al., 2008), and the remnant island arcs and ocean islands of the Oki-Daito, Daito Ridge, and Amami Plateau region to the north (Hickey-Vargas, 1998, 2005; Ishizuka et al., 2011b).

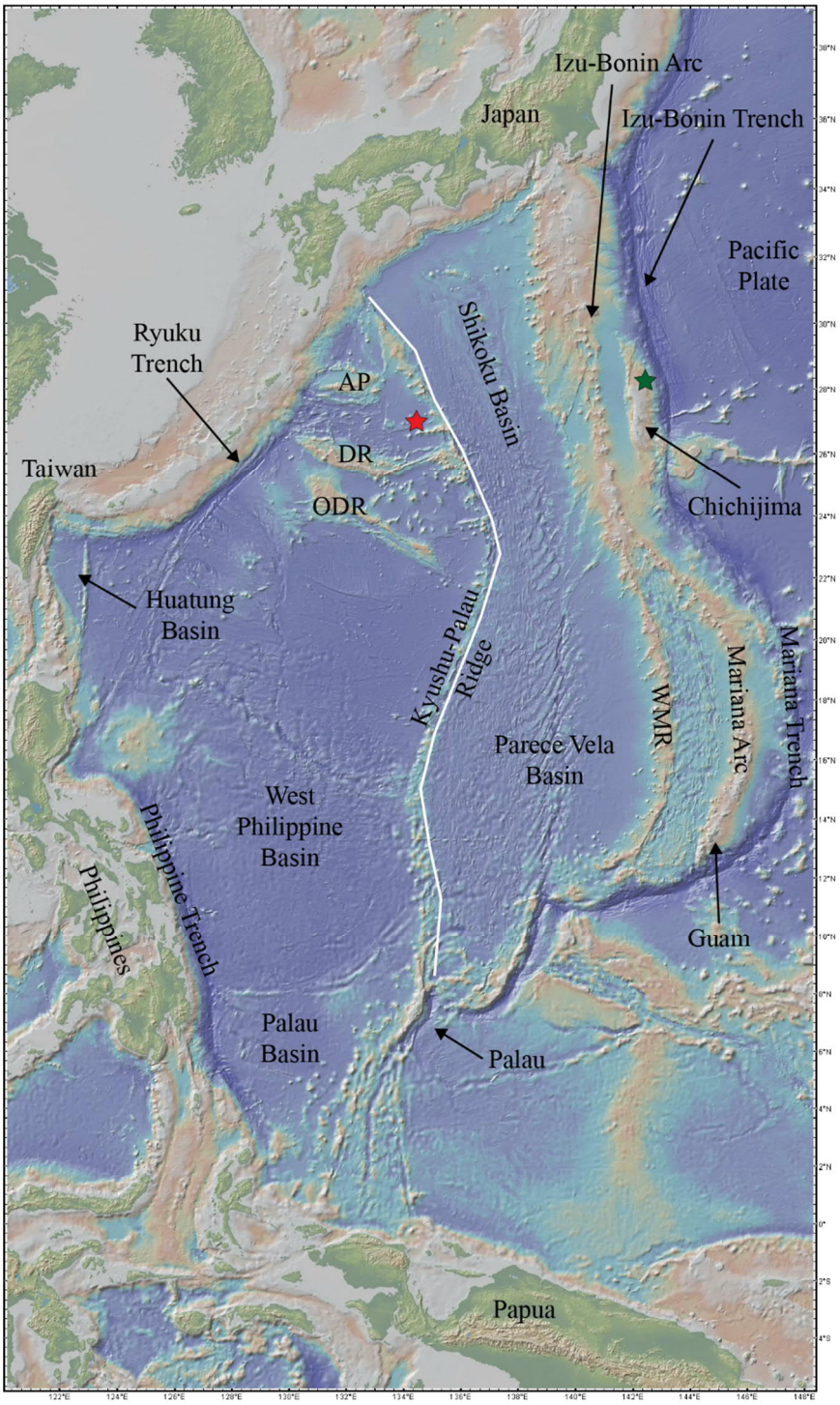

Figure 2.5: Annotated map of the Philippine Microplate. AP = Amami Plateau, DR = Daito Ridge, ODR = Oki-Daito Ridge, WMR = West Mariana Ridge. Red Star = Site U1448 of IODP Expedition 351. Green Star = drilling sites for IODP Expedition 352 and dredging/diving missions carried out by JAMSTEC. Image made using GeoMapApp (Ryan et al., 2009).

Subduction initiated along what is now the eastern side of the Philippine Sea Plate during the Eocene (52 Ma, Ishizuka et al., 2011a; Reagan et al., 2019). This event generated a large volume of crust which is now preserved along the entirety of the IBM forearc (Reagan et al., 2013). Initial magmatism formed two distinct types of magmas, in sequence, over a brief time span (< 2 Myr, Reagan et al., 2019): fore-arc basalt (FAB, Reagan et al., 2010) and younger boninite (Ishizuka et al., 2011a; Reagan et al., 2017).

The West Philippine Basin formed either immediately before or contemporaneously with IBM subduction initiation (Deschamps and Lallemand, 2002; Ishizuka et al., 2011b; Savov et al., 2006). It is the largest marginal basin in the world and is bordered to the north by the Oki-Daito Ridge, to the south by the Mindano Fracture Zone (Taylor and Goodliffe, 2004), to the northwest by the Ryuku Trench, to the west by the Philippine Trench and the Gagua Ridge (Deschamps et al., 2000), and to the east by the Kyushu-Palau Ridge (KPR). The KPR is a remnant arc that separated from the modern IBM arc system during the Oligocene with the opening of the Shikoku and Parece Vela back-arc basins (Mrozowski and Hayes, 1979; Okino et al., 1994). The basement of the KPR formed during the Eocene (48.7 Ma, Ishizuka et al., 2018) after subduction had already initiated, and the oldest arc rocks sampled along the KPR are 32 Myr old, while the youngest are Miocene in age (22 Ma, Ishizuka et al., 2011b). The southern part of the IBM arc system has undergone additional back-arc rifting with the opening of the Mariana trough at *c.* 6 Ma (Fryer, 1995). This back-arc basin has created a remnant arc known as the West Mariana Ridge.

Recent research efforts have synthesized this general trend of plate growth, microplate development, collision with SW Japan, and clockwise plate rotation: up to 80° (e.g. Wu et al., 2016). Currently, the Philippine Sea Plate is subducting at the Ryuku Trench at a rate of *c.* 70 mm/year and at the Philippine Trench at a rate of *c.* 103 mm/year (DeMets et al., 2010; Holt et al., 2018; Smoczyk et al., 2013). These motions are relative to the Eurasian Plate and the Sunda Microplate respectively. Relative to the Philippine Plate, the Pacific plate is subducting at a rate of *c.* 46 mm/year near Japan and *c.* 10 mm/year near Palau (DeMets et al., 2010; Smoczyk et al., 2013).

The boninite selected for this study was sourced from the Maruberiwan Formation, Mansakuhama, Ani-jima, with Mansakuhama being a beach on the south side of the island facing Chichi-jima (Figure 2.5). The boninites of Ani-jima have been dated using

Ar/Ar methods to be 45.8 ± 0.3 Myr old, making them the youngest dated boninites of the Chichi-jima island group (Ishizuka et al., 2011a). However, the samples taken for geochronologic study were taken from the other side of the island from Mansakuhama (red star, Figure 2.5). Since the boninite taken for this study and the one dated by Ishizuka et al. (2011a) are from the same formation, I consider them roughly the same age.

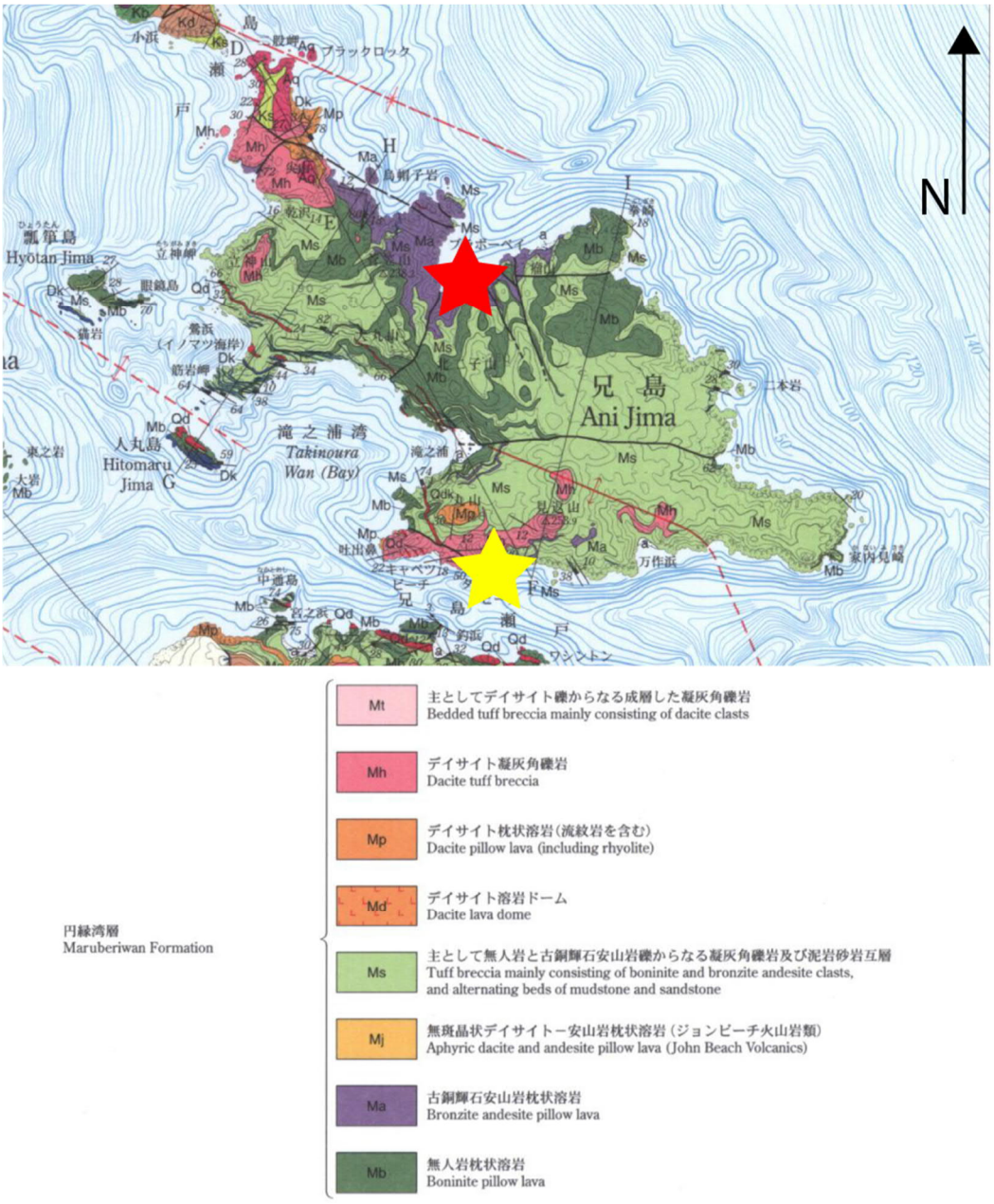

Figure 2.6: Annotated map of Ani-jima taken and adapted from Umino and Nakano (2007). Red star = location of Maruberiwan Fm. boninite sampled by Ishizuka et al. (2011a). Yellow star = location of Mansakuhama beach, where the sample studied here was taken. Ani-jima is located within the Chichijima Island Group (Figure 2.4).

In the temporal context given above, with respect to the development of the IBM and of the Philippine Plate, Ani-jima represents boninite that was generated during the latest stages of magmatism associated with subduction initiation and/or the earliest associated with typical arc magmatism (Reagan et al., 2019).

2.3 H in nominally anhydrous minerals and geohygrometry

2.3.1 Olivine

Wilkins and Sabine (1973) reported a concentration of 0.008 wt.% H_2O in their pioneering publication on the IR spectroscopy of NAMs. For several years, most of the research on this topic constituted rheological studies describing the effect of H on olivine deformation behaviour (e.g. Justice et al., 1982; Karato et al., 1986; Mackwell and Kohlstedt, 1990; Mackwell et al., 1985), and little attention was directly paid to the geochemical interpretation of H in olivine. However, towards the end of the nineteen eighties, the studies of Kitamura et al. (1987) and Miller et al. (1987) showed that olivine, being the dominant silicate in the upper mantle, commonly contains unit-cell scale OH^- inclusions that form defect assemblies consistent with the local substitution of olivine with humite. These defect assemblies are likely the mechanism for H-related weakening of the olivine mineral, and the OH^- inclusions are distinguished from those associated with other secondary mineral formation by their IR spectra (Miller et al., 1987).

More recently, an experimental study published by Mosenfelder et al. (2006) replicated earlier experimental work by Mackwell and Kohlstedt (1990). That is, that synthetic olivines at equilibrium under high pressure-temperature conditions contain OH^- but exhibit absorption bands that are not related to the humite-like point defects observed by Miller et al. (1987). The work of Mosenfelder et al. (2006) offered a synthesis of prior experimental and IR spectroscopic data and proposed a new calibration of IR absorption coefficients based on new thermodynamic and geochemical arguments. They postulated that experimental technique plays a critical role in the synthesis of OH-bearing olivine and that critical analysis of the techniques used should be implemented before proposing H-incorporation mechanisms based on experimental petrology.

Geohygrometric use of olivine has been an area of research for several years now. Feig et al. (2006) demonstrated that the partition coefficient of Ca between olivine and melt

($D_{CaO}^{olivine-melt}$) may vary as a function of melt H concentration. This effect was the focus of Gavrilenko et al. (2016) who calibrated a "Ca-in-Olivine Geohygrometer" and estimated primitive melt H concentrations in magmas sourced from the Kamchatka and Central American Arcs as well as in Mid-Ocean Ridge Basalt (MORB) from the Siqueiros Transform (East Pacific Rise). The Gavrilenko et al. (2016) geohygrometer is calibrated on data gathered from the results of anhydrous olivine-melt equilibrium experiments and studies of olivine hosted melt inclusion H concentrations. Importantly, the geohygrometer is able to recover melt H concentrations consistent with melt inclusion studies performed on the same volcanoes when applied to both olivine-only analyses as well as olivine and their melt inclusions.

The olivine geohygrometer calibration is expressed in terms of parental melt MgO wt.% and range from 8-18 wt.% with distinct equations used for parental melts with low MgO (8-11 wt.%). First an equation to model the anhydrous $D_{CaO}^{olivine-melt}$:

$$D_{CaO}^{olivine-melt}(\text{anhydrous}) = -0.0043 \times MgO_{\text{Primitive Melt}} + 0.072 \qquad \text{Equation 2.1}$$

And second, an equation that uses the difference between model (anhydrous) and observed $D_{CaO}^{Olivine-Melt}$ to recover an estimate of primitive melt H_2O:

$$H_2O^{melt} = 188 \times \Delta D_{CaO}^{olivine-melt} \qquad \text{Equation 2.2}$$

For melts with high MgO (11-18 wt.%), separate equations were derived:

$$D_{CaO}^{olivine-melt}(\text{anhydrous}) = 0.0042 \times MgO_{\text{Primitive Melt}} + 0.0196 \qquad \text{Equation 2.3}$$

And

$$H_2O^{melt} = 397 \times \Delta D_{CaO}^{olivine-melt} \qquad \text{Equation 2.4}$$

For the preceding Equations 2.2 and 2.4, the term $\Delta D_{CaO}^{olivine-melt}$ is the difference between the Ca partition coefficient calculated for an olivine in equilibrium with an anhydrous melt (Equations 2.1 and 2.3) and the calcium partition coefficient for an olivine in equilibrium with a hydrous (wet) melt calculated after modelling (see below). A disadvantage of this preliminary geohygrometer are the uncertainty estimates associated with its calibration. The 1σ uncertainty intervals associated with melt H concentrations are ± 1.4 % for low MgO melts and ± 1.8 % for high MgO melts as

reported by Gavrilenko et al. (2016). We assume that the author intends these values to read as “wt.%” and not a final percentage of the inferred H concentrations. These uncertainties are due to analytical uncertainties associated with the calculation of CaO concentration in olivine as well as secondary fluorescence sourced from glass present in experimental samples (Gavrilenko et al., 2016).

More work involving the partitioning of major/minor elements, thermometry, and the effects of H on these observations for olivine-melt systems is currently being undertaken and published (Pu et al., 2017; Pu et al., 2021). From this work, the difference between apparent $D_{MgO}^{olivine-melt}$ and $D_{NiO}^{olivine-melt}$ may be used to estimate equilibrium melt H concentration.

2.3.2 Pyroxene

The work of Wilkins and Sabine (1973) was among the first to quantify trace H concentrations for a variety of silicate minerals, including diopside. This pioneering effort was enabled by the systematic study of FTIR spectra and coupled electrolytic analysis for each mineral species. In the same issue of *American Mineralogist*, Runciman et al. (1973) identified the peak positions of OH^- absorption spectra during infrared irradiation of enstatite.

Following the studies of Wilkins and Sabine (1973) and Runciman et al. (1973), many complications were identified in the routine FTIR analysis of pyroxene including the presence of microscopic hydrous mineral inclusions (usually amphibole), fluid inclusions, and uncertainties associated with crystallographic orientation. Thus, by the mid-late eighties, most FTIR studies concerned themselves with identifying the orientation-dependent intensities and positions of OH^- absorption bands in common pyroxenes devoid of inclusions (e.g. Beran and Zemann, 1986). Such research allowed for precise hypotheses regarding water incorporation mechanisms to be made for pyroxenes (*op. cit.*). These include a vacancy substitution as well as a coupled substitution mechanism including trivalent cations.

The work of Skogby and Rossman (1989), Ingrin et al. (1989), and Skogby et al. (1990) dramatically accelerated the working knowledge of OH in pyroxene. Skogby and Rossman (1989) studied H incorporation mechanisms and thermal stability in hydrothermal experiments designed to hydrate and/or dehydrate Fe-rich diopside and

esseneite ($CaFeAlSiO_6$). They correlated the increase/decrease in the OH^- absorption peak intensity to the relative abundance of Fe^{3+} and site distribution of Fe^{2+} in these minerals using optical spectroscopy. With this method, they concluded that pyroxene hydration requires a fundamental compositional change within the pyroxene structure. Ingrin et al. (1989) identified two probable incorporation mechanisms. One was previously described by A. Beran in 1976 in a German publication and mainly concerns cation vacancies populated by H to relatively under-bonded local oxygen atoms (see Beran and Zemann, 1986), and the other hypothesizes that the coupled substitution of a trivalent cation plus a hydrogen ion for a tetravalent cation (Si^{4+}) results in the formation of OH^- bonds that contribute to several absorption peaks observed in FTIR spectra that do not correspond to the peaks associated with cation vacancies. They also showed that dehydration likely accompanies oxidation of pyroxene. The synthesis of Skogby et al. (1990) is the first publication to systematically examine the OH^- peak attributes for several dozen pyroxene minerals taken from a wide variety of geologic environments including mantle xenoliths, mafic intrusive rock, basalt, rhyolite, meteoritic samples, synthetic pyroxenes, and metamorphic diopside. This thorough investigation of H in pyroxene realized that H is a minor component in all terrestrial pyroxenes (no OH^- absorption peaks were observed in meteoritic pyroxene), confirmed the compositional systematics described by Ingrin et al. (1989), and proposed that the hydrous components of pyroxene minerals could be utilized to gain an understanding of H activity in most geological systems.

Smyth et al. (1991) showed that omphacite associated with a mantle eclogite taken from South Africa held up to 1,840 μg/g OH within its crystal structure. At the time of publication, this was the highest recorded concentration for H in pyroxene (0.18 wt.%). Meanwhile, the study of Bell and Rossman (1992) provided more data on mantle-derived xenoliths and showed that some heterogeneity exists between mantle domains with respect to H concentration. This study also confirmed pyroxene as the dominant carrier of H (as a NAM) in the upper mantle. By the mid-nineties, studies of H in silicate minerals had become widespread mostly due to the availability of FTIR instrumentation and established methodology (e.g. Bell et al., 1995).

From this point onward, onerous attention was paid towards understanding how H behaves within the pyroxene structure in order to assess the mineral for potential

geohygrometric application. To this end, multiple studies investigated the diffusion and/or uptake characteristics of H in pyroxene minerals (e.g. Hercule and Ingrin, 1999; Woods et al., 2000). Hercule and Ingrin (1999) provided diffusivity data for diopside along with a proposed mechanism of incorporation involving the reduction of structurally bound Fe^{3+} during hydration, which built upon the observations of Ingrin et al. (1989). Hercule and Ingrin (1999) suggest, based on their diffusion law estimates, that as long as diopside is recovered from low-temperature conditions or from rapidly quenched samples it may be used to estimate H activity from the system it formed in. Woods et al. (2000) broadly replicated the observations of Ingrin et al. (1989) regarding diffusivity of H in diopside. They further examined this behaviour and related it to diffusivity of H in other silicates and showed that H likely diffuses as a proton and is likely associated with local electronic defects as it moves through the diopside structure. The experiments of Woods et al. (2000) also examine diffusion as a function of temperature and suggest that diopside in mantle xenoliths may not retain their original H concentrations; as ascending magmas lose their volatile components close to the surface they retain high temperature characteristics, which drives H out of ascending diopside (into melt and then the vapour phase). Thus, Woods et al. (2000) caution against interpreting low H in mantle diopside as representative of their intrinsic H concentrations.

Rauch and Keppler (2002) systematically studied the pressure-compositional dependence of H solubility in nominally pure enstatite. They found that equilibrium OH concentrations increase with increasing pressure. Their preferred mechanism for pure enstatite was incorporation into a cation vacancy. Added Al enhanced H solubility at all pressures. At 1100 °C, the addition of 1 wt.% Al_2O_3 enhanced H uptake by a factor of *c*. 5. Their preferred model of incorporation was the coupled substitution mechanism.

Mierdel and Keppler (2004) expanded upon this work by assessing the temperature dependence of H solubility in pure enstatite at 15 kbar. They integrated their thermodynamic data with those of Rauch and Keppler (2002) to give an empirical model describing H solubility as a function of water fugacity (f_{H_2O}) and the change in volume (of enstatite) during hydration. The authors then used this empirical architecture to describe how mantle temperature anisotropy (in the form of plumes) may scavenge H from the surrounding upper mantle.

Stalder et al. (2005) performed an extensive study of the effects of several trivalent cations upon H solubility in orthopyroxene (Fe-bearing enstatite, ferrosilite, and either Al+Cr or Fe^{3+}+Cr orthopyroxene) under isobaric (2.5 GPa) conditions. They found sufficient evidence to write that "a general statement concerning the hydrogen solubility is not possible" in naturally occurring orthopyroxene because the chemical reactions that give the equilibrium constants for the formation of defects in orthopyroxene (currently) require too much unknown information. The authors call for more experiments before a solution can be expressed.

As of yet no substantial experimental work has been published since this last paper. Recently, however, Lloyd et al. (2016) were able to show that H concentrations rapidly fall in clinopyroxene when the mineral is trapped in a sub-aerial flow that cools for hours-days. When the same clinopyroxenes were erupted in a tephra, their original H concentrations could be observed with minimal dehydration near the crystal edges. This research places a fundamental constraint on the sort of sample material that must be taken in order to accurately infer a magmatic water concentration from the concentration of H in pyroxenes.

2.3.3 Feldspar

Feldspar is the most common mineral in the crust. Since it is so common, much effort has been made to investigate the capability of this NAM to hold structurally bound OH. Wilkins and Sabine (1973) reported a concentration of 0.55 wt.% H_2O for an andesine sourced from Norway. In the mid-1980s, IR spectroscopy shed light on the mineralogic aspects of H incorporation in feldspar including its control on colouration (Hofmeister and Rossman, 1985a, b, 1986). However, a general geochemical assessment of H incorporation was not published until Beran (1986) who revealed that, in alkali feldspar, H_2O incorporated into feldspar M-sites exhibit two distinct absorption bands corresponding to two OH stretching frequencies. This doublet was observed to be pleochroic, and H_2O was determined to lie parallel to the symmetry plane in their mineral samples. Beran (1987) built on this framework by studying labradorite absorption bands and proposed that OH dipoles are oriented perpendicular to (001) and that OH preferentially forms on "deficient" oxygens within the feldspar crystal structure.

For many years, these foundational papers enabled several researchers to conduct experiments and coupled IR analyses to determine the hydration/dehydration characteristics of feldspar minerals and their effects on crystal structure, stoichiometry, and rheology. In the early 2000s, Johnson and Rossman (2003) used magic-angle spinning nuclear magnetic resonance (NMR) spectroscopy to infer a "universal absorption coefficient" for IR analysis of feldspar minerals for their OH and H_2O concentrations. The authors studied eight feldspar minerals, including multiple plagioclase feldspars. The latter minerals were observed to contain 210-510 μg/g H_2O as structural OH, while microcline was observed to contain 1,000-1,400 μg/g H_2O as structural H_2O, and sanidine 170 μg/g H_2O as OH. Johnson and Rossman (2003) discovered a linear correlation between total integrated mid-IR absorbance and the concentration of structural H, as determined from NMR. From this correlation, they were able to derive an absorption coefficient for natural feldspars that contain either OH or H_2O. Their analyses suggest that using unpolarized IR spectra are unable to reliably estimate feldspar H concentrations. A year later, Johnson and Rossman (2004) published a survey of feldspars for their H concentrations. They found that feldspars contain 0-512 μg/g H_2O as OH, 0-1,350 μg/g H_2O as H_2O, and 0-1,500 μg/g H_2O as NH_4^+ (whose incorporation was first described by Solomon and Rossman, 1988). Their analysis revealed that volcanic feldspars contain only structural OH.

SIMS experiments on feldspar minerals conducted by Mosenfelder et al. (2015) were foundational to the *in situ* analysis of micro-scale feldspar minerals for their H concentrations. Previously, IR analysis of feldspar was limited to large crystals, which precluded its use for practical geohygrometry. The SIMS and IR spectroscopy data compared well, and with these inferences, the authors proposed refinements to be made to the "universal absorption coefficient" given by Johnson and Rossman (2003) in accordance with their theoretical framework. One major implication of their data was that literature data on H in plagioclase feldspar had been, up to that point, been overestimated by a factor of *c*. 2.

Mosenfelder et al. (2020) conducted several experiments across a wide variety of pressure-temperature-f_{O_2} space to synthesize H-bearing plagioclase minerals along a wide compositional range (An_{15}-An_{94}). Their experiments showed that H solubility is enhanced under relatively reducing conditions and that the reduction of tetrahedral Fe^{3+}

to Fe^{2+} may facilitate H incorporation in adjacent M-site vacancies. The bonding of H to O adjacent to M-site vacancies was also described by Behrens and Müller (1995) who studied synthetic end-member "hydrous feldspar".

The geohygrometric analysis of feldspar has been widely studied. Putirka (2008) reviews a multitude of mineral-liquid and mineral-mineral geothermobarometers. When Putirka (2008) rearranges and reformulates the plagioclase-melt thermometer equation (Equation H, Putirka, 2005), the melt H_2O term becomes the dependent variable, and its concentration is calculated as a function of plagioclase Anorthite content, pressure, temperature, and melt CaO, MgO, $KO_{0.5}$, $AlO_{1.5}$, and SiO_2 cation fractions:

$$H_2O(\text{wt.}\%) = 25.95 - 0.0032T(^{\circ}C)\ln\left[\frac{X_{An}^{crystal}}{X_{CaO}^{melt}\left(X_{AlO_{1.5}}^{melt}\right)^2\left(X_{SiO_2}^{melt}\right)^2}\right] - 18.9\left(X_{KO_{0.5}}^{liquid}\right) + 14.5\left(X_{MgO}^{liquid}\right) - 40.3\left(X_{CaO}^{liquid}\right) + 5.7\left(X_{An}^{crystal}\right)^2 + 0.108P(\text{kbar}). \qquad \text{Equation 2.5}$$

The thermometer is calibrated on experimental phase equilibrium data taken from the Library of Experimental Phase Relations (LEPR, Hirschmann et al., 2008). This model is quite sensitive to temperature, as Putirka (2008) calculated that 38 °C error in the temperature estimate results in a 1.0 wt% error in calculated melt H_2O concentration. Putirka (2008) also state that the utility of this geohygrometer is limited to samples similar to those used to calibrate the original thermometer formula.

Lange et al. (2009) offered a geohygrometer based on a synthesis of thermodynamic data, which integrated data from several calorimetric and volumetric studies of Albite, Anorthite, and their liquid counterparts. Lange et al. (2009) studied the effects of temperature, pressure, and melt H_2O concentration on the exchange reaction:

$$CaAl_2Si_2O_8^{crystal} + NaAlSi_3O_8^{liquid} = CaAl_2Si_2O_8^{liquid} + NaAlSi_3O_8^{crystal} \qquad \text{Equation 2.6}$$

Derivation of an activity-composition relationship from this equation is the basis for the geohygrometer (see Equation 6, Lange et al., 2009). The key contribution of this research was to quantify the effect dissolved H_2O has on the activities of the liquid components in the above equation. With this theoretical framework, Lange et al. (2009) derived a regression equation from a database comprised of plagioclase-liquid equilibrium experiments. Of the filters Lange et al. (2009) apply to their database, one is important to reiterate here; the experimental samples used to calibrate the

geohygrometer were either anhydrous or saturated in a pure H_2O fluid. That is, no data on fluid under-saturated sample material were integrated in the calibration of Lange et al. (2009). The stated reason for this was that during fluid under-saturated experiments hydrogen diffuses through the metal container and is thus lost from the system. With saturated samples, the H_2O concentration of the glass was inferred using the solubility model of Moore et al. (1998).

A refinement of this model has already been published (Waters and Lange, 2015), and the utility of this geohygrometer was expanded. The geohygrometer of Lange et al. (2009) could only be applied to melts with SiO_2 concentrations between 46-74 wt.%, H_2O concentrations between 0-7 wt.%, temperatures between 825-1230 °C, pressures between 0-300 MPa, and in equilibrium with plagioclase with compositions between An_{37}-An_{93}. Because a larger experimental database was used to recalibrate the geohygrometer; 214 experiments in Waters and Lange (2015) vs 71 experiments in Lange et al. (2009), Waters and Lange (2015) offered a geohygrometer that could be applied to a larger set of natural samples:

$$H_2O\ (wt.\%) = m'x + a'' + \frac{b''}{T} + \sum X_i d_i'' \qquad \text{Equation 2.7}$$

where X is the mole fraction of element oxide i in plagioclase, x is calculated as:

$$x = \frac{\Delta H°(T)}{RT} - \frac{\Delta S°(T)}{R} + \frac{\int_1^P \Delta V_T^\circ(P)dp}{RT} + \ln\left(\frac{X_{CaAl_2Si_2O_8}^{Ideal\ Liquid}}{X_{NaAlSi_3O_8}^{Ideal\ Liquid}}\right) + \ln\left(\frac{a_{NaAlSi_3O_8}^{Crystal}}{a_{CaAl_2Si_2O_8}^{Crystal}}\right) \qquad \text{Equation 2.8}$$

and m', a'', b'', and d'' are calculated by the regression:

$$m' = 0.39 \pm 0.12, a'' = -17.3 \pm 2.53, b'' = 2.99 \pm 0.07 \qquad \text{Equation 2.9}$$

with d'' varying based on element oxide, i (Table 2.1).

Element Oxide, *i*	d" value ± 1σ
SiO_2	7.83 ± 2.52
Al_2O_3*	-50.1 ± 3.53
FeO^T	14.1 ± 3.30
MgO	24.0 ± 3.05
CaO	-15.9 ± 3.45
Na_2O	18.6 ± 4.32
$K_2Al_2O_4$	24.0 ± 6.73

Table 2.1: Values of d" for various element oxides measured in plagioclase, *Al_2O_3 = moles Al_2O_3 - moles K_2O (Waters and Lange, 2015)

The range of acceptable input melt compositions were expanded: SiO_2 concentrations can range between 45-80 wt.%, Alkali concentrations (Na_2O+K_2O) from 0-10 wt.%, and H_2O concentrations between 0-8 wt.%. A wider range of melt pressure-temperature conditions are also acceptable: 750-1244 °C and 0-350 MPa, and the equilibrium plagioclase compositional range was also significantly expanded (An_{17}-An_{93}). The standard error of estimate values for both versions of the geohygrometer are similar: 0.32 wt.% H_2O from Lange et al. (2009), and 0.35 wt.% from Waters and Lange (2015). To test the application of their geohygrometer to water under-saturated melts, Waters and Lange (2015) applied their model to products of experiments conducted by Hamada and Fujii (2008), which were performed under fluid under-saturated conditions. They found agreement between calculated H_2O concentrations and concentrations inferred through IR spectroscopy (Hamada and Fujii, 2008).

Hamada et al. (2013) published data on the partitioning behaviour of H between plagioclase and melt. By equilibrating An_{96} plagioclase with variably hydrated basaltic glass (0.8-5.5 wt.% H_2O) in an internally-heated pressure vessel, Hamada et al. (2013) were able to calculate how partitioning behaviour changes as a function of temperature, pressure, and composition. They reported that the partition coefficient of H between plagioclase and melt changed from low melt H_2O concentrations (0.01 ± 0.005 at < 1 wt.%) to high melt H_2O concentrations (0.005 ± 0.001 at > 4 wt.%). That is, the partitioning of H does not follow Henry's Law for compositions between these two bounds. Hamada et al. (2013) did not conclusively state the reasoning for this

distinction in H partitioning behaviour, but they postulated that perhaps changes in the manner H is incorporated into the plagioclase crystal structure are responsible. This hypothesis appertains to an observed shift in the peaks present in IR spectra gathered from their experimental products. They postulated that perhaps the tetrahedral site of plagioclase is doubly occupied by H and a trivalent or bivalent cation which together function as a quadrivalent or trivalent cation respectively. A result of these findings is that Hamada et al. (2013) were not successful in formulating a relationship between plagioclase and melt for melt with H_2O concentrations ranging from 1-4 wt.%. Instead, they formulated two end-member equations that they suggested to be used to estimate the H_2O concentration of melt or plagioclase. For less hydrous systems (where H_2O in the melt is ≤ 1 wt.%):

$$H_2O^{plag.}(\mu g\ g^{-1}) \approx 80 \times H_2O^{liquid}(wt.\%) \qquad \text{Equation 2.10}$$

For more hydrous systems (where H_2O in the melt is ≥ 4 wt.%):

$$H_2O^{plag.}(\mu g\ g^{-1}) \approx 40 \times H_2O^{liquid}(wt.\%) \qquad \text{Equation 2.11}$$

The hygrometer of Hamada et al. (2013), as formulated and reported, has an uncertainty estimate of ± 20 μg/g H_2O for the low H_2O system and ± 40 μg/g H_2O for the high H_2O system. It was not stated whether this relationship is true for all plagioclase or not, but the authors acknowledge that partitioning behaviour seems to be different for alkali feldspars (Seaman et al., 2006).

2.3.4 Spinel

The earliest reference to H in spinel was given in Wickersheim and Lefever (1960). Here, the authors briefly detail a correlation between the intensity of the "3 μ" absorption peak (the OH peak) and the degree of *non-stoichiometry* of the synthetic host spinel. Thus, the tendency for non-stoichiometric spinel to partition H has been well-known in the material science community for quite some time (cf. Fukatsu et al., 2002; Okuyama et al., 2006; Wang, 1969).

It is important to note that the material science community has published information on $MgAl_2O_4$ spinel only. In these studies, non-stoichiometry is defined as an excess of one of the cations (in this case, Al) in the spinel unit cell. The excess in spinel is compensated for by imposing a degree of *inversion* on the unit cell and by propagating a

cation vacancy into the unit cell (Lavina et al., 2002). Normally structured spinels have divalent cations (e.g. Mg, Fe^{2+}, etc.) that are situated in tetrahedral coordination, while octahedral sites are populated by trivalent cations (e.g. Cr, Al, Fe^{3+}). Inversion is where these cations switch places in the spinel structure. The propagation of a cation vacancy is necessary to maintain charge balance and is achieved by removing the other cation (Mg, in the case of $MgAl_2O_4$ spinel) from the unit cell. These modifications of the spinel structure necessitate change in local bond distances and the distribution of oxygens within the unit cell such that the general formula for non-stoichiometric $MgAl_2O_4$ is written as $Mg_{1-x}Al_2O_{4-x}$ (Lavina et al., 2002).

By this mechanism, H is incorporated into the sites where Mg has been expelled in order to maintain local charge balance. This was shown by Lenaz et al. (2008). Later work by Bromiley et al. (2010) refined our understanding of where and how H is incorporated by examining several experimentally equilibrated defect spinels with variable degrees of intrinsic non-stoichiometry.

Every study cited in this sub-section used IR spectroscopy to infer the presence and concentration of H in spinel. There is an inherent limitation in the study of spinel as a NAM that is directly related to this analytical method. Widely available FTIR instruments are capable of quantifying H without the need for standard analysis. They are fast, relatively cheap, and thoroughly understood in terms of reproducing spectra. However, natural spinel minerals are complex solid solutions that often contain an abundance of Fe. When Fe^{2+} is in tetrahedral coordination, the local band region near the OH peak position inflates (Figure 1.2, Lenaz et al., 2008). This dramatically raises the detection limit of H in spinel, which all but renders FTIR useless in assessing H in ferrous spinel. Thus, no information on the Fe-bearing spinel species exist with respect to H concentration.

A new methodology to detect H in synthetic Fe-bearing spinels will be developed and presented as a chapter of this thesis. The detection of H in natural spinels will comprise a separate chapter.

2.4 Synthesis of spinels in petrologic experiments

Initial interest in the stability of spinels was driven by the industrial application of such minerals in high-temperature settings. The refractory nature of the minerals was noted

by Muan and Osborn (1956), and, while their experiments were not directly applicable to geologic systems, the data they generated laid a foundation for future petrologic studies. In particular, the attention these workers paid to the influence of f_{O_2} on the stability of spinels allowed Osborn (1959) to present his seminal work on the influence f_{O_2} has on the differentiation of magmas. This early synthesis of observations made by material scientists and geochemists culminated in Osborn (1959) suggesting that the functional difference between tholeiitic and calc-alkaline differentiation trends is the availability of oxygen to the system during crystallization.

Early petrologic experiments, such as those carried out by Roeder and Osborn (1966), explored the degree to which f_{O_2} controls the products of crystallization in more complex systems that better simulate natural specimens. In addition to these, continued interest in spinel mineralization brought the syntheses of Irvine (1965, 1967), who was among the first to publish on the utility of spinel as a "petrogenetic indicator".

The first major petrologic study to describe how f_{O_2} controls spinel mineralization in natural silicate liquids was that of Hill and Roeder (1974). These authors synthesized spinels from two natural mafic melts at atmospheric pressure and a wide range of f_{O_2} conditions extending from 1 atmosphere to *c*. 3 log units above the iron-wüstite buffer. Their contributions include the observations that spinel and melt ferrous/ferric Fe ratios are correlated, that silicate melt always has a higher ratio value than co-existing spinel, and that Cr concentrations are a dominant control on chromian spinel stability at high temperature and low f_{O_2}. These authors also present evidence that supports a hypothesis published by Irvine (1967), which postulates that early chromian spinel fractionation terminates with a peritectic reaction involving pyroxene. In this case, pyroxene exhausts the Cr concentration of the liquid, and the abundance of other trivalent cations are not sufficient to enable further spinel crystallization. In fact, continued crystallization of clinopyroxene may actually destabilize chromite and consume it (Hill and Roeder, 1974). At higher f_{O_2}, the Fe^{3+}, Mg, and Ti concentrations of the melt control spinel stability and oxide-silicate phase relations.

Schreiber and Haskin (1976) described the partitioning of Cr between the silicate phases present in a series of experimental products formed using simple synthetic mixtures analogous to basalt. The significance of this study is their description of the oxidation

state of Cr as a function of f_{O_2} in lunar as well as terrestrial basaltic melts. Although the focus of this research was not on spinel mineralization, the authors recognized that the stabilization of spinels in basaltic melt has implications for both the oxidation state of the melt as well as the petrogenetic evolution of both the melt and the co-existing silicate phases. Their experiments conducted using Fe-free synthetic melts are of particular interest. They were able to parameterize the oxidation of Cr from divalent to trivalent as a function of f_{O_2}, which allowed them to discuss Cr solubility in silicate liquids as a function of Cr^{2+}/Cr^{3+}.

Fisk and Bence (1980) conducted experiments similar to those of Hill and Roeder (1974) using primitive basalts collected from the FAMOUS area (Langmuir et al., 1977). The studied basalt contained three compositionally distinct populations of spinel, and the results of the experiments Fisk and Bence (1980) performed allowed them to formulate a modelled crystallization sequence that replicates the observed variance in spinel composition by imposing variation in the physicochemical state of the melt. Their findings replicate the observed dependence of spinel stability on the Cr concentration of the melt (Hill and Roeder, 1974) as well as the observation that high temperature crystallization of chromite results in spinel with a higher chromite component ($FeCr_2O_4$) than spinel component (spinel *sensu stricto*, i.e. $MgAl_2O_4$). A trend first pointed out by Irvine (1965). In other words, the spinels that Fisk and Bence (1980) synthesized had higher Cr^{3+} and Fe^{2+} concentrations than spinels synthesized at lower temperatures and at the same f_{O_2}. At low temperature, the spinels that crystallized from the FAMOUS basalt had much higher Fe^{3+} contents than spinels crystallized at higher temperature; thus replicating trends observed by Hill and Roeder (1974) in that raising f_{O_2} also results in higher Fe^{3+} contents.

A series of experiments conducted by Maurel and Maurel (1982b) focused on Al partitioning between chromite and melt and on quantifying the relationship between Fe^{2+}/Fe^{3+} of spinels and the same ratio in coexisting basaltic melt. Broadly, their studies replicated the earlier results of Hill and Roeder (1974) and Fisk and Bence (1980).

Murck and Campbell (1986) used atmospheric gas mixing furnaces to equilibrate spinel with synthetic “basic” to “ultrabasic” silicate melts while varying temperature and f_{O_2}. They determined that the compositional dependence of Cr partitioning can be described

by the exchange of $FeCr_2O_4$ between the spinel and melt phases. With this observation, Murck and Campbell (1986) postulate that Cr^{3+} exists almost entirely as an octahedrally coordinated network-modifying cation in metaluminous melts.

Roeder and Reynolds (1991) further parameterized the equilibrium distribution behaviour of Fe and Cr between spinel and a diverse set of mafic melts under a wide range of physicochemical conditions (varying temperature, pressure, and f_{O_2}). They also showed that Al distribution is heavily influenced by the co-stable silicate mineral assemblage and does not vary significantly with pressure. The latter result concerning pressure variation conflicted with the hypotheses of both Sigurdsson and Schilling (1976) and Fisk and Bence (1980).

The last series of experiments worth noting came from Liermann and Ganguly (2003). These researchers determined the equilibrium distribution behaviour of Fe^{2+}-Mg between orthopyroxene and spinel at high pressures and temperatures. Their formulations allow for precise thermometry of silicic natural rocks that lack olivine, which is employed in the tholeiite system using the formulations of O'Neill and Wall (1987) and Ballhaus et al. (1991).

Broadly, the aforementioned studies have all considered the formation of *chromian* spinel or, informally, chromite. Formally, the petrologic work that has been performed up until recently has been compiled into an empirical model by Nikolaev et al. (2018a). Relatively little attention has been paid to the Fe-Ti spinels (magnetite/titanomagnetite) in this sphere. This is likely because chromite forms much earlier in the liquid line of descent of most if not all terrestrial magmas, and this aspect of their formation allows the details of primitive magmas to be inferred by petrologists.

The pioneering study of magnetite-ilmenite thermometry-oxybarometry is that of Buddington and Lindsley (1964). However, even though it has been widely cited in the study of evolved igneous rocks, it took several decades for this work to be refined (e.g. Hou et al., 2021; Sauerzapf et al., 2008). Few studies have explicitly investigated the systematics of melt-magnetite relationships in complex silicate liquids besides Thy and Lofgren (1994) and Toplis and Carroll (1995). These latter studies systematically explored oxide-melt stability in a similar manner as the pioneering studies of Hill and Roeder (1974) and Fisk and Bence (1980). Otherwise, most studies of magnetite were

more concerned with the partitioning behaviour of certain elements of interest between magnetite and melt (e.g. Nielsen and Beard, 2000; Tacker and Candela, 1987). The early work on magnetite-melt systematics has also been formally organized as an empirical model by Ariskin and Barmina (1999).

Chapter 3: Methodology

*Note: many sub-sections of this chapter were published as supplementary material with Chapter 4. These sections are denoted with a * at the end of the title. In general, they appear as they do in the published version. However, all have been reformatted to fit this dissertation, and minor changes have been made, where appropriate, to generalize the methods that have been used in Chapters 4 and 5.*

3.1 Experimental petrology: Starting material treatment, experiment design, principles of fugacity control in IHPV systems, and estimation of imposed fugacity within each sample capsule*

Initial sample preparation took place in Orléans, France. Rock fragments used as the starting materials for our experiments were powdered and fluxed in an atmospheric muffle furnace for 1.5 hours at 1500 ℃ (for boninite) and 1300 ℃ (for basalt) prior to quenching to form glass. Quenched glasses were powdered under acetone and set to dry in an oven set to 100 ℃. Some glass fragments were set aside for spectrometric analysis. Spinel seed material was taken from either a piece of chromitite ore found within the mantle section of the Troodos Ophiolite (Cyprus) or the Marquette Iron Range near Ishpeming, Michigan, and the seeds were made by crushing and sieving raw whole rock.

Nominally pure Pt capsules are better suited than Au for high temperature experiments, as Au melts at 1064 ℃ (compared to 1768 ℃ for Pt). The capsules used had an outer diameter of 2.4 mm and an interior diameter of 2 mm and were *c.* 1 cm in length. The capsules were first weighed empty, again after loading with sample mixture, then after hydration, and finally after welding to detect water loss due to welding.

A single experiment in an internally heated pressure vessel (IHPV) can process as many as seven capsules at a time. For each set of capsules, one redox sensor was included; usually in the middle of the alumina sample holder used for each experiment (see below). The experiments were designed with two principle intensive variables and one extensive variable. These were temperature, f_{O_2}, and melt water concentration. Pressure was fixed at *c.* 2 kbar, which corresponds to a crustal depth of *c.* 7 km.

Both IHPVs used in these experiments (one at the Institut des Sciences de la Terre d'Orleans, or ISTO, and one at the Geological survey of Japan, or GSJ) used sample holders suspended from quench rods by Pt wires. The wire of the holder held the samples in a region of focused heating along a *c*. 5 cm length of the inner part of a doubly wound molybdenum furnace. Two S-type thermocouples (Pt-Rh10%/Pt) were used to monitor temperature. The length of each thermocouple was adjusted in order to detect and monitor the thermal gradient present in the hot zone for the duration of a given experiment. Temperature and pressure were displayed and controlled via a Eurotherm pressure indicator, with the temperature monitor connected to the thermocouples. Quench occurred when an electric current fused the Pt wire holding the sample holder. This allowed the holder to fall to the bottom of the vertically aligned furnace into the cold zone. Optimum quenching should be achieved at rates of *c.* 300 °C/s (Roux and Lefevre, 1992). The IHPV used at GSJ was a standard hot isostatic pressing (HIP) unit manufactured by KOBELCO licensed under the "Dr. HIP" series. This unit can impose pressures up to 2 kbar, uses a molybdenum furnace, and is outfitted for rapid-cooling capability. The sample holder and quench mechanism for this experiment were similar to those used at ISTO.

For each experiment, samples were suspended from the quench rod, loaded into the furnace, and inserted into the pressure vessel prior to sealing. Atmospheric gas was purged from the IHPV using nominally pure Ar gas prior to pressurization in order to eliminate reactive components from the system (notably H). If the desired oxidation state imposed by the system was lower than the intrinsic f_{O_2} of the IHPV (see below), we added a controlled partial pressure of H (p_{H_2}) to the IHPV. Then, Ar was added using a pressure multiplier. Pressurization stopped short of the target pressure since heating of the furnace would cause greater pressurization within the fixed volume of the IHPV.

The experiments were conducted at 1100 °C, 1150 °C, and 1200 °C. Temperature directly controls final crystallinity. Therefore, temperature also controls the concentration of water in residual melts, as the crystallization of nominally anhydrous minerals concentrates water in the melt phase of the system. The concentration of water (bulk) in each capsule was *c.* 1 wt.%, which is lower than the saturated water concentration (5-6 wt.% for boninite, 4-5 wt.% for basalt) of the bulk composition at 2

kbar (calculated using the solubility model of Zhang et al., 2007). In principle, this allowed us to obtain not only variable crystallinity but also potentially different mineral assemblages.

Over the course of *c*. 1 hour, target magmatic pressure and temperature conditions were achieved as conditions within the IHPV stabilized. Stable thermal conditions were achieved when no thermal gradient in the furnace was detected over the space where the samples were held. A successful quench is required in order to preserve the mineralogical and chemical state of the sample material at the experimental conditions. Successful quenches were observed by monitoring the pressure during the quench process, which occurred when the hot sample holder fell into the cold zone, causing observed pressures to increase ≥ 30 bars before reverting to the previous stable condition.

Since the Pt capsule is permeable to H, the f_{O_2} imposed upon each synthetic system inside of every IHPV experiment is buffered by the p_{H_2} within the gas pressure medium. Functionally, p_{H_2} imposes a constant f_{H_2} and buffers the f_{O_2} of the sample assemblage following the "general buffer reaction" (after Jakobsson et al., 2014):

$$\log f_{O_2} = 2 \log K_W - 2 \log f_{H_2} + 2 \log a H_2O \qquad \text{Equation 3.1}$$

Where K_w is the formation constant of water (Robie and Hemingway, 1995). A continuous range of oxidation states may be imposed on a set of samples during a given experiment based on p_{H_2}. When no H gas is added to pressurize the system (i.e. p_{H_2} = 0), the only remaining sources of H available to the system are impurities present in the Ar used to purge and pressurize the IHPV (as H_2O), H trapped in the metals comprising the IHPV inner chamber and furnace (essentially a memory effect from previous H-buffered experiments), and any atmospheric H remaining after purging (Scaillet et al., 1992). This setting imposes what is known as the intrinsic f_{O_2} of the system onto each sample capsule. Thus, because many potential sources of H contamination exist within the system, it is likely that the p_{H_2} of the pressure medium for an experiment buffered to the intrinsic f_{O_2} condition is never truly equal to zero but that the intrinsic f_{O_2} setting is defined at minimum p_{H_2} conditions for an IHPV experiment when the IHPV is sufficiently purged.

Previous experiments have shown that the intrinsic f_{O_2} is highly oxidizing (NNO+2 to NNO+4, Scaillet et al., 1992; Taylor et al., 1992) in IHPV systems. This implies that neither the furnace, which would buffer the system to the molybdenum-molybdenum oxide buffer (O'Neill, 1986), nor the iron vessel, which would buffer the system to the iron-wüstite buffer, are effective f_{O_2} buffers of the sample material. Instead, since the Shaw Bomb method utilizes f_{H_2} and the permeable quality of the noble metal container as described above, it is likely that the intrinsic f_{O_2} truly reflects minimum p_{H_2} conditions achievable using this method. Highly oxidizing intrinsic f_{O_2} conditions are also observed in laboratories that do not use the gas mixture method (GSJ).

In order to infer f_{O_2} within a given sample capsule from a given experiment, solid sensors were used during each experiment following the methodology of Scaillet et al. (1995), with the *X*Ni value (cation Ni/[Ni+Pd]) of each sensor alloy being used to infer f_{O_2} for each sensor capsule (Pownceby and O'Neill, 1994). Because each sensor capsule was made to be water saturated, $aH_2O = 1$, and the general buffer equation is simplified to:

$$\log f_{O_2}\,(\text{buffer}) = 2\log K_W - 2\log f_{H_2} \qquad \text{Equation 3.2}$$

Essentially, the activity-composition data of Pownceby and O'Neill (1994) negate the need to directly measure or calculate f_{H_2} in IHPV systems. As long as *X*Ni is precisely determined for each sensor alloy, the calibrations provided by Pownceby and O'Neill (1994) provide log f_{O_2} (buffer) as a function of the set IHPV pressure-temperature condition.

It becomes necessary to recalculate f_{O_2} when sample melts are undersaturated with respect to water vapour because f_{O_2} will then vary as a function of water fugacity (f_{H_2O}) within the melt (Whitney, 1972). Functionally, aH_2O is reduced to < 1, and Equations 3.1 and 3.2 are then combined such that:

$$\log f_{O_2} = 2\log f_{O_2}\,(\text{buffer}) + 2\log a H_2O \qquad \text{Equation 3.3}$$

This latest equation was used to calculate sample f_{O_2} relative to the f_{O_2} value inferred for each included sensor capsule for each experiment. In order to accurately model aH_2O, hydrous glass compositions were processed through the activity model of

Burnham (1979). Since all sample melts crystallized a large proportion of nominally anhydrous pyroxene, residual melt water concentrations were calculated according to volume reduction:

$$V_1 \times C_1 = V_2 \times C_2 \qquad \text{Equation 3.4}$$

V_1 is the initial glass proportion, C_1 is the initial bulk concentration of water, V_2 is the final glass proportion, and C_2 is the unknown final water concentration:

$$C_2 = (V_1 \times C_1)/V_2 \qquad \text{Equation 3.5}$$

This is how we calculated the f_{O_2} value for each sample capsule in our experimental dataset.

3.2 Analytical methods

3.2.1 Electron probe microanalysis (EPMA)

3.2.1.1 Synthetic samples produced by IHPV experiments

Following removal of the sample holder from the IHPV, each capsule was weighed to assess for mass loss during the experiment. The capsules were then mounted in epoxy and ground to expose their interiors. Ni-Pd alloys recovered from each sensor capsule were separated from powdered ZrO_2 and mounted in epoxy. These sample materials were then polished for imaging and microprobe analysis, using SiC lapwheels and diamond grit paste.

JEOL JXA-8230 Superprobes were used for mineral, glass, and alloy (redox sensor) analyses at The University of Iowa and at Victoria University of Wellington. A JEOL JXA-8800R was used for additional spinel analyses at Hokkaido University.

Beam conditions were set to 15kV for all analyses; silicate minerals were analysed under 12 nA and glass 9 nA, while chromites and redox sensors were analysed under 20 nA.

EPMA count times (in seconds) were [*chromite-pyroxene-glass*]: Si [10-15-15], Al [15-20-15], Ti [15-15-10], Fe [15-15-15], Mn [10-25-10], Mg [15-15-15], Na [*not applicable*-5-0.5 and 1 (2 acquisitions)], K [*not applicable-not applicable*-10], Cr [15-

30-10], and Ni [10-30-10]. Total background count times were 15 s for all elements during all analyses. Based on observed standard signal intensity, lower limits of detection (in wt.%) for each element were: Si [0.04], Al [0.03], Ti [0.02], Fe [0.03], Mn [0.03], Mg [0.05], Na [0.04], K [0.03], Cr [0.04], and Ni [0.03]. Glass analyses were performed using a Na-loss mitigation strategy. No Na-loss was observed.

Secondary standards were provided by the Smithsonian Institution Department of Mineral Sciences as well as the Max Planck Institute for Chemistry for all mineral and glass analyses except for those performed in Hokkaido, Japan, which utilized synthetic mineral standards by Astimex. Sensor alloy compositions were quantified using metal standards produced by Astimex. Secondary standard analysis provided a quantitative estimation of accuracy during EPMA. Accuracies associated with glass analyses were determined to be within 1% for SiO_2, Al_2O_3, MgO, and CaO, 5% for TiO_2, FeO, and K_2O, 10% for Na_2O, and 20% for MnO, while silicate mineral analyses were determined to be within 1% for SiO_2, MgO, CaO, and Na_2O and 2% for FeO, Cr_2O_3, MnO, and Al_2O_3. Spinel analyses were determined to be accurate to 5% for all major elements besides MnO, which was determined to be accurate to 40%. Secondary standard compositions are taken from Jarosewich et al. (1980); Jochum et al. (2006); and Jochum et al. (2005).

3.2.1.2 Natural spinel minerals

Natural spinels were analysed by a JEOL JXA-8800 electron microprobe at the Graduate School of Science, Hokkaido University, Japan. Beam conditions were set to 15 kV and 20 nA with peak and background counting times set to 20 s and 10 s, respectively. Standards included both synthetic oxide and natural spinel standards, and data were corrected using the ZAF method. Similar detection limits for these spinels were realized for spinels analysed in the synthetic charges as described in the previous sub-section.

3.2.2 Scanning electron microscopy (SEM)

At Massey University, an FEI Quanta 200 Environmental SEM was used to image samples produced at ISTO. Semi-quantitative energy dispersive spectroscopy (EDS) was used here to analyse calcic silicate minerals in some boninite samples produced at GSJ. Additional imaging of the samples produced at GSJ, and some samples produced

at ISTO was performed at the Creative Research Institute of Hokkaido University using a JEOL JSM-7000F Field Emission SEM. An XMAX 150 EDS attached to this SEM was used to analyse the Pt walls in contact with sample melts so that Fe loss from the sample to the Pt could be detected and quantified (see below). These analyses were quantified by calibrating the EDS signal intensity to pure Co.

The same JEOL JSM-7000F described above was used to image the natural samples analysed by SIMS.

3.2.3 Ion microprobe experiments

3.2.3.1 Secondary Ion Mass Spectrometry (SIMS) using a stacked CMOS active pixel sensor (SCAPS) for synthetic spinel

For the analysis of ^{2}H-bearing synthetic spinel minerals (Ch. 5), a SCAPS detector was used to produce secondary ion (isotopographic) images of polished sample surfaces. SCAPS sensors are a stigmatic sensor, which is inserted directly into the stream of aligned secondary ions produced by sputtering. The geometry of the surface area is preserved along two dimensions after mass filtering, and the SCAPS method provides constant ion detection sensitivity with a wide dynamic range (Yurimoto et al., 2003). A primary beam of $^{133}Cs^{+}$ ions was used to homogeneously excavate the sample surface. The beam conditions were set to 20 keV and *c.* 1 nA for all analyses. Aperture settings were optimized for small spinel minerals (*c*. 15 μm in diameter), and the sampling region corresponded to an elliptical area *c*. 60 μm x 50 μm in size. High mass resolution ($M/\Delta M$ = *c* 7,800) allowed for the collection of several isotopes/dimers of interest. During signal integration, isotope and dimer masses corresponding to ^{18}O (a), $^{16}O^{2}H$ (b), and $^{16}O^{1}H$ (c) were targeted, and isotopographic images representing the relative abundances of these were taken in order: a-b-c-b-a-b-c-b-a. The exposure time was varied for each: a and c = 60 s, while b = 500 s. The repeated analysis of ^{18}O was performed to assess for variation in beam intensity, since ^{18}O is the reference element needed to convert signal intensity into a concentration for spinel (Appendix 1).

Signal intensity for spinel was inferred using image analysis techniques. For each spinel grain, the signal was determined to be homogeneous or heterogeneous by sub-sampling each sample area and performing analysis-of-variance (ANOVA) modelling. When no significant difference is observed between the mean values for each sub-sample, then

the signal for that spinel is said to be homogeneous. In some cases, structural artefacts (e.g. topography) can perturb signal intensity. ANOVA modelling is strongly affected by such artefacts, and thus, ANOVA modelling is a robust method for optimizing sample area selection. Profiles of signal intensity across a spinel grain and the adjacent phase(s) provide quantitative estimation of grain boundary thickness (Yurimoto et al., 2003). The application of a median filter was determined to preserve mean signal intensity while reducing statistical noise. Background correction also reduced noise attributable to the sensor and connected electronics. Using the signal intensities recovered from SCAPS imaging and RSF information (Appendix 1) for the Cameca IMS-1270, H concentrations were quantified for synthetic spinels.

3.2.3.2 Routine beam analysis for natural Fe-bearing spinel

For natural spinels, routine beam analysis was performed with a focused (*c*. 30 μm diameter) $^{133}Cs^{+}$ primary ion beam, which was set to *c*. 30 nA. A normal incident electron gun compensated for positive surface charging of the sputtered region. A 50×50 μm rastered beam was used to pre-sputter and perform mass calibration. Mass calibration (with mass resolution $M/\Delta M$ = *c*. 5,000) was performed while stigmatically imaging the sample surface in order to identify sources of signal contamination: grain boundaries, cracks, and hydrous micro-inclusions. Calibration clearly separated $^{16}O^{1}H$ from ^{17}O secondary ion counts.

Sample pits were pre-sputtered with a 30×30 μm rastered beam in order to remove surface contamination, excavated at 25×25 μm, but only the inner 2-3 μm of the beam area was taken for sampling via the use of a field aperture. Both the field aperture and contrast aperture were set to 100 μm. A high beam density is an effective method in improving the detection limit of sample hydrogen during SIMS analysis (Yurimoto et al., 1989). Water contamination due to the aforementioned contamination sources were avoided as evidenced by the flat stable secondary ion beam intensities. Secondary ion yields for $^{16}O^{1}H$, ^{17}O, and ^{18}O were collected sequentially by electron multiplier. Analysis time for each spot was *c*. 6 minutes in duration. Average signal intensity was used to calculate $^{16}O^{1}H/^{18}O$ for the ablated material, which was then converted into concentration information using the RSF method (Appendix 1).

3.2.4 Estimation of background OH using rastered beam techniques during routine SIMS analysis

Estimation of background followed the observation of varying count rate (signal intensity) with a change in beam power density (constant current, varying raster size, Figures 3.1 and 3.2). In principle, signal that is intrinsic to the sample material is positively correlated with beam power density (i.e. intrinsic signal yield increases with sputtering rate), while background signal intensity is correlated with beam diameter (i.e. background signal yield increases with sputtering area). In the case where the intrinsic OH signal is equal to the background signal, little to no variation in signal intensity with beam density is expected (i.e. $^{16}O^{1}H$ profiles should be relatively flat, cf. Figure 3.1).

H is a gaseous background component during SIMS analysis even at high vacuum conditions. Routine estimation of background H concentration is normally achieved by analysing standards with known H concentrations. Such standards should be isostructural with respect to the unknown sample material to preclude matrix effects. The ratio of the isotope/dimer of interest over a chosen matrix element (here OH/O) will vary with change in beam power density (see above). Since higher beam power density translates directly to an increase in sample sputtering rate, this constitutes a background H mitigation technique (Magee, 1983; Stevie et al., 2016). By plotting

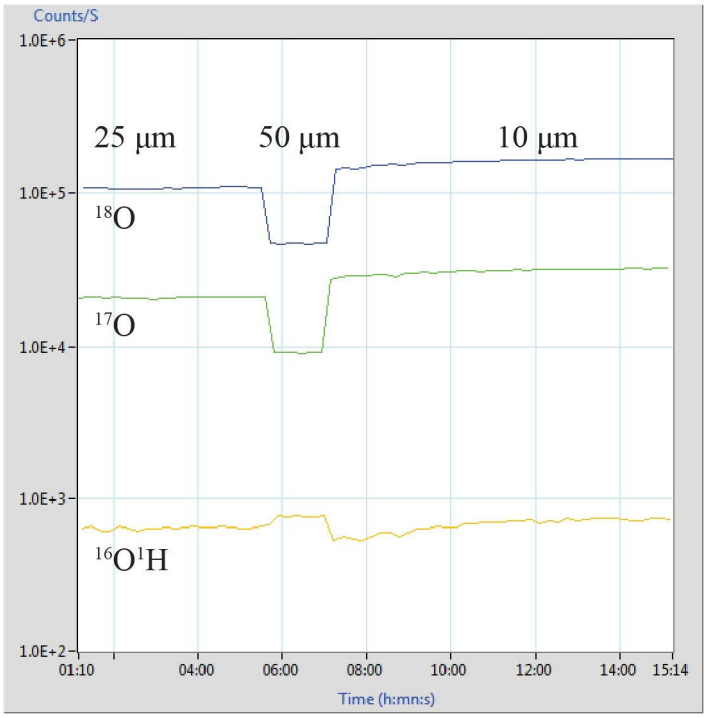

Figure 3.1: Time-series plot of signal intensity taken for a Troodos chromite. Signal shift in O-isotope signal intensity is diagnostic of an intrinsic signal (derived from the sample). Surface charge effects are observed at 10 µm (unstable beam condition and unsteady ionization). Roughly horizontal trends in the $^{16}O^{1}H$ signal can be interpreted as signal intensity being equally derived from background and intrinsic sources. Dimension is raster diameter.

OH/O versus beam power density (Figure 3.3), one can observe systematic decrease in OH/O as the beam is narrowed. At some point, the signal ratio would stabilize and remain invariant with further increase in beam power density because the background contribution will be minimized at this condition. This enables users to optimize the beam condition for a given analytical session.

This method of signal optimization could not be implemented here. Due to surface charge effects evidenced by signal instability at high beam power density (i.e. 10 μm condition, Figure 3.1), a lower limit on raster size is imposed by the material properties of spinel. Figure 3.3 shows that the signal intensity still drops between 25×25 μm and 10×10 μm, and it is unknown at precisely which beam power densities background contributions are minimized. Thus, it was decided instead to estimate the background contribution to the observed signal intensity and subtract this background from this signal to obtain the intrinsic OH concentrations characteristic of the sample material.

The intensity plots for the two spinel samples (Figures 3.1 and 3.2) were generated by collecting secondary ions over a period of *c*. 6 minutes. Over this period, raster area was varied starting with a 25×25 μm area, then 50×50 μm, and finally ending the analysis with a raster area of 10×10 μm. Unlike $^{16}O^{1}H$, the characteristic shifts in ^{18}O and ^{17}O secondary ion yield indicate that these elements are positively correlated with beam power density, and the consistent ratio (*c*. 5.08-5.15) between them indicates that the isotopic signatures of these matrix elements are i) well above background levels and ii) that variance in beam density does

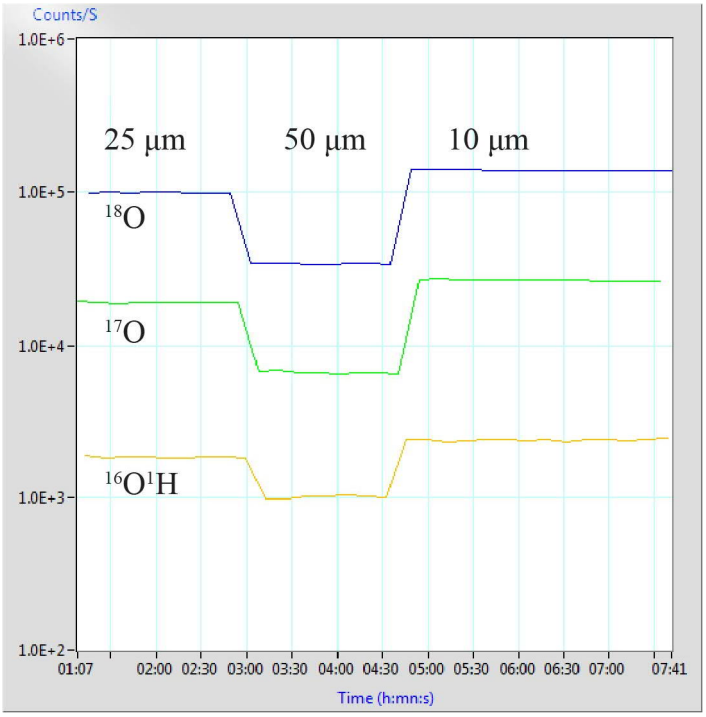

Figure 3.2: Time-series plot of signal intensity for a Taranaki titanomagnetite. Same characteristics as before. The $^{16}O^{1}H$ signal profile shape indicates that a majority of the signal intensity is intrinsic. Dimension is raster diameter.

not affect relative information gained by analysis of signal intensity.

In contrast, $^{16}O^{1}H$ profiles differ dramatically between the two samples. The first set of spectra were gathered from a chromite taken from the ultramafic section of the Troodos Ophiolite, and the second set from a titanomagnetite sourced from Taranaki Volcano, New Zealand. The $^{16}O^{1}H$ signal for the Troodos chromite is completely different in form from both O-isotope signals and is relatively flat (Figure 3.1), while the same signal in the Taranaki titanomagnetite is very similar in form to its respective O-isotope signals with a plateau-trough-plateau shape (Figure 3.2). A schematic cartoon representing change in OH signal intensity (ion yield) characteristics as a function of both raster area and the starting ratio between background and intrinsic H sources (b/i) is given in Figure 3.4.

In principle, the background contribution to each analysis may be estimated based on the systematic shifts in $^{16}O^{1}H$ (ρOH) and ^{18}O (ρO) signal intensities with change in beam power density between 25×25 μm and 50×50 μm raster areas. Here, ρOH and ρO are the ratios (25×25 μm ion yield/50×50 μm ion yield) for dimer and isotope signals, respectively.

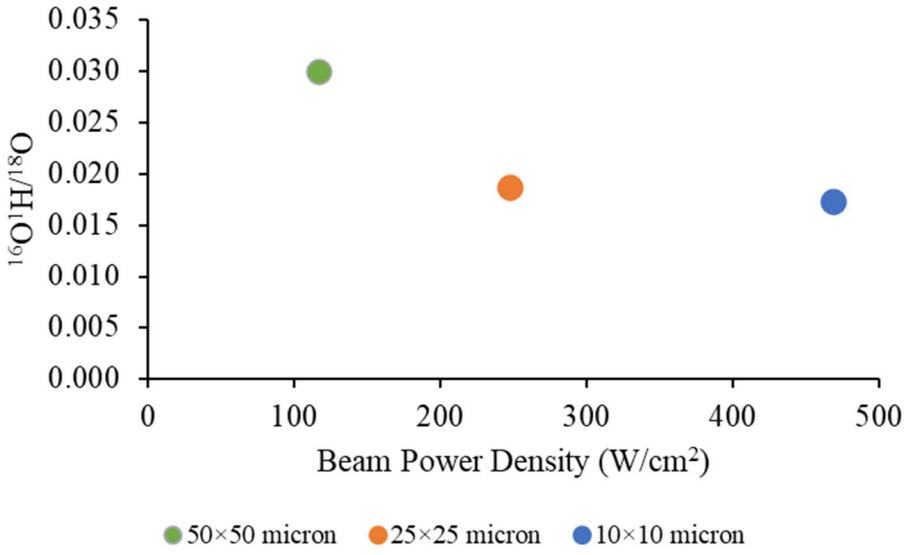

Figure 3.3: Beam power density vs observed OH/O signal. Ratio data were derived by averaging the signal intensities for $^{16}O^{1}H$ and ^{18}O using a large (> 10) number of points from the time-series plot for Taranaki titanomagnetite (Figure 3.2).

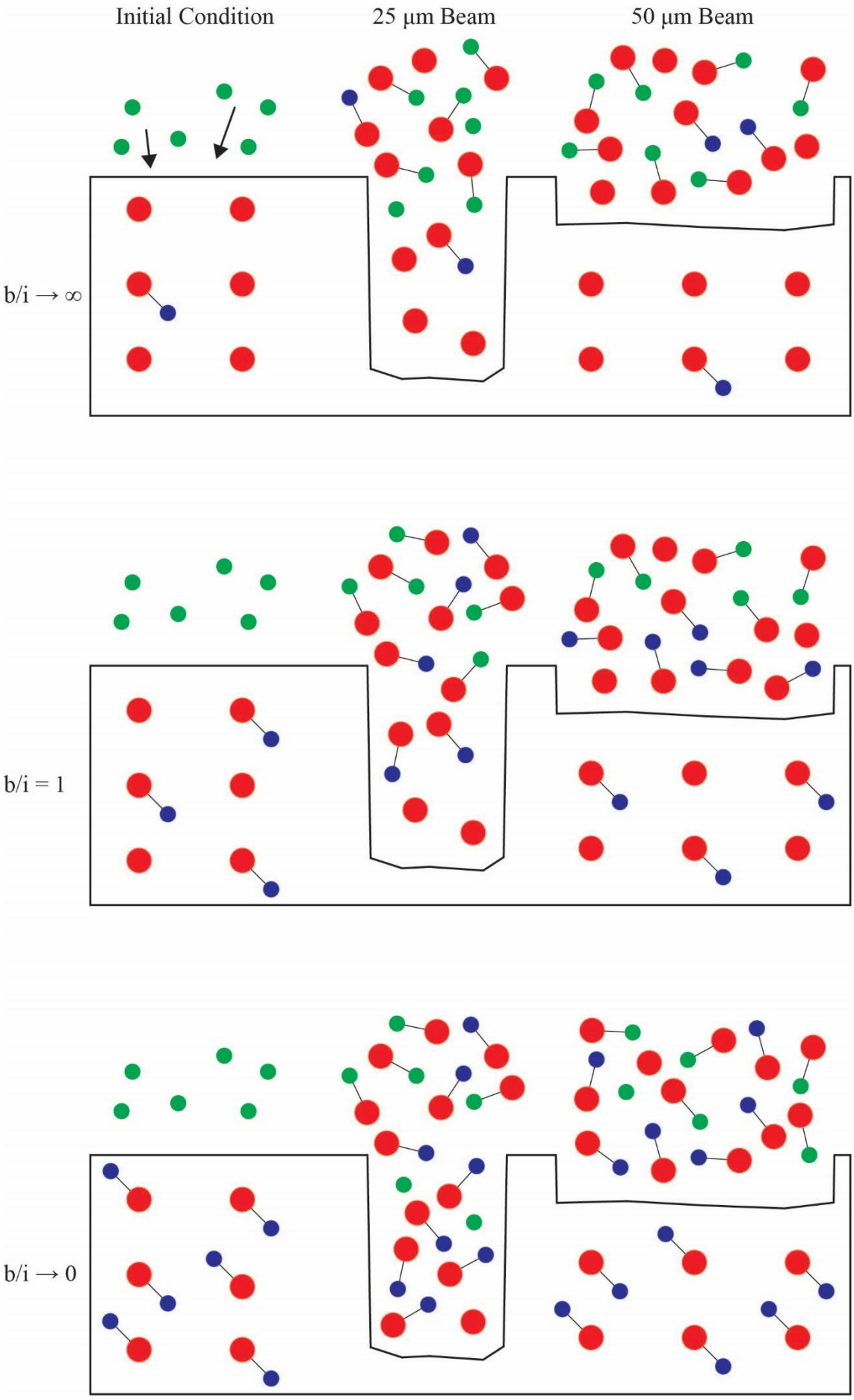
Initial Condition
25 μm Beam
50 μm Beam
b/i → ∞
b/i = 1
b/i → 0

Figure 3.4: Extreme b/i ratios are illustrated by the relative abundances of the green circles (background H cations sourced from the SIMS analysis chamber) to the blue circles (structurally bound H within a volume of spinel). In the analysis chamber, gaseous background H will adhere to the sample surface continuously during analysis (arrows), which is not explicitly shown here. The red circles are O^{2-} anions, which are not all shown. Only a subset of O^{2-} anions are shown to simplify the figure. As b/i approaches infinity, very little H will originate from the sample. Using a 25 µm beam will more efficiently generate secondary OH^- dimers from the sample, but background dimer formation will still outpace sample dimer yield. At 50 µm, sample sputtering rate is much lower, and less OH^- will originate from the sample. Background dimer formation will be maximized under this condition. If b/i = 1 (or is very close to 1), then the overall dimer production will remain invariant between beam conditions. As b/i approaches 0, a significant amount of OH^- will be sputtered from the sample surface. This is optimized under the 25 µm condition, though collection with a beam set to 50 µm may still yield a satisfactory signal intensity. For the purpose of this diagram, background is assumed to be constant, which is the case during a given SIMS analytical session.

To achieve this, the following model was developed. As stated before, all O-isotope signals are well above background levels, and any O-contribution of the background is negligible. Thus, if ρOH equals ρO, the background contribution is negligible and all of the signal is contributed by intrinsic OH; if ρOH equals 1, equal amounts of the OH signal are contributed from intrinsic and background H; if ρOH equals the inverse of ρO, there is no intrinsic OH and all observed signal intensity is attributable to background H. The ratio ρOH/ρO is a direct comparison in signal shift. If this ratio is equal to 1, then the $^{16}O^{1}H$ signal is said to be completely intrinsic; that is, it is completely attributable to the sample and very little can be attributed to background sources (since it behaves in the same way as the O-isotope signal). If this ratio is observed to vary between 1 and 1/ρO, then the $^{16}O^{1}H$ yield coming from the sample material is still greater than the signal contributed by the background. In the case where it varies between 1/ρO and $1/\rho O^2$, the background contribution is higher than the intrinsic $^{16}O^{1}H$ signal, and although the intrinsic $^{16}O^{1}H$ signal may still be significant, quantification of this intrinsic $^{16}O^{1}H$ signal is not reliable given the high background contribution to signal intensity, particularly in cases where the ratio approaches $1/\rho O^2$.

Here, b/i is related to ρOH/ρO through the following equation:

$$\frac{\rho OH}{\rho O} = \left(1 - \frac{1}{\rho O}\right) \times \left(1 - \frac{b}{i}\right) + \frac{1}{\rho O} \qquad \text{Equation 3.6}$$

Equation 3.6 enables solving b/i for any unknown ρOH/ρO between 1 and 1/ρO. On the other hand, for a signal whose ρOH/ρO value falls below 1/ρO, b/i is related to ρOH/ρO through the following equation:

$$\frac{\rho OH}{\rho O} = \frac{i\left(\frac{1}{\rho O} - \frac{1}{\rho O^2}\right)}{b} + \frac{1}{\rho O^2} \qquad \text{Equation 3.7}$$

Finally, the intrinsic H signal, $H_{Intrinsic}$, was estimated from the RSF derived total H signal, H_{Total}, using the equation $H_{Intrinsic} = H_{Total}/(b/i + 1)$, where b/i was estimated from ρOH/ρO using the above relationships. The background contribution, $H_{Background}$, is given by H_{Total} - $H_{Intrinsic}$.

3.3 Modelling

*3.3.1 Estimation of Fe loss via analysis of PtFe alloying by energy dispersive spectroscopy and implications for experimental petrology**

In order to assess for sample Fe loss due to alloying with their Pt capsules, the capsule walls of every sample (except Bon1200Ub) were analysed by energy dispersive spectroscopy (EDS). Point analyses were taken every *c*. 3 μm along a vector perpendicular to the sample-capsule contact starting from a point very close to the contact between the wall and sample glass and ending when no Fe was detected.

Appendix 2 provides distance data, observed alloy compositions, calculated alloy densities, partial volumes, mass of Fe per partial volume, total mass of Fe in each capsule alloy, and a final estimation of Fe lost (as % of bulk Fe) during each experiment. Alloy density (ρ) was estimated using the following relationship:

$$\frac{1}{\rho_{alloy}} = \frac{1}{100} \times \left[\left(\frac{wt.\%\ Pt}{\rho_{Pt}}\right) + \left(\frac{wt.\%\ Fe}{\rho_{Fe}}\right)\right] \qquad \text{Equation 3.8}$$

with the densities of Pt and Fe set to 22.5 g/cm^3 and 7.874 g/cm^3 respectively. In order to integrate the compositional data and quantify the total mass of Fe lost to the surrounding capsule, we assumed i) the profile describing alloy composition as a function of distance (Figure 3.5) was constant across the capsule geometry and ii) the capsule geometry may be approximated by that of a perfect hollow cylinder capped on each end by a disc.

To calculate partial volumes, we first calculated the volume of the sample space (V_{sample}) by:

$$V_{sample} = \pi r^2 h \qquad \text{Equation 3.9}$$

where r is the inner radius of the capsule (1 mm) and h denotes capsule length (1 cm). This volume was assumed to be constant across all capsules.

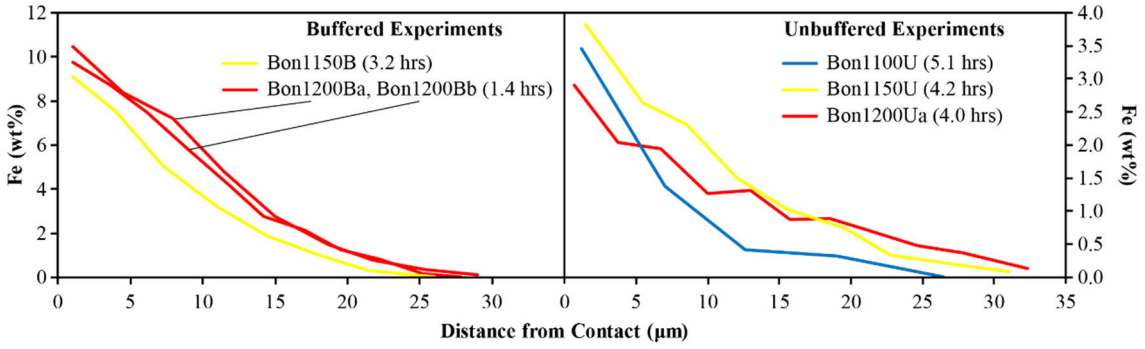

Figure 3.5: Profiles of Fe concentration in capsule walls (in boninitic samples) as a function of distance from the sample-wall contact.

The first partial volume of Pt alloy considered is the innermost slice of the capsule wall plus the discs on either end (dV_1), which is as thick as the distance from the sample-capsule wall contact to the position of the first point analysis (dx_1). This was calculated by:

$$dV_1 = [\pi(r + dx_1)^2 h] + 2[\pi(r + dx_1)^2 dx_1] - V_{sample} \qquad \text{Equation 3.10}$$

Every subsequent partial volume was calculated as:

$$dV_y = [\pi(r + dx_y)^2 h] + 2\left[\pi\left(r + dx_y\right)^2 (dx_y - dx_{y-1})\right] - \sum_{i=1}^{y-1} dV_i - V_{sample} \qquad \text{Equation 3.11}$$

These partial volumes were then multiplied by their respective alloy densities to calculate the mass of each alloy in each partial volume. The contribution of each of these masses to the total amount of Fe loss was then calculated by multiplying each mass by the mass proportion (wt.%) of Fe observed for that sample point. Finally, the sum of these contributions gives the quantification of Fe lost for a sample during a given experiment.

The final quantification of Fe loss is expressed as a percentage of the bulk Fe calculated for the starting sample mixture (BO-G glass plus 2 wt.% seed chromite). In order to calculate this, the value of wt.% FeO given for the normalized bulk composition in Table 4.1 was converted to wt.% Fe (8.87 wt.% FeO = 6.89 wt.% Fe).

Fe loss is minimized under the intrinsic f_{O_2} of the IHPV to *c*. 10%, but in buffered experiments we observed the degree of Fe loss increase by a factor of 2 at 1150 °C and 3-3.5 at 1200 °C. Our results are consistent with the findings of Kessel et al. (2001). Brief experiment durations did not prevent substantial Fe loss in buffered IHPV experiments.

Melt Fe^{2+}/Fe^{3+} should not change from the buffered equilibrium condition due to Fe loss because H diffusion through the Pt capsule is rapid by design (Chou, 1986). Thus, oxidation due to Fe loss is readily compensated by hydration and concomitant sample reduction:

$$FeO^{liquid} + H_2^{gas} + Pt^{capsule} \rightarrow PtFe^{capsule} + H_2O^{liquid} \qquad \text{Equation 3.12}$$

The argument could be made that a high f_{H_2} promotes the formation of PtFe since a high $p_{H_2}^{added}$ will enable the reaction to proceed to the right. In the case where $p_{H_2}^{added}$ is low (i.e. the intrinsic f_{O_2} condition) and the influx of H_2 is minimized, Fe loss is facilitated by:

$$3FeO^{liquid} + Pt^{capsule} \rightarrow PtFe^{capsule} + Fe_2O_3^{liquid} \qquad \text{Equation 3.13}$$

Because the predicted equilibrium conditions (Chapter 4.5.1) are consistently met across our modelling methodology or otherwise obscured by other experimental issues (such as quench crystallization), Fe loss does not significantly affect the equilibrium distribution behaviour of our experimental systems in a way that deviates from established empirical models. The mineral assemblage itself is not affected, as it is constant across all samples. Finally, Fe loss should not affect diffusivity within chromite because intra-crystal diffusivity is itself not dependent on the concentration of the element of interest in the material surrounding chromite (i.e. changing boundary conditions do not affect diffusion coefficients, Crank, 1975).

*3.3.2 Using machine learning to quantify phase proportions using Trainable Weka Segmentation (TWS)**

The FIJI platform (Schindelin et al., 2012) comes pre-loaded with the TWS plug-in (Arganda-Carreras et al., 2017). The images used for segmentation were backscattered electron (BSE) images taken from scanning electron microscopes at Massey University (New Zealand) and Hokkaido University (Japan). Segmentation is the product of the machine learning algorithm built into the TWS plug-in. Briefly, user-defined sets of pixel selections (one set for each phase) are assessed by TWS in order to create a classification scheme that may then be applied to an image. TWS uses a nearest neighbour binning of pixel colours in order to determine which phase a given pixel belongs to. The computer then segments the entire image into a colour-coded representation of that image based on this classification algorithm (Figure 3.6).

The images used for segmentation were determined to be representative based on BSE mapping of each sample surface. Using FIJI, we set the number of classes equal to the number of features in the BSE images ($n = 4$). These features define the groups of pixels that represent the phases; namely: glass, opx, chromite, and vesicles. Then, for each class, we used the pointer to select areas of each phase on the BSE image. Each selection was logged by the plug-in, and after several ($n > 8$) selections were made for each phase, we executed the segmentation protocol (this is where the computer learns to segment and classify the images). Output images (Figure 3.6) may be downloaded and easily interpreted in another image processing tool such as Adobe Photoshop.

Using Photoshop, we isolated each phase by using the magic wand tool to select every pixel of the same colour. The area proportion of each colour was then calculated using the measurement tool. The segmentation training was then repeated using different phase selections (often on different minerals and on different parts of the glass matrix). The number of segmentations used to estimate phase proportions was set to five. Reproducibility using this method is very good for a given image, and overall precision for each phase was observed to be better than ±9% (2σ relative) across all images.

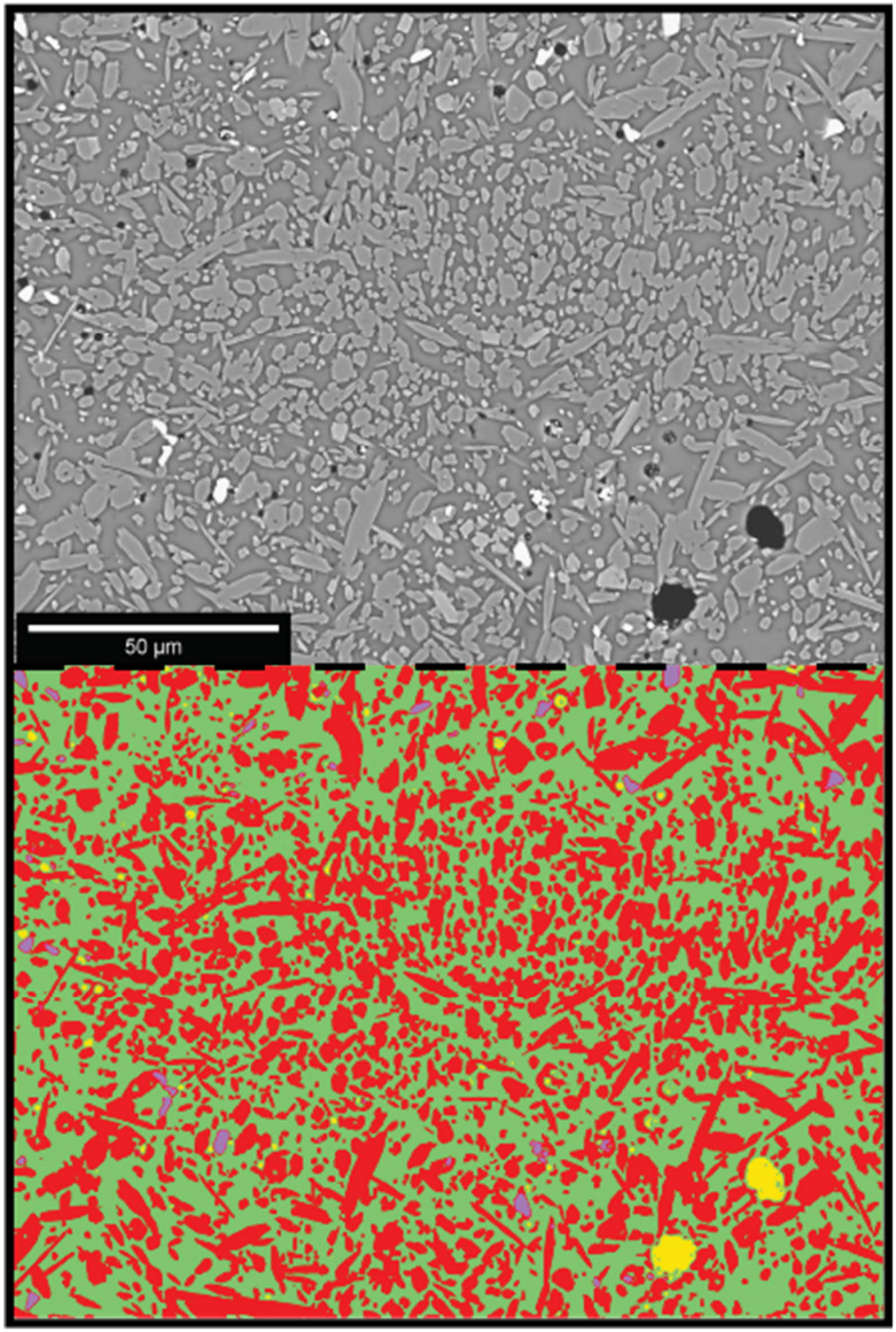

Figure 3.6: Representative BSE image of Bon1100U (top) versus a segmented image generated using TWS (bottom): green = glass, red = orthopyroxene, purple = chromite, and yellow = vesicles.

*3.3.3 Details of MELTS modelling and integration of SPINMELT-2.0 to predict equilibrium chromite compositions for boninitic experimental products**

The purpose of using MELTS (Ghiorso and Sack, 1995) was to model the behaviour of the boninitic glass used in each experiment (starting material BO-G, Table 4.1) under the conditions imposed by the IHPV with the assumption that the composition of the chromite used to seed each experiment would not significantly affect the behaviour of the melt over the brief period of each experiment. The decision to implement this model was made after simple chromite-melt equilibrium tests, based on empirical relationships given by Maurel and Maurel (1982a, 1982b), failed to predict chromite compositions when buffered above QFM (cf. Davis and Cottrell, 2018; Fisk and Bence, 1980; Maurel and Maurel, 1982a, b).

While the ability of the MELTS model to accurately predict equilibrium chromite compositions is disputed (e.g. Davis and Cottrell, 2018; Nikolaev et al., 2018a), MELTS should be able to accurately model the compositions of melt and silicate minerals under the P-T-f_{O_2} conditions imposed by the IHPV. Thus, we modelled equilibrium crystallization under isobaric conditions (2 kbar) of a hydrous melt with composition equal to that of BO-G (plus 1.25 wt.% H_2O). Three model trends were generated; one at each f_{O_2} condition: NNO+1, NNO+2, and NNO+3. Spinel (here: *sensu lato*) crystallized during melt differentiation. Model liquid compositions at temperatures between 1100 °C and 1200 °C (taken at 10 °C steps for each fO_2 setting) were then extracted and loaded into SPINMELT-2.0 to produce alternative model spinel compositions under equilibrium conditions. SPINMELT-2.0 is an update of the algorithm originally developed by Ariskin and Nikolaev (1996) for empirical modelling of chromite composition.

As an independent test of reproducibility, f_{O_2} was input to SPINMELT-2.0 along with melt composition, which then returned a temperature estimate (following Duhem's theorem). The accuracy given by Nikolaev et al. (2018a) for temperature is stated to be ±23 °C, on average, with higher residuals observed as pressure approaches 15 kbar. Based on this uncertainty estimate, the temperatures returned by SPINMELT-2.0 were not observed to be significantly greater than or less than the temperature setting given by the MELTS output when spinel was allowed to crystallize during MELTS modelling.

When spinel was suppressed as a liquidus phase during MELTS modelling, the melt became supersaturated with respect to the oxide phase. When supersaturated melt compositions (from spinel-suppressed MELTS runs) were input to SPINMELT-2.0, increasingly higher model liquidus temperatures were returned. In other words, if spinel is allowed as a crystallizing liquidus phase during isobaric MELTS modelling, then and only then can residual melt compositions be used in conjunction with the SPINMELT-2.0 algorithm.

Hence, we plotted spinel data from each step of MELTS modelling, and this output is discussed alongside SPINMELT-2.0 data as shown in Chapter 4. We note that spinel is a trace phase in all MELTS runs, so that potential inaccuracies in MELTS modelled spinel compositions are negligible with regards to the liquid line of descent of the residual melt, and therefore the stability and composition of co-crystallizing silicates. For buffered experiments that suffered a significant degree of Fe loss, we executed alternative MELTS + SPINMELT-2.0 modelling with bulk FeO concentrations lowered by 30% in order to predict spinel compositions that are in equilibrium with Fe-depleted melts.

*3.3.4 Estimation of interdiffusivity coefficients used to calculate maximum and minimum ascent times for the magmas of the Troodos ophiolite (Cyprus)**

In order to estimate ascent time for the lavas of the Troodos extrusive suite, diffusivity data from Suzuki et al. (2008) and Liermann and Ganguly (2002) were used to quantify $D_{Cr\text{-}Al}$ and $D_{Fe\text{-}Mg}$, respectively. The study of Suzuki et al. (2008) quantified $D_{Cr\text{-}Al}$ as a function of both temperature and Cr#. We used data from their Table 2 to replicate their Arrhenius plot (Figure 3.7) for chromite with Cr# = 0.8. We then fit a linear regression to these data (equation provided on the figure) in order to estimate $D_{Cr\text{-}Al}$ at lower temperatures. Liermann and Ganguly (2002) calculated self-diffusion coefficients for Fe and Mg from observed interdiffusivity relationships in their high-pressure experimental data. A reproduction of their Arrhenius plot is given in Figure 3.8 with linear equations provided. We recovered $D_{Fe\text{-}Mg}$ by using their Equation 4 [a modification of Darken's first Equation (Darken, 1948), after Barrer et al. (1963) and Manning (1968)]. For the calculation, atomic fractions of Mg and Fe were derived using average molar MgO and

FeO calculated for olivine-hosted chromite inclusions sampled by Sobolev et al. (1993) and Golowin et al. (2017), multiplied by Avogadro's number.

We calculated apparent D_{Fe} for the large seed chromite in Figure 1D (Figure 3.9). Here, zonation of the greyscale in the BSE image was assumed to represent Fe diffusion into the chromite grain from the melt phase with no precipitation or resorption occurring. Using Equation 4.3, τ = 0.03-0.04 (Figure 3.9), t = 3.2 hours (Table 4.2), and a = 27 μm, log D_{Fe} was estimated to be -11.7-12.6 cm^2/s at 1150 °C, which is in agreement with the values of Liermann and Ganguly (2002).

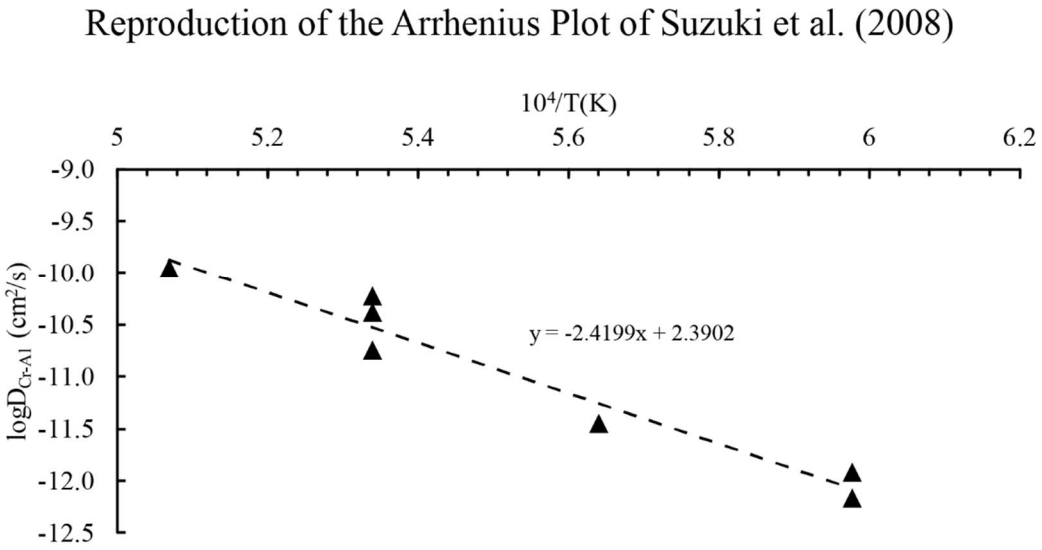

Figure 3.7: Reproduced Arrhenius Plot used to model Cr-Al diffusion in experimental chromite as described in Chapter 4

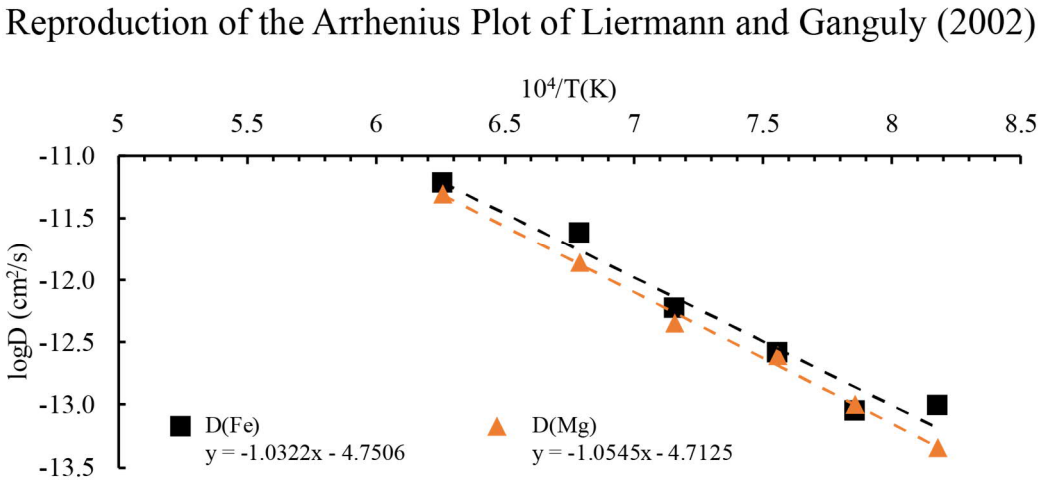

Figure 3.8: Reproduced Arrhenius Plot used to model Fe-Mg diffusion in experimental chromite as described in Chapter 4

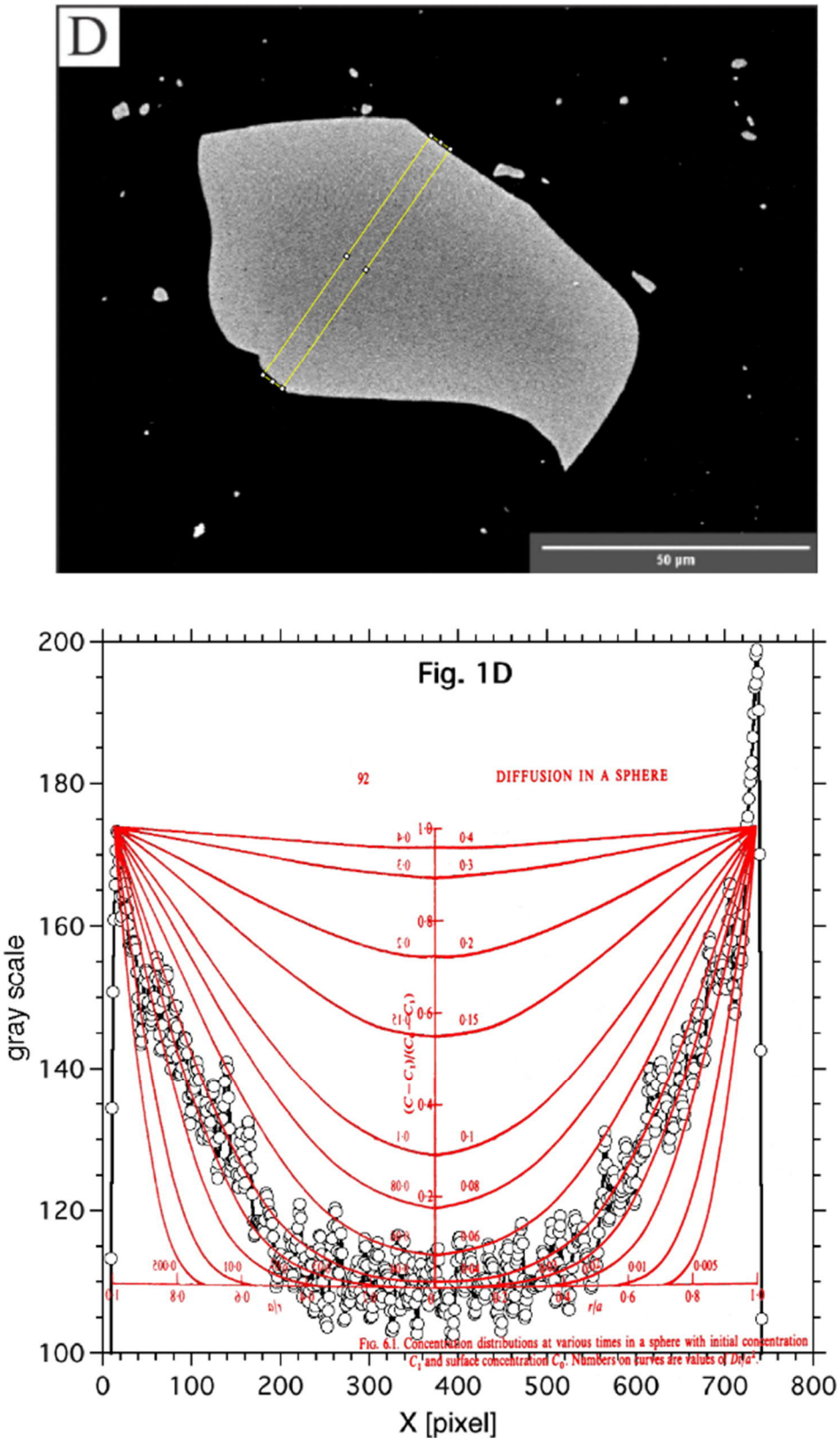

Figure 3.9: Diffusion profile inferred using SEM images of a chromite grain in a boninitic sample. The profile was fit to an idealized "diffusion in a sphere" diagram taken from Crank (1975), which we then used to infer that the chromite displayed a diffusivity features consistent with products of experiments conducted by Liermann and Ganguly (2002).

Chapter 4: Petrogenetic implications of chromite-seeded boninite crystallization experiments: Providing a basis for chromite-melt diffusion chronometry in an oxybarometric context

4.1 Abstract

Boninites are rare high magnesium andesites that often contain trace chromites. These chromites precipitate from primitive boninitic melts and are thought to be carried to the surface in melts that continue to crystallize a significant volume of silicate minerals. Such magmatic differentiation drives primitive chromite out of equilibrium with the residual melt with respect to both divalent and trivalent cation proportions. Diffusion then operates to alter primitive chromite toward a composition in equilibrium with residual melt. To simulate this process, we have performed internally heated pressure vessel experiments, providing insights into the processes of chromite-melt re-equilibration through time. While Fe-Mg exchange at magmatic temperatures equilibrates the tetrahedrally coordinated divalent cations in chromite in less than 6 hours, equilibration of trivalent cations in octahedral coordination with residual melts is slower. Our experimental results show that chromite Al concentrations are ubiquitously lower, and Fe^{2+}/Fe^{3+} values are ubiquitously higher than modelled equilibrium values, indicating that there was insufficient time for significant Al and Fe^{3+} replacement of Cr. Similar observations can be made for natural chromite compositions in the extrusive sequence of the Troodos ophiolite (Cyprus). Based on a simple model of diffusive equilibration, we estimate that microphenocrystic chromites up to 60 μm in diameter take between 60 days and *c.* 170 years to equilibrate under conditions analogous to the physiochemical state of melt immediately prior to eruption. For the Troodos ophiolite extrusive sequence, this implies that mafic magmas are erupted less than *c.* 170 years after extraction from the mantle for disequilibrium textures and compositions to be preserved.

4.2 Introduction

Boninites are rare high magnesium andesites that are produced by the melting of highly depleted mantle (harzburgite) under shallow and hydrous conditions (Pearce and Reagan, 2019). The paucity of this rock type in the geologic record may be attributed to

the exotic nature of these petrogenetic conditions and/or the tendency of boninites to erupt in places with a low preservation potential (e.g. forearc regions, Stern and Bloomer, 1992). Nevertheless, boninites are generated in several tectonic settings including intraoceanic arcs (Meijer, 1980), intracontinental arcs (Tatsumi, 2006), back-arc basins (Falloon et al., 1992), and oceanic plateaus (Golowin et al., 2017). Additionally, several boninites have been found in ophiolite terranes (e.g. Bédard, 1999; Cameron, 1985; Dilek and Thy, 2009; Ishikawa et al., 2002; Meffre et al., 1996), though the tectonic settings of some ophiolites are topics of rigorous debate (cf. Gass, 1968; Metcalf and Shervais, 2008; Miyashiro, 1973; Moores et al., 2000; Pearce and Robinson, 2010; Regelous et al., 2014; Woelki et al., 2020; Woelki et al., 2018).

A cogenetic relationship between boninitic melt and podiform chromitite deposits found in some ophiolitic mantle sections has been hypothesized (Arai, 1997; Arai and Yurimoto, 1994, 1995; Rollinson, 2008; Rollinson et al., 2018; Zhou and Robinson, 1997; Zhou et al., 1994). With regard to podiform chromitite formation, it has been suggested that primitive hydrous melts react with depleted mantle, become silica-enriched via the incongruent melting of orthopyroxene (implying olivine crystallization), and crystallize a large volume of high-Cr# chromite due to change in the number of available melt octahedral sites (Edwards et al., 2000). Separately, mechanisms of chromitite formation have been experimentally explored assuming immiscibility between melt-melt or melt-fluid components (Ballhaus, 1998; Matveev and Ballhaus, 2002). Initial immiscibility has been observed in other experimental studies that focused on the formation of boninitic melts via the same petrogenetic mechanism (i.e. incongruent melting, Fisk, 1986), and the boninitic composition of melts are preserved in equilibrium experiments that simulate melt-peridotite reactions (Mitchell and Grove, 2016). It is noteworthy that one experiment (C608) of Mitchell and Grove (2016) not only produced boninite melt in equilibrium with a dunite residual mantle mineral assemblage, but that the composition of the residual mineral assemblage overlaps with the most depleted end of the olivine-spinel mantle array in compositional space (Arai, 1994a). Ultimately, few studies have explicitly attempted to reconcile the links between boninite magma genesis, chromitite formation, and/or, more generally, chromite crystallization (Arai, 1997; Arai and Yurimoto, 1994, 1995; Rollinson, 2008; Rollinson et al., 2018; Zhou et al., 1994; Zhou et al., 1996).

If boninitic melts are generated during concomitant olivine and chromite precipitation as described above, then the appearance of high-Cr# chromite (and forsteritic olivine) in boninites may be due to their removal from a mantle domain rather than crystallization from extracted melts in the crustal domain, where chromite has not been observed to crystallize under experimental conditions analogous to those that are realistic for primitive melt differentiation (e.g. pressures > 1 bar, Umino and Kushiro, 1989).

It is important to specify the full implications of this model of boninite + chromitite petrogenesis, namely that boninite and chromitite appear to be linked by a cogenetic relationship based on observations of each in ophiolitic assemblages, that the underlying relationship is essentially a reactive transport process that occurs in the shallow subarc mantle, and that information on such processes may be inferred by detailed studies of chromite-melt or chromite-olivine-melt geochemistry; the systematics of which are preserved to different degrees in natural volcanic and plutonic suites (e.g. Kamenetsky et al., 2001). Further, if chromites are plucked from the melt-mantle petrogenetic system, then their melt inclusions (e.g. Kamenetsky et al., 2002; Umino et al., 2018; Umino et al., 2015) may give valuable information regarding the nature of magma genesis in the reactive transport regime.

In the present study, we conducted a series of high-pressure (*c.* 2 kbar) experiments to create systems wherein high silica boninite crystallized over brief time periods in the presence of stable chromite. The data presented here demonstrate that chromite is little affected by crystallization processes over short timescales unless unrealistically oxidizing conditions are imposed. Silicate mineral assemblages form via equilibrium crystallization in hydrous melts without significantly altering chromite compositions save for Mg-Fe exchange when buffered near the nickel-nickel oxide (NNO) buffer. We propose that the systems represented by these experiments may be regarded as approximations of what occurs in natural chromite-bearing primary melts during their crustal differentiation (Scowen et al., 1991). Similar observations on partial chromite-melt equilibration in natural samples from the Troodos ophiolite (Cyprus) allow a coarse quantification of the extraction time for the mafic magmas of the extrusive suite, but more detailed diffusion chronometry on the chemical zonation patterns of natural chromites will be required to provide tight constraints.

4.3 Materials and experimental methods

Crystallization experiments were performed using internally heated pressure vessels (IHPVs) at the Institut des Sciences de la Terre d'Orléans (ISTO), Université d'Orléans, France, as well as at the Geological Survey of Japan (GSJ) in Tsukuba, Japan. Additional sample preparation took place at ISTO and at the Japan Agency for Marine-Earth Science and Technology (JAMSTEC) in Yokosuka, Japan.

4.3.1 Starting materials

Table 4.1 provides major element data for the starting materials as well as the bulk composition of the mixture used for the experiments. Analyses of the starting materials are given alongside sample data in the Appendices (Appendices 3 and 4). A fragment of high-Si boninite taken via dredging from the Mariana forearc (sample YK0612 974-R6, Reagan et al., 2010) was chosen as a suitable starting material based on observed chromite phenocrysts and microphenocrysts in thin section, which indicated chromite stability. The fragment was powdered and fluxed to form glass, which was analysed during our routine spectrometric analysis (BO-G, Appendix 3) and re-powdered for sample loading. Chromite seeds sourced from the mantle section of the Troodos Ophiolite were added to glass powders with the intent of fostering further growth of chromite from boninitic melts. These seeds are unzoned and are homogeneous (avg. Mg# = 62, $Cr/[Al+Cr+Fe^{3+}] = 70$). Two sample mixtures were made by mixing powdered glass with one size fraction of chromite (either > 160 μm or < 32 μm in size), and each starting mixture contained 2% added chromite (by mass). The size of the seeds added to powdered glass were initially varied in order to test if seed size affects the resultant modal mineralogy of the sample.

Table 4.1: Starting material compositions

	High-Si Boninite	*Troodos Chromitite*	*Boninite Glass*	*Normalized Mixture Composition*
	*YK0612 974-R6	**Chromite Seed	**BO-G	BO-G with 2 wt.% added Chromite
SiO_2	56.74	0.05	57.92	55.51
TiO_2	0.17	0.05	0.04	0.17
Cr_2O_3	***0.19	53.81	0.19	1.26
Al_2O_3	10.66	15.11	10.69	10.73
FeO	8.75	15.34	8.38	8.87
MnO	0.23	0.24	0.16	0.23
MgO	15.04	14.01	14.62	15.01
CaO	5.54	-	6.16	5.42
Na_2O	2.01	-	1.86	1.97
K_2O	0.82	-	0.46	0.80
P_2O_5	0.03	-	0.08	0.03
Total	100.18	98.72	100.48	100.00

*Composition from Reagan et al. (2010, XRF Analysis)

**All analyses of starting materials are provided in Appendices 3 and 4

***Converted from ppm Cr to wt% Cr_2O_3

- = not quantified

Nominally pure platinum capsules were used as sample containers. Sample mixtures were first loaded and then hydrated with heavy water (^2H_2O) using a microsyringe before the capsules were welded shut. Each capsule contained *c.* 1 wt.% ^2H_2O prior to welding (Table 4.2). ^2H_2O was used instead of ^1H_2O to allow future analysis of H_2O using secondary ion mass spectrometry, with this substitution enabling easy distinction between added H_2O and background H. The quality of the welds was checked by

immersing each capsule in hot oil. All capsules were adequately sealed (poor welds emit a bubble stream, indicating an inadequate seal).

NiO+NiPd redox sensors added to each experiment allowed for the H fugacity (f_{H_2}) imposed by the IHPV pressure medium to be evaluated, as redox sensors accurately reflect the oxygen fugacity (f_{O_2}) imposed by the gas buffer (Pownceby and O'Neill, 1994; Taylor et al., 1992). These sensors were made by packing two pellets into inert ZrO_2 powder within a Pt capsule so that the pellets are not in contact with the capsule wall. One pellet was made of 50% NiO and 50% Ni_xPd_{1-x} and the other was made of 50% NiO and 50% Ni_yPd_{1-y}, with x = 0.5 and y = 0.85. Deionized H_2O was added until the capsule interior became visibly saturated. Then the capsule was welded shut. Welds were checked in the same way for the sensors as they were for the sample capsules.

4.3.2 Experimental design

The IHPVs used at ISTO and GSJ both employed Mo furnaces to perform the high temperature experiments described here. Since the same amount of H_2O was initialized in each sample, by varying the temperature of the experiments between 1200, 1150, and 1100 °C, variable degrees of crystallinity are achieved in each sample. This determines the concentration of H_2O in residual melts, as the crystallization of nominally anhydrous mafic minerals enriches the melt volume in incompatible volatile elements. The experiments were performed under isobaric conditions, which means the final variable to consider is the f_{O_2} of the system.

Target oxygen fugacities were *c*. 1-3 log units above the NNO buffer, which are analogous to magmas generated in subduction zone settings (Brandon and Draper, 1996; Evans et al., 2012; Kelley and Cottrell, 2009; Parkinson and Arculus, 1999). The oxidation states were either left unbuffered or buffered by pressurizing the IHPV with an Ar-H_2 gas mixture ($p_{H_2}^{added}$, Table 4.2). Pt capsules are permeable to H, which diffuses through the capsule wall to bond with oxygen in the melt so that reduction of the sample volume occurs (Chou et al., 1978; Shaw, 1963). Since the volume of the pressure medium is much greater than the volume of the sample capsule, the pressure medium is effectively an infinite reservoir with respect to H. Thus, the effective concentration of H available to each capsule during a given experiment, f_{H_2}, may be considered constant. Unbuffered experiments cause the redox state of melts to approach

a condition known as the intrinsic f_{O_2} of the IHPV. The intrinsic f_{O_2} of IHPV systems is highly oxidizing (NNO+2 to NNO+4, Scaillet et al., 1992; Taylor et al., 1992, see further discussion in Chapter 3.1).

The experiments described here each lasted less than 6 hours. The utility of short-period experiments is multifaceted. From a volcanological perspective, fast ascending magmas are extracted from their crustal domains and extruded onto the surface in as little as tens of minutes (Lloyd et al., 2016) when melts are hot (> 1000 °C) and volatile rich. Short timescales of the order of hours to days have also been inferred for volatile poor arc magmas (Lormand et al., 2020). In a rapidly ascending melt, a variety of concomitant processes may alter the physicochemical state of the melt volume, including syn-eruptive mixing (e.g. Tomiya et al., 2013; Wolf and Eichelberger, 1997), crystallization (e.g. Blundy and Cashman, 2005; Cashman and Blundy, 2000), and whole-rock contamination (e.g. Mattioli et al., 2006). Such processes, along with subtleties such as the inclusion of antecrystic minerals, produce disequilibrium mineral assemblages that provide valuable insight into the latest stages of magmatism (Couch et al., 2001; La Spina et al., 2016; Ubide et al., 2014; Zellmer et al., 2016; Zellmer et al., 2014). Thus, for natural magmatic systems, brief durations on the order of hours represent an end member in an ascent period context, and disequilibrium characteristics may be useful if properly placed into a petrogenetic context. Given boninite petrogenesis occurs at relatively shallow depths and generates hot and hydrous melts, sometimes in extensional settings (Reagan et al., 2017), rapid ascent rates cannot be precluded. Indeed, this is a knowledge gap that must be addressed. Furthermore, since it is possible that chromites preserved in boninite matrices may have been generated within the source regions of the melts, knowledge of how these minerals react to changes in the physicochemical states of the melts (i.e. experimental observation) is needed in order to assess and contextualize natural sample materials. These considerations provide an incentive to perform experiments on brief timescales and to analyse disequilibrium features.

Table 4.2: Sample identification and characterization, experiment descriptions, and preliminary results

Capsule ID	*IHPV Lab*	*Initial Composition*		*Experimental Conditions*			
		Seed Size (μm)	wt% D_2O (1σ)	T (°C)	P (kbar)	pH_2^{added} (bars)	Duration (hrs)
Bon1200Ua	ISTO	x < 32	1.136 (0.142)	1200	2.13	0.0	4.0
Bon1200Ub	ISTO	160 < x < 250	1.395 (0.155)	1200	2.13	0.0	4.0
Bon1200Ba	ISTO	x < 32	0.916 (0.153)	1200	2.12	1.9	1.4
Bon1200Bb	ISTO	160 < x < 250	0.763 (0.191)	1200	2.12	1.9	1.4
Bon1150U	ISTO	x < 32	0.770 (0.128)	1150	2.16	0.0	4.2
Bon1150B	ISTO	x < 32	0.705 (0.141)	1150	2.14	1.4	3.2
Bon1100U	GSJ	x < 32	1.280 (0.142)	1100	2.00	0.0	5.1

Names: U = intrinsic fO_2, B = buffered fO_2, a and b designate a difference in the seed size of the chromite added

Table 4.2 (continued)

Capsule ID	*Product Phase Proportions (1σ)*			*Activity Model*		*Oxygen Fugacity*		
	Orthopyroxene	Chromite	Glass	Final wt% ^2H_2O (1σ)	aH_2O (1σ)	Sensor X_{Ni} (1σ)	log fO_2 (bars)	ΔNNO (1σ)
Bon1200Ua	0.49 (0.01)	0.02 (0.01)	0.49 (0.02)	2.32 (0.30)	0.34 (0.07)	0.020 (0.004)	-3.69	3.81 (0.17)
Bon1200Ub	0.50 (0.03)	0.02 (0.00)	0.48 (0.03)	2.91 (0.37)	0.48 (0.08)	0.020 (0.004)	-3.39	4.11 (0.17)
Bon1200Ba	0.59 (0.07)	0.01 (0.00)	0.40 (0.07)	2.29 (0.55)	0.31 (0.11)	0.256 (0.003)	-6.77	0.73 (0.26)
Bon1200Bb	0.55 (0.01)	0.01 (0.01)	0.44 (0.01)	1.73 (0.44)	0.22 (0.08)	0.256 (0.003)	-7.07	0.43 (0.27)
Bon1150U	0.40 (0.08)	0.02 (0.00)	0.58 (0.08)	1.33 (0.29)	0.17 (0.07)	0.020 (0.004)	-4.88	3.21 (0.29)
Bon1150B	0.60 (0.06)	0.02 (0.00)	0.38 (0.05)	1.86 (0.44)	0.26 (0.09)	0.194 (0.003)	-7.09	1.00 (0.26)
Bon1100U	0.45 (0.05)	0.01 (0.01)	0.54 (0.05)	2.37 (0.34)	0.32 (0.07)	0.069 (0.009)	-6.21	2.52 (0.16)

4.4 Analytical methods

Analytical facilities at Victoria University of Wellington, Hokkaido University, Massey University, and The University of Iowa were utilized to gather the data presented here.

Following removal of the sample holder from the IHPV, each capsule was weighed to assess for mass loss during the experiment. The capsules were then mounted in epoxy and ground to expose their interiors. Ni-Pd alloys recovered from each sensor capsule was separated from powdered ZrO_2 and mounted in epoxy. These sample materials were then polished for imaging and microprobe analysis, using SiC lapwheels and diamond grit paste.

4.4.1 Electron microbeam techniques

Samples produced at ISTO were imaged using an FEI Quanta 200 Environmental scanning electron microscope (SEM) at the Manawatu Microscopy and Imaging Centre (Massey University). This SEM was also used to perform semi-quantitative analyses of calcic silicate minerals using an attached EDAX energy dispersive spectroscope (EDS). Samples produced at GSJ were imaged at the Creative Research Institute of Hokkaido University using a JEOL JSM-7000F Field Emission SEM. An attached XMAX 150 EDS was used here to analyse the capsule Pt walls in contact with sample melts in order to detect iron loss after each experiment (Chapter 3.2.2, Appendix 2). Quantification of Fe in Pt was achieved by calibrating signal intensity to pure Co.

Electron probe microanalysis (EPMA) occurred at multiple laboratories: at Victoria University of Wellington and The University of Iowa, JEOL JXA-8230 Superprobes were used. Additional chromite analyses were performed at Hokkaido University on a JEOL JXA-8800R. Glass analyses were performed using Na-migration mitigation techniques. In addition to using diffuse beam conditions (spot sizes of 5-10 μm), two Na acquisitions are totalled. If analyses return low concentrations (determined using secondary standards), then sodium loss may be corrected by either: removing the second acquisition (if Na is lost), removing either point (if either indicates loss), or back-calculating time-resolved intensity to correct for Na loss. No analyses reported here experienced significant sodium migration as indicated by multiple analyses of both sample and standard materials.

Secondary standards provided by the Smithsonian Institution Department of Mineral Sciences and/or the Max Planck Institute for Chemistry were included in all glass and mineral analyses. Ni-Pd sensor compositions were quantified using metal standards by Astimex. Repeat analyses of secondary standards provided a basis to assess the accuracy of data gathered during EPMA (Appendix Tables S1-S2, and S4). The accuracies associated with glass analyses have been determined to be within 1% for SiO_2, Al_2O_3, MgO, and CaO, 5% for TiO_2, FeO, and K_2O, 10% for Na_2O, and 20% for MnO. For analyses of silicate minerals, SiO_2, MgO, CaO, and Na_2O are accurate to within 1%, while FeO, Cr_2O_3, MnO, and Al_2O_3 are better than 2%. Chromite standardization was achieved using several mineral and oxide standards. Replicate standard analyses demonstrated that all major elements given are accurate to within 5%, while MnO is accurate to within 40%. Secondary standard compositions are taken from Jarosewich et al. (1980); Jochum et al. (2006); and Jochum et al. (2005).

To ensure analyses of pyroxene were of high quality, raw EPMA data were normalized prior to formulae recalculation using the methods described by Putirka (2008). Analyses that returned cation totals much greater than or less than 4 (on an O = 6 basis) were discarded. In a similar manner, raw chromite analyses were recalculated to cation proportions per 4 oxygens. Recalculation of Fe^{3+} proportions used the equation of Droop (1987). No other multivalent cations (e.g. Mn, Cr) were considered.

4.4.2 Determination of phase proportions

In order to provide high-precision phase proportion data, a computationally inexpensive machine learning tool enabled the analysis of backscattered electron (BSE) images and produced segmented images that we interpreted in terms of phase proportions using Adobe Photoshop. Segmented images are images that have been petrographically interpreted using a machine learning algorithm and are color-coded based on which phase each pixel represents (Chapter 3.3.2). The machine learning tool used is called Trainable Weka Segmentation, and was developed by Arganda-Carreras et al. (2017). The algorithm requires limited user input (5-8 user-defined groups of pixels) to "train" the computer-generated classifier, which segments as many mineral phases as the user defines This tool produced the segmented images used to infer the phase proportions given in Table 4.2. The tool is provided as a plugin on the Fiji Is Just ImageJ (FIJI) platform (Schindelin et al., 2012). A minimum of 5 training sessions were conducted for

each analysis, and the data derived from each segmented image were averaged to produce the given proportions with the calculated standard deviation providing the precision of each phase classification. Images representative of the sample textures were used for segmentation. See Chapter 3.3.2 for more information and an example of a segmented image.

4.4.3 Determination of oxygen fugacities from the solid sensors

Fugacity calculations were performed following the methodology of Scaillet et al. (1995). Sensor compositions, *X*Ni (Ni/[Ni+Pd] calculated using cation proportion), were determined following EPMA. Further discussion of fugacity, including the calculation methodology, is provided in Chapter 3.1.

4.5 Results

Weighing the capsules after quench indicated that no mass was lost during any experiment. Table 4.2 gives information on each sample including the mixture used, initial water concentration, experimental conditions, resultant phase proportions inferred for each sample, sensor compositions, and f_{O_2} data.

The capsule interiors of every sample except for Bon1200Ub were analysed via EDS in order to assess the degree of iron loss from the melt to the Pt of the capsule wall. Line analyses from the sample-wall contact into the capsule wall yielded no detectable Fe *c*. 30 μm from the interface. Integrating concentration profiles demonstrates that Fe loss in unbuffered experiments is limited to 10% or lower (of bulk sample Fe), while buffered experiments lost 20-35% Fe over experiment durations (Chapter 3.3.1, Appendix 2). However, we will demonstrate that none of our discussion topics have been significantly affected by Fe loss.

4.5.1 Petrographic observations

Euhedral-subhedral orthopyroxene (opx) is abundant and is the only silicate phase present at 1200 ℃ and 1150 ℃ (Figure 4.1A). In BSE images, these crystals often have bright caps that form at the apices of euhedral crystal forms (Figure 4.1B). At 1100 ℃, a petrographically distinct trace silicate phase was observed along with abundant opx in Bon1100U (Figure 4.1C). Semi-quantitative EDS analyses of this phase demonstrate that this silicate is rich in Ca, Mg, and Fe. If it is a pyroxene, it is likely augite (*c*. Wo_{31}

En_{57} Fs_{12}). Chromite is stable in all boninitic samples, and BSE images of moderate-sized grains show that chromite mantles have become brighter than cores (Figure 4.1D), indicating that diffusive equilibration was interrupted by quenching in large grains. In general, all chromites appear as anhedral grains with sharp-subrounded corners. These are not indications of chromite growth, suggesting that all observed chromites are the original seeds added to each experiment. Likewise, there is no evidence of dissolution, which indicates that chromite was a stable phase for the full duration of each experiment. This implies that our experiments only produced pyroxene crystallization in the presence of stable chromite. A small number of micro-vesicles occur in all boninitic samples (e.g. Figure 4.1A). The vesicles are spherical and show no indication of clustering. They appear randomly distributed within the sample volume. No vapour films were observed along any of the capsule walls.

4.5.2 Redox sensors and calculation of oxygen fugacity

Average *X*Ni values were calculated for each sensor and used to infer sensor f_{O_2} for each experiment. For water undersaturated sample melts, aH_2O must be modelled in order to accurately calculate f_{O_2}. To this end, the activity model of Burnham (1979) was used in conjunction with major element data and inferred melt water concentrations (Chapter 3.1) to model aH_2O. The uncertainties reported here for f_{O_2} are similar to those reported elsewhere for the solid sensor technique (Jégo et al., 2010; Scaillet et al., 1995). The solubility model of Zhang et al. (2007) was used to calculate maximum water concentrations in residual melts under the experimental conditions, which correspond to *c*. 5.3-5.4 wt.%. According to these model constraints, boninitic melts did not reach saturation (Table 4.2), and the ubiquitous presence of micro-vesicles (Figure 4.1A) is therefore not due to H_2O saturation (exsolution) but likely due to the inclusion of atmospheric gas in the sample capsules during preparation.

Complexities associated with quench crystallization were observed in samples Bon1200Ua Bon1200Ub, Bon1200Ba and Bon1200Bb and are discussed later. A principal effect of quench crystallization is to raise aH_2O in residual melts. Thus, for these high temperature samples, the reported f_{O_2} data are considered maxima.

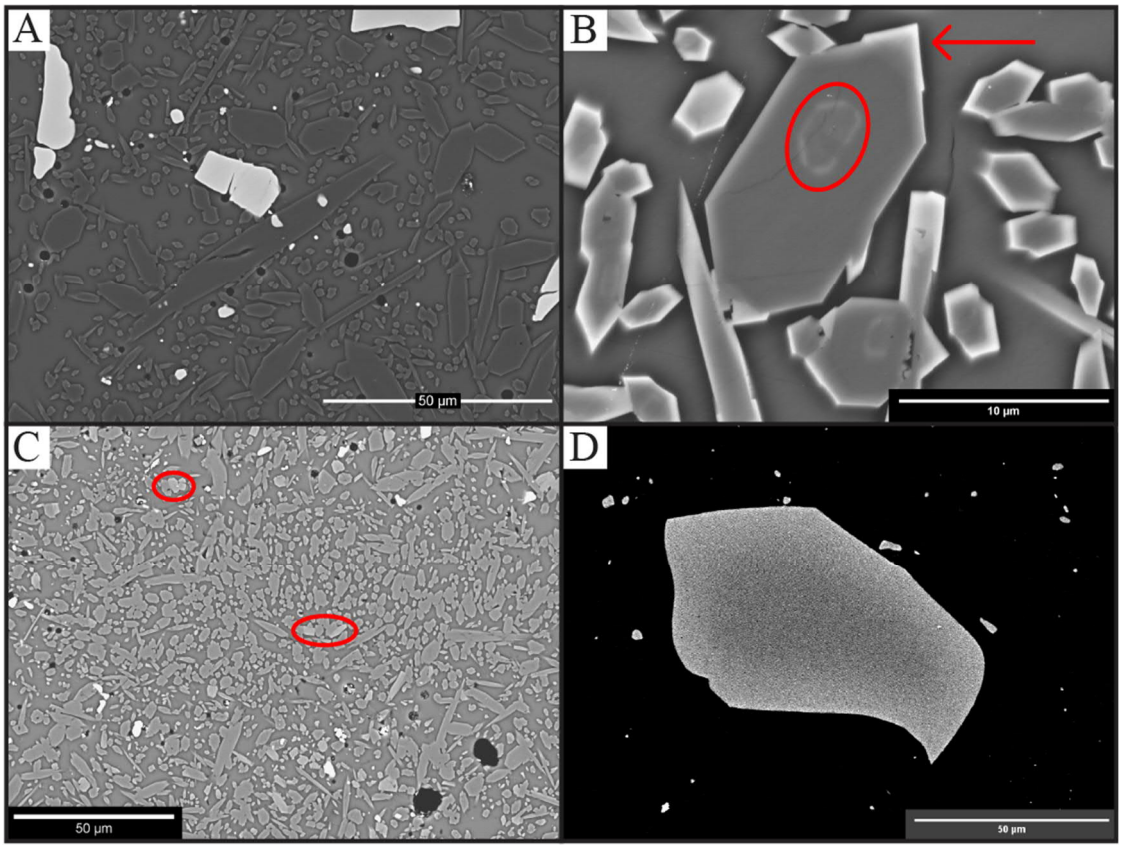

Figure 4.1: Composite images for boninitic samples (A) BSE image of Bon1150U. This image is representative of the ‘‘general” texture observed in the boninitic charges. This includes several examples of euhedral prismatic opx (dark mineral grains) and platy elongated opx (same colour) set in a relatively homogeneous glass with anhedral chromite (bright grains). The black orb-shaped parts are vapour bubbles. (B) Close up of an opx cut parallel to the (0 1 0) plane exhibiting a ghost core (red ellipse). The core is likely related to crystallization occurring within the melt/glass phase before stable thermal conditions were achieved within the IHPV. The arrow points to bright caps that form at the apices of most if not all opx in this sample (from experiment Bon1200B). These caps are thought to have grown during quench. The glass adjacent to these minerals is darker, indicating the loss of iron to the quench-grown rim. (C) Broad view of sample Bon1100U with calcic pyroxene highlighted (red ellipses). Several opx are aligned here, with their c-axes sub-perpendicular to the image plane. (D) BSE image of chromite in Bon1150B after thresholding brightness and contrast to isolate and amplify Fe enrichment textures.

Table 4.3: Representative compositional data of experiment products (average composition)

Sample	*Phase*	*No. Analyses*	SiO_2	TiO_2	Cr_2O_3	Al_2O_3	FeO	MnO	MgO	CaO	Na_2O	K_2O	NiO	Total	Mg#	Cr#	*Fe^{2+}/Fe^{3+}
Bon1200Ua	Glass	6	61.36	0.07	bdl	16.34	5.90	0.10	2.43	6.51	3.08	0.81	-	96.63	-	-	0.77
	Orthopyroxene	15	55.99	bdl	0.69	1.66	6.59	0.20	33.87	1.09	bdl	-	-	100.14	0.90	0.22	-
	Chromite	4	0.27	bdl	48.62	8.49	24.89	0.36	12.57	-	-	-	0.10	95.36	0.47	0.79	1.17
Bon1200Ub	Glass	8	60.57	0.20	bdl	15.98	7.51	0.14	2.79	6.11	2.52	0.69	-	96.52	-	-	0.76
	Orthopyroxene	13	56.35	bdl	0.67	1.49	6.09	0.18	34.30	0.93	bdl	-	-	100.04	0.91	0.23	-
Bon1200Ba	Glass	5	62.08	0.18	bdl	17.90	5.24	0.13	1.64	6.13	2.99	0.84	-	97.17	-	-	3.35
	Orthopyroxene	13	56.34	bdl	0.71	1.88	7.31	0.20	32.68	1.32	0.05	-	-	100.50	0.89	0.22	-
Bon1200Bb	Glass	2	60.95	0.18	bdl	18.14	5.13	0.14	1.11	6.16	2.92	0.84	-	95.56	-	-	3.84
	Orthopyroxene	9	54.99	bdl	0.68	1.56	7.18	0.20	32.28	1.20	0.15	-	-	98.25	0.89	0.23	-
	Chromite	4	0.12	0.05	50.66	14.36	16.20	0.29	13.16	-	-	-	0.11	95.02	0.59	0.70	3.48
Bon1150U	Glass	4	58.52	0.06	0.05	14.47	7.04	0.11	6.12	8.13	2.59	0.65	-	97.74	-	-	1.00
	Orthopyroxene	8	55.02	bdl	0.64	2.47	8.46	0.23	31.23	1.69	0.06	-	-	99.84	0.87	0.15	-
	Chromite-Core	4	0.11	0.04	51.17	11.86	21.57	0.39	11.62	-	-	-	0.12	96.95	0.49	0.74	2.44
	Chromite-Rim	3	0.15	bdl	48.96	9.34	26.09	0.38	10.89	-	-	-	0.15	96.07	0.43	0.78	1.61
Bon1150B	Glass	3	60.34	0.08	bdl	16.20	5.21	0.10	4.63	7.01	2.94	0.75	-	97.29	-	-	2.74
	Orthopyroxene	2	54.98	bdl	0.70	2.37	9.04	0.24	31.57	1.89	bdl	-	-	100.83	0.86	0.16	-
	Chromite	1	0.08	0.05	51.93	14.45	19.41	0.35	11.5	-	-	-	0.10	97.93	0.51	0.71	4.51
Bon1100U	Glass	5	58.96	0.18	0.14	14.75	6.11	0.13	5.97	8.18	2.59	0.68	-	97.71	-	-	1.31
	Orthopyroxene	3	55.20	0.05	0.44	3.33	9.13	0.29	30.01	2.67	0.10	-	-	101.24	0.85	0.08	-
	Chromite	6	0.07	0.14	50.93	14.41	22.28	0.32	10.96	-	-	-	0.09	99.42	0.47	0.70	3.50

**Calculated using either stoichiometric recalculation (after Droop, 1987) for chromite or the model of Kress and Carmichael (1991) for glass*

bdl = below detection limit, - = not analyzed/calculated

4.5.3 Compositional data

Representative compositional data are given in Table 4.3. Full sample datasets for each phase, including secondary standard analyses, data compiled from the literature, and model data, are given in Appendices 3-5. Literature data cited for comparison are provided in Appendix 6.

4.5.3.1 Glass Compositions

Residual melts formed andesitic glasses, the compositions of which are given with other experimental products in Table 4.3. These glasses are depleted in FeO, MnO, MgO, and Cr_2O_3 relative to both the initial boninite glass as well as the bulk composition of the system (Table 4.1). SiO_2, CaO, Al_2O_3, Na_2O, K_2O, and TiO_2 are enriched in residual melt during every experiment, which is consistent with extensive opx crystallization.

The two experiments conducted at high temperature (Bon1200U and Bon1200B) returned four samples with glasses containing low MgO concentrations relative to those from experiments conducted at 1150 °C. This is counterintuitive, because the crystallization of opx at higher temperature should produce a lower proportion of minerals relative to lower temperatures, and overall depletion of MgO and FeO relative to the initial glass composition should be smaller. Additionally, glass compositions inferred for sample Bon1200Ua indicate a high degree of heterogeneity beyond the limit of analytical uncertainty, consistent with inefficient quenching producing local melt heterogeneity. These data, along with relatively high melt K_2O concentrations and the presence of abundant rim formation on opx grains within these samples (Figure 4.1B) indicate that a significant degree of quench crystallization has occurred in the high temperature experiments. These observations are absent from all experiments conducted at 1100-1150 °C, which suggests that quenching was efficient in these latter experiments and that no quench crystallization occurred.

4.5.3.2 Pyroxene compositions

Opx formed under every temperature and redox condition imposed by the IHPV. In order to confirm the identity of low-Ca pyroxenes as opx and not pigeonite, we calculated Ca molar fractions for an opx-clinopyroxene (cpx) dividing line using Equation 38 of Beattie et al. (1991) with the experimental temperatures imposed within

the IHPV as the single independent variable. All pyroxene data presented here fall below these model values, which confirms their identity as opx. Opx compositions are graphically illustrated in Figure 4.2. Plotted alongside these data are data taken from other experiments conducted using boninitic bulk compositions (Tatsumi, 1981; Umino and Kushiro, 1989) and natural opx compositions sourced from boninitic rocks (Mariana trench, Bloomer and Hawkins, 1987; Troodos ophiolite, Cameron, 1985; and Chichijima, Umino, 1986; Yajima and Fujimaki, 2001).

Opx Mg# (molar Mg/[Mg+Fe_{Total}]) positively correlates with temperature, and under buffered redox conditions is lower than in unbuffered products (Figure 4.2). Differences in MgO and FeO concentrations observed in samples processed at 1200 ℃ but different f_{O_2} are on the order of 1-2 wt.% for each element. Thus, lower Mg# is associated both with lower temperature as well as lower f_{O_2}. Minor oxide components in opx include CaO, Na_2O, Cr_2O_3, MnO, TiO_2, and Al_2O_3. The concentrations of each of these oxides are < 5 wt.%, with variation of some concentrations correlating with changes in the intensive parameters of the IHPV. Higher cation proportions of Ca, Al, and Mn are observed in samples synthesized under lower temperatures (Figure 4.2). Cr_2O_3, Na_2O and TiO_2 concentrations are extremely low in all pyroxenes, and potential variations in these oxides due to changes in temperature or redox condition are imperceptible when considering the detection limits for these elements. The effects of imposing variable redox conditions on the melt-opx partitioning of Ca, Al, and Mn cannot be discerned for a given temperature interval because, with regard to these elements, the mean core compositions for all opx synthesized at a given temperature are not observed to significantly change between high and low f_{O_2}.

When natural and other experimental opx compositions are compared to the experimentally synthesized opx presented here, the majority of natural and experimental opx compositions are similar to opx synthesized at 1200 ℃ and under buffered f_{O_2} conditions in terms of their Mg#. Mn proportions broadly overlap with products of high temperature crystallization, while Al and Ca cation proportions from the literature are, respectively, somewhat lower and higher than our experimental products.

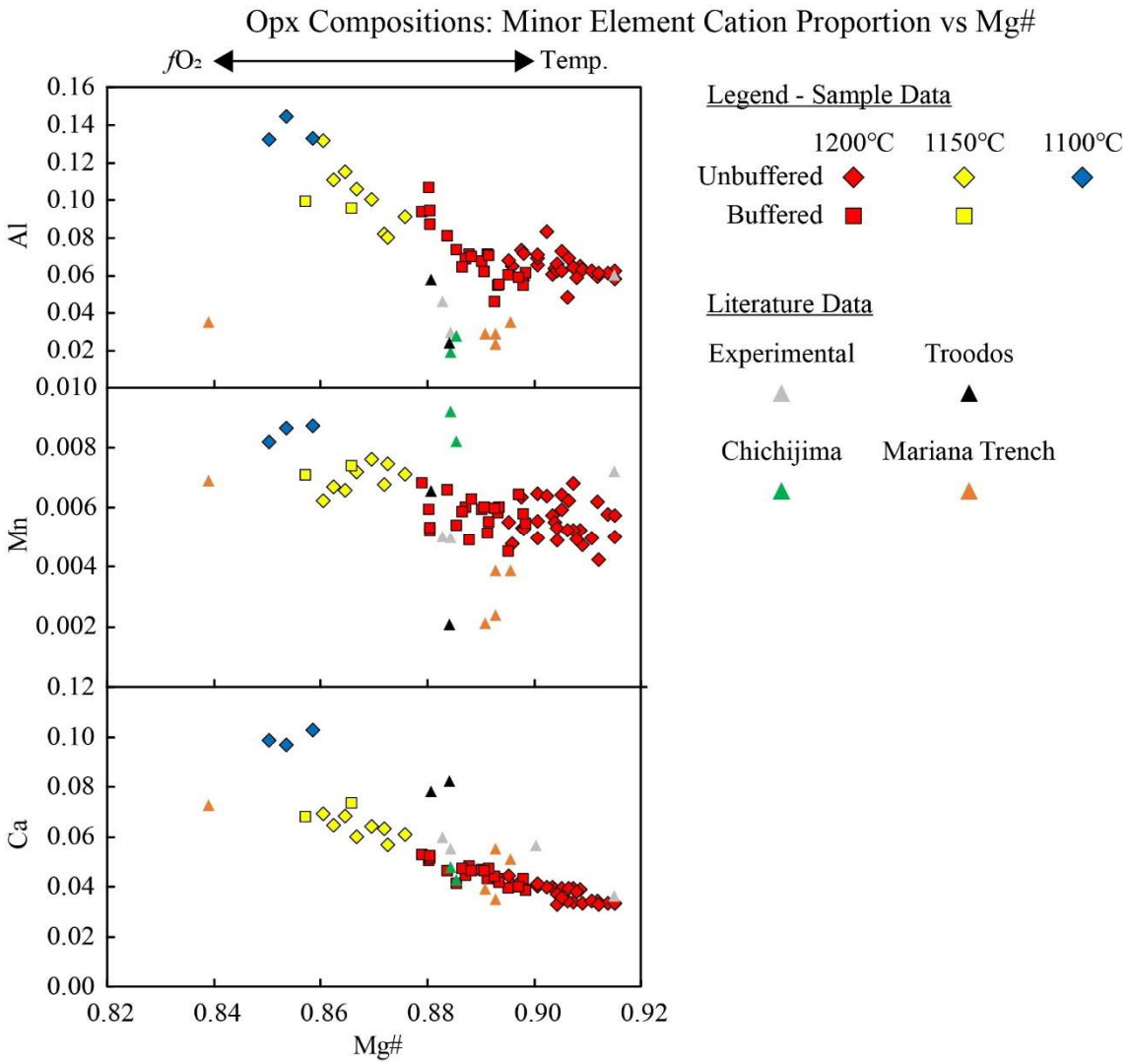

Figure 4.2: Cation proportion (O = 6) vs Mg# (calculated using Fe_{total}) for opx core analyses. Literature data are taken from sources listed in the text. Point uncertainties are within the boundaries of the symbol.

4.5.3.3 Chromite compositions

Initial seed chromite fragments were analysed by EPMA in order to determine if the chromitite pod could be considered homogeneous. Representative data are given in Table 4.1 with other starting material compositions. A single analysis revealed minimal enrichment of FeO and TiO_2 (Appendix 4). Because the level of enrichment is low and rarely observed, we consider the seed chromite to be homogeneous.

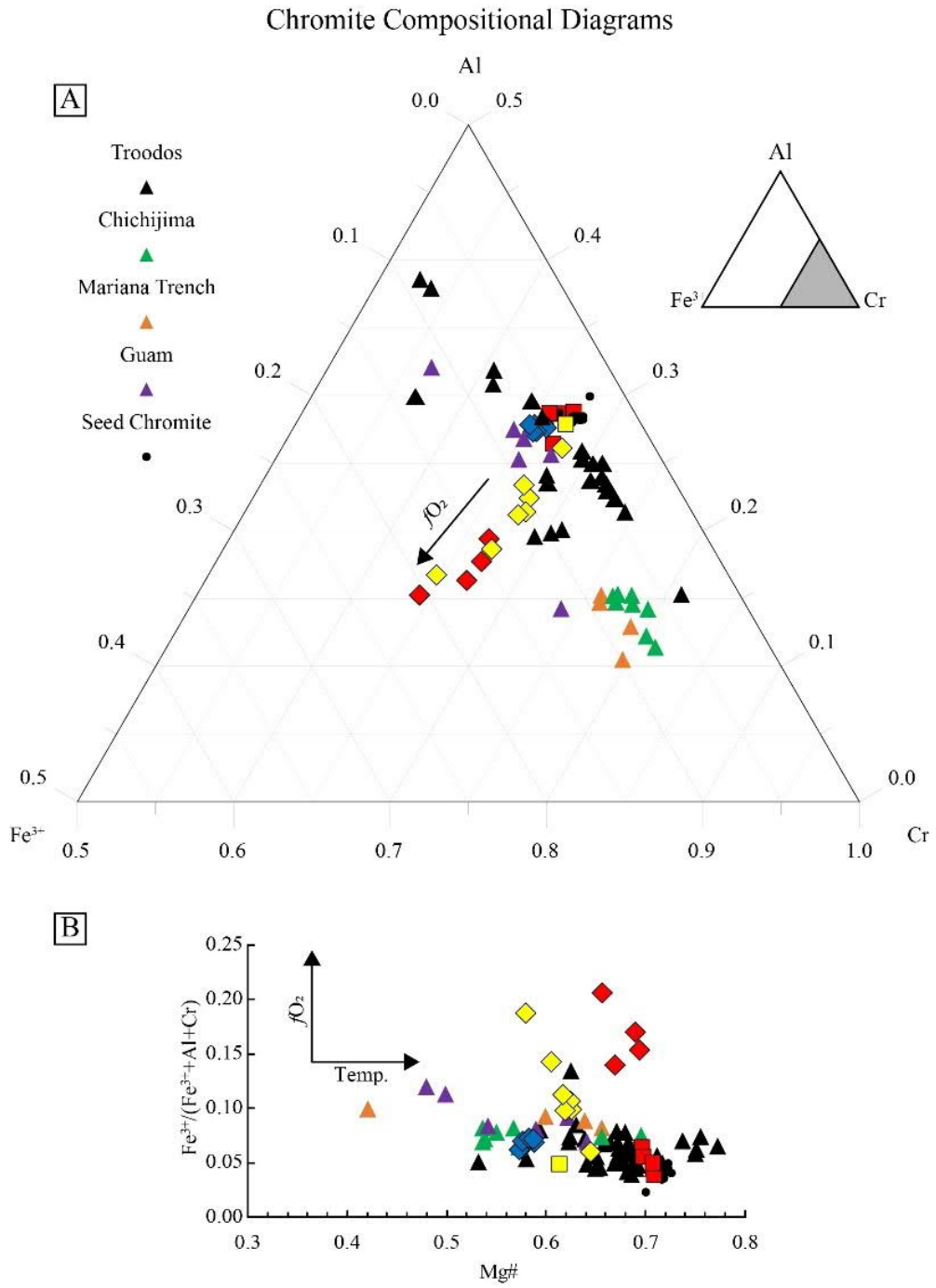

Figure 4.3: Chromite compositional data. (A) A portion of a conventional ternary diagram illustrating the relative proportions of octahedrally coordinated trivalent cations after recalculation (dimensions of the ternary are illustrated on the inset). Literature data are taken from sources listed in the text. (B) Diagram that illustrates Fe incorporation into both octahedral and tetrahedral sites using Mg# and the $Fe^{3+}/(Fe^{3+} + Al + Cr)$ parameter. Symbols same as Fig. 4.2. Analytical uncertainties associated with each composition lie within the symbol boundaries.

Experimental chromite compositions are chromium-rich, typically with 70 < Cr# < 81 (Cr# = molar Cr/[Cr+Al], Table 4.3), and compositional data are illustrated in Figure 4.3. Priority was given to small seed chromites (*c*. 10-15 μm in diameter) that were able to be analysed without significant Si-contamination of the analysis volume from adjacent glass. This was because the initial goal of adding seed chromite was to foster mineral growth from the boninitic liquid. Since this likely did not occur, then the next best action was to analyse material that most likely equilibrated with residual melts by the end of each experiment. Two samples seeded with large chromite fragments (Bon1200Ua and Bon1200Ba) were observed to also contain several small anhedral chromite fragments distributed among the opx crystals (possibly chromite powder contamination from the sieving process). Several of these were analysed in Bon1200Ua, but no analyses of chromite in Bon1200Ba were determined to be free of glass contamination based on high observed concentrations of Si, Ca, and, in some cases, Na. These data were rejected.

Compositions taken from the literature on boninite-hosted chromites sourced from the Mariana trench wall (Bloomer and Hawkins, 1987), the Troodos ophiolite (Bailey et al., 1991; Cameron, 1985; Flower and Levine, 1987; MacLeod, 1988; Thy and Xenophontos, 1991), Guam (Reagan and Meijer, 1984), and Chichijima (Umino, 1986) are provided for comparison. Note that the chromites from Thy and Xenophontos (1991) are olivine-hosted mineral inclusions.

In terms of trivalent cation proportions (i.e. Fe^{3+}, Al, and Cr), f_{O_2} buffered experiments produced chromites with compositions that did not significantly change from the initial seed composition (Figure 4.3A). Chromium is efficiently oxidized above NNO in Fe-bearing melts (Hanson and Jones, 1998). Thus, all Cr in chromite is Cr^{3+}. However, some of these chromites have bright mantles that clearly indicate Fe enrichment (e.g. Figure 1D). Under intrinsic f_{O_2} conditions corresponding to *c.* 3.2-4.0 log units above the NNO buffer and at temperatures of 1200-1150 ℃ (red and yellow diamonds on Fig. 4.3), significant amounts of Fe^{3+} were added to chromite, resulting in an enrichment of total FeO with concentrations > 20 wt.%. For these samples, their trend on Figure 4.3A illustrates significant Fe^{3+}-Al exchange between chromite and melt, as the trend of core compositions runs sub-parallel to lines of equal Cr proportion (which caused the observed increase in Cr# for these chromites). Because this trend is linear

and the samples do not cluster, it is likely that the Fe^{3+}-Al exchange reaction failed to reach equilibrium. It is noteworthy that chromite grains in sample Bon1100U appear to have lost very little Al during the experiments, as Al_2O_3 concentrations are ≤ 1 wt.% different from concentrations in the seed chromite, consistent with the observed invariance of their inferred Fe^{3+} contents. TiO_2 was consistently low in all chromites, reaching a maximum value of 0.14 wt.% under the lowest temperature setting (Bon1100U). NiO concentrations were nearly constant throughout the dataset at *c*. 0.11 wt.%.

The literature data lie on a separate trend on Figure 4.3A that is sub-parallel to lines of constant Fe^{3+} proportion. Of these data, chromite inclusions in olivine from the Kythreotis locality (Troodos, Thy and Xenophontos, 1991) and matrix chromite from Guam appear to be the most aluminous, while sample material from the Mariana Trench and Chichijima plot together near the extreme Cr end of the ternary diagram along with other Troodos chromites. In fact, chromite compositions from Troodos boninites and tholeiites span a wide range on this diagram, plotting between the Kythreotis samples and the highly chromian composition observed for the Kapilio locality (Cameron, 1985). The similarity between some of the chromites observed in Troodos boninites/tholeiites and the seed chromites from the plutonic chromitite is noted, as it was by Cameron (1985).

In Figure 4.3B, Mg# (chromite Mg# = Mg/[Mg+Fe^{2+}] using molar proportions) is plotted against Fe^{3+}/[Fe^{3+}+Cr+Al] (also calculated using molar proportions) in order to visualize the effects of Fe enrichment in a compositional space that is more representative of the spinel (*sensu lato*, hereafter *s.l.*) solid solution. Again, it is evident that buffered experiments (squares) have the same Fe^{3+} proportion as seed chromite. However, it is apparent that some Mg-Fe^{2+} exchange has occurred at 1150 °C, which represents the rim formation reaction observed in BSE images (yellow square). Thus, in f_{O_2} buffered experiments conducted at 1150 °C, Fe^{2+} has been added to chromite and Mg has been lost to the melt. For a given temperature, Mg# appears to decrease with Fe^{3+} incorporation. This is observed for samples recovered from experiments Bon1200U and Bon1150U, which plot to higher Fe^{3+} relative to products of buffered experiments. Interestingly, natural chromite compositions observed in the Troodos ophiolite span a slightly greater range of Mg# than the experimental products. Included

in these data are additional olivine-hosted chromite inclusion data from Sobolev et al. (1993) and Golowin et al. (2017).

4.6 Discussion

4.6.1 Assessment of divalent cation distribution and equilibrium state between chromitite-opx-melt

Because the experiments described here did not produce any discernible chromite growth, instead of discussing chromite crystallization, the following sections discuss the state and kinetics of chromite equilibration. The physicochemical states imposed upon the boninite system are analogous to a shallow-mid crust setting, and thus these experiments are ideally suited to study the effects of chemical disequilibrium on compositional change as a function of temperature and f_{O_2} over brief timescales in this setting.

Based on textural evidence, it is apparent that large seed chromites in the samples presented here failed to reach chemical equilibrium with their residual melts (Figure 4.1D). Since opx crystallization is the process that altered the major element composition of melts during each experiment, it is also the process that determines the extent to which chromite would have to interact with residual melt in order to reach an equilibrium state under the conditions imposed within the IHPV. Thus, it is important to qualify the relationship between opx and residual melt so that chromite-melt relationships can be confidently explored.

In order to test for opx-melt equilibrium, the methodology of Putirka (2008) was used. Specifically, for a given sample, melt cation fractions were calculated (X_d^{liq}, Appendix 3) for each glass analysis. From these values, X_{Si}^{liq} was used to calculate model equilibrium Fe-Mg exchange coefficients (K_D, Table 4.4, Figure 4.4A) using the following relationship given by Putirka (2008):

$$K_D(Fe-Mg)^{opx-liq} = 0.4805 - 0.3733X_{Si}^{liq} \qquad \text{Equation 4.1}$$

An uncertainty (1σ) of ± 0.06 was attributed to these modelled K_D values, which is an order of magnitude higher than the 1σ associated with the distribution of modelled K_D values given in Table 4.4 and is illustrated as areas on Figure 4.4A. Observed K_D

calculations employed molar proportions for opx core analyses and average molar proportions for glass compositions. Average K_D values (including 2σ error bars) for samples Bon1150U and Bon1150B plot completely within their model areas, indicating that the opx sampled in these charges were in equilibrium with their respective residual melts at the time of quenching. K_D values calculated for three opx cores in sample Bon1100U produce an average K_D that is positioned just outside of the model area. However, since the lower error bar stretches into the uncertainty envelope as illustrated, it is reasonable to say that these crystals also equilibrated with their residual melt. There are two negative effects of quench crystallization that impacted K_D calculations and prevented us from determining whether opx in samples processed at 1200 °C were able to reach equilibrium or not. The first is the effect of raising X_{Si}^{liq}, which occurred as quench crystals removed Mg, Fe, and Ca from residual melts. This lowers model K_D values (Equation 4.1). The other effect is the removal of Mg and Fe from the melt phase, which precluded realistic K_D values from being observed (Figure 4.4A). Since opx-melt K_Ds indicate an equilibrium condition for experiments conducted at 1100-1150 °C, none of the Fe loss observed in these samples had an observable effect on the equilibrium partitioning of Fe-Mg between opx and melt. This indicates that our equilibration considerations are not significantly affected by this process.

In order to assess for chromite-opx equilibrium, the model of Liermann and Ganguly (2003) was applied. This model was calibrated at higher pressures than imposed in our experiments. However, because changes between partial molar volumes (of end-member compositions at the standard state) associated with the Fe^{2+}-Mg exchange reaction between chromite and opx appear to exhibit ideal mixing behaviour and because both Fe^{2+} and Mg endmembers exhibit similar and predictable pressure dependencies, Liermann and Ganguly (2003) assumed a pressure normalization scheme (their Equation 5) to process their K_D values and formulate a thermometer for opx-chromite pairs that may be applied under a wide range of pressure conditions. We have rearranged this thermometer (their Equation 8) to predict chromite-opx K_D (Fe^{2+}-Mg, Table 4.4) at 2 kbar (0.2 GPa):

$$K_D(Fe^{2+} - Mg)^{chrm-opx} = \exp\left[\frac{AT(K)+B+122P(GPa)-CX_{Al}^{opx}+DY_{Cr}^{chrm}}{T(K)}\right] \qquad \text{Equation 4.2}$$

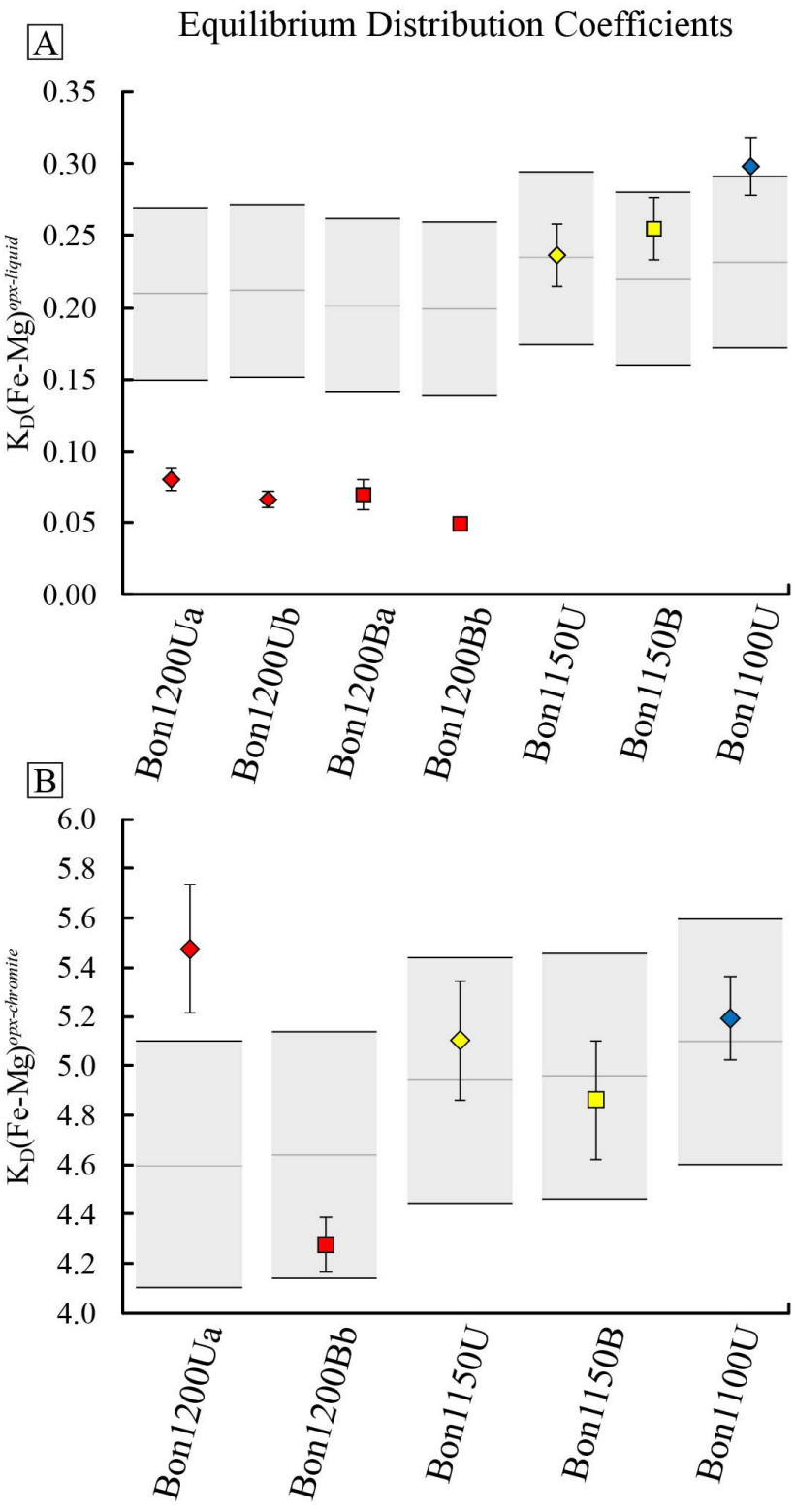

Figure 4.4: Equilibrium exchange coefficients (A) calculated for opx and residual melt. (B) calculated for opx and chromite. Symbols as in Figure 4.2.

Table 4.4: Predicted and observed equilibrium compositional data for orthopyroxene (opx) and chromite (chrm)

Modelled	$K_D(Fe\text{-}Mg)^{opx\text{-}liq}$ (1σ)	$*K_D(Fe\text{-}Mg)^{chrm\text{-}opx}$
Bon1200Ua	0.209 (0.007)	4.594
Bon1200Ub	0.211 (0.003)	-
Bon1200Ba	0.201 (0.005)	-
Bon1200Bb	0.199 (0.002)	4.639
Bon1150U	0.233 (0.001)	4.936
Bon1150B	0.219 (0.003)	4.957
Bon1100U	0.231 (0.009)	5.098
Observed		
Bon1200Ua	0.080 (0.004)	5.475 (0.260)
Bon1200Ub	0.066 (0.003)	-
Bon1200Ba	0.070 (0.005)	-
Bon1200Bb	0.048 (0.001)	4.279 (0.110)
Bon1150U	0.236 (0.011)	5.103 (0.237)
Bon1150B	0.246 (0.013)	4.863 (0.238)
Bon1100U	0.298 (0.010)	5.194 (0.171)

1σ is a quantification of the distribution of modelled/observed values based on analytical precision and detected heterogeneity
**Model uncertainty = c. ±0.157 (1σ) using error propagation*

This K_D equation utilizes opx Al molar proportion (X_{Al}^{opx}), chromite Cr/[Cr+Al+Fe^{3+}] (Y_{Cr}^{chrm}), and constants derived for Al-Fe^{3+} system correction using the charge balance method: A = -0.351 ± 0.102, B = 1217± 120, C = 1,863, and D = 2,345 ± 188 (Table 4 of Liermann and Ganguly, 2003). Uncertainties associated with the model K_Ds were calculated to be ± 0.157 (i.e. better than ± 7%, 2σ relative) based on propagating the uncertainties provided for coefficients A, B, and D. Assuming the compositional parameter for opx does not significantly change, and since Cr proportions for the synthetic chromites are not observed to change significantly between any of the samples (Figure 4.3A), this equation predicts the equilibrium state of chromite-opx with regard to Fe^{2+}-Mg exchange for each experimental condition at the time of quenching (Figure 4.4B, observed K_D values were calculated using molar proportions with chromite X_{FeO} multiplied by molar $Fe^{2+}/\Sigma Fe$ inferred from stoichiometry).

As illustrated on Figure 4.4B, the Fe^{2+}-Mg subcomposition of chromite (given as Mg# in Figure 4.3B) in several samples has equilibrated with the opx-melt subsystem over the brief timescale of these experiments. The relatively large seed shown in Figure 4.1D has a rim that is *c*. 8-10 μm wide. Because our analyses prioritized small chromites that

were *c*. 10-15 μm in diameter, we consider it likely that EPMA sampled chromite that completely equilibrated with respect to Fe^{2+}-Mg through diffusion.

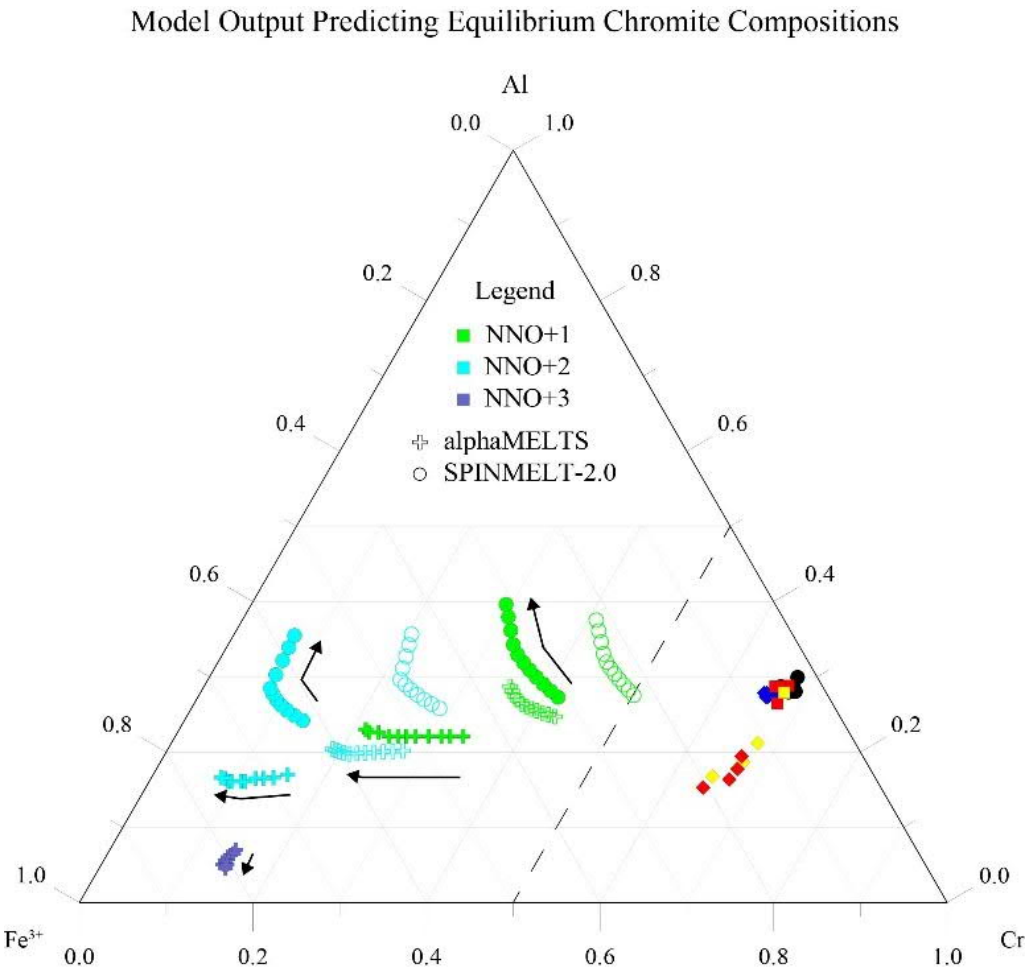

Figure 4.5: Results from MELTS and SPINMELT-2.0 modelling compared to experimental data (the edge of the ternary diagram from Fig. 3A is shown as a dashed line). Lines are drawn in the direction of decreasing temperature from 1200 °C to 1100 °C. Solid symbols represent model data that do not account for iron loss, while empty symbols represent data generated using models with 30% imposed iron loss. MELTS model output at NNO+3 and 30% iron loss directly overlaps the MELTS output at NNO+2 (without iron loss).

Thus, since a self-consistent determination of equilibrium has been established using empirical relationships, then the Fe^{2+}-Mg data provided here describe the equilibrium condition of the melt + opx + chromite system under high temperature and f_{O_2} conditions analogous to those in sub-arc crust. Interestingly, significant degrees of Fe loss should raise the Mg# of the sample bulk composition even when the ratio of Fe^{2+} to Fe^{3+} in melt is maintained by hydration (Chapter 3.3.1). This effect should be observable in product opx compositions, as higher melt Mg# should result in higher opx

Mg#. Since this is not observed (Figure 4.2, Table 4.3), then the observed Fe loss (in the case of Bon1150B, 20% bulk Fe) does not significantly affect the equilibrium distribution of Fe^{2+}-Mg under our experimental conditions.

4.6.2 Assessing chromite-melt equilibrium based on model equilibrium trivalent cation proportions

Since Fe^{2+}-Mg has now been accounted for, it is prudent to also examine the equilibrium state of the trivalent cations in chromite. To this end, multiple modelling methods were integrated to predict equilibrium chromite compositions (with respect to trivalent cation proportions). Our method modelled system compositional data using the alphaMELTS front end (Smith and Asimow, 2005) and the MELTS thermodynamic model (Ghiorso and Sack, 1995) with Rhyolite-MELTS system corrections enabled (Gualda et al., 2012). Nested modelling utilized SPINMELT-2.0 (Nikolaev et al., 2018a, b), which calculated an alternative stable chromite composition for each intermediate MELTS step. These models are likely to bookend actual trivalent cation proportions in spinel (*s.l.*) compositional space (see Davis and Cottrell, 2018; Nikolaev et al., 2018a, for information and discussion on how individual models behave when predicting chromite compositions). A detailed description of the modelling methodology is included in Chapter 3.3.3. SPINMELT-2.0 cannot make sense of MELTS-modelled liquid compositions at NNO+3 because the liquid composition at this condition lies outside of the calibration range for the SPINMELT-2.0 algorithm. Thus, SPINMELT-2.0 data are not available under highly oxidizing conditions.

Figure 4.5 illustrates the relationship between MELTS and SPINMELT-2.0 models and the difference between modelled compositions and the synthetic chromites produced in our experiments. Alternative models were created to observe the effect of 30% Fe loss on the system (empty symbols, Figure 4.5). It appears that under highly oxidizing conditions and 1150-1200 °C, experimental chromite $Fe^{3+}/[Fe^{3+}+Cr+Al]$ values approach values that are attained at NNO+2 in the MELTS models. Still, given the distance on the ternary diagram between modelled chromite compositions and our experimental data, none of the experimental chromites are in equilibrium based on observed trivalent cation proportions. This includes model data that were generated under conditions where Fe loss was accounted for. The principal effect of Fe loss is to reduce the proportion of Fe in equilibrium chromite. The trend to high Fe^{3+}

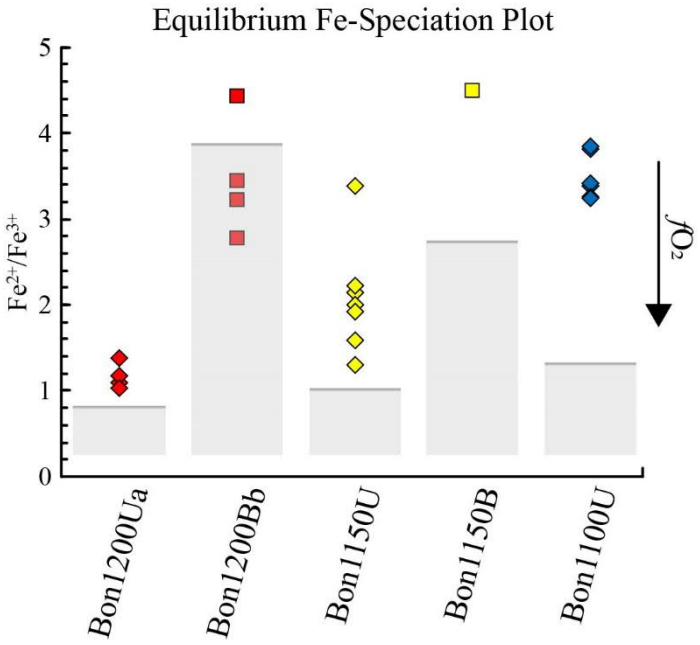

Figure 4.1: Comparison between average chromite Fe^{2+}/Fe^{3+} observed in experimental charges and modelled equilibrium glass values of the same ratio (grey lines). For equilibrium conditions to be met, the symbols for each sample would need to lie below the grey lines.

concentrations observed for the oxidized samples illustrated in Figures 4.3A and 4.5 are likely to represent a segment of a diffusion trend in ternary space. The concept of diffusion in this compositional space is explored below. Since the volume of chromite in the charges is invariant (i.e. no resorption or crystallization has been observed), then the process by which chromite equilibrates can exclusively be attributed to diffusion.

Differences between MELTS and SPINMELT-2.0 output data are surprisingly large but may be attributed to both our modelling strategy (Chapter 3.3.3) as well as inherent limitations of the model platforms. Models in the MELTS family tend to overpredict spinel (*s.l.*) Fe^{3+} proportion and underpredict Cr proportion (Davis and Cottrell, 2018; Nikolaev et al., 2018a), and the creators of SPINMELT-2.0 claim that their model reproduces several petrologically important chemical aspects of chromite chemistry to better than 20% (Cr/Al and Mg/Fe^{2+}, Nikolaev et al., 2018a). What MELTS does describe accurately is Fe-Al exchange within the system during melt evolution and thus likely provides a best fit topology in compositional space (Davis and Cottrell, 2018). Because of these observations, we reiterate that our modelling method likely bookends equilibrium chromite compositions; keeping in mind that multiple experiments were performed beyond the calibration range of SPINMELT-2.0.

In the case where Fe^{2+} in chromite is in equilibrium with the co-existing melt/silicate mineral assemblage, the interdiffusion of trivalent cations should occur in chromite with Fe^{2+}/Fe^{3+} higher than that in coexisting melt, as melt Fe^{2+}/Fe^{3+} should always be higher

than spinel Fe^{2+}/Fe^{3+} (Maurel and Maurel, 1982a). Using Equation 7 of Kress and Carmichael (1991), model melt Fe^{2+}/Fe^{3+} values were generated (Appendix 3) using glass compositions and the intensive parameters imposed by the IHPV to show that most if not all experimental chromites must incorporate more Fe^{3+} before reaching an equilibrium Fe^{2+}/Fe^{3+} threshold (Figure 4.6). That is, in order to reach an equilibrium condition, the observed Fe^{2+}/Fe^{3+} in chromite must incorporate more Fe^{3+} so that their ratio values fall below the grey lines on Figure 4.6. The exception is sample Bon1200Bb, the chromite Fe^{2+}/Fe^{3+} values of which are distributed (mostly) beneath the modelled melt Fe^{2+}/Fe^{3+} value.

The diffusion of major cations within spinel (*s.l.*, e.g. Figure 19 of Van Orman and Crispin, 2010) are ranked by order of decreasing diffusivity (log D, m^2/s) at 1100 °C ($10^4/K$ = *c.* 7.3): Mg-Al (extrapolated, *c.* -13.5), Fe (self-diffusion, *c.* -16), Mg (self-diffusion, *c.* -16.5), and Cr-Al (below x-axis, see below). Thus, $D_{Cr\text{-}Al}$ is likely the limiting factor in chromite-melt diffusive equilibration, though uncertainties associated with $D_{Cr\text{-}Al}$ are reportedly large at high Cr# (Suzuki et al., 2008) and f_{O_2} affects D_{Fe} (Vogt et al., 2015). As stated by Vogt et al. (2015) this behaviour is not well constrained under high-T and high-P conditions. Our results corroborate this inference. Since spinel (*s.l.*) is an isometric mineral, the given diffusivities do not vary with crystallographic orientation, which is convenient for the purpose of textural analysis (Chapter 3.3.4).

As demonstrated in Figure 4.3A, when buffered at NNO+0.4, +1 and +2.5, chromite compositions did not significantly change from the original seed composition with respect to trivalent cation proportion. Only change in Mg# is observed for these chromites (Figure 4.3B). Significant Fe^{3+} incorporation was only observed in unbuffered samples at temperature > 1100 °C and occurred at the expense of Al, since trivalent cation proportions for these samples are distributed along lines of equal Cr proportion (Figure 4.3A). Thus, Al counter-diffusion facilitated Fe^{3+} incorporation in chromite under highly oxidizing conditions at 1150-1200 °C; although it is unlikely these minerals completely equilibrated during the experiments (Figure 4.5).

The Fe-Mg and Fe-Al exchange reactions have also been observed in natural samples that are allowed to equilibrate over decadal timescales (Scowen et al., 1991). Importantly, the observations of Scowen et al. (1991) confirm the rank of the diffusivities outlined above and establish that even though Cr is the most sluggish

element to diffuse, eventually Cr diffusion does occur in natural settings to equilibrate chromite following Fe-Al interdiffusion.

Based on our observations, we hypothesize that Fe^{3+}-Al interdiffusion operates principally as a function of f_{O_2} to equilibrate chromite Fe^{2+}/Fe^{3+} (after equilibration of chromite Mg#) on a shorter timescale than is required to equilibrate Cr in the system. This scenario of diffusive re-equilibration may be conceptualized within a multi-step chemical reaction (Figure 4.7). The first step concerns Fe^{2+}-Mg exchange between chromite and melt. This is the only reaction observed in samples processed under buffered f_{O_2} (and in sample Bon1100U), and since the observed changes in chromite composition are more complex under higher f_{O_2} conditions, we combine this exchange with the observed increase in Fe^{3+} in trivalent cation proportion as reaction 1 (Figure 4.7). Thus, a relatively high $Fe^{2+}/Mg + Fe^{3+}/Al$ composition is generated as a magnetite component ($FeFe_2O_4$) is added to the starting chromite composition. This exchange is facilitated by the counter-diffusion and exchange of Mg and Al, and the spinel (*sensu stricto*, hereafter *s.s.*) component thus diminishes (see Appendix 4for modelled end-member component compositions). With reaction 1, the chromite composition approaches a tie line between $Fe(Al,Cr)_2O_4$ and $Mg(Fe,Cr)_2O_4$ in the compositional space of the spinel (*s.l.*) prism (dashed grey line in Figure 4.7A). Importantly, the chromite compositional trend will not approach the Cr-magnetite solid solution in the prism space but a spinel (*s.l.*) composition intermediate between Cr-magnetite and the $Mg(Fe,Cr)_2O_4$ solid solution, as spinel (*s.l.*) Mg concentration is only being diluted by reaction 1 (i.e. Mg is rearranged within the chromite matrix with some flux across the crystal-melt boundary). In order to equilibrate Cr proportion, which is expected to decrease under all imposed experimental conditions (Figure 4.5), compositions should evolve along lines of equal Fe^{3+}/Al (dashed grey line in Figure 4.7B; reaction 2) in the isothermal state as Cr is lost to the melt phase. An added component with higher Fe^{2+}/Mg is required because Mg# in chromite was not observed to increase in any experiment (Figure 4.3B) and because this is necessary for chromite to equilibrate with the silicate mineral assemblage (Figure 4.4B).

The difference in diffusivities between mineral species provides an interesting constraint on the origin of the polymineralic microlite assemblages described here. In particular, Fe-Mg interdiffusion in opx occurs more slowly (log D = -19.5 at QFM and

high T, Klügel, 2001) than interdiffusion of any of the major cations in chromite. If, in natural samples, it is found that microlitic silicates like opx are in equilibrium with residual melts and matrix chromites are not, then the likely explanation for this observation is that the microlitic silicate formed from the melt it is in (i.e. an equilibrium crystallization process). Crystallization of ferrous phases is one of several oxidizing mechanisms in arc magmatic systems (see Cottrell et al., 2020). This process provides an impetus for diffusive re-equilibration of chromite to begin, and the grounds for oxyspeedometric analysis of the chromite-melt subsystem in a diffusion chronometric context. Chromite crystals sampled from Chichijima (Umino, 1986), the Troodos ophiolite (Bailey et al., 1991), and Guam (Reagan and Meijer, 1984) exhibit chemical zonation consistent with pre-eruptive oxidation, as chromite rim-mantle zone analyses return more ferric compositions than analyses of their cores.

Such features are unique to the pre-eruptive regime but may be confused with compositional trends that are attributable to chemical weathering. Thus, it is important to discern here oxidation of chromite that occurs in this scenario and oxidation that occurs post-eruption (i.e. chemical weathering or metamorphism of chromite). In the literature on the zoned chromites described above, there is no mention of textures consistent with porous-chromite oxidation (Gervilla et al., 2019; Hodel et al., 2020). The volcanic rocks sampled by the studies cited above were observed to be fresh with little to no evidence of alteration, which is not consistent with a weathering environment capable of significantly modifying chromite compositions in either hydrothermal (Hodel et al., 2020) or metamorphic (Gervilla et al., 2019) regimes. Instead, since the chromite FeO and Al_2O_3 concentrations are observed to increase from core to rim (which is a geochemical signature of magmatic oxidation in our model, i.e. reaction 2 of Figure 4.7), we maintain that these zonation patterns are of magmatic rather than secondary origin. With this in mind, the next sections assess natural chromite and glass compositions recovered from the extrusive suite of the Troodos ophiolite in a similar manner as our experimental products, and data available from the literature are used to constrain ascent rates for these lavas.

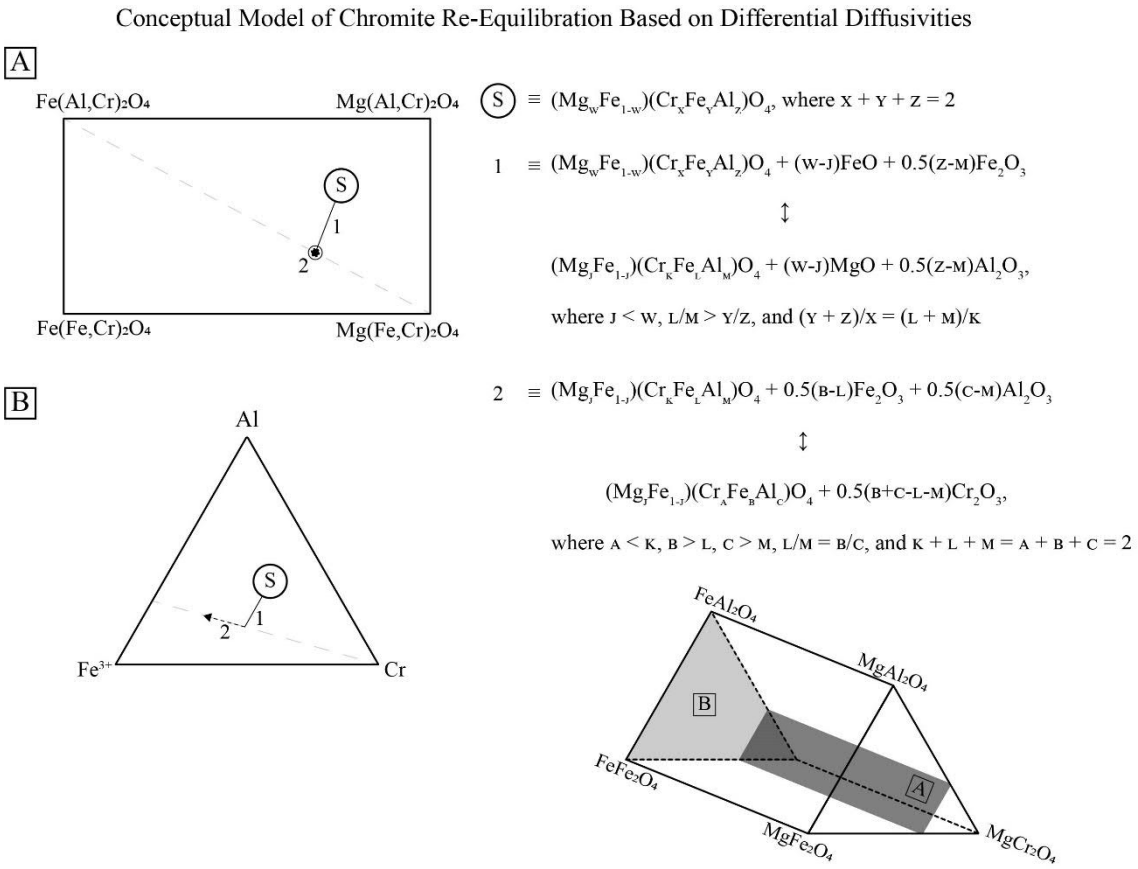

Figure 4.7: Graphical representation of the chemical evolution of chromites within the compositional space of the spinel prism (inset). Hypothesized relationship: Fe-Mg interdiffusivity > Fe-Al interdiffusivity > Cr-(Al, Fe) interdiffusivity. If Fe-Mg and Fe-Al equilibrate chromite Mg#, Fe^{2+}/Fe^{3+}, and Fe^{3+}/Al, with Cr equilibration following, then re-equilibration is a process that may be approximated by reactions (1) and (2) in a multi-step fashion. (A) Reaction (1) displaces chromite compositions to higher Fe^{2+}/Mg and Fe^{3+}/Al as the spinel (*s.s.*) component in chromite decreases. In ternary space, this reaction causes a shift to higher Fe^{3+} concentrations along lines of equal Cr proportion (B). Reaction (2) proceeds along lines of equal Fe^{3+}/Al (dashed grey line in B) as Cr is lost to the melt phase. Reaction (2) proceeds in a direction perpendicular to the page (up) in A.

4.6.3 Experimental observations vs. natural processing in the crustal column

Mafic Troodos glass compositions were taken from the literature for the following localities: the Kalavassos Mine (eastern end of the Limassol Forest Complex), Margi (northern part of the extrusive sequence), and Kapilio (western end of the Limassol Forest Complex). All data were taken from Woelki et al. (2020) with an additional two glass analyses from Golowin et al. (2017) for the Kalavassos Mine locality. The studies cited used laser ablation inductively coupled plasma mass spectrometry to quantify

minor-trace concentrations of Cr for these samples. Data on mineral compositions for these locations are sparse. However, multiple compositions were found and taken from Cameron (1985), Bailey et al. (1991), Flower and Levine (1987), and MacLeod (1988). Here, we assess these data to determine if the aforementioned minerals and melts were in equilibrium at the time of eruption. Chromite data were found neither for the Akaki River Canyon section nor for the Arakapas Fault Belt though Ohnenstetter et al. (1990) performed several analyses, no data are provided in the source. Thus, even though these locations have been widely studied, we are currently unable to assess for chromite-melt equilibrium for these parts of the extrusive sequence.

SPINMELT-2.0 was used to model equilibrium chromite compositions in a similar way as in the experimental scenario discussed above. Physicochemical variables were set to approximate eruption conditions with pressure set to 0.5 kbar, which corresponds to a water depth of 5,000 meters (inferred eruption condition, Woelki et al., 2020), and the f_{O_2} of the system was set to QFM+0.25 (*c.* NNO-0.5), QFM+0.75 (*c.* NNO), and QFM+1.25 (*c.* NNO+0.5). This range compares well with the natural range of f_{O_2} for the Troodos magmas; crystallization of olivine + chromite occurred at fugacities slightly above QFM+0.25 (Golowin et al., 2017); and glasses recovered from a Troodos "upper pillow lava" (Rautenschlein et al., 1985) have Fe^{2+}/Fe^{3+} (recalculated to molar ratios) that return f_{O_2} values ≥ QFM+1.35 (NNO+0.6) using a pressure of 0.5 kbar, a temperature of 1130 °C (upper limit of eruption temperature given by Golowin et al., 2017), a rearranged Equation 7 from Kress and Carmichael (1991), and the fugacity conversions of Frost (1991), providing a reasonable estimate for the upper limit for our fugacity setting.

SPINMELT-2.0 output was treated in a similar way as the experimental data (Chapter 3.3.3). When f_{O_2} is provided, melt Fe^{2+}/Fe^{3+} is calculated internally and used to model chromite composition. Since temperature is not provided to the program, it must be predicted by the algorithm to provide a chromite composition estimate for each input melt composition. For these lavas, liquid temperatures have been inferred to vary between *c.* 1030-1130 °C (Golowin et al., 2017). These temperatures are consistent with temperatures inferred from viscosity models (Schouten and Kelemen, 2002) generated for lavas on the North side of the extrusive sequence and with independent thermometry (inferred to provide a quantification of closure temperature) performed by Dare et al.

(2009) for the Kalavassos Mine locality. SPINMELT-2.0 output was observed to lie within 25 °C of this temperature range for a majority of the glass samples (Appendix 7) for each f_{O_2} condition. Thus, we inferred that our models faithfully replicated equilibrium conditions for chromite-melt at the time of eruption.

Figure 4.8 illustrates the relationships between modelled and observed chromite compositions of the Troodos (cf. Figure 4.5). Sample glass recovered from the Kalavassos Mine produced one major cluster for each f_{O_2} condition and one Al-rich glass sample displaced modelled chromite compositions to higher Al and lower Cr. All glass samples were determined to be "tholeiitic" by Woelki et al. (2020). All of the matrix chromite compositions observed for this locality are similar to olivine-hosted chromite inclusions observed in these same lavas (Golowin et al., 2017). A single natural chromite composition is displaced to higher Al compared with the others. However, according to our models, all of these chromite compositions are too Cr-rich and require Fe^{3+}+Al incorporation to be in equilibrium with residual melts.

Woelki et al. (2020) determined that the glass samples recovered from the Kapilio locality range from boninitic to tholeiitic in composition. The chromite data from this locality include the most chromian spinel (*s.l.*) analysis from the Troodos sample suite (Cameron, 1985) and three relatively simple (number of elements reported = 4) analyses of chromite given by Flower and Levine (1987). These compositions are also far from the modelled chromite compositions. As with the samples from the Kalavassos Mine, Fe^{3+}+Al incorporation is required for re-equilibration. If a tie line is drawn through the natural samples from the Cr apex, it would intersect the model array at the point where the data generated at QFM+0.75 touches the data generated at QFM+1.25.

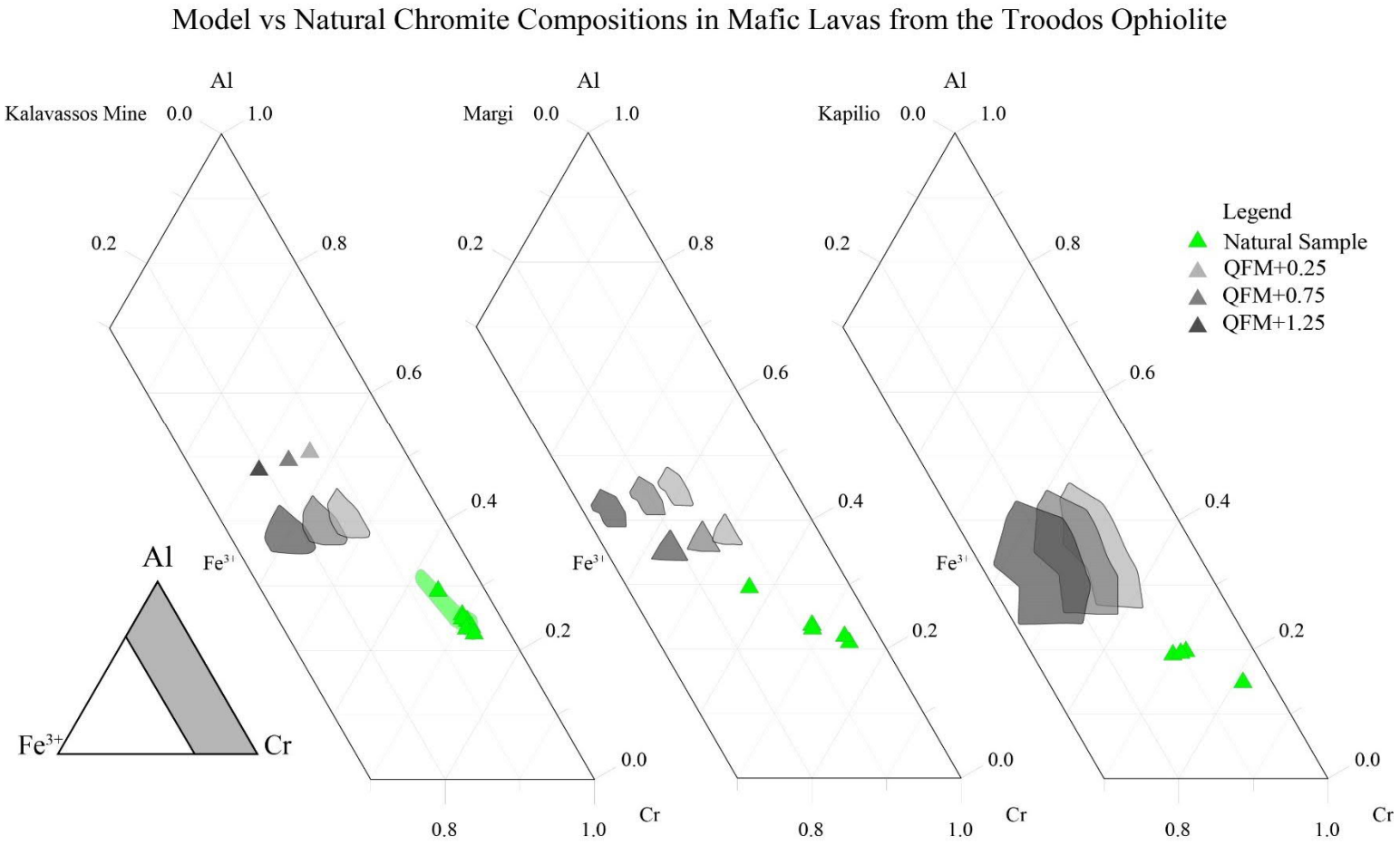

Figure 4.8: Partial ternary diagrams (see inset) generated to compare trivalent cation proportions of natural chromite minerals from the Troodos ophiolite (green triangles) with modelled chromite compositions generated using SPINMELT-2.0. The grey-bordered green area underlying the green triangles on the Kalavassos Mine section represents the compositional range of olivine-hosted chromite inclusions taken from Golowin et al. (2017) and MacLeod (1988).

Finally, chromites taken from the Margi locality exhibit a compositional trend that is similar to that observed in the data from the Kapilio suite. Glasses taken from this locality produced a high-Al and low-Al trend, which reflects a modest separation of the glass data into more and less differentiated populations, respectively. Chromite core analyses given by Bailey et al. (1991) lie in roughly the same area as those of the Kalavassos Mine. However, rim analyses reported in this study are displaced to higher Fe^{3+} concentrations with a single analysis reaching the Fe^{3+} proportion inferred for chromite in equilibrium with melt at QFM+0.75. However, for this mineral rim, Cr-Al interdiffusion must also occur to reach the Al concentration inferred to represent an equilibrium composition. Thus, we conclude that the chromites observed in the Troodos extrusive suite were not in equilibrium with their residual melt compositions at the time of eruption, but in multiple localities these minerals were likely in a state of active equilibration (via diffusion) at the time they were erupted.

Regarding Fe^{2+}, slowly cooled chromites lose Mg to coexisting ferromagnesian silicates (Ozawa, 1984), while rapidly quenched mineral pairs preserve high-temperature compositions (e.g. Scowen et al., 1991). Since the glasses sampled from the Troodos rapidly quenched upon eruption (e.g. Robinson et al., 1983), chromite Mg# may have been preserved. By focusing on a single locality where glass, opx, and chromite data exist, we may treat natural samples in the same way as the experimental products above and test for system Fe^{2+}-Mg equilibrium. To this end, we refocus on the Kapilio locality. Glass data from this site (Woelki et al., 2020) were processed to predict $K_D(Fe\text{-}Mg)^{opx\text{-}liq}$ values using Equation 4.1. Mineral data from this locality are from Flower and Levine (1987). In total, two opx and three chromite compositions were used (their sample AM-4, Table 4.5). Unfortunately, there is no way of determining if these materials come from the same outcrops as the glass, which is why all glass data were used in modelling. Based on model physicochemical constraints outlined above, the opx sampled by Flower and Levine (1987) is in equilibrium with residual melts (within 1σ of the mean model $K_D(Fe\text{-}Mg)^{opx\text{-}liq}$ value). Using a median Y_{Cr}^{chrm} for the matrix chromites (0.70), model $K_D(Fe\text{-}Mg)^{chrm\text{-}opx}$ values (calculated using Equation 4.2) are observed to vary between *c.* 4.68-4.96 at 1130 °C and 0.5 kbar and 5.41-5.86 at 1030 °C and 0.5 kbar (Table 4.5). Varying Y_{Cr}^{chrm} by 0.1 (the actual variation observed among the sample chromites) causes these model K_D values to vary by ± 0.07 (*c.* ± 3%), which

Table 4.5: Assessment of Fe-Mg equilibrium between opx, chromite, and melt in Kapilio lavas

Opx data (norm.)	SiO_2	Al_2O_3	FeO	MnO	MgO	CaO	*Moles MgO*	*Moles FeO*	X_{Al}^{opx}
*AM-4 opx-a	55.38	2.71	9.01	0.00	32.43	0.47	0.805	0.125	0.112
*AM-4 opx-b	56.14	1.65	8.15	0.00	32.63	1.43	0.810	0.113	0.068

Chromite data	Cr_2O_3	Al_2O_3	FeO	MgO	Total			*Average* Y_{Cr}^{chrm}
*AM-4 chrm-a	51.65	9.82	23.73	9.59	94.79		0.238	0.244	0.70
*AM-4 chrm-b	52.71	9.98	23.43	11.60	97.72		0.288	0.216	
*AM-4 chrm-c	53.80	10.18	23.46	11.25	98.69		0.279	0.228	

Glass data and model K_D			**Average Model $K_D(Fe\text{-}Mg)^{opx\text{-}liq}$ (1σ)	**Average melt molar MgO (1σ)	**Average melt molar FeO (1σ)
			0.292 (0.004)	0.232 (0.024)	0.108 (0.004)
Modelled $K_D(Fe\text{-}Mg)^{chrm\text{-}opx}$	opx-a	opx-b	***(1σ)		
1030 °C (0.5 kbar)	4.676	4.955	0.157		
1130 °C (0.5 kbar)	5.408	5.755	^		

Observed K_D *Values*	$K_D(Fe\text{-}Mg)$	****(1σ)	*Equilibrium?*
opx-a and average melt	0.334	0.041	yes
opx-b and average melt	0.300	^	yes
chrm-a and opx-a	6.587	-	no
chrm-a and opx-b	7.324	-	no
chrm-b and opx-a	4.827	-	yes (1030 °C)
chrm-b and opx-b	5.367	-	yes (mod T)
chrm-c and opx-a	5.238	-	yes (mod T)
chrm-c and opx-b	5.824	-	yes (opx-b 1130 °C)

* Taken from Flower and Levine (1987)

** Compiled from all avalable analyses of Kapilio glass from Woelki et al. (2020)

*** Same model uncertainty as in previous table

**** Calculated using error propagation methods applied to average melt composition

^ = Same as above

- = Cannot be calculated using available data

is roughly one half of the magnitude of the uncertainty associated with the model parameters.

Observed $K_D(Fe\text{-}Mg)^{chrm\text{-}opx}$ values are found to vary between 4.8 and 7.3 depending on which chromite-opx pair is used. Two of the three chromite grains are seen to be in equilibrium with at least one of the opx grains based on these K_D models. One other chromite grain in this sample returned high observed K_D values for both opx grains, reflecting low MgO concentrations. This chromite also has a low total EPMA composition (94.79) compared to the other analyses (*c*. 98). Regardless, it is remarkable, given the dearth of mineral data available for the Troodos extrusive sequence, that any equilibrium condition could be established at all. These findings further the point that more mineral data should be gathered from the Troodos ophiolite and other natural chromite-bearing rocks to assess for mineral-mineral/mineral-melt equilibrium.

The effects of natural quench crystallization and syn-eruptive microlite growth on modelling equilibrium chromite composition also needs to be considered. Depending on the Fe-Mg ratio of the minerals that crystallize, Fe^{2+} may be enriched or depleted in the residual melt. Using equilibrium exchange coefficients (e.g. Putirka, 2008), the crystallization of ferromagnesian silicates like olivine and opx are expected to enrich melts in FeO relative to MgO, and the differentiation of melt by these minerals should modestly enrich Fe^{3+} over Fe^{2+} (Birner et al., 2018; Kelley and Cottrell, 2012; O'Neill et al., 2018; Shorttle et al., 2015). Melt Al_2O_3 is expected to increase with the equilibrium crystallization of ferromagnesian silicates. Based on observations of the experimental products made at 1200 °C, melt Al_2O_3 concentrations were not significantly affected by quench crystallization (Table 4.3). Although this effect will depend on the volume of crystallization produced during quenching, which was not constrained, we do not expect minor degrees of quench crystallization to significantly affect melt Al_2O_3 unless an aluminous phase crystallizes. In some relatively differentiated Troodos lavas, plagioclase feldspar is observed (Flower and Levine, 1987; Schmincke et al., 1983). Feldspar crystallization is expected to reduce melt Al_2O_3 and thus modelled chromite Al_2O_3 concentrations, which would cause observed chromite compositions to appear closer to equilibrium. Instead, we propose that (i) the higher chromite Al concentrations predicted by our modelling (Figure 4.8) reflect Al_2O_3 enrichment in the magmas (and

thus the absence of plagioclase in glasses sampled by Woelki et al., 2020) that comprise the Troodos extrusive sequence, which is consistent with the predominate silicate mineral assemblages observed therein; namely olivine, olivine+cpx, or olivine+opx+cpx (Flower and Levine, 1987; Malpas and Langdon, 1984; Schmincke et al., 1983), and that (ii) quench crystallization does not significantly affect these data. Since the most primitive glasses sampled by Woelki et al. (2018) were observed to classify as boninite liquids, we infer that the most Cr-rich equilibrium chromite compositions in our models (Figure 4.8), which correspond to these relatively primitive melt compositions, represent chromite compositions that genuinely reflect the equilibrium composition of chromite in melts unaffected by quench/syn-eruptive crystallization.

4.6.4 Estimation of maximum/minimum ascent time through diffusion modelling

Since stable chromite was driven into chemical disequilibrium during magmatic differentiation, remained in a state of disequilibrium with respect to trivalent cation proportions at the time of eruption, and equilibrated with co-existing silicate minerals with respect to Fe-Mg exchange (divalent cation proportion), magma ascent time may be estimated on the basis of disequilibrium/equilibrium between chromite and the equilibrium condition defined by the physicochemical state of the residual melts. Here, the maximum ascent time was modelled based on the lowest interdiffusivity for the chromite compositional system ($D_{Cr\text{-}Al}$), and minimum ascent time was modelled based on the highest interdiffusivity ($D_{Fe\text{-}Mg}$).

Based on chromite-melt behaviour modelled above and observed in the mafic lavas of the extrusive suite of the Troodos ophiolite, we estimated the maximum and minimum ascent times by calculating the time (t) it would take to equilibrate a hypothetical groundmass chromite microphenocryst [30-60 μm diameter with a composition similar to those of primitive chromite microphenocryst cores and mineral inclusions from the Kalavassos Mine locality (Figure 4.8, Golowin et al., 2017; Sobolev et al., 1993)] with residual melt under the inferred eruptive conditions using the following relationship from Crank (1975):

$$\tau = Dt/a^2 \qquad \text{Equation 4.3}$$

where a is the crystal radius, t is time, τ is non-dimensional time, and D is the interdiffusion coefficient.

$D_{Cr\text{-}Al}$, the interdiffusivity coefficient of Cr-Al in chromite, is positively correlated with both temperature and Cr# (Suzuki et al., 2008). For this reason, we calculated $D_{Cr\text{-}Al}$ for chromite with Cr# = 80 at 1030 ℃ and 1130 ℃ by extrapolating the relationships illustrated in Figures 5 and 10 of Suzuki et al. (2008) to low temperatures. In detail, we reproduced the Arrhenius plot of Suzuki et al. (2008) for chromite with Cr# = 80 and fit linear equations to their diffusivity data to predict $\log D_{Cr\text{-}Al}$ as a function of temperature (Chapter 3.3.4). The following equation was recovered:

$$\log D_{Cr-Al} = -2.4199\left(\frac{10^4}{T(K)}\right) + 2.3902 \qquad \text{Equation 4.4}$$

Using this equation, we estimate $\log D_{Cr\text{-}Al}$ (cm^2/s) to be -16.2 at 1030 ℃ and -14.9 at 1130 ℃ (Table 4.6).

We elected to use self-diffusion coefficients from Liermann and Ganguly (2002) to estimate $\log D_{Fe\text{-}Mg}$ at the same conditions as $\log D_{Cr\text{-}Al}$. We also reproduced their Arrhenius plots for both Fe and Mg self-diffusion (Chapter 3.3.4) and then used their Equation 4 to calculate an interdiffusivity coefficient, $\log D_{Fe\text{-}Mg}$. For this calculation, we used the following linear equations recovered from their Arrhenius plots:

$$\log D_{Fe} = -1.0322\left(\frac{10^4}{T(K)}\right) - 4.7506 \qquad \text{Equation 4.5}$$

$$\log D_{Mg} = -1.0545\left(\frac{10^4}{T(K)}\right) - 4.7125 \qquad \text{Equation 4.6}$$

Using these equations and Equation 4 of Liermann and Ganguly (2002), $\log D_{Fe\text{-}Mg}$ was calculated to be -12.7 at 1030 ℃ and -12.2 at 1130 ℃ (Table 4.6).

Table 4.6: Ascent time calculations

Chromite Radius (μm)	*Maximum Ascent Time from Cr-Al Diffusion (years)*		*Minimum Ascent Time from Fe-Mg Diffusion (days)*	
	at 1030 ℃	*at 1130 ℃*	*at 1030 ℃*	*at 1130 ℃*
15	43	2	56	15
20	77	4	99	27
25	120	6	155	42
30	173	8	223	60
log D (cm^2/sec)	-16.2	-14.9	-12.7	-12.2

With these D values, we calculated maximum ascent time using the simple equation for diffusion in a sphere (Equation 4.3) by assuming $\tau = 0.04$ (i.e. insignificant change in core composition) and minimum ascent time by assuming $\tau = 0.4$ (i.e. complete re-equilibration, Table 4.6). At 1030 °C, in order to preserve a matrix chromite core whose Cr# = 80, a maximum of *c*. 170 years can pass before the core of the chromite begins to equilibrate, which means that the mafic lavas of the Troodos ophiolite, once extracted from their mantle source, crystallized their silicate cargo and erupted in less than *c*. 170 years. If temperature is raised to 1130 °C, the maximum amount of time is reduced to 8 years. Since the interdiffusivity coefficient is positively correlated with Cr#, if chromite has a lower Cr# than 80, then maximum ascent time increases. In fact, when Cr# approaches 0, $D_{Cr\text{-}Al}$ approaches values two orders of magnitude lower than when Cr# = 80 (Suzuki et al., 2008). Maximum ascent times would increase accordingly. However, because the chromites of the Troodos presented here are highly chromian, we expect our maximum ascent times to be within reason. We calculated minimum ascent time (for the same hypothetical chromite grain) at 1030 °C to be *c*. 220 days. At 1130 °C this value is lowered to 60 days. These back-of-the-envelope calculations demonstrate that it will be possible to constrain the ascent rate of boninitic magmas through study of diffusion profiles in matrix chromite crystals that they carry, and this should be done systematically in future research.

Overall, the melt temperature data cited as independent observations for the Troodos extrusive suite are corroborative, but it is important to discuss these data because temperature exerts strong control over diffusion. The three methods of temperature estimation are based on geochemical modelling (Dare et al., 2009; Golowin et al., 2017; Schouten and Kelemen, 2002). Golowin et al. (2017) used olivine-melt compositional data and the equilibrium relationships given by Ford et al. (1983) and Almeev et al. (2007) to quantify minimum crystallization temperatures, which they interpreted as eruption temperatures. Schouten and Kelemen (2002) used the geothermometer of Sisson and Grove (1993) to estimate temperature for their viscosity models. Finally, Dare et al. (2009) calculated temperature using the olivine-spinel thermometer of Ballhaus et al. (1991) and inferred this temperature as a closure temperature for chromite. Taken together, since the present discussion is focused on the kinetics of chromite-melt re-equilibration at pre-eruptive conditions, the estimates of Golowin et al. (2017) represent our preferred liquid temperatures because they are most likely to

constrain melt temperatures prior to significant syn-eruptive crystallization of microlitic pyroxene. Granted, when significant pyroxene crystallization occurs, melt water concentrations assumed by Golowin et al. (2017) for Troodos glasses (*c*. 3 wt.%) represent maxima and their temperatures minima following the liquidus depression relationships given by Almeev et al. (2007). Woelki et al. (2020) quantified water concentrations in boninite glasses to be 1.7-2.7 wt.%, which is slightly below the value provided by Golowin et al. (2017). This means our models may use temperatures that are slightly underestimated. The consequence of this is that our model ascent rates may be minima under high-temperature conditions and that ascent times for the Troodos extrusive sequence may be higher than modelled here. The likelihood of lower liquid temperatures are low due to the high closure temperature of 1100 °C inferred by Dare et al. (2009).

Additional complexity is added when considering the effect of changing Cr# during oxidation. Since $\log D_{Cr\text{-}Al}$ becomes lower as chromite loses Cr (Suzuki et al., 2008), since we elected to regress data provided for the highest Cr# chromites in the study of Suzuki et al. (2008) in order to estimate maximum ascent rate, and since natural chromites have slightly less Cr (Appendix 6), our maximum ascent times may be underestimated. This is an additional knowledge gap that should be addressed with future experimental work.

Because primitive compositional characteristics of the oxide mineral cargo are retained in several chromite crystals in the matrices of lavas of the Troodos ophiolite extrusive sequence and because, in some cases, mineral textures relating to diffusive equilibration seem to be preserved, we propose that chromites in such boninitic-tholeiitic lavas are products of either (i) crystallization from primary magmas or the incongruent melting reaction that is known to produce olivine + chromite in the shallow sub-arc mantle, or (ii) crystallization in complex fluid-melt or melt-melt mixtures in the same part of the magmatic system. In either case, chromite is likely precipitated prior to extensive pyroxene crystallization, as melt fractionation by pyroxene tends to compromise chromite stability in some igneous systems (e.g. layered mafic intrusions or ocean island basalts, Irvine, 1967; Roeder, 1994). Such behaviour appears to be absent in boninites and tholeiites associated with ophiolitic terranes such as the Troodos or the forearc regions of intra-oceanic arc systems (e.g. Whattam et al., 2020). In these rocks,

matrix chromite appears with stable pyroxene minerals as euhedral-subhedral mineral grains with no signs of resorption or breakdown. Thus, chromite is most likely a primitive component of the boninite-tholeiite petrogenetic system that perseveres through differentiation in arc systems and likely records compositional traits that reflect the full range of physicochemical states these magmas undergo prior to eruption (Figure 4.9).

In our petrogenetic model, synthesized in Figure 4.9, chromite forms in equilibrium with primitive boninitic melt prior to the growth of many silicate minerals (Figure 4.9B) and has a primitive composition characterized by high Mg# and Y_{Cr} (Stage 1). Once silicate minerals nucleate (Figure 4.9C), chromite Mg# will immediately begin to re-equilibrate, as this parameter is highly sensitive to the presence of ferromagnesian silicates (Stage 2). As these silicates grow, melt oxidation occurs, and Fe^{3+}-Al exchange begins (Stage 3, Figure 4.9D). Finally, Cr exchange begins to occur with Fe^{3+} and Al (such that chromite Fe^{3+}/Al remains constant, Figure 4.7B) and the volume of chromite at the edge of the grain reaches an equilibrium state with melt prior to eruption (Stage 4). If this chromite grain is entrained in an ascending melt that is quenched upon eruption, then the differential diffusivities of the major trivalent cations in chromite can be interpreted in a chronometric context (Figure 4.9E). Careful analysis of chromite should include a quantification of Fe-speciation (see EPMA methodology of Davis and Cottrell, 2018) so that precise thermometry and fugacity information can be inferred from natural samples.

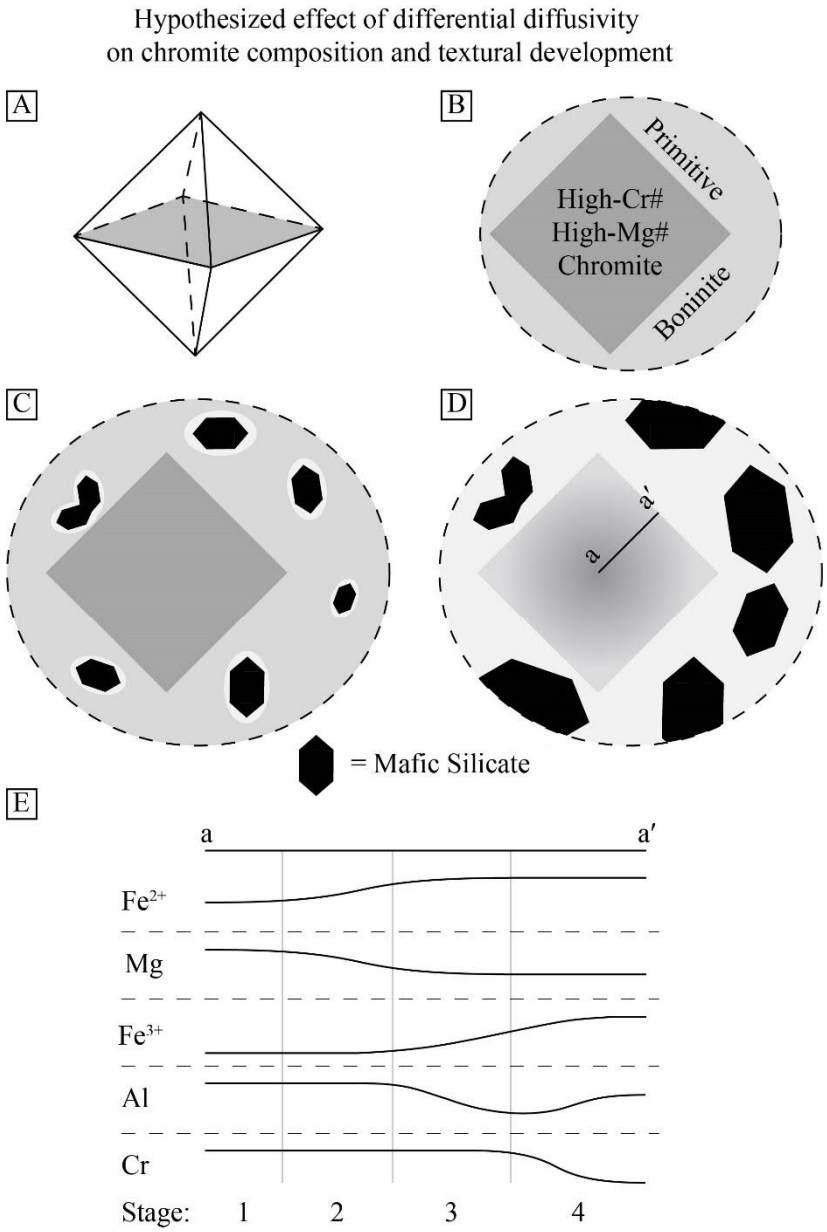

Figure 4.9: Diagram summarizing the petrogenetic model wherein disequilibrium textures are preserved in phenocrystic-microphenocrystic chromite as a function of differences between the diffusivities of the major divalent and trivalent cations in chromite. (A) Spinel octahedron. Subsequent images use a cross section of this hypothetical mineral form. (B) A schematic of the initial condition of chromite in primitive boninite melt without a large proportion of silicate minerals. (C) Silicate mineral nuclei form, immediately depleting the surrounding melt in Fe2+ and Mg. (D) Silicate minerals grow and completely alter the surrounding melt. The melt has acquired an evolved residual composition rich in Fe3+. (E) Hypothetical diffusion trends for all major cations in chromite from a-a0 (not to scale, transect shown in D).

4.7 Conclusions

1. The experiments presented here enabled us to coarsely parameterize ionic diffusion within chromites hosted in boninitic melt. Pyroxene is a ubiquitous component of the experimentally synthesized boninites, and residual melts are andesitic in composition. Matrix glasses preserved in natural boninites (Coulthard Jr et al., 2021; Woelki et al., 2020) demonstrate that olivine ± pyroxene crystallization commonly generates residual melts that are basaltic andesitic to andesitic in composition, similar to the products of these crystallization experiments.
2. The fact that these same natural glasses are enriched in Fe^{3+} upon eruption (Brounce et al., 2019; Rautenschlein et al., 1985) suggests that primitive boninitic melts (i) crystallize chromite under less oxidizing conditions than those characteristic of the pre-eruptive crustal column and within what are likely complex melt-fluid/melt-melt mixtures present in the sub-arc or back-arc mantle, (ii) crystallize olivine/pyroxene phenocrysts under magmatic conditions without significant chromite crystallization in the crust, and (iii) entrain most of their chromite crystal cargo prior to microlitic growth during ascent and eruption, to produce natural boninites and derived andesitic-basaltic andesitic glasses.
3. If chromite, including microlitic matrix chromite, were to crystallize from these residual liquids, then they would incorporate more Fe^{3+} and Al than observed, as shown by the natural samples taken from the extrusive sequence of the Troodos Ophiolite. Thus, most chromites are products of primitive melt crystallization in the crustal domain or of the incongruent melting of orthopyroxene in the mantle domain. When entrained in an evolving magma, melt oxidation perturbs the equilibrium chromite composition to higher Fe^{3+}. If sufficiently oxidizing conditions are achieved, Fe^{3+} replaces Al efficiently such that Fe^{2+}/Fe^{3+} + Fe^{3+}/Al chromite-melt equilibrium is approached. The disequilibrium textures and compositions preserved in some phenocrystic-microphenocrystic chromites should be examined closely to ascertain ascent rates using Fe^{3+} diffusivity.
4. In chromite, Cr-Al/Fe^{3+} equilibrium is achieved over much longer timescales. If considered the limiting factor of chromite-melt equilibration, natural microphenocrystic chromite observed in the extrusive suite of the Troodos ophiolite would equilibrate with residual melts in less than *c.* 170 years.

Diffusion may be much more rapid, and future work on the diffusive equilibration of both experimental and natural chromites should provide tighter constraints.

4.8 Acknowledgements

Thanks go to Mark K. Reagan for providing the natural samples for these experiments, to Michel Pichavant for providing a wealth of insight into interpreting experimental oxygen fugacity data, to Keith Putirka for useful dialogue on opx-melt equilibrium uncertainties, to Fred Davis for insight on chromite equilibria as well as modelling methods, and finally to Alexandre Corgne and an anonymous reviewer for their constructive criticism of this manuscript. This research was funded by the Royal Society of New Zealand through the Marsden Fund (grant MAU1704 to GFZ).

Chapter 5: Detection and quantification of H in synthetic Fe-rich spinel minerals via SCAPS-SIMS isotopography

5.1 Abstract

The detection of H in spinel-structured oxides is analytically challenging since common spectroscopic methods are unable to detect its presence in spinels with significant Fe concentrations. No attempt has therefore been made to detect the presence of an intrinsic H signal in these minerals. Here we present the results of ion microprobe experiments conducted using the products of internally heated pressure vessel experiments. Due to the small size of the spinels in these samples, we elected to use a stacked CMOS active pixel sensor to infer the distribution of OH signal intensity with a high degree of spatial resolution (< 1 μm). While no OH signal was detected in the majority of the samples, one sample with relatively high melt H_2O concentrations (*c*. 4.33 wt.% vs *c*. 1 wt.%) was observed to contain multiple titanomagnetites having *c*. 200 μg/g H_2O, calculated using recently obtained RSFs (Appendix 1). These results demonstrate i) the first conclusive evidence of H incorporation into Fe-rich spinel and ii) that secondary ion mass spectrometry is a suitable method for H detection in these nominally anhydrous minerals.

5.2 Introduction

Nominally anhydrous minerals (NAMs) are the most abundant minerals in the upper mantle (Haggerty, 1995). While nominally anhydrous, silicate minerals present in mantle xenoliths (olivine, garnet, ortho-, and clinopyroxene) have been observed to contain trace concentrations of H using widely available spectroscopic methods (e.g. Bell and Rossman, 1992) and secondary ion mass spectrometry (SIMS, Aubaud et al., 2007; Koga et al., 2003). While the trace partitioning of H into silicate NAMs has been widely acknowledged, it is generally assumed that spinels contain negligible concentrations of H under magmatic conditions (e.g. Keppler and Bolfan-Casanova, 2006).

Spinels are minor mineral phases that are ubiquitously observed within a wide compositional range of igneous rocks. In upper mantle peridotite, spinel is the main aluminous phase at pressures between *c*. 8-18 kbar, where it is replaced at lower

pressures by anorthite (Presnall, 1976) and higher pressures by garnet (O'Neill, 1981; Webb and Wood, 1986). Chromian spinel [general formula of normal structure = $^{IV}(Mg_{1-x}Fe_x)\ ^{VI}(Cr_{2-y}Al_y)O_4$, where IV and VI refer to tetrahedral coordination and octahedral coordination, respectively] has been recognized as a "petrogenetic indicator" by multiple researchers (Allan et al., 1988; Dick and Bullen, 1984; Irvine, 1965, 1967; Sack and Ghiorso, 1991; Wlotzka, 2005). This refers to the use of the chemical composition of chromian spinel to infer physicochemical properties of magmatic liquids (e.g. Arai, 1992; Roeder, 1994) or residual peridotites (Arai, 1994a, b; Ballhaus et al., 1991; Davis and Cottrell, 2018; Gamal El Dien et al., 2019; O'Neill and Wall, 1987).

H can be incorporated into synthetic non-stoichiometric spinel (spinel *sensu stricto* = $MgAl_2O_4$, Fukatsu et al., 2002; Okuyama et al., 2006). Here, non-stoichiometry means an excess of Al is present in the spinel unit cell, which is compensated by partial inversion of the site occupancy among divalent and trivalent cations [general formula = $^{IV}(A_{1-i}B_i)\ ^{VI}(A_iB_{2-i})O_4$, where *i* is the inversion parameter, A is a placeholder for common divalent cations (Mg, Fe^{2+}, Mn) and B for common trivalent cations (Cr, Al, Fe^{3+})] leading to the local modification of bond distances and O distribution at high temperatures (Lavina et al., 2002). This relationship is expressed as a variation of the general chemical composition for the solid solution (e.g. $Mg_{1-x}Al_2O_{4-x}$) and is the mechanism by which H is incorporated into spinel (*sensu stricto*), as vacant tetrahedral sites are populated to maintain local charge balance (Lenaz et al., 2008).

Lenaz et al. (2008) demonstrated that Fourier-transform infrared (FTIR) spectroscopy can detect as little as 10-20 μg/g H_2O in synthetic non-stoichiometric spinel (*sensu stricto*), and that OH absorption peaks were absent in stoichiometric samples. They also replicated earlier observations (Halmer, 2006; Lenaz et al., 2004; Skogby and Hålenius, 2003) detailing the band position of the spin-allowed *d-d* transition in $^{IV}Fe^{2+}$ in stoichiometric spinel with *c.* 0.12 wt.% FeO_{total}. Lenaz et al. (2008) were able to confirm that appreciable concentrations of $^{IV}Fe^{2+}$ saturate the band region where OH absorption peaks in spinel IR spectra are located. This was observed to increase the method detection limit of OH in ferrous spinel, which the authors suggest precludes FTIR as a reliable method of detecting trace OH in spinels with significantly more than 0.12 wt.% FeO_{total}. Thus, for natural igneous spinels, which often contain much higher

concentrations of Fe^{2+} (Barnes and Roeder, 2001), FTIR cannot be used to quantify the concentrations of trace H contained within their crystal structures.

Multiple observations made during routine microanalyses of igneous spinels may lend credence to the presence of a trace structurally bound hydrous component. For example, Melcher et al. (1997) observed higher than anticipated H concentrations in inclusion rich chromites from the Kempirsai Massif. The authors investigated fluid and gaseous inclusions via Raman and IR spectroscopic analyses but could not account for the high H concentrations using these methods. Additionally, Zellmer et al. (2014) observed increases in H secondary ions during ion probe analyses of olivine, attributed to the primary beam encountering hydrous micro-inclusions during excavation. Further, apparent olivine H concentrations were higher in olivines that contained an abundance of chromite micro-inclusions, suggesting that these chromites themselves may have been possible sources of H_2O.

Since H has yet to be conclusively detected as a trace component of ferrous spinels, discussion of its role in the partitioning behaviour of H during petrogenesis or within a geohygrometric context would be premature. Here we present the first data to demonstrate that Fe-rich spinel can host geochemically significant concentrations of H within its crystal structure. Ion microprobe experiments conducted using a stacked CMOS active pixel sensor (SCAPS) have resulted in positive and negative examples of H incorporation into experimentally synthesized igneous spinels. The concentration of H or H_2O in spinel was calculated using recently obtained RSFs (Appendix 1).

5.3 Materials and experiments

Synthetic basalt and boninite samples were produced in a series of experiments performed using internally heated pressure vessels (IHPVs) in Orléans, France and Tsukuba, Japan. Boninite synthesis is detailed in Chapter 4. Basalt synthesis followed the same methods (Chapter 3.1). Here, SIMS data gathered during ion microprobe experiments conducted on five of the synthetic samples (Table 5.1) are reported.

Table 5.1: Sample identification and information

Sample Name	wt.% ^2H_2O (bulk; ± 1σ)	Phases Present
Bas1100U	1.300 (0.130)	Feldspar, Clinopyroxene, Spinel, Glass
Bas1150U	0.596 (0.119)	Spinel, Glass
Bas1200Ub	0.828 (0.166)	Spinel, Glass, Quench Crystals*
Bon1150B	0.705 (0.141)	Orthopyroxene, Spinel, Glass
Bon1200Ua	1.136 (0.142)	Orthopyroxene, Spinel, Glass

*Due to inefficient quenching of the experiment, likely pyroxene or amphibole

Deuterium was added (*c.* 1 wt.% ^2H_2O) to experimental charges because it was assumed that this isotope could be easily distinguished from background ^1H during SIMS analysis. The ubiquitous presence of vesicles in backscattered electron (BSE) images of boninitic samples is likely due to the presence of residual atmosphere sealed in the Pt capsules during welding (Figure 5.1), and none of the samples yielded any detectable mass loss during synthesis.

Sample capsules were polished to expose the interior sample surface prior to the experiments. A precision slow saw was used to slice the polished samples into *c.* 4 mm^2 blocks. The five sample blocks were then pressed into a single In metal plug. Mounting samples in In removes the influence of epoxy, which emits fugitive H under vacuum (Aubaud et al., 2007; Koga et al., 2003). Prior to Au coating of the sample plug, optical microscopy was used to ensure that each sample surface was level and that no In had migrated over the edges onto any sample surface. A *c.* 70 nm Au coat was applied. High vacuum conditions are necessary for background H minimization, as reduction of residual background signal intensity is required to minimize method detection limits. Prior to analysis, the In sample plug was kept under vacuum for several days to eliminate surface H, and vacuum conditions during analysis were *c.* 2×10^{-9} Torr.

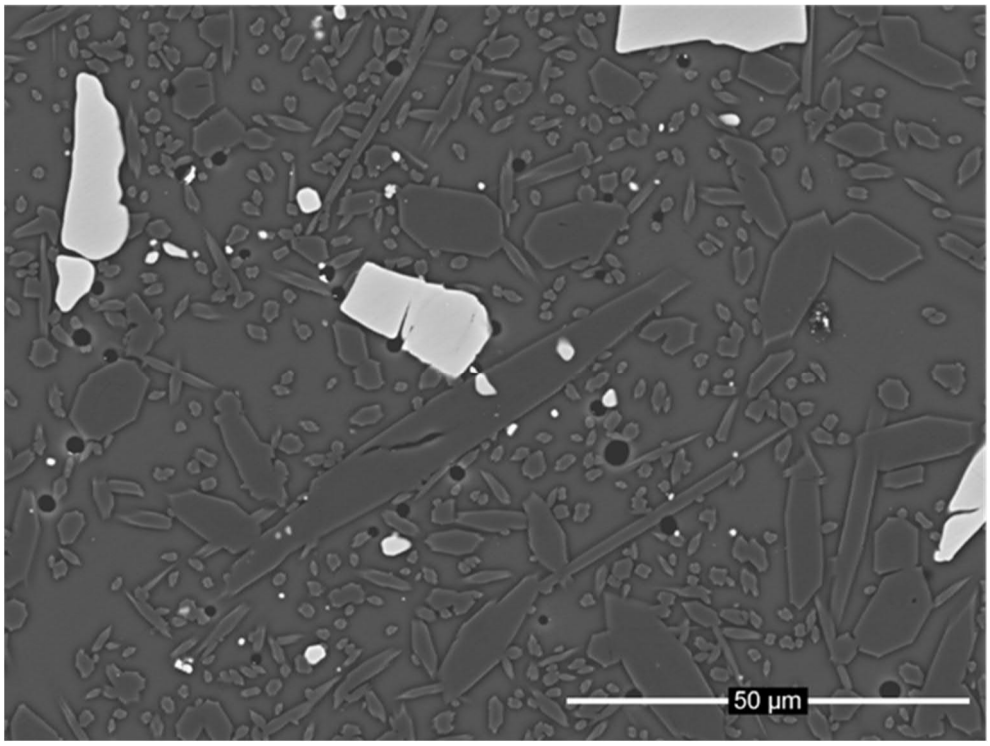

Figure 5.1: BSE image of the general texture observed in boninitic sample charges. Note the vesicles, which are dark circular features often rimmed by a bright ring. Spinel in this sample are anhedral fragments of original seed material, and dark grey crystals are orthopyroxene.

SIMS analyses were performed at the Creative Research Institution, Hokkaido University, Sapporo, Japan (Chapter 3.2.3.1). A Cameca IMS-1270 high mass resolution mass spectrometer outfitted with a SCAPS detector was employed. SCAPS analyses of the experimental charges were conducted with a $^{133}Cs^{+}$ primary ion beam set to 20 keV and a beam current of *c*. 1 nA and allowed simultaneous collection of signal intensity from spinel minerals and adjacent matrix glass. SCAPS detectors are stigmatic detectors with two-dimensional detection capability, a wide dynamic range, and constant ion-detection sensitivities without insensitive periods (Yurimoto et al., 2003). A dewar filled with liquid N kept the SCAPS sensor cooled to 77 K for the duration of the analyses.

Homogeneous irradiation of the sample surface by the primary ion beam was achieved for an elliptical area *c*. 60×50 µm in size. Secondary ion images corresponding to ^{18}O, $^{16}O^{2}H$, and $^{16}O^{1}H$ were taken at high mass resolution (M/ΔM = *c*. 7,800) in the order: ^{18}O-$^{16}O^{2}H$-$^{16}O^{1}H$-$^{16}O^{2}H$-^{18}O-$^{16}O^{2}H$-$^{16}O^{1}H$-$^{16}O^{2}H$-^{18}O, with integrated exposure times for each isotope/dimer: ^{18}O and $^{16}O^{1}H$ = 60 s, and $^{16}O^{2}H$ = 500 s. Repeated analysis of

^{18}O was performed to assess for variation in beam intensity, assuming constant ^{18}O densities of the experimental spinels. No statistically significant fluctuation of the ^{18}O signal was detected during the experiments.

RSFs for the calculation of OH concentrations are density dependent (Appendix 1), so spinel compositional data are required. The density and O density of spinel were calculated from compositions obtained using a JEOL JXA-8800R electron microprobe located at Hokkaido University (Chapter 3.2.1.1). Astimex mineral standards were used to calibrate the analyses performed on spinels observed in each excavated spot after ablation.

5.4 Data processing

Raw frames (5 second exposure time) were first corrected for fixed pixel noise (Kunihiro et al., 2001) prior to integration to produce secondary ion (isotopographic) images for each isotope/dimer. To extract data from each phase of interest, further image processing was necessary to reduce noise and the statistical uncertainty associated with the signal intensities of both spinel and glass. Image processing utilized the FIJI platform (Schindelin et al., 2012).

Homogeneously distributed white noise was then removed from the image via subtraction. The calculation was performed by selecting an area of pixels where the aperture blocked secondary ions (from the sample surface) from interacting with the SCAPS detector and calculating a mean value for these pixels. This value was then subtracted from every pixel to create a corrected image, redistributing this background signal around zero. One-way analysis of variance (ANOVA) models were employed to objectively determine if observed signal intensities (from the area within the aperture) were significantly different from background signals before and after background correction on a phase to phase basis. Single phase areas (within a given image) were sub-sampled to assess for phase homogeneity. ANOVA models were generated using IBM SPSS Statistics 26 with post-hoc testing conducted using the Tukey (HSD) method. Alpha (α) values were set to 0.05 for all models (95% confidence interval), and significance (p) values are provided (in parentheses) where ANOVA modelling has been performed using multiple independent observations of signal intensity. When $p \leq$

α, this indicates that at least one of the input sample means is significantly different, and when p > α, this indicates that all input sample means are insignificantly different.

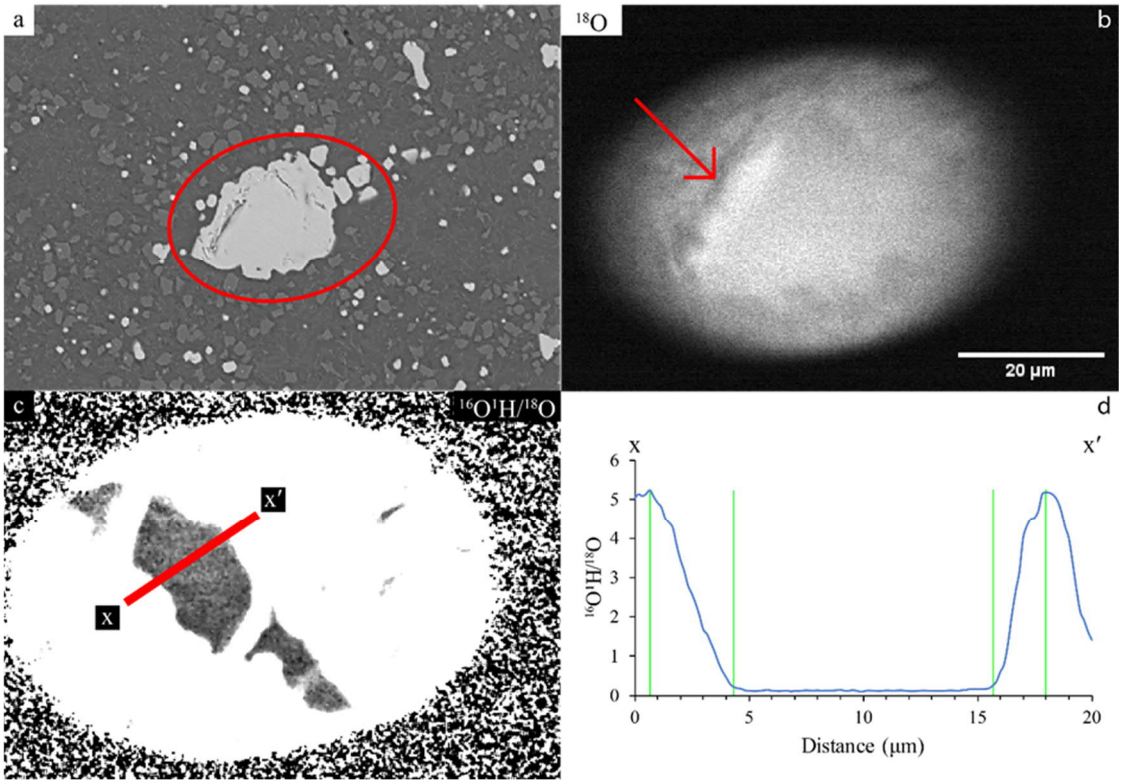

Figure 5.2: Composite image detailing SCAPS-SIMS analysis a) BSE image of Bas1100U. Spinel encircled exhibits a distinct crack at the surface; b) a secondary ion image of the spinel shown in the red ellipse of a).This secondary ion image has a bright streak (arrow) that represents a structural artefact or a specific topographic effect of the primary ion beam interacting with the crack in the spinel grain. The ellipse in a) roughly corresponds to the aperture area of b); c) a secondary ion ratio image after application of a median filter. The red line represents the profile of this signal shown in d); d) the profile shown can be used to estimate phase boundaries. The green lines on either side of the profile illustrate the beginning and end of the region where the phase boundary is assessed.

Phase homogeneity was assessed by visually scanning each image for structural artefacts (e.g. cracks, Figure 5.2a-b), by plotting signal profiles to determine the location of phase boundaries and their effects on signal intensity distribution (Figure 5.2c-d), and via ANOVA modelling. A phase boundary is defined as the pixel distance over which phase signal intensity is reduced by half (Yurimoto et al., 2003), and the edges of spinel-glass boundaries were determined to be *c*. 6 pixels (1 µm) wide with some boundaries defined over longer pixel distances (e.g. Figure 5.2d). The effect of heterogeneous surface charge compensation was corrected by calculating secondary ion

ratio images (see below). Finally, a median filter was applied to the image using a moving 3×3 pixel matrix in order to minimize statistical uncertainties associated with individual phase signal intensities (e.g. Figure 5.2c).

ANOVA modelling confirms that mean unfiltered secondary ion signal intensities for spinel and glass are not significantly different than mean values calculated after application of the median filter ($p = 0.923$ and 0.760 for $^{16}O^{2}H$ and $^{16}O^{1}H$ images, respectively). This confirmed that, for the purpose of signal quantification, applying a median filter does not remove any meaningful information from the images.

After processing, mean ratio values for a significant number ($n \geq 100$) of pixels, when available, were calculated for each phase for the determination of H and H_2O concentrations.

5.5 Results

5.5.1 Description of synthetic basalt samples

Since the boninite samples produced by our experiments are detailed elsewhere (Chapter 4), here we take the opportunity to describe, in detail, the basalts produced during these same experiments. Appendix 8 contains supplementary experiment data for these samples.

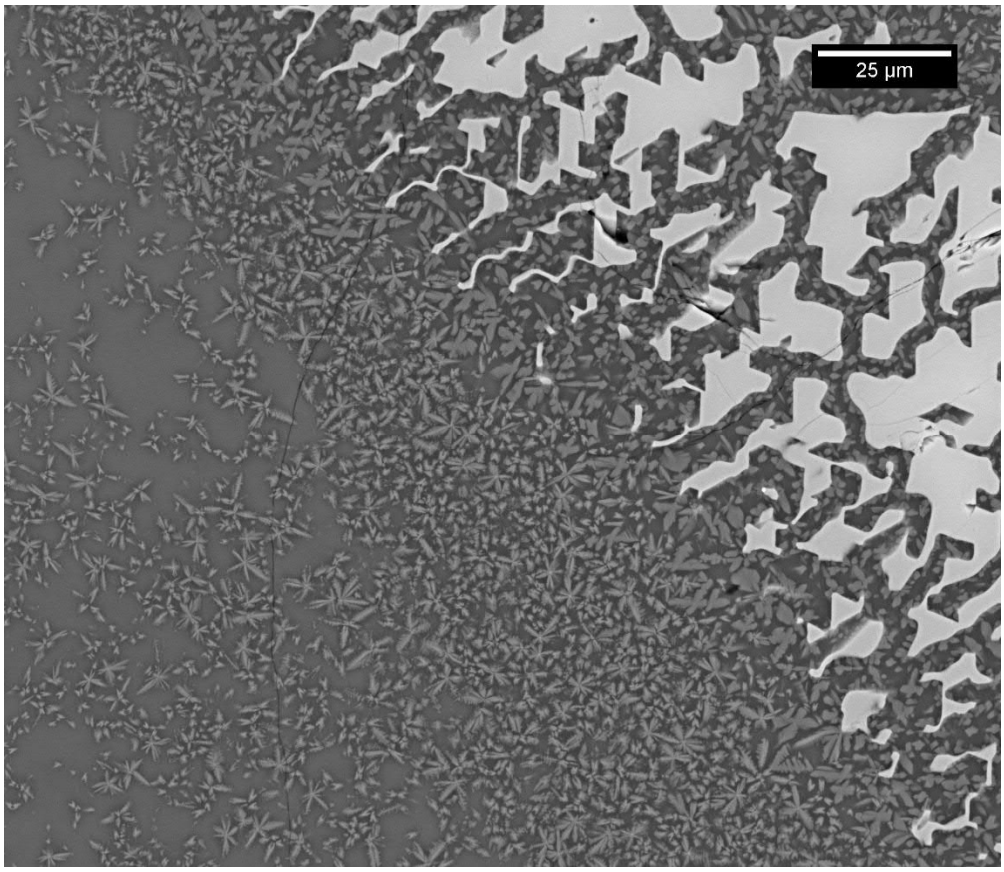

Figure 5.3: General spinel resorption texture observed in basaltic samples. Note the large degree of quench crystallization that occurred near the edge of the resorbing spinel grain. This basalt sample was processed at 1200 ℃ but likely lost water during the experiment. Thus, it is considered a failed sample and is not considered further.

The basalt used for these experiments came from the Manganui-D member of the Manganui formation, Taranaki volcano, New Zealand (Torres-Orozco et al., 2017). Pure magnetite seeds were sourced from the Marquette Iron Range near Ishpeming, Michigan and initially comprised 2 wt.% of each basalt charge included in the IHPV experiments. In samples processed at 1150-1200 ℃, these seeds completely resorbed into their co-existing melts when f_{O_2} was buffered using an Ar-H_2 gas mixture (samples Bas1200Ba, Bas1200Bb, Bas1150B, Appendix 8). Under the highly oxidizing conditions imposed by the intrinsic f_{O_2} of the IHPV, only partial resorption was observed at these same temperature conditions (Figure 5.3). Resorption of magnetite was observed to be limited in the single basalt sample produced at 1100 ℃ under intrinsic f_{O_2}.

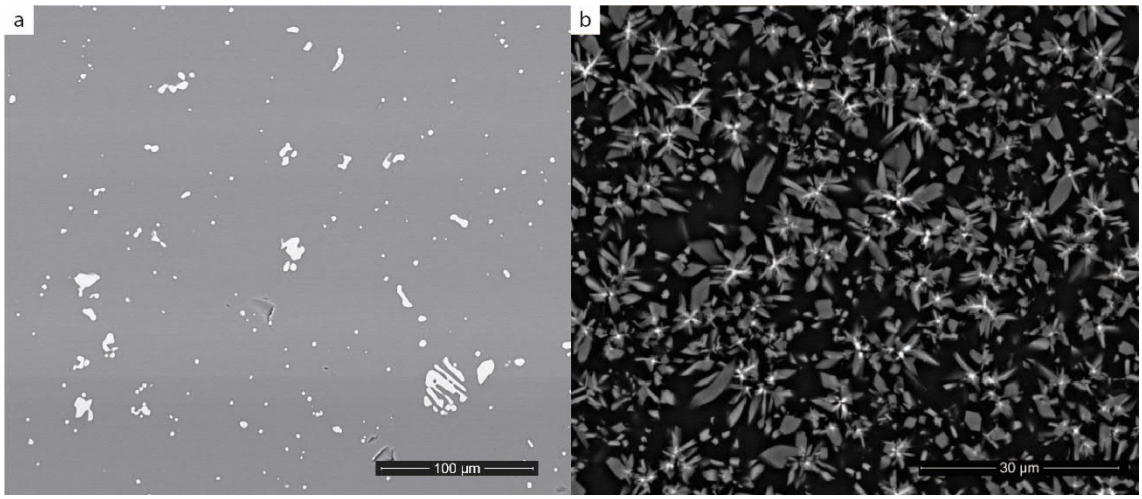

Figure 5.4: More basalt sample observations a) BSE image of Bas1150U. Note the lack of silicate minerals and the resorption textures of the magnetite. b) BSE image of the matrix of Bas1200Ua. Brightness and contrast optimized to show epitaxial texture with oxide cores and silicate mineral overgrowth. The same silicate textures are observed near the spinel grain boundary in Figure 5.3, but no oxide cores were observed in this setting.

Besides quench crystallization, no significant silicate crystallization occurred in the basalts synthesized at 1150-1200 ℃ (Figure 5.4a). Quench crystals present in samples Bas1200Ua and Bas1200Ub exhibit an epitaxial texture, where oxide cores are rimmed by spear-point shaped silicate minerals (Figure 5.4b) These are absent in Bas1200Ba and Bas1200Bb. The oxide cores are dendritic to star-shaped and range from sub-µm (>500 nm) sizes to *c*. 5 µm in diameter. At 1100 ℃ we observe a distinct mineral assemblage. Abundant but small (*c*. 5 µm diameter) calcic pyroxene (cpx, Appendix 8) and microlitic plagioclase feldspar (plag) have joined stable spinel as cotectic phases. The silicate species in this sample occur as segregated masses of cpx + plag and pockets of cpx or plag only with seed spinels distributed randomly throughout the sample (Figure 5.5). There are also abundant micro-vesicles that are dispersed evenly throughout the sample, which are either an indication of vapour saturation or due to the entrapment of atmospheric gas during welding.

The resorption texture exhibited by spinel in Bas1200Ub is replicated in all samples with stable spinel (Figure 5.6). Texturally, the spinels in Bas1100U can be split into two groups. They are either small and subhedral or large anhedral fragments of the original seed material (Figure 5.6c).

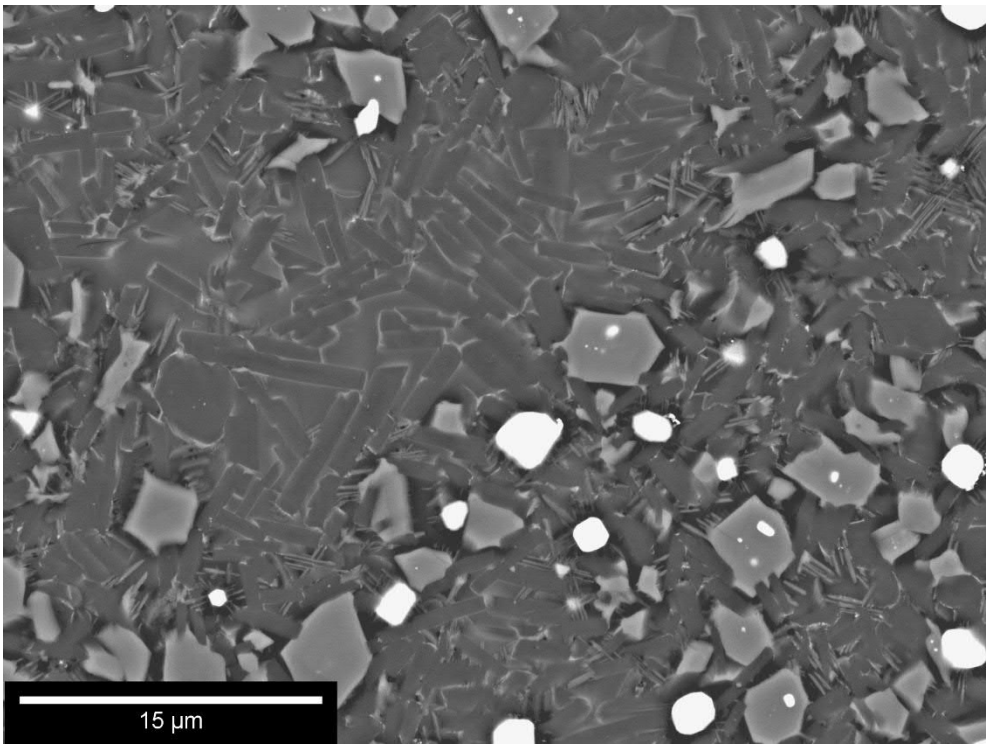

Figure 5.5: BSE image of Bas1100U. Dark tabular shapes are plag crystals, separated from the glassy matrix by very narrow bright boundary layers, while lighter grey silicates are cpx. Spinels are saturated in this image.

5.5.2 Spinel compositions

Spinels observed in Bas1100U, Bas1200Ub, and Bas1150U are no longer magnetite *sensu stricto*. They contain minor concentrations of Ti, Mn, and Cr as well as major concentrations of Mg and Al, which were absent in analyses of the original seed material (Appendix 8). Since larger seeds have the same compositions as smaller spinel. The most straightforward explanation is that small grains have grown from the basaltic melt prior to quenching, while large seed grains re-equilibrated with the melt over the duration of the experiment.

Thus, diffusion and re-equilibration of the seed magnetite occurred in these basaltic samples. Compositions trend away from a homogeneous end-member magnetite composition and approach an equilibrium composition under the imposed pressure-temperature-f_{O_2} condition.

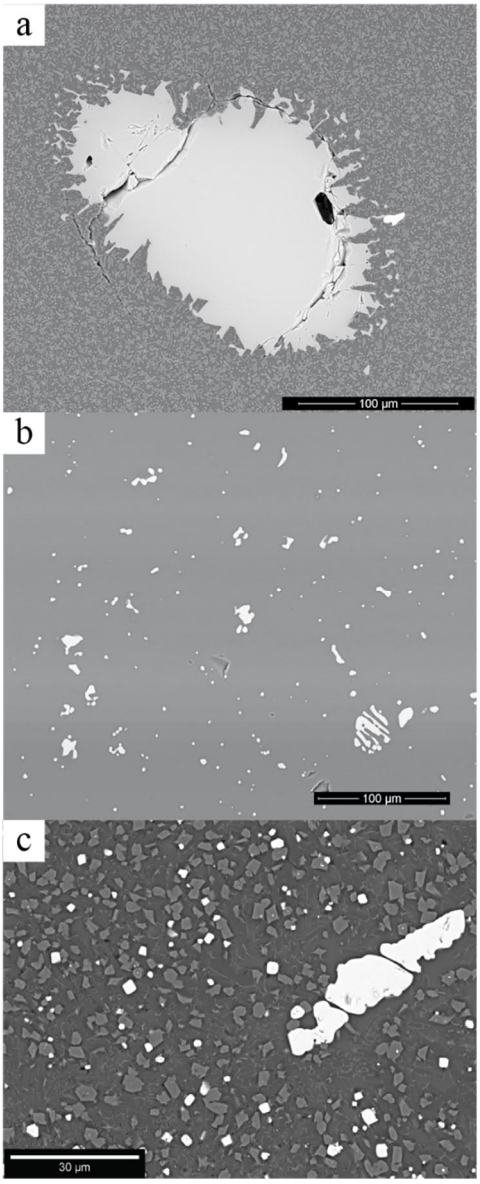

Figure 5.1: Resorption textures common to basaltic samples; a) Bas1200Ub; b) Bas1150U; c) Bas1100U

5.5.3 OH and O data from SCAPS-SIMS isotopography

Mean secondary ion signal intensities, sample space data, ratio values, and detection limits are given in Table 5.2.

ANOVA modelling suggests that, for a given image, there are significant differences between mean secondary ion signal intensities (checked pairwise) calculated for spinel, glass, and background areas ($p << 0.001$). However, for dimer signals, this is not always the case. For some samples, homogeneity of variance (a criteria for applying ANOVA modelling) was established for data recovered from images of the $^{16}O^{2}H$ dimer only. For example, structural artefacts shown elsewhere (Figure 5.2b) impose noise that is not homogeneously distributed. This means ANOVA models cannot be applied to discern the relationship these data have to other phases in the same image. Nevertheless, since $^{16}O^{1}H$ signal intensities, when detected, are generally an order of magnitude higher than $^{16}O^{2}H$ signal intensities for spinel sample surfaces, we do not consider ANOVA modelling imperative in demonstrating that $^{16}O^{1}H$ signal intensities are significantly different from their associated background signals, even though background intensity is also increased by a factor of *c*. 2 in these images. That said, the best method of signal quantification for these samples was to reduce the dimension of the sampling area to avoid structural artefacts and recheck for homogeneity of variance iteratively prior to signal integration. Sub-sampling smaller areas (until $p \leq \alpha$), enabled our identification of homogeneous regions in intra-phase space.

Table 5.2: Raw isotopographic data (ions/pixel/second)

Spot Location	$^{16}O^{2}H$	± 1σ	Area (μm^2)	$^{16}O^{1}H$	± 1σ	Area (μm^2)	$^{16}O^{2}H/^{18}O$	± 1σ	$^{16}O^{1}H/^{18}O$	± 1σ
Spinel Data										
Bas1100U-1	0.6818	0.2362	273	13.9616	2.2813	138	0.0077	0.0027	0.1524	0.0210
Bas1100U-2	0.6280	0.2328	69	8.8159	1.4307	69	0.0081	0.0027	0.1110	0.0169
Bas1150U	0.5681	0.2381	32	2.0519	1.1603	17	0.0073	0.0030	0.0270	0.0147
Bas1200Ub	0.3138	0.2120	43	2.0056	1.1310	27	0.0033	0.0023	0.0213	0.0118
Bon1150B	0.1695	0.2093	103	1.4739	1.0097	65	0.0019	0.0026	0.0174	0.0124
Bon1200Ua	0.1207	0.2237	200	0.7156	0.9963	108	0.0022	0.0032	0.0094	0.0145
Glass Data										
Bas1100U-1	27.52	2.82	7	386.80	35.88	7	0.3880	0.0403	5.3076	0.5352
Bas1100U-2	24.95	1.27	15	309.81	12.30	15	0.4457	0.0279	5.5391	0.2935
Bas1150U	43.63	2.02	41	152.06	7.09	41	0.8171	0.0436	2.8505	0.1605
Bas1200Ub	44.29	1.62	11	214.85	10.29	9	0.6876	0.0373	3.3500	0.1680
Bon1150B	4.20	0.32	12	260.79	6.65	8	0.0687	0.0059	4.6865	0.3151
Bon1200Ua	64.65	1.09	14	219.03	4.83	7	1.0774	0.0565	3.7174	0.1971
Detection Limit	0.12			0.63						

To establish a method detection limit using isotopographic images, aperture areas were analysed to characterize and quantify “zero signal” after noise removal (Chapter 5.3). This way, detection limits will not significantly differ from sample to sample since aperture area signal intensity was not observed to significantly vary between samples after noise removal ($p = 0.726$).

The standard deviation of the mean value of the signal intensity attributed to the aperture area was multiplied by three and added to the mean value to establish a detection limit for $^{16}O^{2}H$ and $^{16}O^{1}H$ images. The aperture area for unfiltered $^{16}O^{2}H$ images has a mean pixel value ($\pm 1\sigma$) of $1.9\times10^{-7} \pm 6.4\times10^{-7}$ V/frame/pixel, while the same value is $4.8\times10^{-7} \pm 3.5\times10^{-6}$ V/frame/pixel for $^{16}O^{1}H$ images. These values translate to detection limits of 2.1×10^{-6} V/frame/pixel and 1.0×10^{-5} V/frame/pixel for $^{16}O^{2}H$ and $^{16}O^{1}H$, respectively and correspond to 0.30 ions/pixel/second and 1.30 ions/pixel/second. Applying the median filter reduces these detection limits by > 50% to 0.12 ions/pixel/second and 0.63 ions/pixel/second for $^{16}O^{2}H$ and $^{16}O^{1}H$, respectively.

If mean secondary ion signal intensities in filtered sample images are at least two standard deviations (standard deviation of the observed signal intensity) higher than these latter values, we consider them to be detectable with 95% confidence (Table 5.2; Figure 5.7).

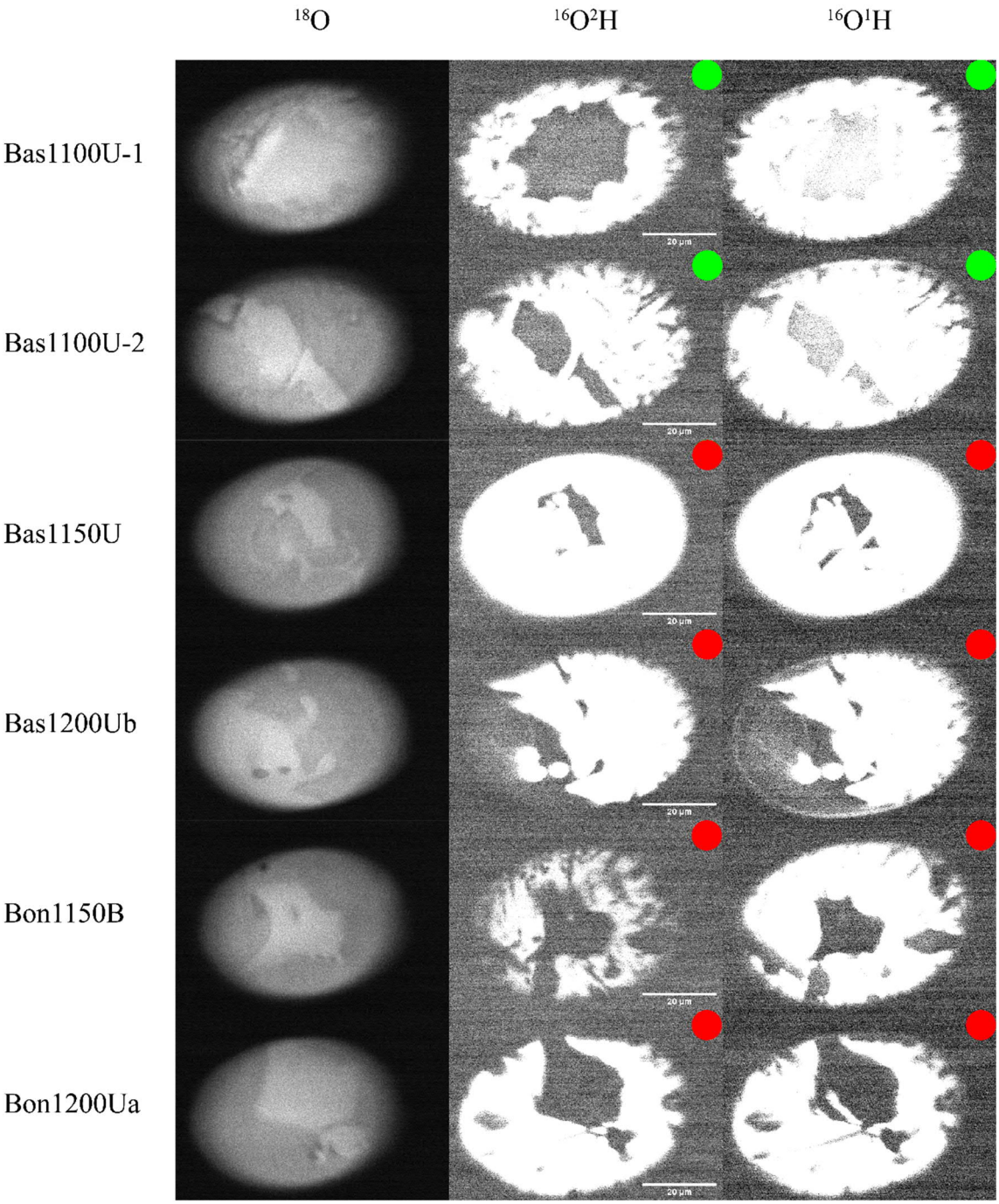

Figure 5.7: Noise corrected isotopographic images. Dimer images are saturated with respect to the glass signal so that the spinel signal is optimized. The brightness and contrast settings for each dimer were set to a uniform setting for comparative purposes. This setting was made by optimizing the signal intensity observed in Bas1150U. No median filter applied. Scale bar is 20 µm. Red circles indicate non-detection, while green circles indicate detection of OH in spinel.

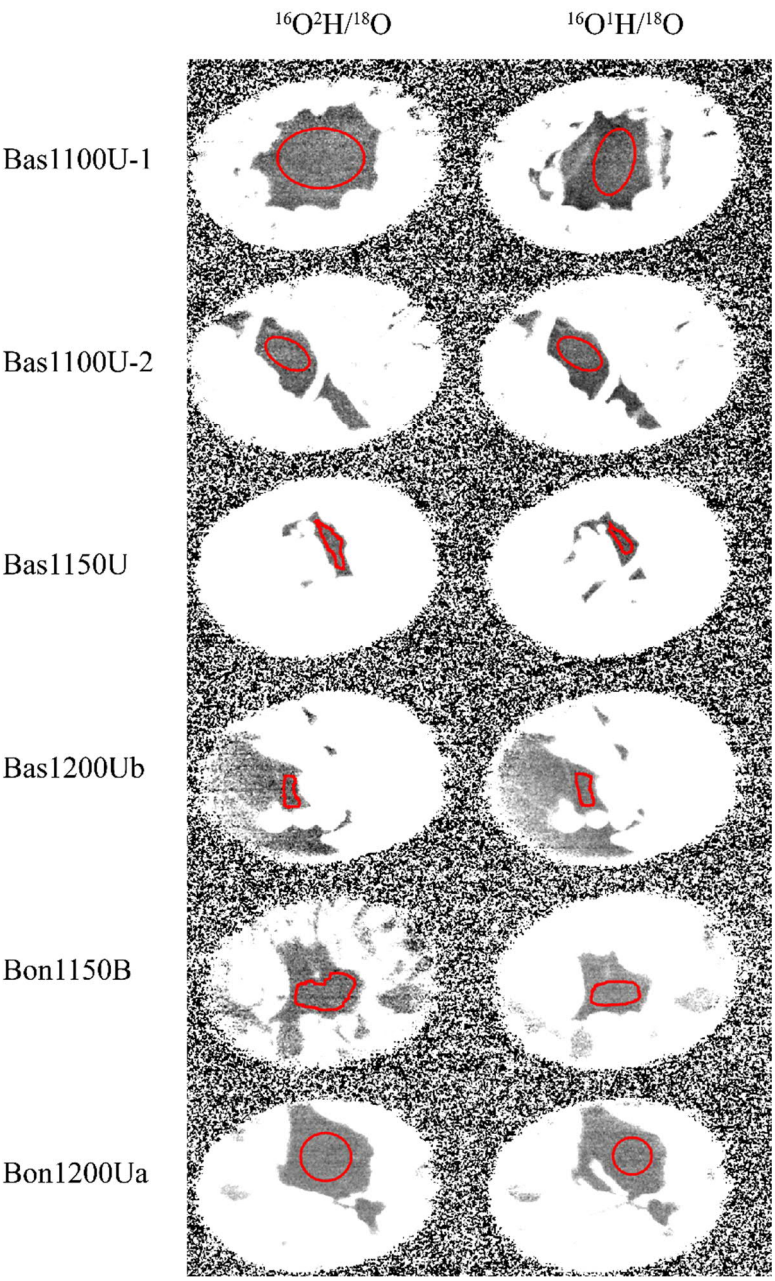

Figure 5.2: Secondary ion ratio images. The areas shown were used to quantify H and H_2O concentrations in each spinel grain. Brightness and contrast settings are set on an image to image basis. A median filter was applied to each image prior to signal calculation.

Dimer detection was achieved for 2 spinel spots from one sample only (Figure 5.7). Bas1100U spinel was observed to produce the only detectable secondary ion intensity with respect to both $^{16}O^{2}H$ and $^{16}O^{1}H$ dimers, demonstrating that H can be detected in Fe-bearing spinel using SIMS. Analysis of samples Bas1150U and Bas1200Ub produced high spinel signal intensities relative to those observed in Bon1200Ua and Bon1150B, but none of these signals were observed to be significant (i.e. from zero). Visually, spinels in these latter samples appear similar to aperture areas even after adjusting brightness and contrast settings to optimize spinel signal intensity (Figure 5.7).

Isotopographic imaging confirmed the hydrous nature of the glasses preserved within multiple sample capsules (Table 5.2; Figure 5.9). Strikingly, $^{16}O^{1}H$ signal intensities were generally higher than $^{16}O^{2}H$ signal intensities, which is surprising at face value given that nominally pure $^{2}H_2O$ was added to each experimental capsule.

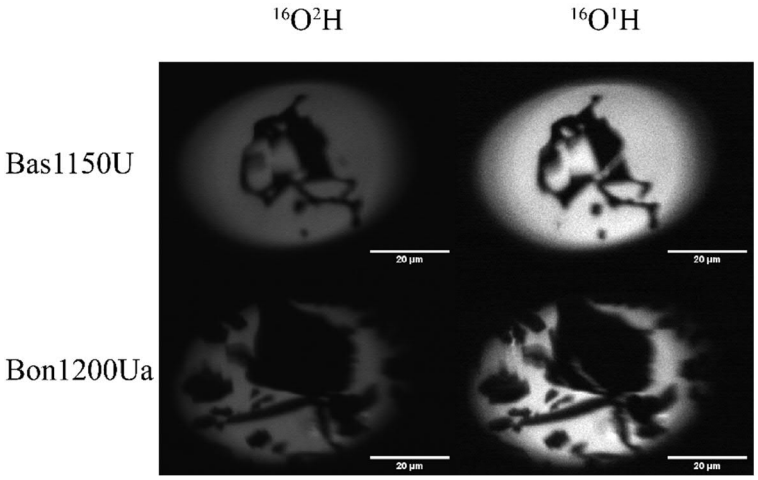

Figure 5.9: Noise corrected isotopographic images with brightness and contrast set to optimize glass signals. These settings are the same for a given sample and were set according to $^{16}O^{1}H$ signal intensity. Scale bar is 20 µm. No median filter applied.

5.6 Discussion

5.6.1 Note on the stabilization and re-equilibration of spinel in basalt during IHPV experiments

The epitaxial relationship observed in basaltic samples Bas1200Ua and Bas1200Ub is a result of inefficient isobaric cooling during quenching. Since the quenching of these samples was not efficient enough to produce microlite-free glass, we infer that the temperature gradient achieved during quench is less than the 300 °C/s cited by Roux and Lefevre (1992). The fact that oxide minerals commonly form the cores of these clusters suggests to us that these melts were saturated with respect to spinel at the time of quenching. This deduction is also supported by the fact that spinel can be efficiently resorbed by melts of this composition (e.g. samples Bas1200Ba and Bas1200Bb) at high temperatures and under less oxidizing conditions yet was not completely resorbed under these same temperatures and the intrinsic f_{O_2} of the IHPV. Sample Bas1150U has a similar texture to sample Bas1200Ua with blobby to subhedral spinel that we interpret as partially resorbed seed spinel. A lack of quench-induced silicate crystallization in Bas1150U indicates that quenching was efficient at the end of this experiment.

If partial seed resorption occurs prior to crystallization of spinel under stable temperature and redox conditions, then the melt progresses from a state of under saturation to a state of saturation within a few hours. This suggests that, with regard to

volume proportion, spinel reached equilibrium within the basaltic samples quickly. With respect to composition, it is likely that the relatively small spinels have completely re-equilibrated with their basaltic melts, as the time scale of the experiments (several hours) provided ample time for the major cations within the spinel structure to diffuse into or out of the spinels within the matrices of Bas1100U, Bas1150U, and Bas1200Ua (diffusivities of major cations are given by Van Orman and Crispin, 2010; they are ranked in order of decreasing diffusivity [log D, m^2/s] at 1100 °C: Mg-Al interdiffusivity = *c*. -13.5, Fe self-diffusivity = *c*. -16, Mg self-diffusivity = *c*. -16.5, and Cr-Al interdiffusivity < -20). However, Bas1200Ub contains much larger seed spinel, which likely did not completely re-equilibrate.

Thus, dissolution occurring in basaltic samples processed under the highly oxidizing intrinsic f_{O_2} of the IHPV operated under Regime 2 of Liang (2000). That is, the dissolution rate was slower than the diffusion rate. We propose that dissolution ceased prior to quenching because, upon quenching in multiple samples (Bas1200Ua, Bas1200Ub), nano-microscopic spinel cores quickly grew and were overgrown with silicate crystals as the melt fell below the silicate liquidus at a depressed thermal gradient. At lower temperature (Bas1100U and Bas1150U), small spinels are abundant and discernible from seed material (e.g. Figure 5.6c), which we infer to indicate spinel crystallized during experiment durations after melts became saturated with respect to the spinel phase. Based on this assessment, the compositions of the small synthetic titanomagnetites represent equilibrium compositions for their pressure-temperature-f_{O_2} conditions.

5.6.2 SCAPS-SIMS can detect water in Fe-bearing spinel

An important distinction must be made regarding the sources of OH contributing to the signal intensities assigned to the spinel minerals described above. Since H is a trace element in spinel, the detection of OH that is intrinsic to the spinel mineral may be hampered by the contribution of gaseous background H to the signal intensities reported here. The level of OH signal intensity attributable to the background is dependent primarily on the quality of the vacuum during analysis, as under high vacuum conditions H_2O is the dominant gas species (Stevie et al., 2016). Functionally, gaseous H atoms in the analysis chamber bond with O atoms at the surface of the sample before being sputtered as ionized secondary dimers that do not originate within the structure of

the sample (Figure 3.3). Background OH formation occurs constantly during a given analytical session, and the formation rate is determined by the arrival rate of the gas phase, the sputtering rate determined by the beam condition and the sample material, and the surface absorption coefficient for the material-gas species pair (also known as a "sticking coefficient", Magee, 1983). All samples were analysed under the same high vacuum condition, beam conditions were constant and optimized for spinel analysis, and we assume the surface absorption coefficient for spinel-H to be constant for the isostructural oxide samples described here. For these reasons, we consider background OH concentration as constant among all observed signals.

For this experiment, the concentration of background OH is less than the method detection limit attributed to chromite. This is evident from assessment of the signal intensity of chromite in Bon1200Ua. Observed signal intensity is identical to the method detection limit (Table 5.2), which we have defined to be the upper limit of "zero signal". Thus, since no signal is observed for this chromite, any background dimer formation that occurs during analysis must be less than that required to produce a detectable signal intensity using the SCAPS detector. Using RSFs, integrated dimer/O ratios ($[^{16}O^{1}H + {}^{16}O^{2}H]/^{18}O$) were processed and converted into concentration information to quantify the method detection limit for chromite to 26 ± 5 μg/g H_2O or 3 ± 1 μg/g H. These values appear as italicized entries in Table 5.3 alongside H and H_2O concentrations for the rest of the sample materials described here as well as the major element data used to calculate RSFs for each spinel spot. For the titanomagnetites, there is reason to believe that the method detection limit (in terms of concentration) is different than for chromite.

During the quantification of RSFs (Appendix 1), the sputtering rate of $^{16}O^{2}H$ was observed to be density dependent with high-density spinel producing relatively high $^{16}O^{2}H$ signal intensities. Each spinel standard was doped with the same flux of ^{2}H, so this difference constitutes a difference in RSF between less and more dense spinel minerals. Thus, Fe-rich spinels can produce detectable secondary dimer signals with less intrinsic OH than for less dense chromites. In order to estimate the method detection limit for titanomagnetite in terms of concentration (independent of background) the signal intensity observed for Bon1200Ua (i.e. essentially "zero signal") and RSFs calculated for the titanomagnetite phases were used to infer a lower method

detection limit of 13 ± 3 μg/g H_2O or *c.* 1 μg/g H for titanomagnetite (using the RSF calculated for sample Bas1200Ua). These values are also given in Table 5.3.

Titanomagnetite in sample Bas1100U contains the only significant concentrations of H observed in this dataset with a maximum (± 2σ relative uncertainty estimate) of 212 (± 46) μg/g H_2O or 24 (± 5) μg/g H. A second grain analysed in this sample returned marginally lower concentrations of 177 (± 38) μg/g H_2O or 20 (± 4) μg/g H, but both signals overlap within the uncertainty bounds of each sample. Concentrations cannot be confidently reported for spinel sampled in Bas1200Ub and Bas1150U because the signal intensities recovered from these materials were not observed to be significant. Since i) the concentration of OH attributable to the background is less than the method detection limit inferred for Bon1200Ua and ii) the concentrations observed for titanomagnetite grains in Bas1100U are at least an order of magnitude higher than the titanomagnetite method detection limit. We conclude the OH signatures of these spinels is dominated by OH that is intrinsic to the sample material.

5.6.3 Partitioning of H between spinel and melt, discussion of H incorporation, and final remarks on experimental observations

A volumetrically significant proportion of nominally anhydrous silicate minerals crystallized in Bas1100U, and a principle consequence of this crystallization reaction is the enrichment of H_2O in the residual melt. Based on a conservative estimate of the degree of crystallization (70%, inferred using the image segmentation technique described in Chapter 3.3.2) and the observation of no mass loss after the experiment was terminated, we expect the melt H_2O concentration in this sample to be greater than or equal to 4.33 wt.% (calculated using Equation 3.5). Textural analysis of this sample is inconclusive regarding vapour saturation, and no glass analyses via EPMA are available due to the abundance of plagioclase microlites. Thus, it is uncertain whether Bas1100U reached vapour saturation or not.

Table 5.3: Major element compositions and inferred H concentrations for synthetic spinel spots

Sample Name	TiO_2	MgO	FeO_t	Cr_2O_3	Al_2O_3	Density (g/cm^3)	Oxygen Density ($atoms/cm^3$)	*H (μg/g)	± 2σ	*H_2O (μg/g)	± 2σ
Bas1100U-1	3.79	6.87	75.06	0.00	7.28	4.69	5.37×10^{22}	23.6	5.1	212.3	45.5
Bas1100U-2	3.66	7.43	74.67	0.03	7.81	4.67	5.36×10^{22}	19.6	4.2	176.9	37.9
Bas1150U	1.31	6.90	69.09	2.95	10.20	4.64	5.43×10^{22}	-		-	
Bas1200Ub	1.29	6.55	76.77	0.08	9.08	4.76	5.38×10^{22}	-		-	
Bon1150B	0.13	11.99	20.01	51.00	14.98	4.46	5.58×10^{22}	-		-	
Bon1200Ua	0.14	15.45	18.73	51.65	12.93	4.40	5.25×10^{22}	*3*	*1*	*26*	*5*

**H concentrations calculated using integrated dimer signals ($^{16}O^{1}H + {}^{16}O^{2}H$)*

italicized entries indicate calculated detection limits using observed signal intensities, which are unaffected by background

- = not calculated

Using this H_2O concentration and the inferred spinel H_2O concentrations observed in Table 5.3, we have calculated a partition coefficient for H_2O between titanomagnetite and melt ($D_{H_2O}^{Ti\ Mag.-Melt}$). An average spinel H_2O concentration of 194.6 ± 15.3 (1σ, calculated using the equation for uncertainty in a mean) for sample Bas1100U returns a calculated $D_{H_2O}^{Ti\ Mag.-Melt}$ = 0.0045 ± 0.0003.

It is now useful to consider how H is incorporated into Fe-bearing spinel. Cr imposes a limit on the degree of Mg-Al inversion in chromian spinel (Bosi and Andreozzi, 2017), which implies that Cr also limits H incorporation associated with spinel (*sensu stricto*) component non-stoichiometry (Lenaz et al., 2008). Based on our limited observation, an alternative incorporation mechanism for chromite may be found to depend on Fe-speciation, which is correlated with system f_{O_2} (e.g. Roeder and Reynolds, 1991). However, our dataset indicates that the solubility of H in chromian spinel is extremely low even though Fe has been enriched in some of these materials (see discussion in Chapter 4). This is not the case for titanomagnetite. Titanomagnetite is a solid solution of magnetite and ulvöspinel. The crystal chemical behaviour of this solid solution exhibits distinct electro-chemical behaviour that is not observed in chromian spinel. For example, electron hopping occurs in titanomagnetite to vary the redox state of adjacent ^{VI}Fe atoms, and the reduction of ^{IV}Fe occurs locally when Ti^{4+} is incorporated (Bosi et al., 2009). These systematics may enable a higher H solubility than in chromian spinel, and future work must engage this question of H incorporation directly.

Considering that heavy water (^2H_2O) was initially added to the experimental charges, the observed higher abundance of ^1H over ^2H in both melt and spinel is striking. These results suggest that when Ar-H_2 is used as a fugacity buffer, hydrothermal IHPV experiments rapidly fractionate H isotopes through the Pt capsule wall under the experimental run conditions. However, some samples were processed without H_2 in the pressure medium. Thus, we conclude that either the Ar-H_2 gas mixture or regular deionized water that was used to saturate redox sensors included in each experiment diffused into the sample capsules and isotope exchange occurred to set the H-isotopic composition of each IHPV experiment. Future experiments may choose to take advantage of this behaviour.

5.7 Conclusions

1. SIMS methods can detect trace H in Fe-bearing spinel. Isotopographic analysis of SCAPS images revealed a hydrous component in titanomagnetite, while chromite lacked a detectable signal intensity.
2. Titanomagnetite equilibrated during the IHPV experiments was observed to contain *c.* 200 μg/g H_2O, which is similar in magnitude to inferred concentrations observed for orthopyroxene, plagioclase feldspar, and some natural clinopyroxenes. $D_{H_2O}^{Ti\ Mag.-Melt}$ was calculated to be *c.* 0.0045.
3. Future experiments should explore the potential effects of variable f_{O_2} and Ti content on H incorporation in Fe-bearing spinel, and on the equilibrium partitioning behaviour of H between spinel and co-existing phases.
4. The IHPV experiments conducted prior to SIMS analysis were performed using low bulk water concentrations (*c.* 1 wt.%). It would be beneficial to conduct future experiments under a wide range of water concentrations.

5.8 Acknowledgements

The authors would like to thank Stuart Mead and Gabor Kereszturi for providing information on ANOVA modelling in image analysis. This project was funded by the Royal Society of New Zealand through the Marsden Fund (grant MAU1704 to GFZ).

Chapter 6: OH concentrations of some natural Fe-bearing spinels

6.1 Abstract

The detection of H in nominally anhydrous spinel-structured oxides is an analytical challenge. However, since spinel i) is the main aluminous phase of the upper mantle and ii) almost ubiquitously observed in mafic volcanic rocks, there is ample reason in investigating their H concentrations. Since commonly available spectroscopic methods cannot be used to quantify trace H abundance in Fe-rich spinels, an alternative method of detection and quantification must be implemented. Here, we detail the results of ion microprobe experiments performed on naturally occurring Fe-rich spinels including chromite and titanomagnetite. Our results comprise the first quantification of H in natural Fe-bearing spinel, as secondary ion yields provide detectable signals for titanomagnetite with H concentration between 0-32 μg/g H_2O. Signal intensity is not considered detectable in chromite, which has *c.* ≤ 5 μg/g H_2O. Our proposed hypothesis regarding incorporation is that Ti^{4+}-associated electron exchange or the reduction of Fe^{3+} allow for the incorporation of H and the formation of structural OH^- in Fe-bearing spinel.

6.2 Introduction

The most common aluminous phase in the upper mantle is the spinel-structured oxide (hereafter spinel, Haggerty, 1995). It is a nominally anhydrous mineral with general formula $^{IV}A^{VI}B_2O_4$, where IV and VI indicate tetra- and octahedral coordination, and A and B are placeholders for common divalent (e.g. Mg, Fe^{2+}, Mn^{2+}) and trivalent (e.g. Al, Cr^{3+}, Fe^{3+}) cations, respectively. The revelation that upper mantle silicate minerals contain trace concentrations of structurally bound H (Bell and Rossman, 1992) signalled a paradigm shift in our observation and understanding of mantle dynamics (Regenauer-Lieb, 2006) and mantle-hosted petrologic processes (Hirschmann, 2006). In the crustal domain, H exerts strong fundamental control over several processes including those operating within magma chambers (Huppert and Woods, 2002), preceding/during volcanic eruptions (Sparks, 2003; Stock et al., 2016), and in ore formation (Candela, 1997). For these reasons, there is ample demand for the capability to observe and quantify the behaviour and abundance of H in nominally anhydrous minerals and systems.

Detecting and quantifying the concentration of H within Earth materials is analytically difficult. For spinel, analysis via Fourier-transform infrared spectroscopy is hampered since i) the band region of the OH^- peak in spectral space overlaps with the band region strongly affected by $^{IV}Fe^{2+}$ (Figure 1.2, Halmer, 2006; Lenaz et al., 2008), and ii) most natural spinel minerals occurring in ultramafic-mafic compositional domains contain sufficient Fe to preclude the detection of trace H bound within their structures using this method (Barnes and Roeder, 2001). Spinels along the titanomagnetite solid solution are certainly removed from this sample domain.

Despite this limitation, the utility of spinel as a petrologic/petrogenetic indicator (Arai, 1992; Tomiya et al., 2013; Wood and Virgo, 1989) warrants the investigation of their H concentrations. To this end, we have performed a series of ion microprobe experiments to elucidate and quantify the concentration of H in natural chromian spinels (chromites) and titanomagnetites. Chromites were sourced from multiple tectonic settings including the ultramafic section of the Troodos Ophiolite (Cyprus), Ani-jima of the Chichi-jima island group (Japan), and Mauna Loa (Hawaii). Titanomagnetite was sourced from Lake Taupo (from a diffuse layer of iron sand near Kinloch beach) and from scoria of the Manganui D formation (MD2 of Torres-Orozco et al., 2016) from two sites on Mt. Taranaki (New Zealand).

The secondary ion mass spectrometry (SIMS) data presented here are the first to conclusively show that natural Fe-rich spinels are H-bearing nominally anhydrous minerals. Previous efforts (Bromiley et al., 2010; Lenaz et al., 2008) suggest that natural $MgAl_2O_4$ spinel contains no detectable H_2O and that the synthetic oversaturation of spinel in Al (the generation of non-stoichiometric spinel) is the mechanism by which cation vacancies are generated and hydrated. There are multiple reasons that this is not likely the mechanism operating in Fe-rich spinel to facilitate H incorporation. Based on major element composition, we propose H is incorporated into cation vacancies associated with Fe affected by the magnetite-ulvöspinel electron exchange reaction (Bosi et al., 2009) or with the local reduction of Fe^{3+} and a proton-polaron diffusion mechanism (Mackwell and Kohlstedt, 1990).

6.3 Preparation and Analytical Methods

Sample spinels were first mounted in Crystalbond™ epoxy for polishing. Then they were removed with acetone, dried, and mounted into a single pressed indium plug to allow for ion microbeam analysis using a Cameca IMS-1270 ion probe at the Isotope Imaging Laboratory of Hokkaido University. Prior to analysis, a *c.* 70 nm gold coat was applied, and the sample was kept in an airlock at 10^{-8} Torr for *c.* 1 week to remove absorbed water. During analysis, vacuum conditions were maintained at *c.* 2×10^{-9} Torr.

A focused (*c.* 30 μm diameter) 10 keV $^{133}Cs^{+}$ primary ion beam sampled the surface with a beam current of *c.* 30 nA. In order to avoid edge effects and any remaining absorbed water on the surface, analysis was performed in raster mode and secondary ions were collected from the central *c.* 2-3 μm of the primary irradiation area only using a field aperture of 100 μm and a 100 μm contrast aperture. The high beam density used was effective in improving the detection limit of sample H using SIMS analysis (Yurimoto et al., 1989). We carefully selected analysis positions using stigmatic imaging during pre-sputtering with a 50×50 μm rastered beam and performed mass calibration under this condition as well. Following an additional 30-60 seconds of pre-sputtering with a 30×30 μm rastered beam, analysis began with a 25×25 μm rastered beam. Water contamination stemming from grain boundaries, cracks, and hydrous microinclusions were avoided as evidenced by flat stable ion beam intensities. A normal incident electron gun was used to compensate for positive charging of the sputtered region due to the primary ion beam. The mass resolution (M/ΔM) was set at *c.* 5,000, which enabled clear separation of $^{16}O^{1}H$ from ^{17}O secondary ion counts; evidenced by the observed natural $^{17}O/^{18}O$ ratio during analysis. Secondary ions of ^{17}O, $^{16}O^{1}H$, and ^{18}O were collected sequentially in an electron multiplier for 1 second, 3 seconds, and 1 second, respectively. This sequence was performed for 30 cycles (totalling *c.* 7 minutes for each spot analysis, including wait time) and averaged to calculate the $^{16}O^{1}H/^{18}O$ ratio of ablated material plus some contribution from the background.

6.4 Results

Typical ion signal intensities were *c.* 10^5 cps and 2×10^4 cps for ^{18}O and ^{17}O, respectively, and ranged between *c.* 700 cps to 3,400 cps for $^{16}O^{1}H$. The background H signal in spinel was estimated by observing count rate variations induced by changing

beam densities via varying raster size using Equations 3.6 and 3.7. Samples with the lowest H concentrations showed only small changes in $^{16}O^{1}H$ secondary ion yield compared to observed changes in ^{17}O and ^{18}O with change in raster size, which indicated that H contents of these samples are at or marginally above background levels, which were determined using a forward model of signal intensity (see Chapter 3.2.4).

For the Troodos chromite, observed $1/\rho O$ was calculated to be 0.3218, and the observed $\rho OH/\rho O$ value was calculated to be 0.2370. Since $1/\rho O > \rho OH/\rho O$, the background contribution to signal intensity was determined to be higher than any intrinsic $^{16}O^{1}H$. Using the trend derived from Equation 3.13, the b/i for this sample was determined to be 1.70. During routine analysis for this chromite (Chapter 3.2.3.2), the integrated observed signal intensity for this sample returned a concentration of 44.4 ± 8.9 atomic ppm H. Using this concentration, $H_{Intrinsic}$ was calculated to be *c.* 13 atomic ppm H or *c.* 4 μg/g H_2O, with $H_{Background}$ a factor of *c.* 2.5 higher at 31.4 ± 6.2 atomic ppm (2σ uncertainty). The high background contribution results in a low reliability of the quantification, so it is most appropriate to say that the H content of the chromite is below background concentration.

The Taranaki titanomagnetite was observed to have a higher $\rho OH/\rho O$ of 0.5784. However, this ratio is far from unity, which indicated that $H_{Background}$ significantly contributes to the inferred H concentration of 78.2 ± 16.7 atomic ppm H. The $1/\rho O$ for this sample was calculated to be 0.2468. Using the linear Equation 3.12, the b/i value for this sample was determined to be 0.56. This value was used to quantify $H_{Intrinsic}$ for the Taranaki titanomagnetite to *c.* 56 atomic ppm H or 17.5 μg/g H_2O. The $H_{Background}$ concentration, 21.9 ± 5.7 atomic ppm H, is within the 2σ uncertainty associated with the background concentration inferred using the Troodos chromite.

With this, the background concentration of H present during the SIMS experiments was estimated to be between 22-31 atomic ppm H. Since the analytical and background conditions for this analysis were invariant between samples, the difference in estimated background H could stem from uncertainties associated with our modelling strategy or it could stem from differences between the surface absorption coefficients of H on either chromian spinel or titanomagnetite, which is beyond the scope of this study.

Since no standard materials exist for the conversion of signal intensity to concentration, an RSF method was used (Appendix 1). This method requires major element data to model spinel density and O-density in order to calculate an RSF for each spot analysis. Major element data were gathered using a JEOL JXA-8800R at Hokkaido University.

Major element data, mineral densities, O-densities, integrated $^{16}O^{1}H/^{18}O$ ratios, and H_2O concentrations are provided in Tables 6.1 and 6.2. H_2O^{total} is calculated after Benninghoven et al. (1987), where $H_2O^{total} = RSF \times {}^{16}O^{1}H/^{18}O$. High density titanomagnetites from Taupo and Taranaki contain various concentrations of structurally bound H, while chromites contain baseline concentrations that are near background concentration. No hydrous nano-inclusions were observed in backscattered electron (BSE) images of the investigated samples (Figure 6.1), which indicates that these H signals are attributable to either an intrinsic H concentration ($H_2O^{intrinsic}$) or background H ($H_2O^{background}$). At the nanoscale, Troodos chromites were observed to exhibit a wormy texture (Figure 6.2), with thin and narrow dark lines standing out in both BSE and secondary electron images (SEI). However, given the low inferred H concentrations for these chromites, these nano-scale structures may be ruled out as a significant source of H. Their origin is unknown, but the material is likely much less dense than the chromite it is hosted in. They may be chemical weathering features.

For $H_2O^{background}$ subtraction (Tables 6.1 and 6.2), the observed $^{16}O^{1}H/^{18}O$ values were manipulated for each spot analysis until calculated H concentrations were equal to the background concentrations inferred above (*c.* 22 atomic ppm H for titanomagnetite and *c.* 31 atomic ppm for chromite):

$$H_2O^{background} = RSF \times y\,{}^{16}O\,{}^{1}H/{}^{18}O \qquad \text{Equation 6.1}$$

where y is a coefficient corresponding to the proportion of background signal intensity. The congruent H_2O concentration for each point was then subtracted from the total amount of H_2O initially calculated using RSFs to obtain $H_2O^{intrinsic}$.

Titanomagnetite sourced from Lake Taupo contains as much as 29.5 μg/g H_2O. Multiple analyses of separate crystals indicate that some spinels from this locality contain no H_2O. Titanomagnetites from Taranaki contain between *c.* 11-32 μg/g H_2O, comprising the highest observed signals in this dataset.

Chromite from Ani-jima contains *c*. 1.6 μg/g H_2O based on repeat analysis of chromite sourced from a subaerially exposed boninite, while one chromite recovered from Papakolea Beach, Hawaii contain *c*. 1-3 μg/g H_2O. Finally, chromites recovered from podiform chromitites of the Troodos Ophiolite contains *c*. 3-5 μg/g H_2O.

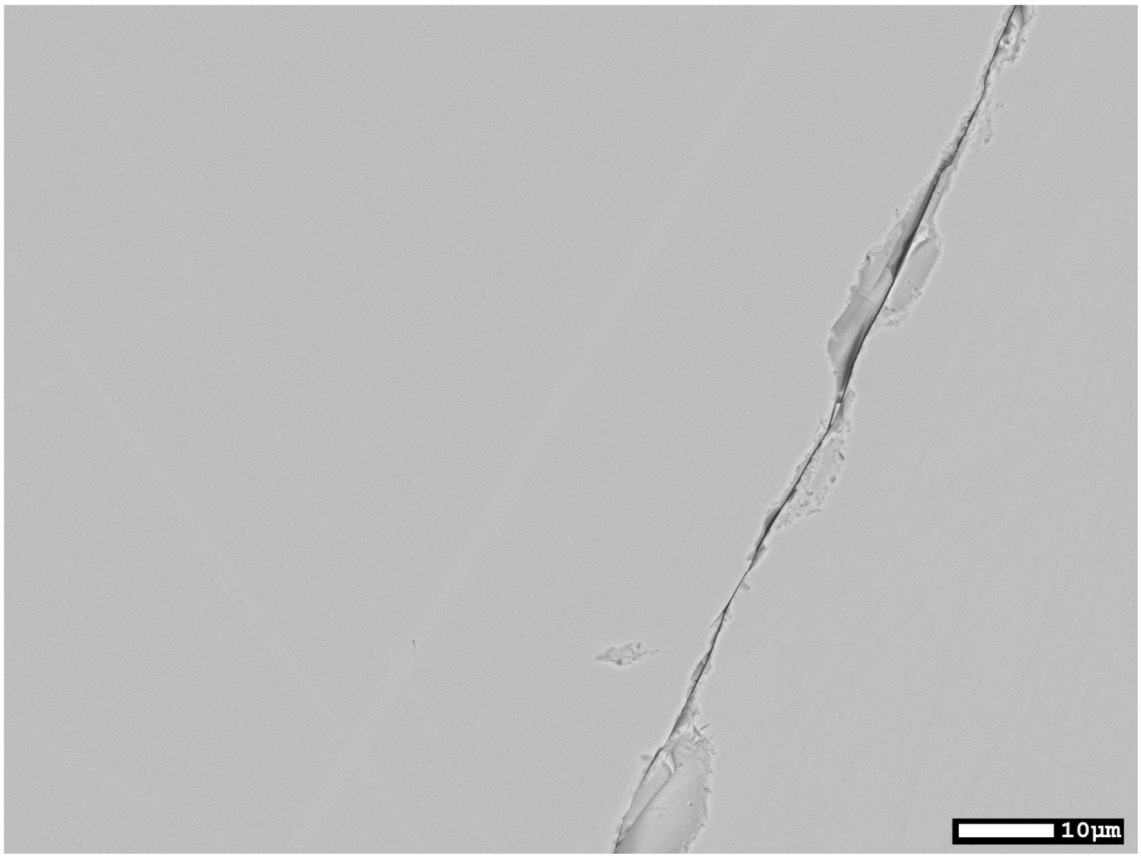

Figure 6.1: BSE image of the surface of sample Taranaki D1. Besides debris and some crack fill, no significant zonation nor inclusions are detected using scanning electron microscopy. Faint bright bands are scratches and not ilmenite exsolution lamellae, which were observed to be absent using high magnification reflected light microscopy

Table 6.1: Major element, RSF, SIMS, and H_2O data for natural titanomagnetites

Provenance	Taupo					Taranaki					
Sample	1a	1b	2	3	4	P1	P2a	P2b	D1	D2	D3
TiO_2	7.88	<	10.43	10.51	10.46	7.09	6.92	<	6.15	5.86	7.53
MgO	0.35		0.66	0.7	0.67	3.93	3.92		4.7	4.78	4.69
FeO^{total}	84.05		81.53	81.38	81.23	76.85	75.21		75.87	75.53	75.82
Cr_2O_3	0.04		*b.d.l.*	*b.d.l.*	0.04	0.03	0.03		0.23	0.35	0.27
Al_2O_3	1.56		1.6	1.6	1.68	6.02	8.91		7.66	7.97	6.44
MnO	0.64		0.65	0.67	0.6	0.39	0.47		0.29	0.31	0.38
Density (g/cm^3)	4.93		4.89	4.89	4.89	4.77	4.74		4.73	4.73	4.74
O-Density ($\times 10^{22}$ atoms/cm^3)	5.22		5.21	5.21	5.21	5.32	5.36		5.35	5.36	5.33
$^{16}O^1H/^{18}O$	0.0073	0.0076	0.0344	0.0133	0.0128	0.0278	0.0356	0.024	0.0197	0.0224	0.0163
H_2O^{total} (μg/g)	7.6	7.9	36.1	14.0	13.4	30.0	38.6	26.0	21.4	24.3	17.6
$H_2O^{background}$ (μg/g)	6.6	6.6	6.6	6.6	6.6	6.8	6.8	6.8	6.8	6.8	6.8
$H_2O^{intrinsic}$ (μg/g, ± 2σ)	*1.0*	*1.3*	**29.5 (5.9)**	**7.4 (1.5)**	**6.8 (1.4)**	**23.2 (4.6)**	**31.8 (6.4)**	**19.2 (3.8)**	**13.6 (2.7)**	**17.5 (3.5)**	**10.8 (2.2)**

< = same composition as previous column, b.d.l. = below detection limit, italicized $H_2O^{intrinsic}$ values are << $H_2O^{background}$ and are not considered significant

For Taranaki samples, P and D in the sample name refer to either Pembroke Road or Dawson Falls

Table 6.2: Major element, RSF, SIMS, and H_2O data for natural chromites

Provenance	Ani-jima		Mauna Loa		Troodos		
Sample	1a	1b	1	2	1a	1b	2
TiO_2	*b.d.l.*	<	1.38	1.11	0.19	<	0.14
MgO	14.25		12.34	12.86	15.57		15.35
FeO^{total}	15.45		22.28	22.52	15.24		15.22
Cr_2O_3	64.66		45.2	48.16	54.26		53.84
Al_2O_3	5.86		14.56	14.99	15.81		15.78
MnO	0.26		0.27	0.26	0.25		0.29
Density (g/cm^3)	4.52		4.41	4.44	4.37		4.37
O-Density ($\times 10^{22}$ atoms/cm^3)	5.53		5.59	5.59	5.61		5.61
$^{16}O^1H/^{18}O$	0.0105	0.0102	0.0061	0.0061	0.0061	0.006	0.0053
H_2O^{total} (μg/g)	11.9	11.6	13.1	11.2	15.1	14.9	13.7
$H_2O^{background}$ (μg/g)	10.1	10.1	10.4	10.4	10.4	10.4	10.4
$H_2O^{intrinsic}$ (μg/g)	*1.8*	*1.5*	*2.7*	*0.8*	*4.7*	*4.5*	*3.3*

All symbols and demarcations are same as in Table 6.1

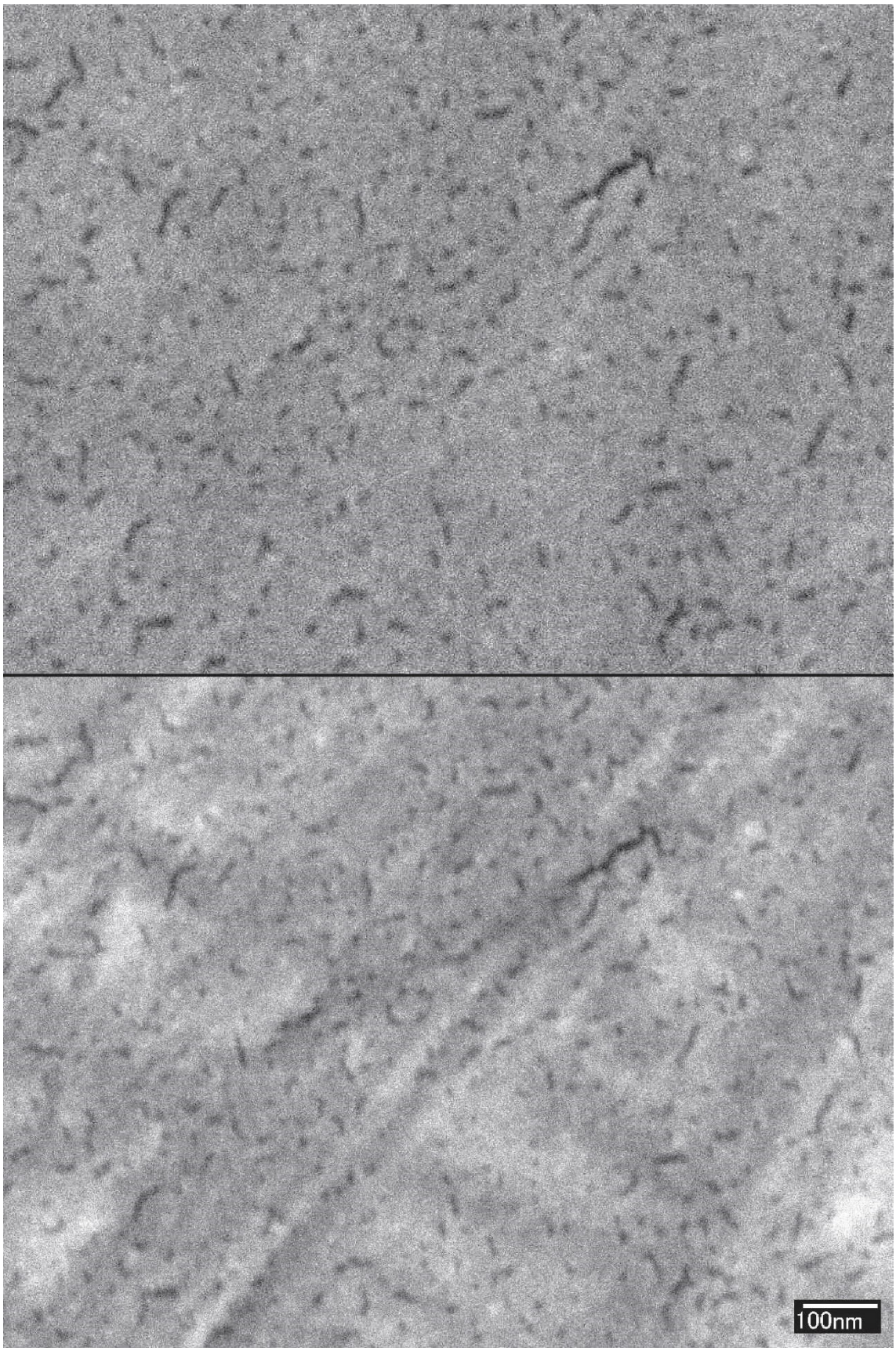

Figure 6.2: BSE image (top) and SEI image (bottom) of Troodos chromite exhibiting the wormy texture of this sample.

6.5 Discussion

Chromites analysed here are poor in H with many samples having concentrations at/below that inferred for the background H signal, and thus, we cannot confidently say that an intrinsic H signal was detected in these minerals. The chromites with the highest observed $^{16}O^{1}H/^{18}O$ are from Ani-jima. However, because these chromites are also relatively dense (with respect to the other chromites in our dataset) their calculated RSFs are low (H_2O = RSF × OH/O, Benninghoven et al., 1987) and their inferred H_2O concentrations are as well (Table 6.2). To summarize, our analyses yield low H concentrations for igneous chromites, including those sampled from ocean island basalt domains (Mauna Loa).

Using high pressure-temperature experiments, Bromiley et al. (2010) showed that several hundred μg/g H_2O may be incorporated into $Mg_{1-x}Al_2O_{4-x}$ (non-stoichiometric) spinel with varying degrees of solubility controlled by the concentration of imposed cation vacancies and degree of Mg-Al disorder. Neither Lenaz et al. (2008) nor Bromiley et al. (2010) achieved OH detection when analysing natural spinels, which were inferred to be stoichiometric. As shown by Bosi and Andreozzi (2017), Cr incorporation limits Mg-Al disorder non-linearly since Cr strongly prefers octahedral coordination. Thus, the incorporation mechanisms inferred for $MgAl_2O_4$ spinel are likely precluded with significant Cr incorporation, which is consistent with the low H concentrations observed here.

Save for a single grain from Lake Taupo, all titanomagnetites described here exhibit a significant intrinsic OH signal (Table 6.1). Samples from Lake Taupo have a wide range of inferred H concentrations, while Taranaki samples contain a narrower range that extends to the highest observed concentrations in our dataset. These results suggest that there is a fundamental difference between chromite and titanomagnetite that allows for the incorporation of a significant amount of H into titanomagnetite.

The stabilization of cation distributions for spinels along the magnetite-ulvöspinel solid solution often involve changes in valence state for both tetra- and octahedrally coordinated Fe (Bosi et al., 2009). Magnetite is inversely ordered with Fe^{2+} completely in octahedral coordination ($^{IV}Fe^{3+}\ ^{VI}[Fe^{2+}\ Fe^{3+}]O_4$), while ulvöspinel is a 4-2 spinel with Fe^{2+} split between tetra- and octahedral coordination ($^{IV}Fe^{2+}\ ^{VI}[Fe^{2+}\ Ti^{4+}]O_4$). The

incorporation of Ti^{4+} into magnetite, which occupies spinel octahedral sites exclusively, necessitates the exchange of electrons between Fe cations within the spinel structure The electron transfer reaction [$^{IV}Fe^{2+} + {}^{VI}Fe^{3+} \leftrightarrow {}^{IV}Fe^{3+} + {}^{VI}Fe^{2+}$] works to relax strained bonds made by the incorporation of the Ti^{4+} cation (giving rise to unit cell expansion, denoted by the so-called *a*-parameter), minimizing the strain within the titanomagnetite solid solution. It operates to different extents depending on how much Ti is present within the spinel unit cell (Bosi et al., 2009) and its crystal-chemical effects are apparent when plots of the *a*-parameter are made against Ti abundance (Figure 6.3).

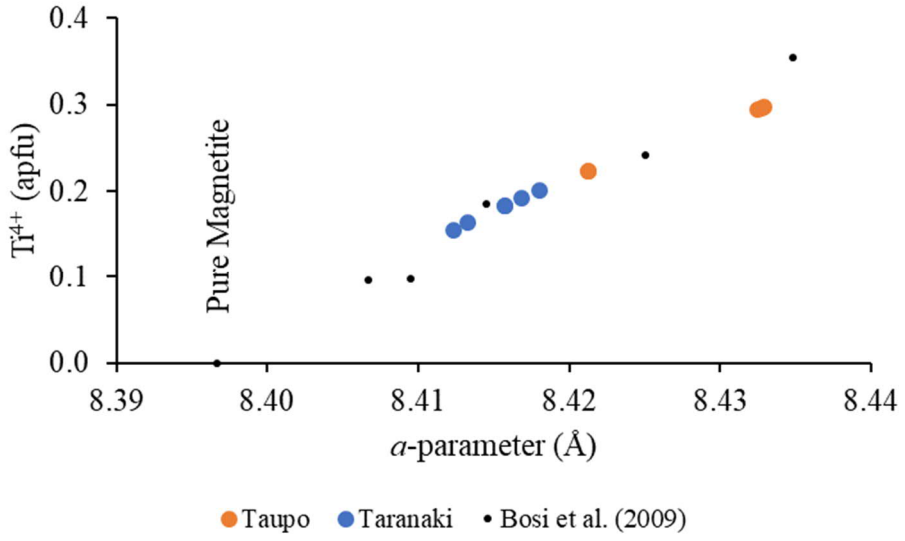

Figure 6.3: Titanium abundance vs spinel *a*-parameter (calculated using the equations given by Bosi et al., 2009) for natural titanomagnetites. Synthetic samples from Bosi et al. (2009) for comparison.

Separately, electron hopping is known to occur between Fe cations in octahedral coordination, as spinel octahedral sites share half of their edges with adjacent octahedrons within a volume of spinel. This phenomenon gives spinel a degree of electrical conductivity. Together, the electron transfer reaction and the electron hopping phenomenon may open avenues to H incorporation, as the incorporation of H into an adjacent vacant tetrahedral site should stabilize $^{VI}Fe^{2+}$. Likewise, the reduction of $^{IV}Fe^{3+}$ may be accomplished by protonation of an adjacent vacant tetrahedral site (Figure 6.4). Thus, H incorporation should cause deviation from ideal crystal-chemical behaviour and, potentially, the geophysical properties of Fe-bearing spinels as they are currently understood. These systematics should be tested directly in future experiments, as natural samples (including those sampled here) may have non-magmatic H concentrations.

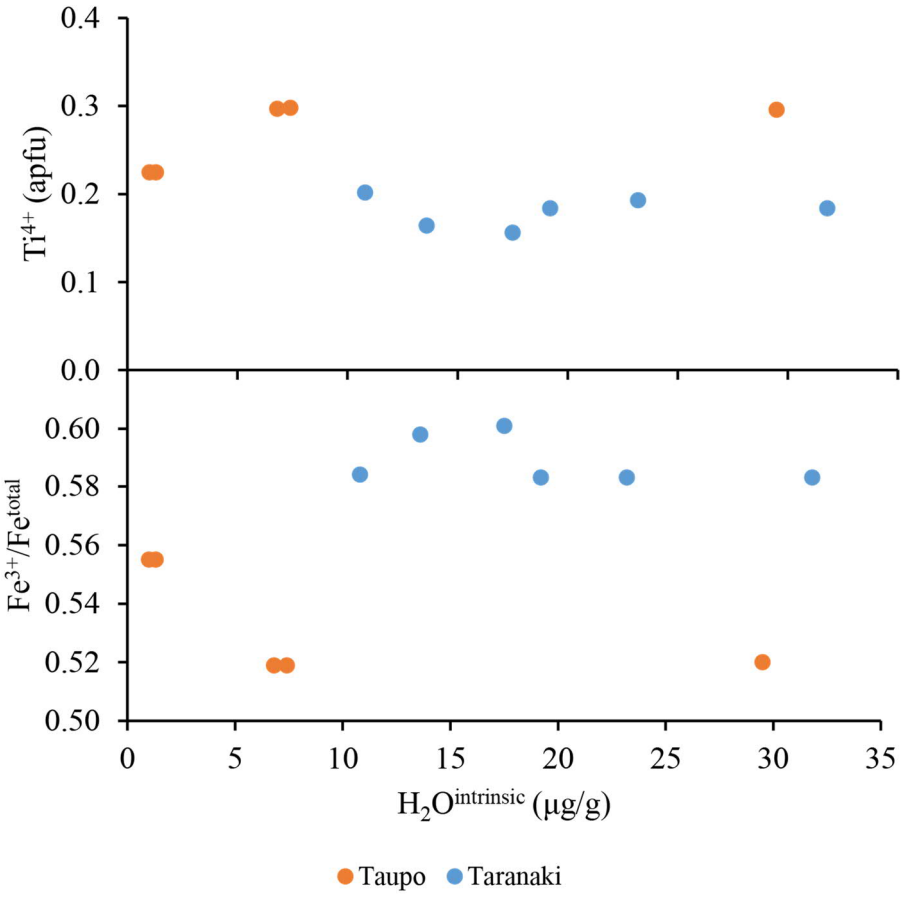

Figure 6.4: Ti-Mag. compositional parameters vs intrinsic H_2O abundance.

There are multiple reasons to believe that the titanomagnetites in this dataset are undersaturated with respect to H. The first reason is that experimentally hydrated Taranaki titanomagnetite contains up to *c.* 200 µg/g H_2O (Chapter 5.5.3). The second reason is that clear variation among grains from the Manganui D member may be diagnostic of post-deposition H loss/gain. Observations of natural clinopyroxenes suggest that crystals deposited in lava flows tend to lose H faster than crystals deposited in tephra (Lloyd et al., 2016), but because i) H diffusion in spinel appears to be slower than in pyroxene (cf. Bromiley et al., 2017; Lloyd et al., 2016) and ii) these titanomagnetites were separated from scoria recovered from the top of the tephra, the scoria itself may be a reworked late-stage eruptive product that was entrained with material derived from Fanthams Peak during the deposition of the Manganui D member. This provides reason to suggest that these sample grains have lost magmatic H. Most of the Taupo titanomagnetites contain significantly less H. They are most likely derived from the nearby rhyolites or ignimbrites of the Taupo Volcanic Zone, whose spinels are similar in major element composition (cf. Brathwaite et al., 2017; Ewart, 1965, 1967;

Shane, 1998; Wilson et al., 2005). Since a majority of the old ignimbrites derived from Taupo are welded (Martin, 1961), they were most likely emplaced at a high initial temperature, and the subsequent cooling interval may have enabled the loss of magmatic H from their titanomagnetites. We note, however, that the younger Oruanui Ignimbrite is unwelded (Wilson, 2001) and was emplaced at lower temperature. Alternative hypotheses for both the Taranaki and Taupo spinels could invoke syn-eruptive H_2O loss driven by either devolatilization of the carrier melt or H_2O undersaturation prior to eruption, e.g. due to the presence of CO_2 in the gas phase (Blundy et al., 2010).

6.6 Conclusions

1. Ion microprobe analysis has enabled the detection and quantification of significant concentrations of structurally bound H in Fe-bearing spinel minerals.
2. Chromites from the Troodos Ophiolite (ultramafic section), Ani-jima, and Mauna Loa have insignificant concentrations of H, which were determined to be at or below background concentrations $\leq$ *c*. 5 μg/g H_2O.
3. Titanomagnetite was observed to contain up to *c*. 30 μg/g H_2O. Based on observations made for spinels recovered from Lake Taupo, these titanomagnetites may have originally contained much more H than shown here.
4. Taranaki titanomagnetites contain at least 10 μg/g H_2O and all sample grains were observed to contain a detectable H signal.
5. Based on our results, H incorporation is likely related to the crystal-chemical behaviour of Fe ± Ti in spinel-group minerals.

6.7 Acknowledgements

The authors would like to thank Mark K. Reagan, Kenichiro Tani, Takashi Sano, Benjamin Swan, Szabolcs Kósik, and Anke Zernack for help with sample characterization, selection, and geologic context. This project was funded by the Royal Society of New Zealand through the Marsden Fund (grant MAU1704 to GFZ).

Chapter 7: Synthesis

7.1 Expanding the utility of chromian spinel as a petrogenetic indicator

Combining experimental petrology with high-precision *in situ* microbeam methods, the "petrogenetic indicator" status of chromian spinel (or natural chromite) may be extended to the interpretation of kinetic processes operating to re-equilibrate chromite prior to and potentially during the eruption of mafic chromite-bearing melts. The compositional sensitivity of this mineral phase to change(s) in the physicochemical state of its carrier melt, especially f_{O_2}, enables the observation and extraction of textural and chemical data that may be interpreted in a oxybarometric context utilizing diffusion modelling. Careful analysis and interpretation of compositional data are necessary to discriminate compositional change due to pre/syn-eruptive magmatic processes and post-depositional alteration or metamorphism.

IHPV experiments have demonstrated the sensitivity of Fe diffusivity to f_{O_2}. Under highly oxidizing conditions, *c.* 2-3 log units above the NNO redox buffer and temperatures between 1150-1200 °C, Fe^{3+}-Al interdiffusion operates to enrich chromite in Fe^{3+}. Thermodynamic and empirical modelling both indicate that the experiments conducted for this study failed to completely equilibrate chromite. Observed Cr concentrations were ubiquitously too high, while Fe^{3+} and Al concentrations were too low, indicating that Cr counter-diffusion had yet to occur prior to experiment termination. Under less oxidizing conditions closer to the NNO redox buffer, little to no diffusion of trivalent cations was observed to have taken place. However, the thermodynamic and empirical models still indicated disequilibrium in the chromites. Thus, we inferred that Fe diffusivity is fugacity-dependent with higher diffusion rates achieved at higher f_{O_2}. In all cases, Fe^{2+}-Mg interdiffusion was able to re-equilibrate chromite Mg# in the smallest chromite grains, as revealed by assessment of $K_D(Fe\text{-}Mg)^{chr\text{-}opx}$.

In natural settings, once removed from a primitive condition, chromite acts as a passive sensor of the physicochemical state of the melt it resides in as long as it remains a liquidus phase. Several processes may operate within the upper mantle and lower crust to alter chromite composition. These include f_{O_2}-insensitive processes such as metasomatism (Birner et al., 2021; Gamal El Dien et al., 2019), but many processes

influence f_{O_2} and thus equilibrium chromite composition. These include the degassing of vapour phases (e.g. Brounce et al., 2017), the hydration of silicate minerals (Tollan and Hermann, 2019), and potentially the fractional crystallization of Fe^{2+}-bearing silicate minerals (Kelley and Cottrell, 2012); although further experimental work is needed to verify a causal link between differentiation and oxidation in natural systems (Cottrell et al., 2020).

In whichever way oxidation is achieved, shallow magmatic systems must adjust with respect to element distribution to re-equilibrate to the new thermodynamic state. This is achieved via the kinetic process of diffusion. While information regarding diffusion in spinel minerals is abundant (e.g. Van Orman and Crispin, 2010), there is little information on how diffusion behaviour varies with system f_{O_2} (Vogt et al., 2015). Our results further demonstrate that compositional re-equilibration is achieved via distinct vectors in compositional space with respect to system f_{O_2}. Naturally occurring chromites exhibit compositional features consistent with oxidation in the absence of pervasive whole-rock alteration (Bailey et al., 1991; Reagan and Meijer, 1984). This precludes a secondary origin for these features, which are observed in multiple settings (Gamal El Dien et al., 2019; Hodel et al., 2020). Additionally, the chromites of the Troodos Massif record high closure temperatures (Dare et al., 2009) bolstering the argument for the magmatic origin of their textures and compositions.

With constraints derived using published diffusivity data for chromian spinel and comprehensive empirical modelling using published compositional data, the compositional textures preserved in chromites sourced from the Troodos Ophiolite are consistent features that developed in less than *c*. 170 years after extraction from a stable petrogenetic condition. That is, pre-eruptive changes of the physicochemical state of the magmatic system that fed portions of the volcanic sequence preserved in the Troodos Massif established a new thermodynamic state that caused stable chromite to incorporate more Al and Fe^{3+}; approaching a composition that would have been in equilibrium with residual melts preserved as pristine volcanic glasses in the same outcrops.

These observations require rapid ascent rates, comparable to those in other geologic settings (Petrelli and Zellmer, 2020), for the Troodos extrusive suite, but further work

will be necessary to place more precise constraint on ascent rates, chronometry, and diffusivity.

Based on our data, no more can be said regarding the diffusivities of the major elements in spinel. While the results, presented in Chapter 4, satisfy the qualitative nature of the first objective of this thesis (Chapter 1.2), little if any quantitative information regarding the dependence of diffusivity on f_{O_2} may be gained from these results.

7.2 Lessons from IHPV experiments performed on basalt from Taranaki Volcano, New Zealand

While not addressed directly in Chapter 5, useful information regarding the generation, ascent, and emission of the Manganui D member of the Manganui Formation may be inferred using the experimental results described in Chapter 5. Briefly, these points are addressed in the next sub-section and draw upon observations made by field geologists as summarized in Chapter 2.2.2.

7.2.1 Liquidus relationships and implications for the emplacement of the Manganui D tephra

Based on the experiments presented here conducted using high-Al basalt recovered from the flanks of Taranaki, spinel is unstable at *c.* 2 kbar and temperatures of 1150-1200 ℃ as f_{O_2} approaches the NNO redox buffer. If f_{O_2} is left unbuffered in the IHPV and the f_{O_2} of the system is allowed to approach a more oxidizing state *c.* 2-3 log units above the NNO buffer under the same pressure-temperature conditions magnetite seeds initially resorb and then stabilize as the melt becomes saturated in spinel. Additionally, no silicate minerals were observed to be present (disregarding quench crystallization) until 1100 ℃ where clinopyroxene and plagioclase feldspar become volumetrically dominant, reaching an inferred volume proportion greater than or equal to 70%. This latter observation is inconsistent with the natural sample material used for the experiments, which is a glass-rich basaltic scoria (Torres-Orozco et al., 2016). Together, these observations imply that i) the liquid that formed the scoria in the Manganui D member was erupted at a temperature greater than 1100 ℃ and ii) the magma storage f_{O_2} condition was more oxidizing than conditions analogous to the NNO buffer.

The compositions of naturally occurring titanomagnetites in the Manganui D member are richer in Ti and poorer in Al and Mg (Damaschke et al., 2017b) than all of the synthetic spinel compositions reported here. This could be an effect of homogenizing a natural rock for a starting material. Natural melts are likely to entrain antecrystic minerals prior to eruption, and there is abundant evidence of this in the lavas sourced from Taranaki, including from Fanthams Peak (D'Mello et al., 2021). If a significant mass of antecrystic minerals are added to a naturally occurring melt and that antecryst-laden magma is erupted, then it would be improper to use the observed bulk composition of the rock to infer petrogenetic aspects of the system pertaining to the genesis of the melt. Thus, based on the equilibrium titanomagnetite compositions reported here, there is likely an abundance of antecrysts included in the scoria of the Manganui D member of the Manganui Formation of Taranaki Volcano; potentially even the titanomagnetites themselves are antecrystic in nature.

7.2.2 Kinetic inferences: Experiment H isotopic signature, magnetite resorption, and silicate mineral growth

The data presented here indicates that the inclusion of $^{2}H_2O$ was not effective in initializing an isotopically distinct sample H signal in the products of the IHPV experiments. This is because H is an extremely mobile element in IHPV systems. When an external source of isotopically distinct H is included in either the pressure medium (as added H_2 gas) or the redox sensor included in each experiment (as normal deionized water), H exchange rapidly occurs between samples, sensors, and the pressure medium to re-equilibrate the H isotopic composition of the system. No significant hydration or dehydration occurred since no mass was gained or lost during any experiment reported here.

Regarding the stability of spinel in basalt, resorption occurred to some degree in all experiments. In relatively oxidizing experiments where f_{O_2} was left unbuffered by the pressure medium, spinel eventually stabilized after a small amount of resorption. Large seed spinels exhibit zonation in BSE images, which indicates that diffusion was ongoing at the termination of the experiment and that complete re-equilibration had not occurred. This condition implies that spinel re-equilibration followed Regime 2 of Liang (2000). Based on this inference, we conclude that the sample spinel compositions near the edges of the large seed grains and those of smaller matrix grains are representative of the

equilibrium composition of spinel for all experiments where spinel did not completely resorb. For chromites in boninite bulk compositions, no resorption textures were observed. Instead, only zonation was observed to be present in some large seed grains. This observation does not change with f_{O_2}. Thus, chromite remains a liquidus phase for every pressure-temperature-f_{O_2} condition imposed in these experiments. It is unclear if some small degree of chromite crystallization occurred at the margins of the seed grains.

Originally, the reason for including spinel seeds was not to detect and infer diffusion information but, rather, to promote the growth of spinel during the IHPV experiments. Since this did not occur the inclusion of seed material is perhaps not suitable for spinel growth. It may be that synthetically oversaturating the starting mixtures in spinel components in the presence of a vapour phase is a better method for synthetic spinel formation in hydrothermal experiments (e.g. Johan et al., 2017).

Quench crystallization is a problem that hampered all experiments conducted at 1200 ℃ and under unbuffered f_{O_2} conditions. Its occurrence indicates that the quench rate achieved in this experiment did not reach the 300 ℃/s achievable using the IHPV quench mechanism (Roux and Lefevre, 1992). Interestingly, the matrices of basaltic samples are commonly observed to contain nano-microscopic star-shaped oxide minerals that are surrounded by spear tip-shaped silicate minerals in an epitaxial relationship. In the areas around large seed spinels these oxide cores are absent, and only silicate minerals are observed to grow. Thus, there is a difference in the energetics of crystal formation during quench between these two melt mediums. In the melt immediately surrounding seed spinel additional oxide mineral precipitation is likely limited to the nearby spinel grain boundary, and silicate mineral growth proceeds as the silicate liquidus is reached and melt temperature remains above the glass transition temperature. Meanwhile, in the matrix, oxide precipitation occurs since the melt is saturated in spinel and no nearby spinel is available to host any additional growth. These small oxides are then overgrown quickly by silicates that nucleate at the oxide-melt boundary. These systematics may have implications for the growth and formation of naturally occurring nano/microlitic phases during natural quenching processes.

Similar features were not observed in boninitic bulk compositions. In boninite samples, the only petrographic evidence for quench crystallization is the presence of bright (Fe-rich) caps at the apices of orthopyroxene grains in BSE images. However subtle these

features are, their formation had an observable effect on the glass compositions recovered from these samples.

7.3 The detection or non-detection of H in Fe-bearing spinel via ion microprobe

These two sub-sections below respectively address the second and third objectives of this thesis and summarize the results and discussion sections of Chapters 5 and 6.

7.3.1 Synthetic spinels

The solubility of H in chromite is likely low due to limitations placed on known incorporation mechanisms involving Mg-Al disorder (Bromiley et al., 2010; Lenaz et al., 2008) by Cr, which strongly prefers octahedral coordination (e.g. Bosi and Andreozzi, 2017). Seed chromites included in the IHPV experiments were partially re-equilibrated under hydrous conditions. Yet, a detectable OH signal was not achieved during SCAPS-SIMS analysis. Melt H_2O concentrations were likely enriched in each boninite sample due to the crystallization of orthopyroxene, but the experiments described here were not saturated in vapour upon termination. Under more hydrous conditions, some H incorporation may still occur. However, based on the signal intensities reported here it is unlikely that chromite can incorporate a significant concentration of H.

The same cannot be said of the Fe-rich spinels. In fact, the only detectable $^{16}O^{2}H$ and $^{16}O^{1}H$ signals observed among the synthetic spinels were observed in Ti-bearing magnetite. Using recently obtained RSF information, two spinel grains from one sample contain as much as *c.* 200 μg/g H_2O based on integrated $[^{16}O^{2}H+^{16}O^{1}H]/^{18}O$ signal intensities.

The differences in crystal chemistry between chromite and Fe-rich spinels like magnetite and titanomagnetite may be the enabling factor behind H solubility in the synthetic spinels produced using hydrous basalt. Multiple electronic processes occur to vary the oxidation states of tetra- and octahedrally coordinated Fe in spinels including electron hopping and electron exchange, the latter of which is related to the incorporation of Ti^{4+}.

Using observed signal intensities and RSFs calculated for each sample pit, the partition coefficient for H_2O between spinel and melt ($D_{H_2O}^{Ti\ Mag.-Melt}$) was calculated to be 0.0045 ± 0.0003 This recovered partition coefficient is intermediate between olivine and garnet, which partition less H_2O, and the pyroxene minerals, which partition more H_2O under H_2O under-saturated conditions (Figure 7.1, Aubaud et al., 2004; Hauri et al., 2006; Koga et al., 2003; Novella et al., 2014; Tenner et al., 2009).

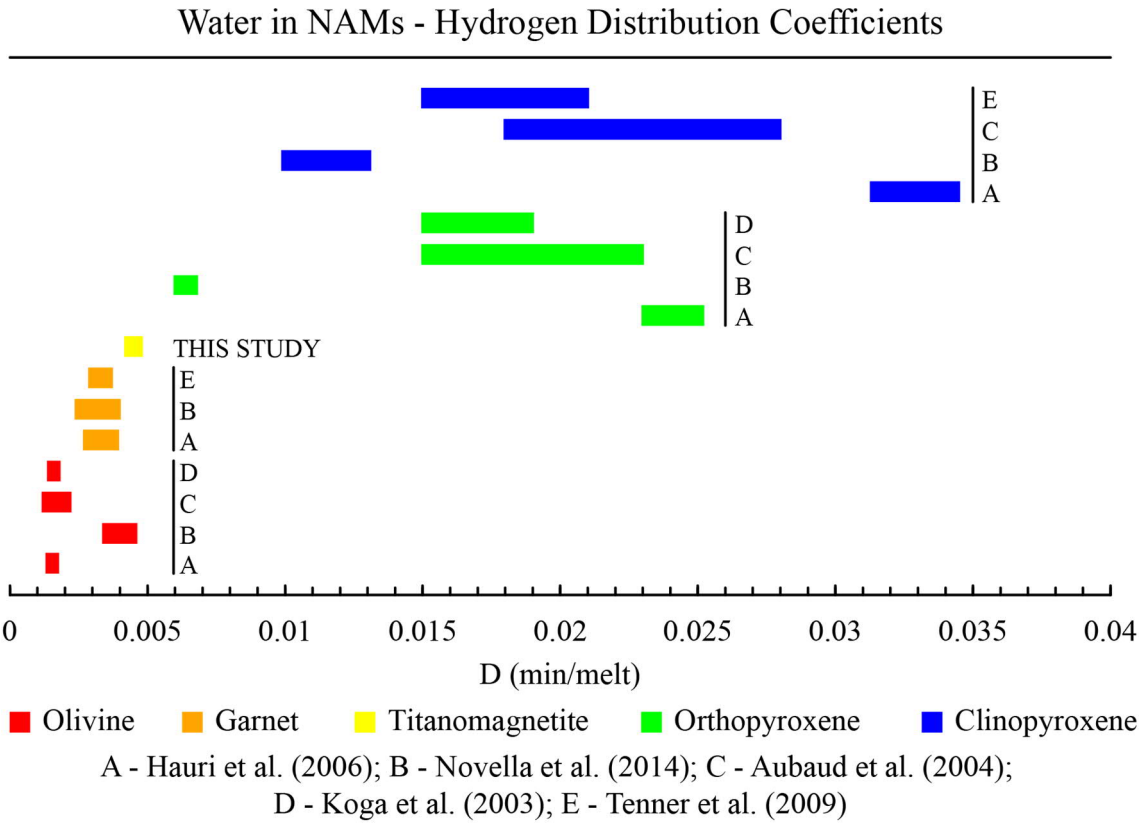

Figure 7.1: H distribution coefficients for multiple NAMs including new data on titanomagnetite described here. Bars for each sample represent the uncertainty provided by the authors or calculated, in the case of titanomagnetite. Data sources are: A = experiment B366, B = average D values, C = average D values, D = experiment B13, E = experiment M372.

7.3.2 Natural spinels

Several natural spinels from distinct tectonic settings were analysed via ion microprobe using routine analysis conditions in order to investigate their OH concentrations. The geologic domains sampled for their spinels included ocean islands (Hawaii, chromite only), ocean island arcs (Ani-jima, chromite only), continental island arc and backarc settings (Taupo and Taranaki volcanoes, titanomagnetite only), and ophiolitic ultramafic sections (Troodos Ophiolite, Cyprus, chromite only).

Of these natural samples, only titanomagnetite from Taranaki and Taupo volcanoes were observed to conclusively contain an intrinsic OH signal. For all chromian spinels, observed OH signal intensities were too low to confidently distinguish background from intrinsic OH signals. Thus, natural chromites were not observed to contain a significant amount of H_2O.

It is likely that the titanomagnetites sampled for this study lost H upon deposition. Titanomagnetite from Taupo were sampled at the shore of Lake Taupo near Kinloch and were most likely derived from the rhyolite cliffs surrounding the bay here. The units immediately surrounding this locality are Taupo Group rhyolite flow/fall deposits and crystal rich lavas, Ongaroto Group rhyolite lavas, and minor volumes of Acacia Bay Formation basaltic scoria are also present. Local deposits of the Oruanui Ignimbrite are located further away from the shore relative to the other units mentioned. If the spinels were derived from the nearby Taupo ± Oruanui Ignimbrites, they could have lost their magmatic H concentrations during cooling, even though these ignimbrites are not welded. The cooling histories of the rhyolites are uncertain. Regarding Taranaki titanomagnetites, the phenocrysts studied here exhibit a ubiquitously low OH signal intensity compared to synthetic magnetite/titanomagnetite described above. Using the partition coefficient given above, calculated melt H_2O concentrations for the Manganui D scoria range between 0.22-0.49 wt.%, which is nowhere near high enough to explain the high sample vesicularity and the explosive nature of the eruptions derived from Fanthams Peak (Torres-Orozco et al., 2016).

The Taranaki titanomagnetites are visually homogeneous with few silicate mineral inclusions and no nano-micro inclusions visible under high-resolution SEM imaging. There are no ilmenite exsolution lamellae present, which indicates that the magma that generated the Manganui D member rapidly ascended prior to eruption (Turner et al., 2008b). Since there is significant variation between titanomagnetites recovered from separate locations along the flanks of Taranaki Volcano, we propose that the scorias sampled at these locations experienced slightly different thermal histories upon deposition, which led to distinct degrees of H-loss in their titanomagnetites. Alternatively, the titanomagnetites may be antecrystic and have naturally low magmatic H, reflecting a low water fugacity within the plutonic section underlying Taranaki volcano.

Regardless, the SIMS analysis of titanomagnetites presented here demonstrates conclusively that H is incorporated into Fe-rich spinel minerals under magmatic conditions and that SIMS is one suitable method of inferring H concentrations in these minerals.

7.4 Expanding the utility of Fe-rich spinel as a petrogenetic indicator

H is more soluble in Fe-bearing spinel than it is in natural $MgAl_2O_4$ spinel, and the preliminary data presented here demonstrate that the solubility of H in Fe-rich spinels is of the same order of magnitude as nominally anhydrous silicates like olivine, plagioclase feldspar, and pyroxene. Based on available diffusion data, which were inferred using non-stoichiometric spinel samples (Bromiley et al., 2017), magmatic H concentrations may be better be preserved in these oxides than in co-existing silicate phases upon eruption (cf. Lloyd et al., 2016). If this is true, Fe-rich spinel like titanomagnetite may in the future become a valuable geohygrometer for the Earth Sciences. Considering its status as a late-forming mineral and a component of established oxybarometers (e.g. Buddington and Lindsley, 1964), it is apt to consider spinel as a petrogenetic indicator for late-stage or evolved magmatic systems in an equivalent sense as chromian spinel is useful for gaining information on the primitive states of magmatic systems.

Chapter 8: Conclusions and Outlook

8.1 Conclusions of this thesis

- Fe^{3+}-Al interdiffusion operates to equilibrate spinel Fe^{2+}/Fe^{3+} over timescales that are much shorter than required to equilibrate Cr concentration. The diffusivity of Fe^{3+} is highly sensitive to the f_{O_2} of the system as is equilibrium Fe^{2+}/Fe^{3+}.
- Based on both thermodynamic and empirical modelling, no equilibrium condition was achieved with respect to the major trivalent cations in spinel during IHPV experiments.
- Spinel Fe^{2+} equilibrates over much faster timescales as evidenced by the attainment of equilibrium $K_D(Fe\text{-}Mg)^{opx\text{-}chrm}$ during IHPV experiments, and the results presented here replicate published Fe diffusivities in spinel.
- Natural chromites sourced from relatively fresh extrusive rocks preserve compositional traits consistent with partial re-equilibration prior to eruption. In fact, the concentrations of the major elements from core to rim imply partial diffusive re-equilibration of the major trivalent cations consistent with pre-eruptive oxidation of the system.
- Samples sourced from the extrusive sequence of the Troodos Ophiolite (Cyprus) were shown to be analogous to the IHPV experimental products presented here; reaching partial equilibrium (for distinct components) of the orthopyroxene-chromite-melt system.
- Simple diffusion arguments suggest that, for compositional heterogeneity to be preserved as chemical zonation, oxidation and eruption of the Troodos extrusives must have occurred within *c*. 200 years of each other.
- Chromite does not partition significant concentrations of H. That is, the partition coefficient of H between chromite and melt is inferred to be extremely low based on ion microprobe experiments conducted using synthetic and natural chromite minerals.
- Fe-rich spinels from the same IHPV experiments were able to produce detectable and quantifiable OH signals. H_2O partition coefficients were calculated to be *c*. 0.004-0.005.
- Natural titanomagnetites were observed to contain up to *c*. 30 μg/g H_2O.

- Based on experimental and petrologic inference, the solubility of H in Fe-rich spinel is comparable to nominally anhydrous silicate minerals. The natural titanomagnetites analysed here likely lost their magmatic H concentrations after deposition.

8.2 Future research directions

8.2.1 Diffusion of trivalent cations in chromite as a function of oxygen fugacity

In light of the distinct behaviour observed between samples produced by the IHPV under buffered versus unbuffered f_{O_2} conditions, I propose to conduct experiments to investigate the diffusivity of Fe in spinel as a function of system f_{O_2} with focus on the trivalent cations Cr^{3+}, Al, and Fe^{3+}. Experiments should be conducted using homogeneous natural spinels representing a broad compositional range in Mg# and in Cr# space. Internally heated pressure vessels and atmospheric gas-mixing furnaces can be used to perform paired low-high pressure experiments with precise control of f_{O_2} enabled. Sample preparation may utilize thin film techniques (e.g. Vogt et al., 2015) or couple anneal methods (e.g. Suzuki et al., 2008).

8.2.2 The synthesis of spinel from silicate melts and immiscible liquids

Matveev and Ballhaus (2002) showed that spinel efficiently nucleates at the boundary between melt and fluid phases. In an earlier publication, Ballhaus (1998) explored similar systematics using immiscible melt-melt mixtures and produced similar results. Finally, Johan et al. (2017) claimed success in growing massive (mm-scale) chromites using COH fluid mixtures. Chemically, immiscible liquid, be it fluid or melt, likely provides a substrate where spinel solubility is negligible relative to the coexisting silicate melt phase.

The role of C in this process was expanded upon only by Johan et al. (2017). To date, no experiments have been performed to systematically study the effect of variable fluid composition (OH ± C/S/Cl, etc.) on the energetics of spinel nucleation and growth. It would be valuable to do so since fostering the growth of large spinel grains is an experimental challenge (Elizabeth Cottrell, personal comm., 2020). Using a high-pressure piston-cylinder apparatus and solid redox buffers (Matjuschkin et al., 2015),

the study of chromite growth at pressures equivalent to those of the upper mantle may be investigated thoroughly.

8.2.3 The synthesis of H-free spinel for SIMS analysis

One of the problems encountered during the preparation of this thesis was the lack of a standard with confirmed zero H. The reason such a standard is so valuable is that it may be used to better quantify the contribution of background H to the observed signal intensity. Unfortunately, since OH sputtering appears to be density dependent, zero standards must be made for spinels representing a large range of densities.

Using the method of Bosi et al. (2008), synthetic stoichiometric spinels may be synthesized under controlled gas flux without the use of H_2 gas as a redox buffer. This method may be the best way to synthesize H-free single crystals of spinel along a compositional range. These spinels may then be used as either zero standards or as a substrate for implantation.

Once implanted or left without H, the spinel minerals should be systematically studied using ion microprobe methods in order to assess spinel minerals for their matrix effects (Deline et al., 1978), preferably while varying vacuum quality to assess for the influence of variable background H concentration (after Magee, 1983). Once this has been achieved, high-precision analysis of H in spinel may be achieved using routine SIMS methods.

8.2.4 The incorporation of H into Fe-rich spinel

Future experimental work must investigate the incorporation of H into Fe-rich spinel directly. The best way to do this is by synthesizing large spinel minerals in melt under controlled f_{O_2} conditions to set spinel Fe^{2+}/Fe^{3+} and Ti^{4+} concentrations. Higher melt H_2O concentrations (than imposed here) are suggested so that the solubility of H in spinel may be known and more partitioning data may be gathered.

Ideally, the spinel crystals would be grown from the melts they are in without abundant silicate phases present. In order to achieve this, natural samples should be avoided and compositionally simple melts should be synthesized using COH fluid mixtures in order to maximize the potential for spinel nucleation and growth. Of course, these

experiments should utilize pressure vessels (either IHPVs or cold-seal pressure vessels) in order to allow for significant concentrations of melt H_2O to be achieved.

References

Allan, J.F., Sack, R.O., Batiza, R., 1988. Cr-rich spinels as petrogenetic indicators; MORB-type lavas from the Lamont seamount chain, eastern Pacific. American Mineralogist 73, 741-753.

Alloway, B., Neall, V.E., Vucetich, C.G., 1995. Late Quaternary (post 28,000 year B.P.) tephrostratigraphy of northeast and central Taranaki, New Zealand. Journal of the Royal Society of New Zealand 25, 385-458.

Almeev, R.R., Holtz, F., Koepke, J.r., Parat, F., Botcharnikov, R.E., 2007. The effect of H_2O on olivine crystallization in MORB: Experimental calibration at 200 MPa. American Mineralogist 92, 670-674.

Arai, S., 1992. Chemistry of chromian spinel in volcanic rocks as a potential guide to magma chemistry. Mineralogical Magazine 56, 173-184.

Arai, S., 1994a. Characterization of spinel peridotites by olivine-spinel compositional relationships: Review and interpretation. Chemical Geology 113, 191-204.

Arai, S., 1994b. Compositional variation of olivine-chromian spinel in Mg-rich magmas as a guide to their residual spinel peridotites. Journal of Volcanology and Geothermal Research 59, 279-293.

Arai, S., 1997. Origin of podiform chromitites. Journal of Asian Earth Sciences 15, 303-310.

Arai, S., Yurimoto, H., 1994. Podiform chromitites of the Tari-Misaka ultramafic complex, southwestern Japan, as mantle-melt interaction products. Economic Geology 89, 1279-1288.

Arai, S., Yurimoto, H., 1995. Possible sub-arc origin of podiform chromitites. Isl. Arc 4, 104-111.

Arganda-Carreras, I., Kaynig, V., Rueden, C., Eliceiri, K.W., Schindelin, J., Cardona, A., Sebastian Seung, H., 2017. Trainable Weka Segmentation: a machine learning tool for microscopy pixel classification. Bioinformatics 33, 2424-2426.

Ariskin, A.A., Barmina, G.S., 1999. An empirical model for the calculation of spinel-melt equilibria in mafic igneous systems at atmospheric pressure: 2. Fe-Ti oxides. Contributions to Mineralogy and Petrology 134, 251-263.

Ariskin, A.A., Nikolaev, G.S., 1996. An empirical model for the calculation of spinel melt equilibria in mafic igneous systems at atmospheric pressure .1. Chromian spinels. Contributions to Mineralogy and Petrology 123, 282-292.

Aubaud, C., Withers, A.C., Hirschmann, M.M., Guan, Y., Leshin, L.A., Mackwell, S.J., Bell, D.R., 2007. Intercalibration of FTIR and SIMS for hydrogen measurements in glasses and nominally anhydrous minerals. American Mineralogist 92, 811-828.

Bailey, D.G., Langdon, G.S., Malpas, J., Robinson, P.T., 1991. Ultramafic and related lavas from the Margi area, Troodos ophiolite, in: Gibson, I.L., Malpas, J., Robinson, P.T., Xenophontos, C. (Eds.), Cyprus Crustal Study Project: Initial Report, Holes Cy-1 and 1a. Geological Survey of Canada, pp. 187-202.

Ballhaus, C., 1998. Origin of podiform chromite deposits by magma mingling. Earth and Planetary Science Letters 156, 185-193.

Ballhaus, C., Berry, R.F., Green, D.H., 1991. High pressure experimental calibration of the olivine-orthopyroxene-spinel oxygen geobarometer: implications for the oxidation state of the upper mantle. Contributions to Mineralogy and Petrology 107, 27-40.

Barnes, S.J., Roeder, P.L., 2001. The Range of Spinel Compositions in Terrestrial Mafic and Ultramafic Rocks. Journal of Petrology 42, 2279-2302.

Barrer, R.M., Bartholomew, R.F., Rees, L.V.C., 1963. Ion exchange in porous crystals: Part II. The relationship between self- and exchange-diffusion coefficients. Journal of Physics and Chemistry of Solids 24, 309-317.

Beattie, P., Ford, C., Russell, D., 1991. Partition coefficients for olivine-melt and orthopyroxene-melt systems. Contributions to Mineralogy and Petrology 109, 212-224.

Bédard, J.H., 1999. Petrogenesis of Boninites from the Betts Cove Ophiolite, Newfoundland, Canada: Identification of Subducted Source Components. Journal of Petrology 40, 1853-1889.

Behrens, H., Müller, G., 1995. An infrared spectroscopic study of hydrogen feldspar ($HA1Si_3O_8$). Mineralogical Magazine 59, 15-24.

Bell, D.R., Ihinger, P.D., Rossman, G.R., 1995. Quantitative analysis of trace OH in garnet and pyroxenes. American Mineralogist 80, 465-474.

Bell, D.R., Rossman, G.R., 1992. Water in Earth's mantle - The role of nominally anhydrous minerals. Science 255, 1391-1397.

Benninghoven, A., Rüdenauer, F.G., Werner, H.W., 1987. Secondary Ion Mass Spectrometry: Basic Concepts, Instrumental Aspects, Applications, and Trends. Wiley, New York.

Beran, A., 1986. A model of water allocation in alkali feldspar, derived from infrared-spectroscopic investigations. Phys. Chem. Miner. 13, 306-310.

Beran, A., 1987. OH groups in nominally anhydrous framework structures: An infrared spectroscopic investigation of danburite and labradorite. Phys. Chem. Miner. 14, 441-445.

Beran, A., Zemann, J., 1986. The pleochroism of a gem-quality enstatite in the region of the OH stretching frequency, with a stereochemical interpretation. Tschermaks Mineralogische und Petrographische Mitteilungen 35, 19-25.

Birner, S.K., Cottrell, E., Warren, J.M., Kelley, K.A., Davis, F.A., 2018. Peridotites and basalts reveal broad congruence between two independent records of mantle fO_2 despite local redox heterogeneity. Earth and Planetary Science Letters 494, 172-189.

Birner, S.K., Cottrell, E., Warren, J.M., Kelley, K.A., Davis, F.A., 2021. Melt addition to mid-ocean ridge peridotites increases spinel Cr# with no significant effect on recorded oxygen fugacity. Earth and Planetary Science Letters 566, 116951.

Bishopp, D.W., 1952. The Troödos Massif, Cyprus. Nature 169, 489-490.

Bloomer, S.H., Hawkins, J.W., 1987. Petrology and geochemistry of boninite series volcanic rocks from the Mariana trench. Contributions to Mineralogy and Petrology 97, 361-377.

Blundy, J., Cashman, K., 2005. Rapid decompression-driven crystallization recorded by melt inclusions from Mount St. Helens volcano. Geology 33, 793-796.

Blundy, J., Cashman, K.V., Rust, A., Witham, F., 2010. A case for CO_2-rich arc magmas. Earth and Planetary Science Letters 290, 289-301.

Bosi, F., Andreozzi, G.B., 2017. Chromium influence on Mg-Al intracrystalline exchange in spinels and geothermometric implications. American Mineralogist 102, 333-340.

Bosi, F., Hålenius, U., Skogby, H., 2008. Stoichiometry of synthetic ulvöspinel single crystals. American Mineralogist 93, 1312-1316.

Bosi, F., Hålenius, U., Skogby, H., 2009. Crystal chemistry of the magnetite-ulvöspinel series. American Mineralogist 94, 181-189.

Brandon, A.D., Draper, D.S., 1996. Constraints on the origin of the oxidation state of mantle overlying subduction zones: An example from Simcoe, Washington, USA. Geochimica et Cosmochimica Acta 60, 1739-1749.

Brathwaite, R.L., Gazley, M.F., Christie, A.B., 2017. Provenance of titanomagnetite in ironsands on the west coast of the North Island, New Zealand. Journal of Geochemical Exploration 178, 23-34.

Bromiley, G.D., Brooke, J., Kohn, S.C., 2017. Hydrogen and deuterium diffusion in non-stoichiometric spinel. High Pressure Research 37, 360-376.

Bromiley, G.D., Nestola, F., Redfern, S.A.T., Zhang, M., 2010. Water incorporation in synthetic and natural $MgAl_2O_4$ spinel. Geochimica et Cosmochimica Acta 74, 705-718.

Brounce, M., Reagan, M.K., Coulthard Jr., D.A., Kelley, K.A., Cottrell, E., 2019. The oxidation states of iron and volatile compositions of Expedition 352 glasses, Goldschmidt 2019, Barcelona, Spain.

Brounce, M., Stolper, E., Eiler, J., 2017. Redox variations in Mauna Kea lavas, the oxygen fugacity of the Hawaiian plume, and the role of volcanic gases in Earth's oxygenation. Proceedings of the National Academy of Sciences 114, 8997-9002.

Buddington, A.F., Lindsley, D.H., 1964. Iron-Titanium Oxide Minerals and Synthetic Equivalents. Journal of Petrology 5, 310-357.

Burnham, C.W., 1979. The importance of volatile constituents, in: Yoder, H.S., Jr. (Ed.), The evolution of the igneous rocks. Princeton University Press, Princeton, New Jersey, pp. 439-482.

Cameron, W.E., 1985. Petrology and origin of primitive lavas from the Troodos ophiolite, Cyprus. Contributions to Mineralogy and Petrology 89, 239-255.

Candela, P.A., 1997. A Review of Shallow, Ore-related Granites: Textures, Volatiles, and Ore Metals. Journal of Petrology 38, 1619-1633.

Cashman, K., Blundy, J., 2000. Degassing and crystallization of ascending andesite and dacite. Philosophical Transactions of the Royal Society of London. Series A: Mathematical, Physical and Engineering Sciences 358, 1487-1513.

Chou, I.-M., 1986. Permeability of precious metals to hydrogen at 2kb total pressure and elevated temperatures. American Journal of Science 286, 638-658.

Chou, I.M., Eugster, H.P., Berens, P., Weare, J.H., 1978. Diffusion of hydrogen through platinum membranes at high pressures and temperatures. Geochimica et Cosmochimica Acta 42, 281-288.

Cottrell, E., Birner, S., Brounce, M., Davis, F.A., Waters, L.E., Kelley, K.A., 2020. Oxygen Fugacity Across Tectonic Settings, in: Neuville, D.R., Moretti, R. (Eds.), AGU Geophysical Monograph Redox variables and mechanisms in magmatism and volcanism. Wiley.

Couch, S., Sparks, R.S.J., Carroll, M.R., 2001. Mineral disequilibrium in lavas explained by convective self-mixing in open magma chambers. Nature 411, 1037-1039.

Coulthard Jr, D.A., Reagan, M.K., Shimizu, K., Bindeman, I.N., Brounce, M., Almeev, R.R., Ryan, J., Chapman, T., Shervais, J., Pearce, J.A., 2021. Magma Source Evolution Following Subduction Initiation: Evidence From the Element Concentrations, Stable Isotope Ratios, and Water Contents of Volcanic Glasses From the Bonin Forearc (IODP Expedition 352). Geochemistry, Geophysics, Geosystems 22, e2020GC009054.

Crank, J., 1975. The Mathematics of Diffusion. Oxford University Press, London.

Cronin, S.J., Wallace, R.C., Neall, V.E., 1996. Sourcing and identifying andesitic tephras using major oxide titanomagnetite and hornblende chemistry, Egmont volcano and Tongariro Volcanic Centre, New Zealand. Bulletin of Volcanology 58, 33-40.

D'Mello, N.G., Zellmer, G.F., Negrini, M., Kereszturi, G., Procter, J., Stewart, R., Prior, D., Usuki, M., Iizuka, Y., 2021. Deciphering magma storage and ascent processes of Taranaki, New Zealand, from the complexity of amphibole breakdown textures. Lithos 398-399, 106264.

Damaschke, M., Cronin, S.J., Holt, K.A., Bebbington, M.S., Hogg, A.G., 2017a. A 30,000 yr high-precision eruption history for the andesitic Mt. Taranaki, North Island, New Zealand. Quaternary Research 87, 1-23.

Damaschke, M., Cronin, S.J., Torres-Orozco, R., Wallace, R.C., 2017b. Unifying tephrostratigraphic approaches to redefine major Holocene marker tephras, Mt. Taranaki, New Zealand. Journal of Volcanology and Geothermal Research 337, 29-43.

Dare, S.A.S., Pearce, J.A., McDonald, I., Styles, M.T., 2009. Tectonic discrimination of peridotites using fO_2–Cr# and Ga–Ti–Fe^{III} systematics in chrome–spinel. Chemical Geology 261, 199-216.

Darken, L., 1948. Diffusion, mobility and their interrelation through free energy in binary metallic systems. Trans. Aime 175, 184-201.

Davis, F.A., Cottrell, E., 2018. Experimental investigation of basalt and peridotite oxybarometers: Implications for spinel thermodynamic models and Fe^{3+}

compatibility during generation of upper mantle melts. American Mineralogist 103, 1056-1067.

Deer, W., Howie, R., Zussman, J., 1992. An Introduction to the Rock-Forming Minerals. Longman Scientific and Technical, Essex.

Deline, V.R., Katz, W., Evans Jr., C.A., Williams, P., 1978. Mechanism of the SIMS matrix effect. Applied Physics Letters 33, 832-835.

DeMets, C., Gordon, R.G., Argus, D.F., 2010. Geologically current plate motions. Geophysical Journal International 181, 1-80.

Deschamps, A., Lallemand, S., 2002. The West Philippine Basin: An Eocene to early Oligocene back arc basin opened between two opposed subduction zones. Journal of Geophysical Research: Solid Earth 107, EPM 1-1-EPM 1-24.

Deschamps, A., Monié, P., Lallemand, S., Hsu, S.K., Yeh, K.Y., 2000. Evidence for Early Cretaceous oceanic crust trapped in the Philippine Sea Plate. Earth and Planetary Science Letters 179, 503-516.

Dick, H.J.B., Bullen, T., 1984. Chromian spinel as a petrogenetic indicator in abyssal and alpine-type peridotites and spatially associated lavas. Contributions to Mineralogy and Petrology 86, 54-76.

Dilek, Y., Thy, P., 2009. Island arc tholeiite to boninitic melt evolution of the Cretaceous Kizildag (Turkey) ophiolite: Model for multi-stage early arc–forearc magmatism in Tethyan subduction factories. Lithos 113, 68-87.

Droop, G.T.R., 1987. A general equation for estimating Fe^{3+} concentrations in ferromagnesian silicates and oxides from microprobe analyses, using stoichiometric criteria. Mineralogical Magazine 51, 431-435.

Edwards, S.J., Pearce, J.A., Freeman, J., 2000. New insights concerning the influence of water during the formation of podiform chromitite. Geological Society of America Special Papers 349, 139-148.

Evans, K.A., Elburg, M.A., Kamenetsky, V.S., 2012. Oxidation state of subarc mantle. Geology 40, 783-786.

Ewart, A., 1965. Mineralogy and Petrogenesis of the Whakamaru Ignimbrite in the Maraetai area of the Taupo volcanic zone, New Zealand. New Zealand Journal of Geology and Geophysics 8, 611-679.

Ewart, A., 1967. Pyroxene and magnetite phenocrysts from the Taupo quaternary rhyolitic pumice deposits, New Zealand. Mineralogical Magazine and Journal of the Mineralogical Society 36, 180-194.

Falloon, T.J., Malahoff, A., Zonenshaina, L.P., Bogdanova, Y., 1992. Petrology and geochemistry of back-arc basin basalts from Lau Basin spreading ridges at 15°, 18° and 19°S. Mineralogy and Petrology 47, 1-35.

Feig, S.T., Koepke, J., Snow, J.E., 2006. Effect of water on tholeiitic basalt phase equilibria: an experimental study under oxidizing conditions. Contributions to Mineralogy and Petrology 152, 611-638.

Fisk, M.R., 1986. Basalt magma interaction with harzburgite and the formation of high-magnesium andesites. Geophysical Research Letters 13, 467-470.

Fisk, M.R., Bence, A.E., 1980. Experimental crystallization of chrome spinel in FAMOUS basalt 527-1-1. Earth and Planetary Science Letters 48, 111-123.

Flower, M.F.J., Levine, H.M., 1987. Petrogenesis of a tholeiite-boninite sequence from Ayios Mamas, Troodos ophiolite: evidence for splitting of a volcanic arc? Contributions to Mineralogy and Petrology 97, 509-524.

Ford, C., Russell, D., Craven, J., Fisk, M., 1983. Olivine-liquid equilibria: temperature, pressure and composition dependence of the crystal/liquid cation partition coefficients for Mg, Fe^{2+}, Ca and Mn. Journal of Petrology 24, 256-266.

Frost, B.R., 1991. Introduction to oxygen fugacity and its petrologic importance. Reviews in Mineralogy and Geochemistry 25, 1-9.

Fryer, P., 1995. Geology of the Mariana Trough, in: Taylor, B. (Ed.), Backarc Basins: Tectonics and Magmatism. Springer US, Boston, MA, pp. 237-279.

Fukatsu, N., Kurita, N., Shiga, H., Murai, Y., Ohashi, T., 2002. Incorporation of hydrogen into magnesium aluminate spinel. Solid State Ionics 152-153, 809-817.

Gamal El Dien, H., Arai, S., Doucet, L.-S., Li, Z.-X., Kil, Y., Fougerouse, D., Reddy, S.M., Saxey, D.W., Hamdy, M., 2019. Cr-spinel records metasomatism not petrogenesis of mantle rocks. Nature Communications 10, 5103.

Gass, I.G., 1958. Ultrabasic Pillow Lavas from Cyprus. Geological Magazine 95, 241-251.

Gass, I.G., 1968. Is the Troodos Massif of Cyprus a Fragment of Mesozoic Ocean Floor? Nature 220, 39-42.

Gass, I.G., Masson-Smith, D., 1963. The geology and gravity anomalies of the troodos massif, cyprus. Philosophical Transactions of the Royal Society of London. Series A, Mathematical and Physical Sciences 255, 417-467.

Gass, I.G., Neary, C.R., Plant, J., Robertson, A.H.F., Simonian, K.O., Smewing, J.D., Spooner, E.T.C., Wilson, R.A.M., 1975. Comments on “the troodos ophiolitic complex was probably formed in an island arc”, by A. Miyashiro and subsequent correspondence by A. Hynes and A. Miyashiro. Earth and Planetary Science Letters 25, 236-238.

Gavrilenko, M., Herzberg, C., Vidito, C., Carr, M.J., Tenner, T., Ozerov, A., 2016. A Calcium-in-Olivine Geohygrometer and its Application to Subduction Zone Magmatism. Journal of Petrology 57, 1811-1832.

Gervilla, F., Asta, M.P., Fanlo, l., Grolimund, D., Ferreira-Sánchez, D., Samson, V.A., Hunziker, D., Colas, V., González-Jiménez, J.M., Kerestedjian, T.N., Sergeeva, I., 2019. Diffusion pathways of Fe^{2+} and Fe^{3+} during the formation of ferrian chromite: a µXANES study. Contributions to Mineralogy and Petrology 174, 65.

Ghiorso, M.S., Sack, R.O., 1995. Chemical mass transfer in magmatic processes IV. A revised and internally consistent thermodynamic model for the interpolation and extrapolation of liquid-solid equilibria in magmatic systems at elevated temperatures and pressures. Contributions to Mineralogy and Petrology 119, 197-212.

Golowin, R., Portnyagin, M., Hoernle, K., Sobolev, A., Kuzmin, D., Werner, R., 2017. The role and conditions of second-stage mantle melting in the generation of low-

Ti tholeiites and boninites: the case of the Manihiki Plateau and the Troodos ophiolite. Contributions to Mineralogy and Petrology 172, 104.

Gualda, G.A., Ghiorso, M.S., Lemons, R.V., Carley, T.L., 2012. Rhyolite-MELTS: a modified calibration of MELTS optimized for silica-rich, fluid-bearing magmatic systems. Journal of Petrology 53, 875-890.

Haggerty, S.E., 1995. Upper mantle mineralogy. Journal of Geodynamics 20, 331-364.

Halmer, M.M., 2006. Limitations of FTIR Spectroscopy for Detection of Water in Spinel Group Minerals, When $^{IV}Fe^{2+}$ is Incorporated into the Crystal Structure. Spectroscopy Letters 39, 181-186.

Hamada, M., Fujii, T., 2008. Experimental constraints on the effects of pressure and H_2O on the fractional crystallization of high-Mg island arc basalt. Contributions to Mineralogy and Petrology 155, 767-790.

Hamada, M., Ushioda, M., Fujii, T., Takahashi, E., 2013. Hydrogen concentration in plagioclase as a hygrometer of arc basaltic melts: Approaches from melt inclusion analyses and hydrous melting experiments. Earth and Planetary Science Letters 365, 253-262.

Hanson, B., Jones, J.H., 1998. The systematics of Cr^{3+} and Cr^{2+} partitioning between olivine and liquid in the presence of spinel. American Mineralogist 83, 669-684.

Hauri, E.H., Gaetani, G.A., Green, T.H., 2006. Partitioning of water during melting of the Earth's upper mantle at H_2O-undersaturated conditions. Earth and Planetary Science Letters 248, 715-734.

Hercule, S., Ingrin, J., 1999. Hydrogen in diopside: Diffusion, kinetics of extraction-incorporation, and solubility, American Mineralogist, p. 1577.

Hickey-Vargas, R., 1998. Origin of the Indian Ocean-type isotopic signature in basalts from Philippine Sea plate spreading centers: An assessment of local versus large-scale processes. Journal of Geophysical Research: Solid Earth 103, 20963-20979.

Hickey-Vargas, R., 2005. Basalt and tonalite from the Amami Plateau, northern West Philippine Basin: New Early Cretaceous ages and geochemical results, and their petrologic and tectonic implications. Isl. Arc 14, 653-665.

Hickey-Vargas, R., Bizimis, M., Deschamps, A., 2008. Onset of the Indian Ocean isotopic signature in the Philippine Sea Plate: Hf and Pb isotope evidence from Early Cretaceous terranes. Earth and Planetary Science Letters 268, 255-267.

Hill, R., Roeder, P., 1974. The Crystallization of Spinel from Basaltic Liquid as a Function of Oxygen Fugacity. The Journal of Geology 82, 709-729.

Hirschmann, M.M., 2006. Water, melting, and the deep Earth H_2O cycle. Annu. Rev. Earth Planet. Sci. 34, 629-653.

Hirschmann, M.M., Ghiorso, M.S., Davis, F.A., Gordon, S.M., Mukherjee, S., Grove, T.L., Krawczynski, M., Medard, E., Till, C.B., 2008. Library of Experimental Phase Relations (LEPR): A database and Web portal for experimental magmatic phase equilibria data. Geochemistry, Geophysics, Geosystems 9.

Hodel, F., Macouin, M., Trindade, R.I.F., Araujo, J.F.D.F., Respaud, M., Meunier, J.F., Cassayre, L., Rousse, S., Drigo, L., Schorne-Pinto, J., 2020. Magnetic Properties of Ferritchromite and Cr-Magnetite and Monitoring of Cr-Spinels Alteration in Ultramafic and Mafic Rocks. Geochemistry, Geophysics, Geosystems 21, doi: 10.1029/2020GC009227.

Hofmeister, A.M., Rossman, G.R., 1985a. A model for the irradiative coloration of smoky feldspar and the inhibiting influence of water. Phys. Chem. Miner. 12, 324-332.

Hofmeister, A.M., Rossman, G.R., 1985b. A spectroscopic study of irradiation coloring of amazonite: structurally hydrous, Pb-bearing feldspar. American Mineralogist 70, 794-804.

Hofmeister, A.M., Rossman, G.R., 1986. A spectroscopic study of blue radiation coloring in plagioclase. American Mineralogist 71, 95-98.

Holt, A.F., Royden, L.H., Becker, T.W., Faccenna, C., 2018. Slab interactions in 3-D subduction settings: The Philippine Sea Plate region. Earth and Planetary Science Letters 489, 72-83.

Hou, T., Botcharnikov, R., Moulas, E., Just, T., Berndt, J., Koepke, J., Zhang, Z., Wang, M., Yang, Z., Holtz, F., 2021. Kinetics of Fe–Ti Oxide Re-equilibration in Magmatic Systems: Implications for Thermo-oxybarometry. Journal of Petrology.

Huppert, H.E., Woods, A.W., 2002. The role of volatiles in magma chamber dynamics. Nature 420, 493-495.

Hynes, A., 1975. Comment on “the troodos ophiolitic complex was probably formed in an island arc”, by A. Miyashiro. Earth and Planetary Science Letters 25, 213-216.

Ingrin, J., Latrous, K., Doukhan, J.-C., Doukhan, N., 1989. Water in diopside: an electron microscopy and infrared spectroscopy study. European Journal of Mineralogy 1, 327-342.

Irvine, T.N., 1965. Chromian spinel as a petrogenetic indicator. Part I. Theory. Canadian Journal of Earth Sciences 2, 648-672.

Irvine, T.N., 1967. Chromian spinel as a petrogenetic indicator. Part 2. Petrologic applications. Canadian Journal of Earth Sciences 4, 71-103.

Ishikawa, T., Nagaishi, K., Umino, S., 2002. Boninitic volcanism in the Oman ophiolite: Implications for thermal condition during transition from spreading ridge to arc. Geology 30, 899-902.

Ishizuka, O., Hickey-Vargas, R., Arculus, R.J., Yogodzinski, G.M., Savov, I.P., Kusano, Y., McCarthy, A., Brandl, P.A., Sudo, M., 2018. Age of Izu–Bonin–Mariana arc basement. Earth and Planetary Science Letters 481, 80-90.

Ishizuka, O., Tani, K., Reagan, M.K., Kanayama, K., Umino, S., Harigane, Y., Sakamoto, I., Miyajima, Y., Yuasa, M., Dunkley, D.J., 2011a. The timescales of

subduction initiation and subsequent evolution of an oceanic island arc. Earth and Planetary Science Letters 306, 229-240.

Ishizuka, O., Taylor, R.N., Yuasa, M., Ohara, Y., 2011b. Making and breaking an island arc: A new perspective from the Oligocene Kyushu-Palau arc, Philippine Sea. Geochemistry, Geophysics, Geosystems 12.

Jakobsson, S., Blundy, J., Moore, G., 2014. Oxygen fugacity control in piston-cylinder experiments: a re-evaluation. Contributions to Mineralogy and Petrology 167, 1007.

Jarosewich, E., Nelen, J.A., Norberg, J.A., 1980. Reference Samples for Electron Microprobe Analysis*. Geostandards Newsletter 4, 43-47.

Jégo, S., Pichavant, M., Mavrogenes, J.A., 2010. Controls on gold solubility in arc magmas: An experimental study at 1000 C and 4 kbar. Geochimica et Cosmochimica Acta 74, 2165-2189.

Jochum, K.P., Stoll, B., Herwig, K., Willbold, M., Hofmann, A.W., Amini, M., Aarburg, S., Abouchami, W., Hellebrand, E., Mocek, B., Raczek, I., Stracke, A., Alard, O., Bouman, C., Becker, S., Dücking, M., Brätz, H., Klemd, R., de Bruin, D., Canil, D., Cornell, D., de Hoog, C.-J., Dalpé, C., Danyushevsky, L., Eisenhauer, A., Gao, Y., Snow, J.E., Groschopf, N., Günther, D., Latkoczy, C., Guillong, M., Hauri, E.H., Höfer, H.E., Lahaye, Y., Horz, K., Jacob, D.E., Kasemann, S.A., Kent, A.J.R., Ludwig, T., Zack, T., Mason, P.R.D., Meixner, A., Rosner, M., Misawa, K., Nash, B.P., Pfänder, J., Premo, W.R., Sun, W.D., Tiepolo, M., Vannucci, R., Vennemann, T., Wayne, D., Woodhead, J.D., 2006. MPI-DING reference glasses for in situ microanalysis: New reference values for element concentrations and isotope ratios. Geochemistry, Geophysics, Geosystems 7.

Jochum, K.P., Willbold, M., Raczek, I., Stoll, B., Herwig, K., 2005. Chemical Characterisation of the USGS Reference Glasses GSA-1G, GSC-1G, GSD-1G, GSE-1G, BCR-2G, BHVO-2G and BIR-1G Using EPMA, ID-TIMS, ID-ICP-MS and LA-ICP-MS. Geostandards and Geoanalytical Research 29, 285-302.

Johan, Z., Martin, R.F., Ettler, V., 2017. Fluids are bound to be involved in the formation of ophiolitic chromite deposits. European Journal of Mineralogy 29, 543-555.

Johnson, E.A., Rossman, G.R., 2003. The concentration and speciation of hydrogen in feldspars using FTIR and ^{1}H MAS NMR spectroscopy. American Mineralogist 88, 901-911.

Johnson, E.A., Rossman, G.R., 2004. A survey of hydrous species and concentrations in igneous feldspars. American Mineralogist 89, 586-600.

Justice, M.G., Jr., Graham, E.K., Tressler, R.E., Tsong, I.S.T., 1982. The effect of water on high-temperature deformation in olivine. Geophysical Research Letters 9, 1005-1008.

Kamenetsky, V.S., Crawford, A.J., Meffre, S., 2001. Factors controlling chemistry of magmatic spinel: An empirical study of associated olivine, Cr-spinel and melt inclusions from primitive rocks. Journal of Petrology 42, 655-671.

Kamenetsky, V.S., Sobolev, A.V., Eggins, S.M., Crawford, A.J., Arculus, R.J., 2002. Olivine-enriched melt inclusions in chromites from low-Ca boninites, Cape Vogel, Papua New Guinea: evidence for ultramafic primary magma, refractory mantle source and enriched components. Chemical Geology 183, 287-303.

Karato, S.-I., Paterson, M.S., FitzGerald, J.D., 1986. Rheology of synthetic olivine aggregates: Influence of grain size and water. Journal of Geophysical Research: Solid Earth 91, 8151-8176.

Kelley, K.A., Cottrell, E., 2009. Water and the Oxidation State of Subduction Zone Magmas. Science 325, 605-607.

Kelley, K.A., Cottrell, E., 2012. The influence of magmatic differentiation on the oxidation state of Fe in a basaltic arc magma. Earth and Planetary Science Letters 329-330, 109-121.

Keppler, H., Bolfan-Casanova, N., 2006. Thermodynamics of water solubility and partitioning. Reviews in Mineralogy and Geochemistry 62, 193-230.

Kessel, R., Beckett, J.R., Stolper, E.M., 2001. Thermodynamic properties of the Pt-Fe system. American Mineralogist 86, 1003-1014.

Kitamura, M., Kondoh, S., Morimoto, N., Miller, G.H., Rossman, G.R., Putnis, A., 1987. Planar OH-bearing defects in mantle olivine. Nature 328, 143-145.

Klügel, A., 2001. Prolonged reactions between harzburgite xenoliths and silica-undersaturated melt: implications for dissolution and Fe-Mg interdiffusion rates of orthopyroxene. Contributions to Mineralogy and Petrology 141, 1-14.

Koga, K., Hauri, E., Hirschmann, M., Bell, D., 2003. Hydrogen concentration analyses using SIMS and FTIR: Comparison and calibration for nominally anhydrous minerals. Geochemistry, Geophysics, Geosystems 4.

Kress, V.C., Carmichael, I.S.E., 1991. The compressibility of silicate liquids containing Fe_2O_3 and the effect of composition, temperature, oxygen fugacity and pressure on their redox states. Contributions to Mineralogy and Petrology 108, 82-92.

Kunihiro, T., Nagashima, K., Takayanagi, I., Nakamura, J., Kosaka, K., Yurimoto, H., 2001. Noise characteristics of stacked CMOS active pixel sensor for charged particles. Nuclear Instruments and Methods in Physics Research Section A: Accelerators, Spectrometers, Detectors and Associated Equipment 470, 512-519.

La Spina, G., Burton, M., de' Michieli Vitturi, M., Arzilli, F., 2016. Role of syn-eruptive plagioclase disequilibrium crystallization in basaltic magma ascent dynamics. Nature Communications 7, 13402.

Lange, R.A., Frey, H.M., Hector, J., 2009. A thermodynamic model for the plagioclase-liquid hygrometer/thermometer. American Mineralogist 94, 494-506.

Langmuir, C.H., Bender, J.F., Bence, A.E., Hanson, G.N., Taylor, S.R., 1977. Petrogenesis of basalts from the FAMOUS area: Mid-Atlantic Ridge. Earth and Planetary Science Letters 36, 133-156.

Lavina, B., Salviulo, G., Della Giusta, A., 2002. Cation distribution and structure modelling of spinel solid solutions. Phys. Chem. Miner. 29, 10-18.

Lenaz, D., Skogby, H., Nestola, F., Princivalle, F., 2008. OH incorporation in nearly pure $MgAl_2O_4$ natural and synthetic spinels. Geochimica et Cosmochimica Acta 72, 475-479.

Lenaz, D., Skogby, H., Princivalle, F., Hålenius, U., 2004. Structural changes and valence states in the MgCr2O4–FeCr2O4 solid solution series. Phys. Chem. Miner. 31, 633-642.

Leonard, G.S., Begg, J.G., Wilson, C.J.N., 2010. Geology of the Rotorua area. GNS Science, Lower Hutt.

Liang, Y., 2000. Dissolution in molten silicates: effects of solid solution. Geochimica et Cosmochimica Acta 64, 1617-1627.

Liermann, H.-P., Ganguly, J., 2002. Diffusion kinetics of Fe^{2+} and Mg in aluminous spinel: experimental determination and applications. Geochimica et Cosmochimica Acta 66, 2903-2913.

Liermann, H.P., Ganguly, J., 2003. Fe^{2+}–Mg fractionation between orthopyroxene and spinel: experimental calibration in the system $FeO–MgO–Al_2O_3–Cr_2O_3–SiO_2$, and applications. Contributions to Mineralogy and Petrology 145, 217-227.

Lloyd, A.S., Ferriss, E., Ruprecht, P., Hauri, E.H., Jicha, B.R., Plank, T., 2016. An Assessment of Clinopyroxene as a Recorder of Magmatic Water and Magma Ascent Rate. Journal of Petrology 57, 1865-1885.

Lormand, C., Zellmer, G.F., Kilgour, G.N., Németh, K., Palmer, A.S., Sakamoto, N., Yurimoto, H., Kuritani, T., Iizuka, Y., Moebis, A., 2020. Slow ascent of unusually hot intermediate magmas triggering Strombolian to sub-Plinian eruptions. Journal of Petrology.

Mackwell, S.J., Kohlstedt, D.L., 1990. Diffusion of hydrogen in olivine: Implications for water in the mantle. Journal of Geophysical Research-Solid Earth and Planets 95, 5079-5088.

Mackwell, S.J., Kohlstedt, D.L., Paterson, M.S., 1985. The role of water in the deformation of olivine single crystals. Journal of Geophysical Research: Solid Earth 90, 11319-11333.

MacLeod, C.J., 1988. The tectonic evolution of the Eastern Limassol Forest Complex, Cyprus, Department of Earth Sciences. The Open University.

Magee, C.W., 1983. Analysis of hydrogen and deuterium by secondary ion mass spectrometry as applied to fusion technology. Journal of Vacuum Science & Technology A 1, 901-906.

Malpas, J., Langdon, G., 1984. Petrology of the Upper Pillow Lava suite, Troodos ophiolite, Cyprus. Geological Society, London, Special Publications 13, 155-167.

Manning, J.R., 1968. Diffusion Kinetics for Atoms in Crystals. D. Van Nostrand Company.

Manville, V., 2001. Sedimentology and history of Lake Reporoa: an ephemeral supra-ignimbrite lake, Taupo Volcanic Zone, New Zealand, in: White, J., Riggs, N. (Eds.), VOLCANICLASTIC SEDIMENTATION IN LACUSTRINE SETTINGS. Blackwell Science Ltd, pp. 109-140.

Martin, R.C., 1961. Stratigraphy and structural outline of the Taupo Volcanic Zone. New Zealand Journal of Geology and Geophysics 4, 449-478.

Matjuschkin, V., Brooker, R.A., Tattitch, B., Blundy, J.D., Stamper, C.C., 2015. Control and monitoring of oxygen fugacity in piston cylinder experiments. Contributions to Mineralogy and Petrology 169, 9.

Mattioli, M., Renzulli, A., Menna, M., Holm, P.M., 2006. Rapid ascent and contamination of magmas through the thick crust of the CVZ (Andes, Ollagüe region): Evidence from a nearly aphyric high-K andesite with skeletal olivines. Journal of Volcanology and Geothermal Research 158, 87-105.

Matveev, S., Ballhaus, C., 2002. Role of water in the origin of podiform chromitite deposits. Earth and Planetary Science Letters 203, 235-243.

Maurel, C., Maurel, P., 1982a. Étude expérimentale de l'équilibre Fe^{2+} -Fe^{3+} dans les spinelles chromifères et les liquides silicatés basiques coexistants, à 1 atm. Comptes Rendus des Séances de l'Académie des Sciences 295.

Maurel, C., Maurel, P., 1982b. Étude expérimentale de la distribution de l'aluminium entre bain silicaté basique et spinelle chromifère. Implications pétrogénétiques: teneur en chrome des spinelles. Bulletin de Mineralogie 105, 197-202.

Meffre, S., Aitchison, J.C., Crawford, A.J., 1996. Geochemical evolution and tectonic significance of boninites and tholeiites from the Koh ophiolite, New Caledonia. Tectonics 15, 67-83.

Meijer, A., 1980. Primitive arc volcanism and a boninite series: examples from western Pacific island arcs, in: Hayes, D.E. (Ed.), The Tectonic and Geologic Evolution of Southeast Asian Seas and Islands. American Geophysical Union, pp. 269-282.

Melcher, F., Grum, W., Simon, G., Thalhammer, T.V., Stumpfl, E.F., 1997. Petrogenesis of the ophiolitic giant chromite deposits of Kempirsai, Kazakhstan: a study of solid and fluid inclusions in chromite. Journal of Petrology 38, 1419-1458.

Metcalf, R.V., Shervais, J.W., 2008. Suprasubduction-zone ophiolites: Is there really an ophiolite conundrum? Special Papers-Geological Society of America 438, 191.

Mierdel, K., Keppler, H., 2004. The temperature dependence of water solubility in enstatite. Contributions to Mineralogy and Petrology 148, 305-311.

Miller, G.H., Rossman, G.R., Harlow, G.E., 1987. The natural occurrence of hydroxide in olivine. Phys. Chem. Miner. 14, 461-472.

Mitchell, A.L., Grove, T.L., 2016. Experiments on melt–rock reaction in the shallow mantle wedge. Contributions to Mineralogy and Petrology 171, 107.

Miyashiro, A., 1973. The Troodos ophiolitic complex was probably formed in an island arc. Earth and Planetary Science Letters 19, 218-224.

Miyashiro, A., 1975a. Origin of the troodos and other ophiolites: A reply to Hynes. Earth and Planetary Science Letters 25, 217-222.

Miyashiro, A., 1975b. Origin of the troodos and other ophiolites: A reply to Moores. Earth and Planetary Science Letters 25, 227-235.

Moore, G., Vennemann, T., Carmichael, I.S.E., 1998. An empirical model for the solubility of H 2 O in magmas to 3 kilobars. American Mineralogist 83, 36-42.

Moore, J.G., 1987. Subsidence of the Hawaiian ridge. Volcanism in Hawaii 1, 85-100.

Moores, E.M., 1975. Discussion of “origin of troodos and other ophiolites: A reply to Hynes”, by Akiho Miyashiro. Earth and Planetary Science Letters 25, 223-226.

Moores, E.M., Kellogg, L.H., Dilek, Y., 2000. Tethyan ophiolites, mantle convection, and tectonic" historical contingency": A resolution of the" ophiolite conundrum". Geological Society of America Special Papers 349, 3-12.

Moores, E.M., Vine, F.J., 1971. The Troodos Massif, Cyprus and other ophiolites as oceanic crust: evaluation and implications. Philosophical Transactions of the Royal Society of London. Series A, Mathematical and Physical Sciences 268, 443-467.

Mosenfelder, J.L., Andrys, J.L., von der Handt, A., Kohlstedt, D.L., Hirschmann, M.M., 2020. Hydrogen incorporation in plagioclase. Geochimica et Cosmochimica Acta 277, 87-110.

Mosenfelder, J.L., Deligne, N.I., Asimow, P.D., Rossman, G.R., 2006. Hydrogen incorporation in olivine from 2–12 GPa. American Mineralogist 91, 285-294.

Mosenfelder, J.L., Rossman, G.R., Johnson, E.A., 2015. Hydrous species in feldspars: A reassessment based on FTIR and SIMS. American Mineralogist 100, 1209-1221.

Mrozowski, C.L., Hayes, D.E., 1979. The evolution of the Parece Vela Basin, eastern Philippine Sea. Earth and Planetary Science Letters 46, 49-67.

Muan, A., Osborn, E.F., 1956. Phase Equilibria at Liquidus Temperatures in the System MgO-FeO-Fe2O3-SiO2. Journal of the American Ceramic Society 39, 121-140.

Murck, B.W., Campbell, I.H., 1986. The effects of temperature, oxygen fugacity and melt composition on the behaviour of chromium in basic and ultrabasic melts. Geochimica et Cosmochimica Acta 50, 1871-1887.

Nielsen, R.L., Beard, J.S., 2000. Magnetite–melt HFSE partitioning. Chemical Geology 164, 21-34.

Nikolaev, G.S., Ariskin, A.A., Barmina, G.S., 2018a. SPINMELT-2.0: Simulation of spinel–melt equilibrium in basaltic systems under pressures up to 15 kbar: I. model formulation, calibration, and tests. Geochemistry International 56, 24-45.

Nikolaev, G.S., Ariskin, A.A., Barmina, G.S., 2018b. SPINMELT-2.0: Simulation of Spinel–Melt Equilibrium in Basaltic Systems under Pressures up to 15 Kbar: II. Description of the Program Package, the Topology of the Cr-spinel–Melt Model System, and Petrological Implications. Geochemistry International 56, 125-135.

Novella, D., Frost, D.J., Hauri, E.H., Bureau, H., Raepsaet, C., Roberge, M., 2014. The distribution of H_2O between silicate melt and nominally anhydrous peridotite and the onset of hydrous melting in the deep upper mantle. Earth and Planetary Science Letters 400, 1-13.

O'Neill, H.S.C., 1981. The transition between spinel lherzolite and garnet lherzolite, and its use as a Geobarometer. Contributions to Mineralogy and Petrology 77, 185-194.

O'Neill, H.S.C., 1986. Mo-MoO2 (MOM) oxygen buffer and the free energy of formation of MoO2. American Mineralogist 71, 1007-1010.

O'Neill, H.S.C., Berry, A.J., Mallmann, G., 2018. The oxidation state of iron in Mid-Ocean Ridge Basaltic (MORB) glasses: Implications for their petrogenesis and oxygen fugacities. Earth and Planetary Science Letters 504, 152-162.

O'Neill, H.S.C., Wall, V.J., 1987. The olivine - orthopyroxene - spinel oxygen geobarometer, the nickel precipitation curve, and the oxygen fugacity of the earth's upper mantle. Journal of Petrology 28, 1169-1191.

Ohnenstetter, M., Bechon, F., Ohnenstetter, D., 1990. Geochemistry and mineralogy of lavas from the Arakapas Fault Belt, Cyprus: Consequences for magma chamber evolution. Mineralogy and Petrology 41, 105-124.

Okino, K., Shimakawa, Y., Nagaoka, S., 1994. Evolution of the Shikoku Basin. Journal of geomagnetism and geoelectricity 46, 463-479.

Okuyama, Y., Kurita, N., Fukatsu, N., 2006. Defect structure of alumina-rich nonstoichiometric magnesium aluminate spinel. Solid State Ionics 177, 59-64.

Osborn, E.F., 1959. Role of oxygen pressure in the crystallization and differentiation of basaltic magma. American Journal of Science 257, 609-647.

Ozawa, K., 1984. Olivine-spinel geospeedometry: Analysis of diffusion-controlled Mg-Fe2+ exchange. Geochimica et Cosmochimica Acta 48, 2597-2611.

Parkinson, I.J., Arculus, R.J., 1999. The redox state of subduction zones: insights from arc-peridotites. Chemical Geology 160, 409-423.

Pearce, J.A., Reagan, M.K., 2019. Identification, classification, and interpretation of boninites from Anthropocene to Eoarchean using Si-Mg-Ti systematics. Geosphere 15, 1008-1037.

Pearce, J.A., Robinson, P.T., 2010. The Troodos ophiolitic complex probably formed in a subduction initiation, slab edge setting. Gondwana Research 18, 60-81.

Petrelli, M., Zellmer, G.F., 2020. Rates and Timescales of Magma Transfer, Storage, Emplacement, and Eruption, Dynamic Magma Evolution, pp. 1-41.

Pownceby, M.I., O'Neill, H.S.C., 1994. Thermodynamic data from redox reactions at high temperatures. III. Activity-composition relations in Ni-Pd alloys from EMF measurements at 850–1250 K, and calibration of the NiO+Ni-Pd assemblage as a redox sensor. Contributions to Mineralogy and Petrology 116, 327-339.

Presnall, D., 1976. Alumina content of enstatite as a geobarometer for plagioclase and spinel lherzolites. American Mineralogist 61, 582-588.

Pu, X., Lange, R.A., Moore, G., 2017. A comparison of olivine-melt thermometers based on DMg and DNi: The effects of melt composition, temperature, and pressure with applications to MORBs and hydrous arc basalts. American Mineralogist 102, 750-765.

Pu, X., Moore, G.M., Lange, R.A., Touran, J.P., Gagnon, J.E., 2021. Experimental evaluation of a new H_2O-independent thermometer based on olivine-melt Ni partitioning at crustal pressure. American Mineralogist 106, 235-250.

Putirka, K.D., 2005. Igneous thermometers and barometers based on plagioclase + liquid equilibria: Tests of some existing models and new calibrations. American Mineralogist 90, 336-346.

Putirka, K.D., 2008. Thermometers and Barometers for Volcanic Systems. Reviews in Mineralogy and Geochemistry 69, 61-120.

Rauch, M., Keppler, H., 2002. Water solubility in orthopyroxene. Contributions to Mineralogy and Petrology 143, 525-536.

Rautenschlein, M., Jenner, G.A., Hertogen, J., Hofmann, A.W., Kerrich, R., Schmincke, H.U., White, W.M., 1985. Isotopic and trace element composition of volcanic glasses from the Akaki Canyon, Cyprus: implications for the origin of the Troodos ophiolite. Earth and Planetary Science Letters 75, 369-383.

Reagan, M.K., Heaton, D.E., Schmitz, M.D., Pearce, J.A., Shervais, J.W., Koppers, A.A.P., 2019. Forearc ages reveal extensive short-lived and rapid seafloor spreading following subduction initiation. Earth and Planetary Science Letters 506, 520-529.

Reagan, M.K., Ishizuka, O., Stern, R.J., Kelley, K.A., Ohara, Y., Blichert-Toft, J., Bloomer, S.H., Cash, J., Fryer, P., Hanan, B.B., Hickey-Vargas, R., Ishii, T., Kimura, J.-I., Peate, D.W., Rowe, M.C., Woods, M., 2010. Fore-arc basalts and subduction initiation in the Izu-Bonin-Mariana system. Geochemistry Geophysics Geosystems 11.

Reagan, M.K., McClelland, W.C., Girard, G., Goff, K.R., Peate, D.W., Ohara, Y., Stern, R.J., 2013. The geology of the southern Mariana fore-arc crust: Implications for

the scale of Eocene volcanism in the western Pacific. Earth and Planetary Science Letters 380, 41-51.

Reagan, M.K., Meijer, A., 1984. Geology and geochemistry of early arc-volcanic rocks from Guam. GSA Bulletin 95, 701-713.

Reagan, M.K., Pearce, J.A., Petronotis, K., Almeev, R.R., Avery, A.J., Carvallo, C., Chapman, T., Christeson, G.L., Ferré, E.C., Godard, M., Heaton, D.E., Kirchenbaur, M., Kurz, W., Kutterolf, S., Li, H., Li, Y., Michibayashi, K., Morgan, S., Nelson, W.R., Prytulak, J., Python, M., Robertson, A.H.F., Ryan, J.G., Sager, W.W., Sakuyama, T., Shervais, J.W., Shimizu, K., Whattam, S.A., 2017. Subduction initiation and ophiolite crust: new insights from IODP drilling. Int. Geol. Rev. 59, 1439-1450.

Regelous, M., Haase, K.M., Freund, S., Keith, M., Weinzierl, C.G., Beier, C., Brandl, P.A., Endres, T., Schmidt, H., 2014. Formation of the Troodos Ophiolite at a triple junction: Evidence from trace elements in volcanic glass. Chemical Geology 386, 66-79.

Regenauer-Lieb, K., 2006. Water and geodynamics. Reviews in mineralogy and geochemistry 62, 451-473.

Riggs, N., Ort, M., White, J., Wilson, C., Houghton, B., Clarkson, R., 2001. Post-1.8-ka marginal sedimentation in Lake Taupo, New Zealand: effects of wave energy and sediment supply in a rapidly rising lake, in: White, J., Riggs, N. (Eds.), VOLCANICLASTIC SEDIMENTATION IN LACUSTRINE SETTINGS. Blackwell Science Ltd, pp. 151-178.

Robertson, A.H.F., 1977. Tertiary uplift history of the Troodos massif, Cyprus. GSA Bulletin 88, 1763-1772.

Robie, R.A., Hemingway, B.S., 1995. Thermodynamic properties of minerals and related substances at 298.15 K and 1 bar (10^5 pascals) pressure and at higher temperatures, Bulletin. U.S. Geological Survey, Reston, Virginia, pp. iv, 461.

Robinson, P.T., Melson, W.G., O'Hearn, T., Schmincke, H.-U., 1983. Volcanic glass compositions of the Troodos ophiolite, Cyprus. Geology 11, 400-404.

Roeder, P.L., 1994. Chromite; from the fiery rain of chondrules to the Kilauea Iki lava lake. The Canadian Mineralogist 32, 729-746.

Roeder, P.L., Osborn, E.F., 1966. Experimental data for the system MgO-FeO-Fe 2 O 3-CaAl 2 Si 2 O 8-SiO 2 and their petrologic implications. American Journal of Science 264, 428-480.

Roeder, P.L., Reynolds, I., 1991. Crystallization of chromite and chromium solubility in basaltic melts. Journal of Petrology 32, 909-934.

Rollinson, H., 2008. The geochemistry of mantle chromitites from the northern part of the Oman ophiolite: inferred parental melt compositions. Contributions to Mineralogy and Petrology 156, 273-288.

Rollinson, H., Mameri, L., Barry, T., 2018. Polymineralic inclusions in mantle chromitites from the Oman ophiolite indicate a highly magnesian parental melt. Lithos 310-311, 381-391.

Roux, J., Lefevre, A., 1992. A fast-quench devce for internally heated pressure-vessels. European Journal of Mineralogy 4, 279-281.

Rubin, M., Gargulinski, L.K., McGeehin, J.P., 1987. Hawaiian radiocarbon dates. US Geological Survey Professional Paper 1350, 213-242.

Runciman, W.A., Sengupta, D., Marshall, M., 1973. The polarized spectra of iron in silicates. I. Enstatite. American Mineralogist 58, 444-450.

Ryan, W.B.F., Carbotte, S.M., Coplan, J.O., O'Hara, S., Melkonian, A., Arko, R., Weissel, R.A., Ferrini, V., Goodwillie, A., Nitsche, F., Bonczkowski, J., Zemsky, R., 2009. Global Multi-Resolution Topography synthesis. Geochemistry, Geophysics, Geosystems 10.

Sack, R.O., Ghiorso, M.S., 1991. Chromian spinels as petrogenetic indicators: thermodynamics and petrological applications. American Mineralogist 76, 827-847.

Sauerzapf, U., Lattard, D., Burchard, M., Engelmann, R., 2008. The Titanomagnetite–Ilmenite Equilibrium: New Experimental Data and Thermo-oxybarometric

Application to the Crystallization of Basic to Intermediate Rocks†. Journal of Petrology 49, 1161-1185.

Savov, I.P., Hickey-Vargas, R., D'antonio, M., Ryan, J.G., Spadea, P., 2006. Petrology and Geochemistry of West Philippine Basin Basalts and Early Palau–Kyushu Arc Volcanic Clasts from ODP Leg 195, Site 1201D: Implications for the Early History of the Izu–Bonin–Mariana Arc. Journal of Petrology 47, 277-299.

Scaillet, B., Pichavant, M., Roux, J., 1995. Experimental crystallization of leucogranite magmas. Journal of Petrology 36, 663-705.

Scaillet, B., Pichavant, M., Roux, J., Humbert, G., Lefevre, A., 1992. Improvements of the Shaw membrane technique for measurement and control of fH2 at high temperatures and pressures. American Mineralogist 77, 647-655.

Schindelin, J., Arganda-Carreras, I., Frise, E., Kaynig, V., Longair, M., Pietzsch, T., Preibisch, S., Rueden, C., Saalfeld, S., Schmid, B., 2012. Fiji: an open-source platform for biological-image analysis. Nature methods 9, 676.

Schmincke, H.-U., Rautenschlein, M., Robinson, P.T., Mehegan, J.M., 1983. Troodos extrusive series of Cyprus: A comparison with oceanic crust. Geology 11, 405-409.

Schouten, H., Kelemen, P.B., 2002. Melt viscosity, temperature and transport processes, Troodos ophiolite, Cyprus. Earth and Planetary Science Letters 201, 337-352.

Schreiber, H.D., Haskin, L.A., 1976. Chromium in basalts: Experimental determination of redox states and partitioning among synthetic silicate phases, Lunar and Planetary Science Conference Proceedings, pp. 1221-1259.

Scowen, P.A.H., Roeder, P.L., Helz, R.T., 1991. Reequilibration of chromite within Kilauea Iki lava lake, Hawaii. Contributions to Mineralogy and Petrology 107, 8-20.

Seaman, S.J., Dyar, M.D., Marinkovic, N., Dunbar, N.W., 2006. An FTIR study of hydrogen in anorthoclase and associated melt inclusions. American Mineralogist 91, 12-20.

Shane, P., 1998. Correlation of rhyolitic pyroclastic eruptive units from the Taupo volcanic zone by Fe–Ti oxide compositional data. Bulletin of Volcanology 60, 224-238.

Shaw, H.R., 1963. Hydrogen-Water Vapor Mixtures: Control of Hydrothermal Atmospheres by Hydrogen Osmosis. Science 139, 1220-1222.

Shorttle, O., Moussallam, Y., Hartley, M.E., Maclennan, J., Edmonds, M., Murton, B.J., 2015. Fe-XANES analyses of Reykjanes Ridge basalts: Implications for oceanic crust's role in the solid Earth oxygen cycle. Earth and Planetary Science Letters 427, 272-285.

Sigurdsson, H., Schilling, J.G., 1976. Spinels in Mid-Atlantic Ridge basalts: Chemistry and occurrence. Earth and Planetary Science Letters 29, 7-20.

Simonian, K.O., Gass, I.G., 1978. Arakapas fault belt, Cyprus: A fossil transform fault. GSA Bulletin 89, 1220-1230.

Sisson, T.W., Grove, T.L., 1993. Temperatures and H_2O contents of low-MgO high-alumina basalts. Contributions to Mineralogy and Petrology 113, 167-184.

Skogby, H., Bell, D.R., Rossman, G.R., 1990. Hydroxide in pyroxene; variations in the natural environment. American Mineralogist 75, 764-774.

Skogby, H., Hålenius, U., 2003. An FTIR study of tetrahedrally coordinated ferrous iron in the spinel-hercynite solid solution. American Mineralogist 88, 489-492.

Skogby, H., Rossman, G.R., 1989. OH- in pyroxene; an experimental study of incorporation mechanisms and stability. American Mineralogist 74, 1059-1069.

Smith, P.M., Asimow, P.D., 2005. Adiabat_1ph: A new public front-end to the MELTS, pMELTS, and pHMELTS models. Geochemistry, Geophysics, Geosystems 6.

Smith, R.C.M., 1991. Landscape Response to a Major Ignimbrite Eruption, Taupo Volcanic Center, New Zealand, in: Fisher, R.V., Smith, G.A. (Eds.), Sedimentation in Volcanic Settings. SEPM Society for Sedimentary Geology, p. 0.

Smoczyk, G.M., Hayes, G.P., Hamburger, M.W., Benz, H.M., Villaseñor, A., Furlong, K.P., 2013. Seismicity of the Earth 1900-2012 Philippine Sea plate and vicinity, Open-File Report, Reston, VA.

Smyth, J.R., Bell, D.R., Rossman, G.R., 1991. Incorporation of hydroxyl in upper-mantle clinopyroxenes. Nature 351, 732-735.

Sobolev, A., Portnyagin, M., Dmitriev, L., Tsameryan, O., Danyushevsky, L., Kononkova, N., Shimizu, N., Robinson, P., 1993. Petrology of ultramafic lavas and associated rocks of the Troodos massif, Cyprus. Petrology 1, 331-361.

Solomon, G.C., Rossman, G.R., 1988. NH^{+4} in pegmatitic feldspars from the southern Black Hills, South Dakota. American Mineralogist 73, 818-821.

Sparks, R., 2003. Dynamics of magma degassing. Geological Society, London, Special Publications 213, 5-22.

Stalder, R., Klemme, S., Ludwig, T., Skogby, H., 2005. Hydrogen incorporation in orthopyroxene: interaction of different trivalent cations. Contributions to Mineralogy and Petrology 150, 473-485.

Stearns, H.T., Macdonald, G.A., 1946. Geology and ground-water resources of the island of Hawaii. Honolulu Advertising.

Stern, R.J., Bloomer, S.H., 1992. Subduction zone infancy: Examples from the Eocene Izu-Bonin-Mariana and Jurassic California arcs. GSA Bulletin 104, 1621-1636.

Stevie, F.A., Zhou, C., Hopstaken, M., Saccomanno, M., Zhang, Z., Turansky, A., 2016. SIMS measurement of hydrogen and deuterium detection limits in silicon: Comparison of different SIMS instrumentation. Journal of Vacuum Science & Technology B 34, 03H103.

Stock, M.J., Humphreys, M.C.S., Smith, V.C., Isaia, R., Pyle, D.M., 2016. Late-stage volatile saturation as a potential trigger for explosive volcanic eruptions. Nature Geoscience 9, 249.

Suzuki, A.M., Yasuda, A., Ozawa, K., 2008. Cr and Al diffusion in chromite spinel: experimental determination and its implication for diffusion creep. Phys. Chem. Miner. 35, 433.

Tacker, R.C., Candela, P.A., 1987. Partitioning of molybdenum between magnetite and melt; a preliminary experimental study of partitioning of ore metals between silicic magmas and crystalline phases. Economic Geology 82, 1827-1838.

Tatsumi, Y., 1981. Melting experiments on a high-magnesian andesite. Earth and Planetary Science Letters 54, 357-365.

Tatsumi, Y., 2006. High-Mg Andesites in the Setouchi Volcanic Belt, Southwestern Japan: Analogy to Archean Magmatism and Continental Crust Formation? Annual Review of Earth and Planetary Sciences 34, 467-499.

Taylor, B., Goodliffe, A.M., 2004. The West Philippine Basin and the initiation of subduction, revisited. Geophysical Research Letters 31.

Taylor, J.R., Wall, V.J., Pownceby, M.I., 1992. The calibration and application of accurate redox sensors. American Mineralogist 77, 284-295.

Tenner, T.J., Hirschmann, M.M., Withers, A.C., Hervig, R.L., 2009. Hydrogen partitioning between nominally anhydrous upper mantle minerals and melt between 3 and 5 GPa and applications to hydrous peridotite partial melting. Chemical Geology 262, 42-56.

Thy, P., Lofgren, G.E., 1994. Experimental constraints on the low-pressure evolution of transitional and mildly alkalic basalts: the effect of Fe-Ti oxide minerals and the origin of basaltic andesites. Contributions to Mineralogy and Petrology 116, 340-351.

Thy, P., Xenophontos, C., 1991. Crystallization Orders and Phase Chemistry of Glassy Lavas from the Pillow Sequences, Troodos Ophiolite, Cyprus. Journal of Petrology 32, 403-428.

Tollan, P., Hermann, J., 2019. Arc magmas oxidized by water dissociation and hydrogen incorporation in orthopyroxene. Nature Geoscience 12, 667-671.

Tomiya, A., Miyagi, I., Saito, G., Geshi, N., 2013. Short time scales of magma-mixing processes prior to the 2011 eruption of Shinmoedake volcano, Kirishima volcanic group, Japan. Bulletin of Volcanology 75, 750.

Toplis, M.J., Carroll, M.R., 1995. An Experimental Study of the Influence of Oxygen Fugacity on Fe-Ti Oxide Stability, Phase Relations, and Mineral—Melt Equilibria in Ferro-Basaltic Systems. Journal of Petrology 36, 1137-1170.

Torres-Orozco, R., 2017. Understanding the largest-scale explosive volcanism at Mt. Taranaki, New Zealand: a thesis presented in partial fulfilment of the requirements for the degree of Doctor of Philosophy in Earth Science, Massey University, Palmerston North, New Zealand. Massey University.

Torres-Orozco, R., Cronin, S.J., Damaschke, M., Pardo, N., 2017. Diverse dynamics of Holocene mafic-intermediate Plinian eruptions at Mt. Taranaki (Egmont), New Zealand. Bulletin of Volcanology 79, 76.

Torres-Orozco, R., Cronin, S.J., Pardo, N., Palmer, A.S., 2016. New insights into Holocene eruption episodes from proximal deposit sequences at Mt. Taranaki (Egmont), New Zealand. Bulletin of Volcanology 79, 3.

Turner, M.B., Cronin, S.J., Bebbington, M.S., Smith, I.E.M., Stewart, R.B., 2011. Integrating records of explosive and effusive activity from proximal and distal sequences: Mt. Taranaki, New Zealand. Quaternary International 246, 364-373.

Turner, M.B., Cronin, S.J., Smith, I.E., Stewart, R.B., Neall, V.E., 2008a. Eruption episodes and magma recharge events in andesitic systems: Mt Taranaki, New Zealand. Journal of Volcanology and Geothermal Research 177, 1063-1076.

Turner, M.B., Cronin, S.J., Stewart, R.B., Bebbington, M., Smith, I.E.M., 2008b. Using titanomagnetite textures to elucidate volcanic eruption histories. Geology 36, 31-34.

Ubide, T., Galé, C., Larrea, P., Arranz, E., Lago, M., 2014. Antecrysts and their effect on rock compositions: The Cretaceous lamprophyre suite in the Catalonian Coastal Ranges (NE Spain). Lithos 206-207, 214-233.

Umino, S., 1986. Magma mixing in boninite sequence of Chichijima, Bonin Islands. Journal of Volcanology and Geothermal Research 29, 125-157.

Umino, S., Kanayama, K., Kitamura, K., Tamura, A., Ishizuka, O., Senda, R., Arai, S., 2018. Did boninite originate from the heterogeneous mantle with recycled ancient slab? Isl. Arc 27, e12221.

Umino, S., Kitamura, K., Kanayama, K., Tamura, A., Sakamoto, N., Ishizuka, O., Arai, S., 2015. Thermal and chemical evolution of the subarc mantle revealed by spinel-hosted melt inclusions in boninite from the Ogasawara (Bonin) Archipelago, Japan. Geology 43, 151-154.

Umino, S., Kushiro, I., 1989. Experimental studies on boninite petrogenesis, in: Crawford, A.J. (Ed.), Boninites: And Related Rocks. Unwin and Hyman, London, pp. 89-111.

Umino, S., Nakano, S., 2007. Geology of the Chichijima Rettō District. Geological Survey of Japan, AIST.

Van der Heide, P., 2014. Secondary ion mass spectrometry: an introduction to principles and practices. John Wiley & Sons.

Van Orman, J.A., Crispin, K.L., 2010. Diffusion in Oxides. Reviews in Mineralogy and Geochemistry 72, 757-825.

Vogt, K., Dohmen, R., Chakraborty, S., 2015. Fe-Mg diffusion in spinel: New experimental data and a point defect model†. American Mineralogist 100, 2112-2122.

Vogt, P.R., Higgs, R.H., 1968. An aeromagnetic survey of the eastern mediterranean sea and its interpretation. Earth and Planetary Science Letters 5, 439-448.

Walker, G.P.L., 1992. Puu Mahana Near South Point in Hawaii Is a Primary Surtseyan Ash Ring, Not a Sandhills-type Littoral Cone. Pacific Science 46, 1-10.

Wang, C.C., 1969. Growth and Characterization of Spinel Single Crystals for Substrate Use in Integrated Electronics. Journal of Applied Physics 40, 3433-3444.

Waters, L.E., Lange, R.A., 2015. An updated calibration of the plagioclase-liquid hygrometer-thermometer applicable to basalts through rhyolites. American Mineralogist 100, 2172-2184.

Webb, S.A.C., Wood, B.J., 1986. Spinel-pyroxene-garnet relationships and their dependence on Cr/Al ratio. Contributions to Mineralogy and Petrology 92, 471-480.

Whattam, S.A., Shervais, J.W., Reagan, M.K., Coulthard Jr., D.A., Pearce, J.A., Jones, P., Seo, J., Putirka, K., Chapman, T., Heaton, D., Li, H., Nelson, W.R., Shimizu, K., Stern, R.J., 2020. Mineral compositions and thermobarometry of basalts and boninites recovered during IODP Expedition 352 to the Bonin forearc. American Mineralogist.

Whitney, J.A., 1972. The effect of reduced H_2O fugacity on the buffering of oxygen fugacity in hydrothermal experiments. American Mineralogist 57, 1902-1908.

Wickersheim, K., Lefever, R., 1960. Optical properties of synthetic spinel. Journal of the Optical Society of America 50, 831-832.

Wieland, E., Wehrli, B., Stumm, W., 1988. The coordination chemistry of weathering: III. A generalization on the dissolution rates of minerals. Geochimica et Cosmochimica Acta 52, 1969-1981.

Wilkins, R., Sabine, W., 1973. Water content of some nominally anhydrous silicates. American mineralogist 58, 508-516.

Wilson, C.J.N., 1985. The Taupo eruption, New Zealand. II. The Taupo Ignimbrite. Philosophical Transactions of the Royal Society of London. Series A, Mathematical and Physical Sciences 314, 229-310.

Wilson, C.J.N., 2001. The 26.5ka Oruanui eruption, New Zealand: an introduction and overview. Journal of Volcanology and Geothermal Research 112, 133-174.

Wilson, C.J.N., Blake, S., Charlier, B.L.A., Sutton, A.N., 2005. The 26·5 ka Oruanui Eruption, Taupo Volcano, New Zealand: Development, Characteristics and Evacuation of a Large Rhyolitic Magma Body. Journal of Petrology 47, 35-69.

Wilson, C.J.N., Walker, G.P.L., 1985. The Taupo eruption, New Zealand I. General aspects. Philosophical Transactions of the Royal Society of London. Series A, Mathematical and Physical Sciences 314, 199-228.

Wlotzka, F., 2005. Cr spinel and chromite as petrogenetic indicators in ordinary chondrites: Equilibration temperatures of petrologic types 3.7 to 6. Meteoritics & Planetary Science 40, 1673-1702.

Woelki, D., Michael, P., Regelous, M., Haase, K., 2020. Enrichment of H_2O and fluid-soluble trace elements in the Troodos Ophiolite: Evidence for a near-trench origin. Lithos 356-357, 105299.

Woelki, D., Regelous, M., Haase, K.M., Romer, R.H.W., Beier, C., 2018. Petrogenesis of boninitic lavas from the Troodos Ophiolite, and comparison with Izu–Bonin–Mariana fore-arc crust. Earth and Planetary Science Letters 498, 203-214.

Wolf, K.J., Eichelberger, J.C., 1997. Syneruptive mixing, degassing, and crystallization at Redoubt Volcano, eruption of December, 1989 to May 1990. Journal of Volcanology and Geothermal Research 75, 19-37.

Wood, B.J., Virgo, D., 1989. Upper mantle oxidation state: Ferric iron contents of Iherzolite spinels by ^{57}Fe Mössbauer spectroscopy and resultant oxygen fugacities. Geochimica et Cosmochimica Acta 53, 1277-1291.

Woods, S.C., Mackwell, S., Dyar, D., 2000. Hydrogen in diopside: Diffusion profiles. American Mineralogist 85, 480-487.

Wu, J., Suppe, J., Lu, R., Kanda, R., 2016. Philippine Sea and East Asian plate tectonics since 52 Ma constrained by new subducted slab reconstruction methods. Journal of Geophysical Research: Solid Earth 121, 4670-4741.

Yajima, K., Fujimaki, H., 2001. High-Ca and low-Ca boninites from Chichijima, Bonin (Ogasawara) archipelago. Japanese Magazine of Mineralogical and Petrological Sciences 30, 217-236.

Yurimoto, H., Kurosawa, M., Sueno, S., 1989. Hydrogen analysis in quartz crystals and quartz glasses by secondary ion mass spectrometry. Geochimica et Cosmochimica Acta 53, 751-755.

Yurimoto, H., Nagashima, K., Kunihiro, T., 2003. High precision isotope micro-imaging of materials. Applied Surface Science 203-204, 793-797.

Zellmer, G.F., Sakamoto, N., Hwang, S.-L., Matsuda, N., Iizuka, Y., Moebis, A., Yurimoto, H., 2016. Inferring the Effects of Compositional Boundary Layers on Crystal Nucleation, Growth Textures, and Mineral Chemistry in Natural Volcanic Tephras through Submicron-Resolution Imaging. Frontiers in Earth Science 4.

Zellmer, G.F., Sakamoto, N., Iizuka, Y., Miyoshi, M., Tamura, Y., Hsieh, H.-H., Yurimoto, H., 2014. Crystal uptake into aphyric arc melts: insights from two-pyroxene pseudo-decompression paths, plagioclase hygrometry, and measurement of hydrogen in olivines from mafic volcanics of SW Japan. Geological Society, London, Special Publications 385, SP385. 383.

Zhang, Y., Xu, Z., Zhu, M., Wang, H., 2007. Silicate melt properties and volcanic eruptions. Reviews of Geophysics 45.

Zhou, M.-F., Robinson, P.T., 1997. Origin and tectonic environment of podiform chromite deposits. Economic Geology 92, 259-262.

Zhou, M.F., Robinson, P.T., Bai, W.J., 1994. Formation of podiform chromitites by melt/rock interaction in the upper mantle. Mineralium Deposita 29, 98-101.

Zhou, M.F., Robinson, P.T., Malpas, J., Li, Z., 1996. Podiform chromitites in the Luobusa ophiolite (Southern Tibet): Implications for melt-rock interaction and chromite segregation in the upper mantle. Journal of Petrology 37, 3-21.

Appendix 1: Derivation of RSFs for quantification of spinel OH

Routine Dynamic SIMS analysis of a material with a known structure and an unknown composition often requires that several isostructural calibration standards (matrix-matched reference standards, or a set of samples whose compositions are accurately quantified and span a statistically significant range with respect to the element of interest) are analysed during the same analytical session. The reasons for this are that i) signal intensity often varies between analytical sessions due to small but significant changes in the environment or analysis conditions, and ii) isostructural standards are necessary to overcome the matrix effect, which determines the production rate of secondary ions during sputtering based on the material properties of the sample (Deline et al., 1978). Otherwise, only qualitative information may be gained in SIMS analysis, as secondary ion signal intensity provides relative information alone.

Because the H concentrations of spinel have never been thoroughly investigated via SIMS methods, and those of Fe-bearing spinels cannot be determined by FTIR or other presently available techniques, there are no calibration standards available for routine analysis. The only other way to accurately quantify trace element concentration is via the RSF method (e.g. Benninghoven et al., 1987). The RSF method is a comparative method. It utilizes one or more internal reference standards to calibrate signal intensity for an element or molecule of interest using the signal intensity of a matrix element or molecule whose concentration is known accurately. Once RSFs are determined using the internal reference standards, the concentration of an element or molecule of interest may be calculated using the following formula:

$$c_i = \mathrm{RSF}\left(\frac{I_i}{I_m}\right) \qquad \text{Equation A1.1}$$

where c_i is the concentration of the element or molecule of interest (in units determined by the value assigned to the reference standard), I_i is the observed signal intensity (in counts/second) of the element or molecule of interest, and I_m is the observed signal intensity of the matrix element (same units) used to internally calibrate signal intensity.

Internal reference standards must be synthesized and analysed using the same instrument and conditions that will be used to analyse samples with unknown compositions to calculate RSFs. The materials chosen for determination of RSF values

here span a wide compositional range in Mg-Fe-Ti-Al-Cr-Mn-Zn spinel-structured oxide solid solutions. Naturally, these materials will have significantly different mineral densities and hardnesses, which may contribute to the SIMS matrix effect.

In order to estimate these parameters, mineral compositions were determined using a JEOL JXA-8800 electron microprobe located at Hokkaido University. Both oxide and natural standards were used, and data were reduced using the ZAF correction method. Estimation of spinel density requires derivation of molar volume and the atomic molar masses of the cations that comprise each internal standard. In turn, molar volume depends on the unit cell edge length, *a*, which varies as a function of atomic radii of the structurally bound cations. Of course, other effects like multi-valency, site distribution, and structural inversion also affect bond lengths and must be considered during calculation of crystal chemical parameters. Unfortunately, these parameters cannot be determined using EPMA. However, they may be modelled.

Estimation of spinel density was achieved by first populating tetrahedral sites with divalent cations and octahedral sites with purely trivalent Al and Cr (which is commonly trivalent under relevant magmatic conditions). Then, multivalent cations such as Fe, Mn, and Ni were attributed to the octahedral sites in order until achieving charge balance. The following modified relationship was used to calculate *a* for spinel minerals (after Deer et al., 1992):

$$a(\text{Å}) = 5.970 + 0.95R^{2+} + 2.79R^{3+} \qquad \text{Equation A1.2}$$

where R^{2+} and R^{3+} refer to the ionic radii of divalent and trivalent cations, respectively. The experimental results of Bosi et al. (2009) were used to estimate the degree of *a* extension due to the substitution of Ti^{4+} in octahedral coordination. Spinel molar volume was then calculated on the basis of 32 oxygen atoms and 24 cations per unit cell. Spinel density was calculated by dividing the sum of the atomic molar masses (inferred using EPMA) by the estimated molar volume.

Once the density of each internal standard was inferred, the samples were implanted with a fixed dosage of ^{2}H using a NISSIN Co. LTD. RD-200 device housed at the Advanced Institute of Science and Technology in Tsukuba, Japan. A dose of 1×10^{15} atoms/cm^2 were implanted at ambient conditions with an accelerating voltage of 40 keV.

Subsequent depth profiling using a Cameca IMS-1270 mass spectrometer housed within the Isotope Imaging Laboratory at Hokkaido University was used to determine ^{2}H, $^{16}O^{2}H$, $^{17}O^{1}H$, and ^{18}O signal intensities. High mass resolution ($M/\Delta M = c.\ 8{,}700$) was achieved for the purpose of separating the dimer species from one another. After analysis, crater depth was measured using a Keyence VK-X200 laser microscope (also at Hokkaido University). Then the RSF was calculated using ^{18}O as a reference element (the concentration of which is constant) using the following relationship (after Van der Heide, 2014):

$$\mathrm{RSF} = \frac{(\delta \times \mathrm{I}_m \times \mathrm{C} \times \mathrm{t})}{(d\Sigma \mathrm{I}_i - d\Sigma \mathrm{I}_b \times \mathrm{C})} \qquad \text{Equation A1.3}$$

where I_m and I_i are the same as above, δ is the dose of the implanted ion (in atoms/cm^2), C is the number of data points over the course of the depth profile, t is the analysis time (or sputtering time), d is the crater depth (in cm), ΣI is the summed signal intensity over the depth profile, and I_b is the background signal intensity (in counts/second).

Analysis of the RSF values determined for both ^{2}H and $^{16}O^{2}H$ revealed the changes in these isotopes/dimers with depth and allowed for the correlation of the RSF values calculated for each to the density of the spinel mineral in question. Crucially,$^{16}O^{2}H$ production was observed to be much greater than ^{2}H production in the signal spectra, which guided our analysis of unknown sample materials. RSF values were calculated as a function of spinel density with respective accuracies of ± 30% (2σ) and ± 24% (2σ) for ^{2}H and $^{16}O^{2}H$ (above densities of 4.5 g/cm^3). At lower density, the RSF for $^{16}O^{2}H$ was observed to be almost an order of magnitude higher. These RSFs provide a quantitative basis for investigating H concentrations of natural spinel minerals using the Cameca IMS-1270. A table summarizing the results of RSF calculation is given below (Table A1.1).

Table A1.1: Standard and RSF information for quantifying OH in spinel

Sample ID	Fe-Spinel	Mg-Chromite	Jakobsite	Magnetite	Franklinite
a (Å, estimated)	8.12	8.29	8.46	8.48	8.46
density (g/cm^3)	3.72	4.39	4.68	4.98	5.14
^{2}H RSF* (Avg.)	1.26	1.00	0.88	1.22	1.18
Rel. SD (2σ)	6%	8%	19%	22%	12%
$^{16}O^2H$ RSF* (Avg.)	27.05	6.85	3.09	3.37	3.89
Rel. SD (2σ)	11%	-	-	-	7%

**RSF is × 10^{22} atoms/cm^3 for ^{2}H and × 10^{20} atoms/cm^3 for $^{16}O^2H$, - = not available*

Appendix 2: Data used to estimate Fe-loss to Pt capsule walls

See electronic supplement.

Appendix 3: Glass analyses

See electronic supplement.

Appendix 4: Chromite analyses

See electronic supplement.

Appendix 5: Orthopyroxene analyses

See electronic supplement.

Appendix 6: Literature data used for comparison to synthetic products

See electronic supplement.

Appendix 7: SPINMELT-2.0 model output for natural samples from the Troodos Ophiolite

See electronic supplement.

Appendix 8: Supplemental data for basaltic samples produced by IHPV experiments

This appendix provides additional compositional, textural, and calculated f_{O_2} values for basaltic samples produced during the same IHPV experiments as detailed in Chapters 3.1 and 4.

To review, the starting materials for these experiments were Manganui D2 scoria (Chapter 2.2.2) and magnetite from the Marquette Iron Range (Ishpeming, Michigan, USA). Glass was made from the scoria using an atmospheric muffle furnace. Whole rock powder was placed into a Fe-saturated Pt crucible and held at 1300 ℃ for *c*. 5 hours before quenching under water. Most of the glass was re-powdered for sample loading. However, several small pieces were mounted and polished for EPMA and textural analysis (BA-G, Table A8.1). No microlites were visible during SEM imaging.

Table A8.1: Starting material compositions

Sample	BA-G	Magnetite
No. Analyses	12	20
SiO_2	50.45 (0.23)	-
TiO_2	0.45 (0.02)	-
Al_2O_3	18.30 (0.16)	-
FeO	9.46 (0.31)	91.79 (0.95)
MnO	0.15 (0.04)	-
MgO	4.79 (0.07)	-
CaO	10.09 (0.09)	-
Na_2O	3.04 (0.10)	-
K_2O	1.57 (0.03)	-
P_2O_5	0.14 (0.08)	-
Total	98.48	91.79

- = not detected

During EPMA, no minor elements were detected in the Marquette magnetite, confirming its purity. No Cr was detected during EPMA of any of the starting materials for these experiments.

Table A8.2 gives experiment and sample information. No phases other than spinel (disregarding quench crystallization) were stable in products produced at 1150-1200 ℃. At 1100 ℃, clinopyroxene and plagioclase feldspar appear as liquidus phases. Data on

Table A8.2: Sample identification, characterization, experiment descriptions, and preliminary results

Capsule ID	*IHPV Lab*	*Initial Composition*		*Experimental Conditions*			
		Seed Size (μm)	wt.% D_2O (1σ)	T (°C)	P (kbar)	pH_2^{added} (bars)	Duration (hrs)
Bas1200Ua	ISTO	x < 32	1.765 (0.147)	1200	2.13	0	4
Bas1200Ub	ISTO	160 < x < 250	0.828 (0.166)	1200	2.13	0	4
Bas1200Ba	ISTO	x < 32	0.794 (0.159)	1200	2.12	1.9	1.4
Bas1200Bb	ISTO	160 < x < 250	0.791 (0.198)	1200	2.12	1.9	1.4
Bas1150U	ISTO	x < 32	0.596 (0.119)	1150	2.16	0	4.2
Bas1150B	ISTO	x < 32	0.904 (0.151)	1150	2.14	1.4	3.2
Bas1100U	GSJ	x < 32	1.300 (0.130)	1100	2	0	5.1

Naming conventions same as Table 4.2

Table A8.2 (continued)

Activity Model		*Oxygen Fugacity*		
Final wt.% ^2H_2O (1σ)	aH_2O (1σ)	Sensor X_{Ni} (1σ)	log fO_2 (bars)	ΔNNO (1σ)
#	*0.19 (0.02)	0.020 (0.004)	-4.39	3.31 (0.09)
#	*0.05 (0.02)	0.020 (0.004)	-5.55	2.15 (0.29)
#	0.05 (0.02)	0.256 (0.003)	-8.56	-0.86 (0.30)
#	0.05 (0.02)	0.256 (0.003)	-8.56	-0.86 (0.30)
#	0.03 (0.02)	0.020 (0.004)	-6.58	1.70 (0.44)
#	0.06 (0.02)	0.194 (0.003)	-8.55	-0.27 (0.30)
4.33	0.60 (0.23)	0.069 (0.009)	-5.99	2.92 (0.28)

*# = same as before, * = calculated using starting material composition*

Table A8.3: Bas1100U clinopyroxene

Analysis	SiO_2	TiO_2	Al_2O_3	FeO	MnO	MgO	CaO	Na_2O	Total
1	51.25	0.91	14.13	7.13	0.19	9.55	15.62	1.65	100.40
2	50.95	0.88	12.11	7.77	0.23	10.54	15.51	1.42	99.47
3	53.13	0.83	17.38	6.85	0.18	7.42	14.02	2.25	100.94
4	52.02	0.92	12.84	7.42	0.22	9.64	14.12	1.72	99.25
5	52.36	0.89	7.22	7.81	0.23	13.94	19.94	0.69	100.49

feldspar is not available due to the small size of the minerals grown (≤ 5 μm diameter). Analyses of clinopyroxene are provided in Table A8.3.

Using Trainable Weka Segmentation (Chapter 3.3.2), the ratio of feldspar to clinopyroxene is roughly 8:1. However, based on the textural variability between sections of this sample (as described in Chapter 5), it would be improper to say that this ratio is true for the sample in sum. The feldspar produced in this experiment is very difficult to distinguish from the melt phase (see Figure 5.5), and the estimate given above was produced by a single image segmentation. Reproducibility for the phase proportions exceeded 5% relative for this image owing to the rims surrounding plagioclase crystals and thus the heterogeneity of the glass phase.

Bas1200Ba and Bas1200Bb both completely resorbed their seed magnetites, and Bas1150B did as well (Figure A8.1). These samples are nearly crystal-free, as Bas1150U contains a very small amount of quench-produced crystals (Figure A8.2).

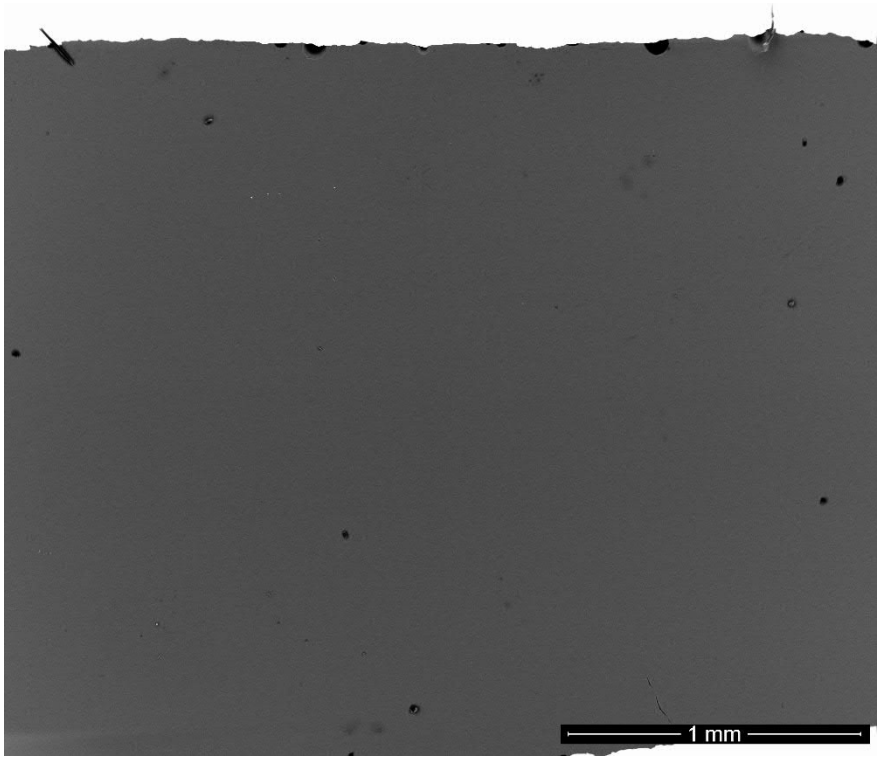

Figure A8.1: Sample Bas1200Bb. No seed magnetite is visible, indicating its complete resorption into the sample melt. Minor vesicularity is due to trapped atmosphere.

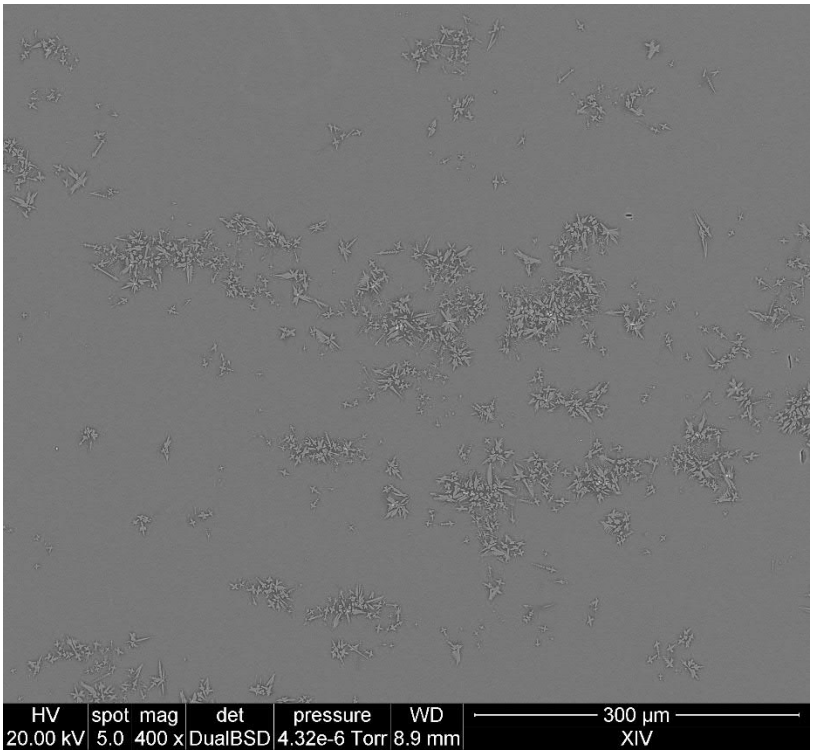

Figure A8.2: Sample Bas1150B showing sparse quench crystallization.

MASSEY UNIVERSITY
TE KUNENGA KI PŪREHUROA
UNIVERSITY OF NEW ZEALAND

GRADUATE RESEARCH SCHOOL

STATEMENT OF CONTRIBUTION
DOCTORATE WITH PUBLICATIONS/MANUSCRIPTS

We, the candidate and the candidate's Primary Supervisor, certify that all co-authors have consented to their work being included in the thesis and they have accepted the candidate's contribution as indicated below in the *Statement of Originality*.

Name of candidate:	Daniel A Coulthard Jr.
Name/title of Primary Supervisor:	Professor Georg F. Zellmer
In which chapter is the manuscript /published work:	Chapter 4

Please select one of the following three options:

(●) The manuscript/published work is published or in press

- Please provide the full reference of the Research Output:

Coulthard Jr, D. A., Zellmer, G. F., Tomiya, A., Jégo, S., & Brahm, R. (2021). Petrogenetic implications of chromite-seeded boninite crystallization experiments: Providing a basis for chromite-melt diffusion chronometry in an oxybarometric context. Geochimica et Cosmochimica Acta. https://doi.org/10.1016/j.gca.2021.01.017

( ) The manuscript is currently under review for publication – please indicate:

- The name of the journal:

- The percentage of the manuscript/published work that was contributed by the candidate:

- Describe the contribution that the candidate has made to the manuscript/published work:

( ) It is intended that the manuscript will be published, but it has not yet been submitted to a journal

Candidate's Signature:	Daniel A Coulthard Jr. Digitally signed by Daniel A Coulthard Jr. DN: cn=Daniel A Coulthard Jr., c=NZ, o=Massey University, email=d.a.coulthard@massey.ac.nz Date: 2021.06.24 11:04:12 +12'00'
Date:	24-Jun-2021
Primary Supervisor's Signature:	Georg F. Zellmer Digitally signed by Georg F. Zellmer DN: cn=Georg F. Zellmer, c=NZ, o=Massey University, ou=School of Agriculture and Environment, email=g.f.zellmer@massey.ac.nz Date: 2021.06.24 11:07:26 +12'00'
Date:	24-Jun-2021

This form should appear at the end of each thesis chapter/section/appendix submitted as a manuscript/ publication or collected as an appendix at the end of the thesis.

MASSEY UNIVERSITY
TE KUNENGA KI PŪREHUROA
UNIVERSITY OF NEW ZEALAND

GRADUATE RESEARCH SCHOOL

STATEMENT OF CONTRIBUTION
DOCTORATE WITH PUBLICATIONS/MANUSCRIPTS

We, the candidate and the candidate's Primary Supervisor, certify that all co-authors have consented to their work being included in the thesis and they have accepted the candidate's contribution as indicated below in the *Statement of Originality*.

Name of candidate:	Daniel A Coulthard Jr.
Name/title of Primary Supervisor:	Professor Georg F. Zellmer
In which chapter is the manuscript /published work:	Chapter 5

Please select one of the following three options:

○ The manuscript/published work is published or in press

- Please provide the full reference of the Research Output:

○ The manuscript is currently under review for publication – please indicate:

- The name of the journal:

- The percentage of the manuscript/published work that was contributed by the candidate:

- Describe the contribution that the candidate has made to the manuscript/published work:

◉ It is intended that the manuscript will be published, but it has not yet been submitted to a journal

Candidate's Signature:	Daniel A Coulthard Jr. Digitally signed by Daniel A Coulthard Jr. DN: cn=Daniel A Coulthard Jr., c=NZ, o=Massey University, email=d.a.coulthard@massey.ac.nz Date: 2021.06.23 15:01:43 +12'00'
Date:	23-Jun-2021
Primary Supervisor's Signature:	Georg F. Zellmer Digitally signed by Georg F. Zellmer DN: cn=Georg F. Zellmer, c=NZ, o=Massey University, ou=School of Agriculture and Environment, email=g.f.zellmer@massey.ac.nz Date: 2021.06.23 17:08:42 +12'00'
Date:	23-Jun-2021

This form should appear at the end of each thesis chapter/section/appendix submitted as a manuscript/ publication or collected as an appendix at the end of the thesis.

MASSEY UNIVERSITY
TE KUNENGA KI PŪREHUROA
UNIVERSITY OF NEW ZEALAND

GRADUATE RESEARCH SCHOOL

STATEMENT OF CONTRIBUTION
DOCTORATE WITH PUBLICATIONS/MANUSCRIPTS

We, the candidate and the candidate's Primary Supervisor, certify that all co-authors have consented to their work being included in the thesis and they have accepted the candidate's contribution as indicated below in the *Statement of Originality*.

Name of candidate:	Daniel A Coulthard Jr.
Name/title of Primary Supervisor:	Professor Georg F. Zellmer
In which chapter is the manuscript /published work:	Chapter 6

Please select one of the following three options:

○ The manuscript/published work is published or in press

- Please provide the full reference of the Research Output:

○ The manuscript is currently under review for publication – please indicate:

- The name of the journal:

- The percentage of the manuscript/published work that was contributed by the candidate:

- Describe the contribution that the candidate has made to the manuscript/published work:

◉ It is intended that the manuscript will be published, but it has not yet been submitted to a journal

Candidate's Signature:	Daniel A Coulthard Jr. Digitally signed by Daniel A Coulthard Jr. DN: cn=Daniel A Coulthard Jr., c=NZ, o=Massey University, email=d.a.coulthard@massey.ac.nz Date: 2021.06.23 15:03:21 +12'00'
Date:	23-Jun-2021
Primary Supervisor's Signature:	Georg F. Zellmer Digitally signed by Georg F. Zellmer DN: cn=Georg F. Zellmer, c=NZ, o=Massey University, ou=School of Agriculture and Environment, email=g.f.zellmer@massey.ac.nz Date: 2021.06.23 17:07:41 +12'00'
Date:	23-Jun-2021

This form should appear at the end of each thesis chapter/section/appendix submitted as a manuscript/ publication or collected as an appendix at the end of the thesis.